



X-ray and Gamma-ray Study of TeV Blazars with *RXTE*,
XMM-Newton, and the Whipple 10 m Telescope

Jeffrey Grube

November 21, 2007

*Submitted in accordance with the requirements for
the degree for Doctor in Philosophy.*

The University of Leeds
School of Physics & Astronomy

The candidate confirms that the work submitted is her own and that appropriate credit
has been given where reference has been made to the work of others.

This copy has been supplied on the understanding that it is copyright material
and that no quotation from the thesis may be published without proper acknowledgement



For Alice Kain. (Above) *Flight into Egypt* by Adam Elsheimer in 1609, the first oil painting to feature the Milky Way. During the same year Galileo resolved the Milky Way into a band of individual stars with his newly built refractor telescope.

Abstract

This thesis presents long-term X-ray and TeV γ -ray observations from 2000 to 2006 of three TeV blazar type Active Galactic Nuclei (AGN): Mrk 421, Mrk 501, and H1426+428. Standard emission models for TeV blazars predict correlated and highly variable X-ray and TeV γ -ray radiation from accelerated electrons in a jet orientated along our line of sight. By using a large sample of near simultaneous observations, this thesis examines potential flux and spectral correlations between the X-ray and TeV γ -ray energy bands. Joint nightly observations of Mrk 421 with the X-ray instrument *RXTE* PCA, and at 0.5–10 TeV γ -ray energies with the Whipple 10 m telescope during periods ranging from a week to 6 months revealed complicated, high amplitude flaring. Spectral variability was investigated for the rising and decay phases of large isolated day timescale flares. Generally, the X-ray and TeV γ -ray spectra hardened with increasing integral flux, but a consistent spectral evolution was not shown between individual flares. Absorption of the TeV γ -ray energy spectrum by the extragalactic background light (EBL) was corrected for. During a large flare in March 2001, tentative evidence was found for a highly curved intrinsic TeV γ -ray energy spectrum peaking at 0.85 ± 0.22 TeV simultaneous to a curved X-ray spectrum peaking at 2.14 ± 0.19 keV. *RXTE* PCA and Whipple 10 m campaigns on Mrk 501 and H1426+428 showed significant X-ray spectral variability, however the TeV γ -ray integral flux remained near the detection limit of the Whipple 10 m. The broadband 0.6–20 keV X-ray spectrum of the 3 TeV blazars was investigated with *XMM-Newton* and *RXTE* PCA observations.

In addition to simultaneous day timescale variability, the large sample of Whipple 10 m observations from 2000 to 2006 allowed for a detailed study of long-term γ -ray variability. For Mrk 421, a weak correlation with large spread is shown for the Whipple 10 m integral flux above 0.6 TeV and *RXTE* ASM X-ray rate on month timescales. From 2001 to 2006, Mrk 501 was recorded by the Whipple 10 m in a low flux state of 27% of the integral flux from the Crab nebula supernova remnant. In July 2005, the MAGIC telescope recorded large TeV γ -ray flaring in Mrk 501 by a factor > 3 of the Crab nebula flux. This high flux state occurred after the Whipple 10 m observing period on Mrk 501 in June 2005, and so could not be verified in this work. The detection of H1426+428 at TeV γ -ray energies by the Whipple 10 m in 2001 is confirmed in this work, however the source was not detected again by the Whipple 10 m over a 5 year period. The detailed study of TeV blazar X-ray and γ -ray variability in this work highlights the need for high sensitivity observations to better resolve complicated and unpredictable flaring states.

Contents

List of figures	iv
List of tables	v
List of Abbreviations	vi
Preface	vii
1 The Blazar Class of Active Galactic Nuclei	1
1.1 Historical Background to Blazar Studies	2
1.2 Properties of TeV Blazars	12
2 X-ray Instrumentation and Data Reduction Methods	19
2.1 Introduction to Past and Current X-ray Observatories	19
2.2 The <i>RXTE</i> Observatory	22
2.3 The <i>XMM-Newton</i> Observatory	26
3 Ground Based Gamma-ray Detection	33
3.1 Imaging Atmospheric Cherenkov Technique	34
3.2 The Whipple 10 m Telescope	42
3.3 Whipple 10 m Calibration and Simulations	48
4 Whipple 10 m Data Reduction	53
4.1 Image Processing	53
4.2 Angular and Energy Reconstruction	56
4.3 γ -ray Selection	60
4.4 Flux and Energy Spectrum Determination	64
4.5 Results from Crab Nebula Observations	67
5 Long-term Observations of TeV Blazars with the Whipple 10 m Telescope	73
5.1 Whipple 10 m Observations	74
5.2 Month Timescale TeV γ -ray Variability in Mrk 421	77

5.3	Results from Long-term Observations of Mrk 501	85
5.4	Results from Long-term Observations of H1426+428	89
6	X-ray and TeV γ-ray Variability in TeV Blazars	93
6.1	Joint <i>RXTE</i> PCA and Whipple 10 m Observations	93
6.2	<i>XMM-Newton</i> Observations	99
6.3	Results from <i>RXTE</i> PCA and Whipple 10 m Campaigns in 2001–2006	100
6.4	<i>XMM-Newton</i> Spectrum of Mrk 421, Mrk 501, and H1426+428	122
7	Interpretation	127
7.1	Correlation of X-ray and TeV γ -ray Flux States	127
7.2	Spectral Energy Distributions of TeV Blazars	129
7.3	Long-term X-ray and TeV γ -ray Flux Variability	132
7.4	Conclusion	134
	Acknowledgements	145

List of Figures

1.1	Optical images of M101 and M59 from Hubble in 1926	2
1.2	Optical images of the jet in M87 from 1956 and 1998	3
1.3	Optical spectrum and polarization of BL Lacertae	6
1.4	Gamma-ray flux variability in 3C 279 and Mrk 421	8
1.5	X-ray and γ -ray flux and spectral variability in Mrk 501 during 1997	10
1.6	Average spectral energy distributions from a sample of 126 blazars	11
1.7	Spectral energy distribution of PKS 2155-304 from Oct. to Nov. 2003	13
1.8	X-ray flux versus radio flux from a large sample of blazars	14
1.9	Spectral energy distribution of the extragalactic background light (EBL)	17
1.10	Optical depth of the extragalactic background light to γ -rays	18
2.1	The <i>RXTE</i> observatory	22
2.2	Effective area of <i>RXTE</i> PCA	23
2.3	<i>RXTE</i> PCA source and modeled background spectrum	26
2.4	The <i>XMM-Newton</i> Observatory	27
2.5	Effective areas of the <i>XMM-Newton</i> X-ray instruments	28
2.6	<i>XMM-Newton</i> MOS and PN Full Frame images of Mrk 421	30
2.7	<i>XMM-Newton</i> PN Small Window and Timing images of Mrk 421	32
3.1	Simulated air showers initiated by a 1 TeV γ -ray and cosmic ray proton	35
3.2	Cherenkov light spectra from vertical γ -ray air showers	37
3.3	Simulated Cherenkov light density initiated by a γ -ray and cosmic ray proton	38
3.4	Detection principle of IACT telescope systems	39
3.5	Photographs of currently operating IACT γ -ray telescope systems	40
3.6	Photograph of the Whipple 10 m telescope	42
3.7	Schematic diagram of the Whipple 10 m signal path	44
3.8	Whipple 10 m trigger rate versus hardware threshold	45

3.9	The Whipple 10 m system dead-time	46
3.10	Whipple 10 m observing efficiency during 2006	47
3.11	Whipple 10 m event rate from Crab nebula observations	48
3.12	Calibration method using muon images.	50
3.13	Whipple 10 m detection efficiency from 2000–2006 measured by muon images.	51
4.1	Whipple 10 m image cleaning using the islands method	54
4.2	Illustration of the Hillas image parameters and Disp optimization	55
4.3	Whipple 10 m reconstructed γ -ray direction for the Crab nebula	56
4.4	Lookup tables for mean simulated energy, Width, and Length	58
4.5	Relative error in the energy reconstruction	59
4.6	Whipple 10 m image parameter distributions for the Crab nebula	61
4.7	Crab nebula Alpha parameter distribution and cut efficiency	63
4.8	Effective Area of the Whipple 10 m telescope	65
4.9	Differential rate expected for the Crab nebula	66
4.10	Integral flux light curve of the Crab nebula during 2000–2006	69
4.11	Whipple 10m energy spectrum of the Crab nebula from 2000–2006	69
4.12	Total Whipple 10 m Crab nebula spectrum compared to previous TeV γ -ray results	70
5.1	Whipple 10 m Alpha distribution of Mrk 421 in Mar. 2001 and Apr. 2003	77
5.2	Long-term X-ray and TeV γ -ray light curve of Mrk 421 during 2000-2006	78
5.3	Correlation for Mrk 421 of the X-ray rate and TeV γ -ray flux	80
5.4	TeV γ -ray energy spectrum of Mrk 421 from “monthly” Whipple 10 m observations	82
5.5	Estimate on the intrinsic TeV γ -ray energy spectrum of Mrk 421 in a high flux state	83
5.6	Whipple 10 m Alpha distribution of Mrk 501 in Apr. 2004 and Jun. 2005	86
5.7	Light curve of Mrk 501 at X-ray and TeV γ -ray energies from 2001 to 2006	87
5.8	TeV γ -ray energy spectrum of Mrk 501 at a low to medium flux state	88
5.9	Whipple 10 m Alpha distribution of H1426+428 in Mar. 2001 and Apr.–May 2002	89
5.10	Light curve of Mrk H1426+428 at X-ray and TeV γ -ray energies during 2001–2006	90
5.11	TeV γ -ray energy spectrum of H1426+428 in March 2001	91
6.1	Light curve of Mrk 421 with <i>RXTE</i> PCA and <i>XMM-Newton</i> observing periods	97
6.2	Light curve of Mrk 501 with <i>RXTE</i> PCA and <i>XMM-Newton</i> observing periods	98
6.3	Light curve of H1426+428 with <i>RXTE</i> PCA and <i>XMM-Newton</i> observing periods	99
6.4	Spectral curvature in the <i>RXTE</i> PCA spectrum of Mrk 421	103
6.5	Comparison of X-ray spectra with <i>RXTE</i> PCA Standard Products	104

6.6	<i>RXTE</i> PCA and Whipple 10 m light curve on Mrk 421 in Jan. and Mar. to Apr. 2001	105
6.7	<i>RXTE</i> PCA and Whipple 10 m correlation plots for Mrk 421 in Jan. and Mar. to Apr. 2001	106
6.8	Simultaneous <i>RXTE</i> PCA and Whipple 10 m spectra of Mrk 421 in Mar. 2001 . .	108
6.9	<i>RXTE</i> PCA and Whipple 10 m light curve of Mrk 421 in Dec. 2002 and Jan. 2003	110
6.10	<i>RXTE</i> PCA and Whipple 10 m correlation plots for Mrk 421 in Dec. 2002 and Jan. 2003	111
6.11	Simultaneous <i>RXTE</i> PCA and Whipple 10 m spectra of Mrk 421 in Jan. 2003 . .	112
6.12	Light curve of the <i>RXTE</i> PCA campaign on Mrk 421 from Feb. to May 2003 . . .	113
6.13	<i>RXTE</i> PCA and Whipple 10 m correlation plots during Feb. to May 2003	114
6.14	Light curve of the <i>RXTE</i> PCA campaign on Mrk 421 from Dec.2003 to May 2004	115
6.15	<i>RXTE</i> PCA and Whipple 10 m correlation plots from Dec.2003 to May 2004 . . .	116
6.16	Simultaneous <i>RXTE</i> PCA and Whipple 10 m spectra of Mrk 421 in Apr. 2004 . .	117
6.17	Light curve of the <i>RXTE</i> PCA campaign on Mrk 421 from Jan. to May 2006 . . .	118
6.18	<i>RXTE</i> PCA and Whipple 10 m correlation plots from Jan. to May 2006	119
6.19	Simultaneous <i>RXTE</i> PCA and Whipple 10 m spectra of Mrk 421 in Jan. 2006 . .	119
6.20	Light curve of the <i>RXTE</i> PCA campaign on Mrk 501 in Jun. 2004	120
6.21	<i>RXTE</i> PCA flux and spectral correlation of Mrk 501 in Jun. 2004	121
6.22	Light curve of the <i>RXTE</i> PCA campaign on H1426+428 from Mar. to Jun. 2002 .	122
6.23	<i>RXTE</i> PCA flux and spectral correlation of H1426+428 in Apr. 2002	123
6.24	Spectral curvature in the <i>XMM-Newton</i> spectrum of Mrk 421	123
6.25	<i>XMM-Newton</i> PN energy spectrum of Mrk 421 and H1426+428	124
7.1	Flux correlation of Mrk 421 from all joint <i>RXTE</i> PCA and Whipple 10 m observations	128
7.2	Spectral energy distributions of Mrk 421 in a high and low flux state	129
7.3	Spectral energy distributions of Mrk 501	130
7.4	Spectral energy distributions of H1426+428	131
7.5	Correlation of derived <i>RXTE</i> ASM fluxes with <i>RXTE</i> PCA fluxes using Mrk 421 .	132
7.6	Long-term X-ray and TeV γ -ray light curve of Mrk 421, Mrk 501, and H1426+428	133

List of Tables

1.1	TeV blazars detected as of November 2007	15
2.1	Performance of current X-ray satellite missions	21
3.1	Performance of current IACT telescopes	41
4.1	Whipple 10 m selection cuts	64
4.2	Whipple 10 m observations of the Crab nebula	68
4.3	Energy spectrum of the Crab nebula with the Whipple 10 m	71
5.1	Whipple 10 m observations of Mrk 421 during 2000–2006	75
5.2	Whipple 10 m observations of Mrk 501 from 2001–2006	76
5.3	Whipple 10 m observations of H1426+428 from 2001–2006	76
5.4	Best fit model parameters to the monthly TeV γ -ray energy spectra of Mrk 421	84
6.1	<i>RXTE</i> PCA Observations of Mrk 421 from 2001 to 2006	95
6.2	Whipple 10 m observations of Mrk 421 during <i>RXTE</i> PCA observing periods	96
6.3	<i>RXTE</i> PCA Observations of Mrk 501 and H1426+428 from 2001 to 2006	97
6.4	Whipple 10 m observations of Mrk 501 and H1426+428	98
6.5	<i>XMM-Newton</i> PN Observations of Mrk 421 from 2000 to 2006	101
6.6	<i>XMM-Newton</i> PN Observations of Mrk 501 and H1426+428 from 2000 to 2006	102
6.7	Best fit model parameters to <i>XMM-Newton</i> PN energy spectra of Mrk 421	125
6.8	Best fit model parameters to <i>XMM-Newton</i> PN energy spectra of Mrk 501 and H1426+428	126

List of Abbreviations

ASM	All-Sky Monitor
AGN	Active Galactic Nuclei
CAT	Cherenkov Array at Themis
CGRO	Compton Gamma-Ray Observatory
CORSIKA	Cosmic Ray Simulations for Kascade and Auger
EBL	Extragalactic Background Light
EPIC	European Photon Imaging Camera
ESA	European Space Agency
FR	Fanaroff-Riley
HWFM	Full Width at Half Maximum
FOV	Field of View
FSRQ	Flat Spectrum Radio Quasar
GLAST	Gamma-ray Large Area Space Telescope
HEAO	High Energy Astrophysical Observatories
HEASARC	High Energy Astrophysics Science Archive Research Center
HEGRA	High Energy Gamma-Ray Astronomy
H.E.S.S	High Energy Stereoscopic System
HST	Hubble Space Telescope
IACT	Imaging Atmospheric Cherenkov Technique
MAGIC	Major Atmospheric Gamma-ray Imaging Cherenkov
MJD	Modified Julian Date
NASA	National Aeronautics and Space Administration
NSB	Night Sky Background
PCA	Proportional Counter Array
PMT	Photomultiplier
PSF	Point Spread Function
RGS	Reflection Grating Spectrometer
RMS	Root-Mean-Square
RXTE	Rossi X-ray Timing Experiment
SED	Spectral Energy Distribution
SSC	Synchrotron Self-Compton
VERITAS	Very Energetic Radiation Imaging Telescope Array System
VLBI	Very Long Base Line Interferometry

Preface

The aim of this thesis is to expand on previous blazar variability studies by measuring the X-ray and TeV γ -ray flux and spectrum of three TeV blazars over a long-term 6 year period. This preface is intended to clarify the thesis organization and content by examining each chapter:

- **Chapter 1** The discovery and early investigations of blazar type Active Galactic Nuclei (AGN) are reviewed in order to provide a general context to the TeV blazar results presented in chapters 5–7. Pioneering work toward the accepted blazar framework of relativistically beamed jet emission is highlighted, concluding with an overview on current leptonic and hadronic emission models and characteristic blazar spectral energy distributions (SEDs).
- **Chapter 2** Current X-ray satellite observatories are introduced, and their performance compared. Data reduction methods are described for the >800 hours of *RXTE* PCA data and >200 hours of *XMM-Newton* data analyzed in this thesis work.
- **Chapter 3** After an overview of air shower physics and the imaging atmospheric Cherenkov technique (IACT) of TeV γ -ray telescopes, operations with the Whipple 10 m telescope are described. Gain calibration and a large set of γ -ray air shower and detector simulations generated in this work are discussed.
- **Chapter 4** The Whipple 10 m telescope data reduction methods developed in this work are described in detail. The flux and energy spectrum of the Crab nebula was measured from 2000–2006 with the Whipple 10 m telescope to test the analysis procedures on long timescales, since the Crab is a bright non-variable calibration source at TeV γ -ray energies. The Whipple 10 m results on the Crab nebula were shown to agree within systematic errors to recent results from other IACT γ -ray telescopes.
- **Chapter 5** Long-term TeV γ -ray flux and spectra results of Mrk 421, Mrk 501, and H1426+428 are presented from the >600 hours of Whipple 10 m observations. The TeV energy spectrum of Mrk 421 was measured over a large range of flux states, with a weak correlation of spectra hardening at increasing flux levels. The energy spectrum of Mrk 501 and H1426+428 were also measured and corrected for absorption by the extragalactic background light (EBL).
- **Chapter 6** Joint *RXTE* PCA and Whipple 10 m observations of TeV blazars from 2001–2006 were investigated for variability on day timescales. Seven observing campaigns on Mrk 421 ranging from a week to 6 months displayed conflicting flaring behavior between

the X-ray and TeV γ -ray energy bands. In particular, simultaneous X-ray and TeV spectral evolution during the rising and decaying phase of day timescale flares differed significantly between observing periods. Mrk 501 was observed in a low flux state in June 2004, with little variability shown in the X-ray band. Stronger X-ray variability was shown for H1426+428 over the period of March to June 2002.

- **Chapter 7** Three key aspects in TeV blazar studies are addressed, drawing on the results in chapters 5 and 6. First, the X-ray and TeV γ -ray flux states from simultaneous observations are shown to be weakly correlated, contradicting previous claims of a strong flux correlation. Second, SEDs of the three blazars are constructed with past measurements, and are discussed in the framework of the Synchrotron Self-Compton (SSC) model. Third, long-term X-ray and TeV γ -ray flux variability is compared between the three blazars. One immediate conclusion from this large sample of TeV blazar observations is that higher sensitivity observations with better temporal sampling are needed to disentangle the variability timescales of TeV blazars.

Chapter 1

The Blazar Class of Active Galactic Nuclei

Increasingly large surveys of over 10^5 galaxies reveal that only a small percentage contain strong non-thermal activity in their core (Hao et al. 2005). The study of Active Galactic Nuclei (AGN) began in 1943 when Seyfert detected nuclear emission lines in the cores of 12 galaxies (Seyfert 1943). A small class of AGN termed BL Lac objects were discovered in the 1970s with variable, highly polarized, and nearly featureless continuum emission in the radio and optical bands. These unique observational properties were interpreted within the framework of relativistically beamed synchrotron emission emerging from the base of a centrally powered jet oriented along our line of sight (Blandford and Rees 1978). Showing similar indications of beaming effects, but differing in the relative strength of emission lines, BL Lac objects were jointly classified with flat spectrum radio quasars (FSRQs) as blazars (Angel and Stockman 1980). The detection of rapid γ -ray variability in the blazar 3C 279 by EGRET onboard the *CGRO* satellite, and hour timescale variability detected in Mrk 421 at energies above 0.5 TeV by the Whipple 10 m ground based telescope provided strong evidence of relativistic Doppler boosted emission (Maraschi et al. 1992; Punch et al. 1992). A characteristic spectral energy distribution (SED) for blazars was constructed with two broad components extending over a continuum emission from radio to γ -ray energies. The energy output in the first SED component (attributed to synchrotron radiation) was shown for powerful blazars to peak in the infrared to optical band, while for low luminosity blazars the synchrotron peak is located at UV to X-ray energies (Fossati et al. 1998a). The location of the second peak in the SED is closely correlated to the synchrotron peak energy, and for low power blazars is expected to lie in the GeV and TeV band. A growing population of blazars have been detected at TeV energies (termed TeV blazars), and demonstrate rapid flux and spectral variability. Drawing from a

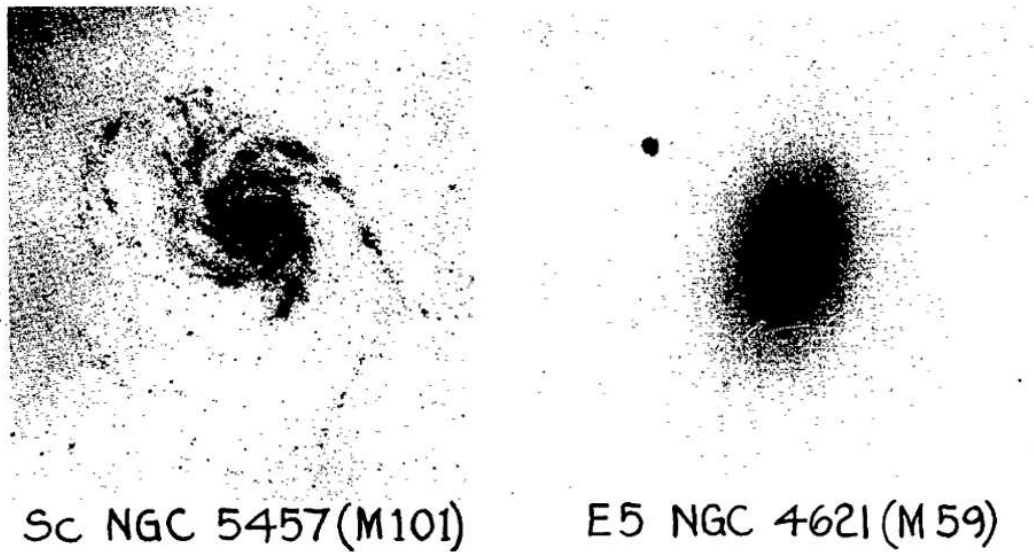


Figure 1.1: Optical images with the Mt. Wilson 100 inch telescope from (Hubble 1926). Shown (left) is the spiral galaxy M101, and (right) the elliptical galaxy M59.

large sample of over 6 years of X-ray and TeV γ -ray observations, this work investigates long-term variability in the TeV blazars Mrk 421, Mrk 501 and H1426+428. The purpose of this chapter is mostly twofold: first, to provide an overview on the progress made in the observational study of blazars using an historical approach, and second, to address the current status and interpretation of X-ray and γ -ray observations of TeV blazars. Section 1.1 reviews selective highlights from a century of galaxy observations and interpretation that lead to the discovery and classification of blazars in the center of certain elliptical galaxies. Section 1.2 provides an updated description blazars detected at TeV energies.

1.1 Historical Background to Blazar Studies

Evidence for distant galaxies beyond our own was first clearly shown in 1925 by Edwin Hubble when he resolved Cepheid stars with high apparent brightness in M31 and M33 using the Mt. Wilson 100 inch (2.5 m) telescope (Hubble 1925; Trimble 1995). The Hubble sequence of galaxy morphology was soon constructed based on optical images of elliptical, spiral, and irregular galaxies (Hubble 1926). Figure 1.1 shows Hubble's optical images of (left) the nearby spiral galaxy M101, and (right) the elliptical galaxy M59. Many years later in 1943 Seyfert published the first sample of 12 galaxies with nonstellar like activity (Seyfert 1943). In some cases, the galactic cores were nearly as bright in optical light as the entire galaxy, showing broad emission lines exclusively in the nuclei. The study of these peculiar galaxies developed with the advent of

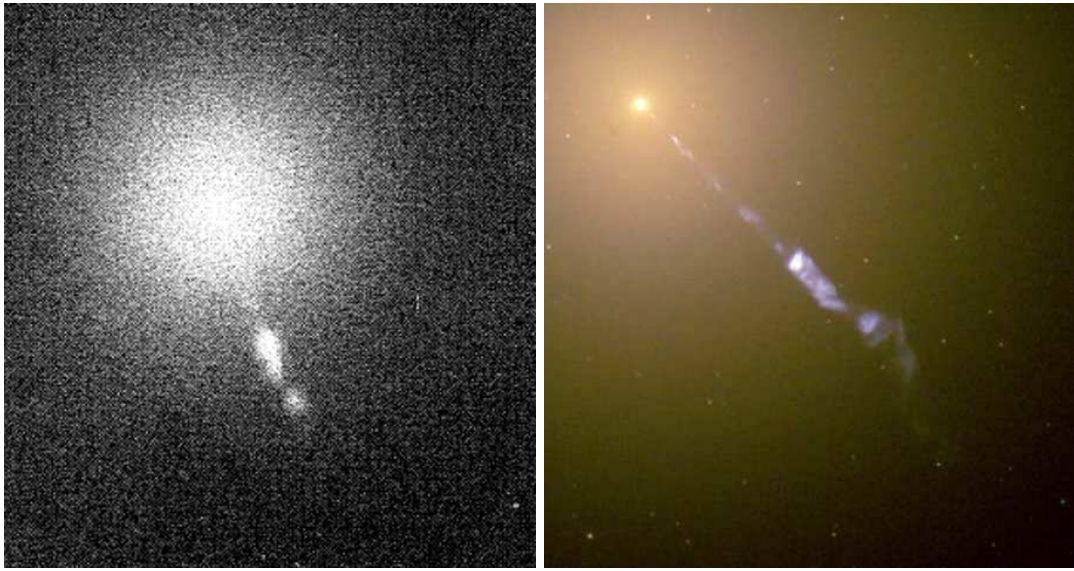


Figure 1.2: (Left) Polarized optical image of M87 taken in March 1956 with the 200 inch Hale telescope from (Baade 1956). Shown (right) is a Hubble Space Telescope (HST) image of the jet and inner region of M87 from observations in 1998 by Biretta et al. (Hubble Heritage Project). Note for scale, the 2.4 kpc long optical jet imaged by HST terminates within the inner part of the elliptical galaxy (Sparks et al. 1996). The full size of M87 is not clearly defined, since beyond the effective radius $R_e \simeq 7$ kpc of surface brightness more than $\sim 10^4$ globular clusters are believed to extend out to a radius > 30 kpc (Wu and Tremaine 2006).

radio astronomy in the late 1940's, which opened a new window to nonthermal emission (Shields 1999).

Synchrotron Radiation in M87 (1956)

In 1950, Alfven and Herlofson proposed the newly discovered synchrotron process could explain nonthermal and highly polarized emission in radio observations, assuming the sources contain relativistic electrons in magnetic fields (Alfven and Herlofson 1950). The total power P per frequency ω of synchrotron emission from a relativistic electron in a magnetic field B is given by:

$$P(\omega, \gamma) = \frac{\sqrt{3}e^3 B \sin \alpha}{2\pi m_e c^2} F\left(\frac{\omega}{\omega_c}\right), \quad \omega_c = \frac{3\gamma^2 e B \sin \alpha}{2m_e c}$$

where γ is the Lorentz factor, e and m_e are the charge and mass of an electron, α is the angle between the magnetic field and electron velocity, c is the speed of light, and $F(\frac{\omega}{\omega_c})$ includes a modified Bessel function with the critical frequency ω_c (Wiedemann 2003). Synchrotron radiation is partially polarized due to the perturbation of electric field lines as the electron is accelerated. Key evidence for synchrotron emission in galactic cores came from optical observations by Baade

and Minkowski, who identified the bright radio source Vir A inside the massive elliptical galaxy M87 (Baade and Minkowski 1954; Mushotzky 2004). Two clues pointed to the nucleus of M87 being the source of the radio plasma: first, the nucleus contained ionized gas, and second, the radio source coincided with a bright narrow 1 kpc long optical jet (first detected in 1917 by Curtis) emanating from the core (Curtis 1917; Ferrarese and Ford 2005). Follow-up observations of the jet in M87 revealed that the optical continuum is polarized, showing clear signs of synchrotron radiation (Baade 1956). Figure 1.2 (left) shows Baade’s polarized image of M87 with the 200 inch Hale telescope from 1956, and (right) the jet in M87 from high resolution optical observations with the Hubble Space Telescope (HST) from 1998.

Insights from the Powerful Quasar 3C 273 (1964)

The revised Cambridge 3C survey identified 328 strong radio sources, many of which are known by their 3C number (Bennett 1962). Radio observations of 3C 273 with the Parkes 210 ft telescope during moon occults revealed two components, one centered on a 13 mag “star” (the nucleus of 3C 273), and the other separated by 20 arcsec showing an unrecognized radio spectrum (Hazard et al. 1963). The second component was found to coincide with an optical jet pointing away from the “star” (Shields 1999). Greenstein and Schmidt conducted a detailed study of 3C 273 and 3C 48, calculating a mass of $\sim 10^9 M_{\odot}$ in the nucleus of 3C 273 to account for the $\geq 10^6$ year energy lifetime implied by the jet (Greenstein and Schmidt 1964). It was argued this mass was needed to confine the line emitting gas, which would disperse quickly if it expanded at the observed speeds of 100 km/s (Shields 1999). Rees offered a relativistic model to explain the strong radio variability seen in 3C 273 (Rees 1966). Section 1.2 describes the current interpretation of a supermassive black hole powering large scale jets in the core of certain active elliptical galaxies.

Optical Quasar Surveys (1960’s)

Throughout the 1960’s quasars were discovered in the optical band as blue point like objects with redshifted broad emission lines and strong variable continuum (Collin 2006). The Mt. Wilson and Palomar observatories carried out systematic searches for quasars, with 44 sources reviewed in detail (Sandage 1965). In Armenia, Markarian undertook searches for sources with a strong ultra-violet continuum, discovering 1515 galaxies in total (Markarian 1969). A review of this discovery period of galactic nuclei was presented by Burbidge in 1970, in which he categorized the nuclei from both normal galaxies, and from “galaxies with highly active or explosive nuclei” (Burbidge 1970).

Fanaroff and Riley Classification of Radio Galaxies (1974)

Important galactic surveys were also undertaken in the radio band during the late 1960's. The Cambridge One Mile telescope mapped radio emission from 199 sources comprising the 3C complete sample with 23 arcsec resolution at 1.4 GHz (Macdonald et al. 1968; Mackay 1971). Fanaroff and Riley examined these observations, together with a subset of 57 sources at 6 arcsec resolution, and divided 31% of the sources into two distinct classes (now known as FR I and FR II type radio galaxies) based on their morphology and radio power (Fanaroff and Riley 1974). The primary class distinction was distance of the "hot spots" in the jets to the galactic core. Fanaroff and Riley also discovered a sharp total luminosity divide between the classes. Nearly all low luminosity radio galaxies were brighter toward the inner part of the jet (FR I), while most FR II sources showed high luminosity. Physical reasons for the FR I/II divide are currently still under debate (Ghisellini and Celotti 2001).

Synchrotron Self-Compton Model of Quasar Emission (1974)

In two successive papers Jones et al. first developed (paper 1), and then applied (paper 2) a Synchrotron Self-Compton (SSC) model with the aim of determining the magnetic field strength and angular size for 10 known variable synchrotron emitting quasars (Jones et al. 1974a; Jones et al. 1974b). Theoretical predictions of the angular size relied on source parameters, such as the ratio of Compton and synchrotron fluxes, based on radio energy spectrum measurements and X-ray flux upper limits from *Uhuru*. The derived angular size of the SSC emitting region showed good agreement with high angular resolution Very Long Base Line Interferometry (VLBI) radio estimates from (Kellermann et al. 1971). Two highly variable sources BL Lacertae and OJ 287 (now known to be blazars) indicated relativistic motion, prompting Jones et al. to argue for relativistic beaming of a closely aligned particle jet to the line of sight among two other possibilities for the observed rapid variability (Jones et al. 1974b). Observational insights into BL Lacertae and classification schemes for similar objects are described below.

Classification of BL Lacertae type Objects (BL Lacs) (1976)

In 1974 Oke and Gunn determined the redshift and energy distribution of the elliptical galaxy BL Lacertae, which hosts a strongly variable nonthermal nucleus (Oke and Gunn 1974). The nucleus was first observed in 1929, thought to be a variable star in 1941, and in 1969 polarization and variability were found both by optical and radio observations (Hoffmeister 1929; Andrew et al. 1969; Visvanathan 1969; Beckmann 2001). Figure 1.3 (left) shows the optical spectrum of BL Lacertae in Jan. 1970 from the total galaxy emission, and from a core removed annulus revealing the thermal absorption features of the elliptical galaxy. The total spectrum from Oct. 1973 is also shown

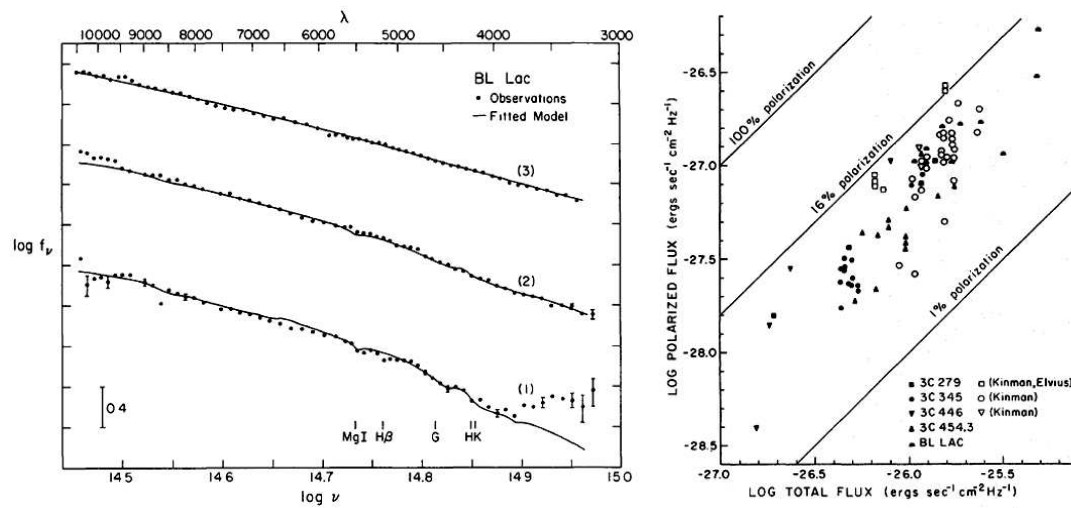


Figure 1.3: (Left) Optical spectra of BL Lacertae from (Oke and Gunn 1974). Spectra labeled (1) and (3) are from Jan. 1970 with the 5 m Hale telescope, (1) is the total galaxy emission, and (3) the core removed annulus of the elliptical galaxy. The total optical spectrum from Oct. 1973 is shown in (2). (Right) Optical B wavelength polarized flux versus total B continuum flux from BL Lacertae and four other sources with similar optical properties (Visvanathan 1973).

as an example of the optical flux variability observed in BL Lacertae. On the (right) in figure 1.3 is shown the optical polarization level of BL Lacertae and five other sources. A small number of elliptical galaxies were soon identified as hosting BL Lacertae type objects (BL Lacs) in their nuclei based on their variable and nearly featureless optical spectrum, including the Markarian galaxies Mrk 421 and Mrk 501 (Ulrich 1973; Veron and Veron 1975; Khachikian and Weedman 1974). In total, 30 BL Lacs (8 with known redshift) were identified based on similar optical and radio behavior, more specifically: strong variability, high polarization, a nonthermal continuum, and in the optical spectrum a lack of clear emission lines (Stein et al. 1976). It's important to note at that time the only BL Lac detected at X-ray energies was Mrk 421 by the Ariel V satellite (Ricketts et al. 1976).

A Core Located Supermassive Black Hole and Relativistic Jet Beaming in Blazars (1978)

In 1977 Rees outlined theoretical arguments for accretion onto a supermassive black hole in modeling a mass concentration of $10^6 - 10^9 M_{\odot}$ within a region of ≤ 1 pc at the core of quasars (Rees 1977). Osterbrock investigated observational support for the model of a rotating disk of broad-line emitting gas outside and around the black hole accretion disk (Osterbrock 1978). The same year Blandford and Rees supported the theoretical model of relativistic beaming to explain the continuum emission seen in BL Lacertae-type galactic nuclei (Blandford and Rees 1978). Although

stationary synchrotron emission could produce the generally observed high polarization and power law spectra, the high optical luminosity and strong variability suggested synchrotron emissions regions are seen moving relativistically downstream to within a few degrees of the observer, the same conclusion as (Jones et al. 1974b). Blandford and Rees also predicted that BL Lacs are the beamed counterparts to the base of jets found in radio galaxies. Angel and Stockman reviewed the collected optical and radio observations of BL Lacs, promoting the use of *blazar*, coined first by Spiegel, to merge the separate classifications for BL Lacs and variable polarized quasars based on the relativistic beaming model (Angel and Stockman 1980).

Radio to X-ray Multiwavelength Study of Mrk 501 (1978)

The study of X-ray emission in blazars was established following the launch of NASA's three High Energy Astrophysical Observatories (HEAOs) in three successive years: HEAO-1 in 1977, HEAO-2 in 1978 (renamed *Einstein* after launch), and HEAO-3 in 1979. The second BL Lac detected at X-ray energies was Mrk 501 from HEAO-1 observations (Schwartz et al. 1978). A large multiwavelength campaign on Mrk 501 used contemporaneous radio, infrared, optical, ultraviolet, and X-ray (HEAO-1) observations to sample the continuum spectrum over 8 decades in energy and build a reliable Spectral Energy Distribution (SED) with which to test emission models (Kondo et al. 1981). Reasonable agreements were found for either a synchrotron or Synchrotron Self-Compton (SSC) model for the radio to X-ray SED. Kondo et al. favored the SSC model, implying that the optical to X-ray emission is from Compton scattering. The current interpretation for Mrk 501 is synchrotron radiation over the radio to X-ray energy range, with inverse Compton emission at gamma-ray energies.

Distinguishing Radio and X-ray Selected Blazar Samples (1986)

In 1986 Maraschi et al. compiled flux values for 75 blazars observed in the X-ray, radio, and optical bands (Maraschi et al. 1986). Twelve blazars first discovered at X-ray energies were defined as "X-ray selected", while the other 62 blazars termed "radio selected" were discovered by radio and optical surveys taken from (Angel and Stockman 1980). The majority of X-ray flux values were from *Einstein* observations, detailed in (Schwartz and Ku 1983). All 12 X-ray selected blazars showed a lack of strong emission lines in the optical spectrum, fitting the BL Lac classification. Maraschi et al. constructed broadband spectral indices between the radio, ultraviolet, and X-ray band, revealing that X-ray selected blazars on average appeared flatter in the UV to X-ray energy range with lower radio luminosities than the radio selected sample, indicating the SED peak is at higher energies for the X-ray selected blazars. This study hinted at a blazar sequence based on the

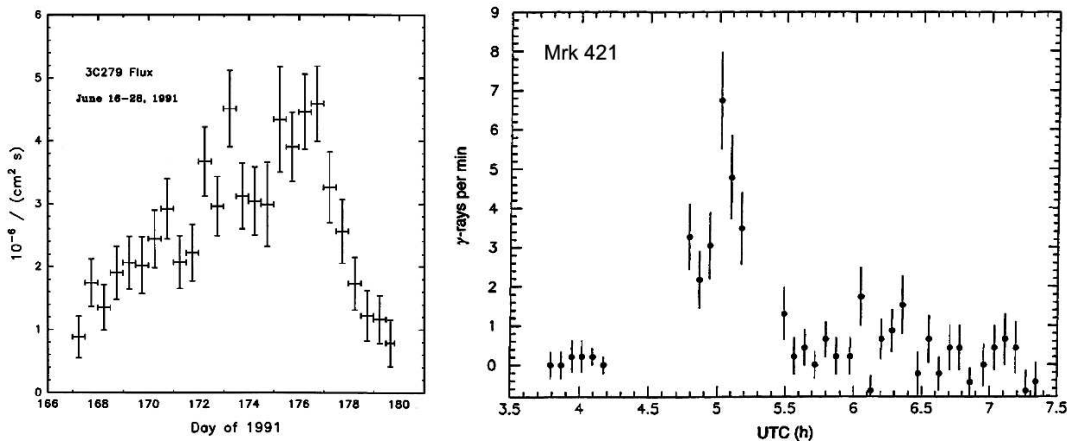


Figure 1.4: Gamma-ray lightcurves for the blazars 3C 279 (left) and Mrk 421 (right). The 3C 279 γ -ray flux measurements are from EGRET (>0.1 GeV) during June 1991 (Kniffen et al. 1993). The Mrk 421 lightcurve shows the Whipple 10 m γ -ray rate (>0.35 TeV) during 15 May 1996 (Gaidos et al. 1996).

total SED shape (limited by selection effects), detailed at the end of this section.

Gamma-ray Variability in 3C 279 and Mrk 421: Evidence for Jet Beaming (1991–1996)

The first blazar detected at γ -ray energies was 3C 273 by *COS-B* in 1976 (Swanenburg et al. 1978). In 1991, NASA launched the Compton Gamma-Ray Observatory (*CGRO*) carrying 4 γ -ray instruments. The EGRET instrument on *CGRO* detected 3C 279 in a viable high flux state at energies >0.1 GeV, with flux doubling timescales of ~ 2 days during a period of 12 days (Hartman et al. 1992; Kniffen et al. 1993). Figure 1.4 (left) shows the EGRET >0.1 GeV flux measurements of 3C 279 during June 1991. Maraschi et al. applied a Synchrotron Self-Compton (SSC) model to demonstrate that with this assumed framework for the IR to γ -ray emission, the high luminosity and rapid γ -ray variability in 3C 279 offered strong evidence for relativistic beaming toward the observer (Maraschi et al. 1992). The primary constraint to the SSC model was that for γ -rays to escape a spherical source (of radius R), the optical depth to pair production $\tau_{\gamma\gamma}$ must be less than or equal to unity. The 2 day γ -ray variability Δt_{obs} was used with relativistic beaming assumptions to define the size of the emission region R by the Doppler factor δ and speed of light c , such that $R = c \Delta t_{\text{obs}} \delta$. Using this relation, a source compactness can be defined as:

$$S = \frac{\delta^{-5} L_{\text{obs}} \sigma_{\text{T}}}{\Delta t_{\text{obs}} m_e c^4}$$

where L_{obs} is the observed γ -ray luminosity, σ_{T} is the Thomson cross section, and m_e is the electron mass. The the optical depth $\tau_{\gamma\gamma}$ is directly proportional to the source compactness S , for example

at 511 keV where $\tau_{\gamma\gamma} \sim S/60$. Applying the optical depth limit, a Doppler beaming $\delta \geq 6$ was estimated in 3C 279 from the derived source compactness.

Mrk 421 was the first BL Lac detected at γ -ray energies in 1992 by EGRET (0.05–5 GeV), and at energies >0.5 TeV by the Whipple 10 m telescope (Lin et al. 1992; Punch et al. 1992). EGRET detected a power-law γ -ray spectrum for Mrk 421 with a photon index $\Gamma = 1.96 \pm 0.14$ in the 0.05–5 GeV band. No flux variability was found in the EGRET or Whipple 10 m detections, however Mrk 421 was in a relatively low γ -ray flux state at the time (Schubnell et al. 1996). In May 1994, the Whipple 10 m observed a γ -ray flare in Mrk 421 with a flux doubling timescale of ~ 2 day during a large X-ray flare measured by ASCA (Kerrick et al. 1995; Takahashi et al. 1996). During 1995 and 1996 Mrk 421 was at a stable medium γ -ray flux level, until May 1996 when two rapid γ -ray flares were observed by the Whipple 10 m (Buckley et al. 1996; Gaidos et al. 1996). Figure 1.4 (right) shows the Whipple 10 m γ -ray rate for events >0.35 TeV from Mrk 421 during 15 May 1996. At hours 4–5 the dramatic rise and fall (flare) in the γ -ray rate by a factor >10 implied a doubling timescale of ~ 15 minutes. Using the pair production opacity arguments described above, a Doppler factor $\delta \geq 10$ was derived for Mrk 421 from the 15 May 1996 γ -ray flaring event (Celotti et al. 1998). Whipple 10 m observations of Mrk 421 from 2000 – 2006 are presented in chapters 5 and 6, showing rapid γ -ray flaring from multiple years.

Extensive X-ray and TeV Gamma-ray Study of Mrk 501 (1995–1998)

The second blazar detected at energies >0.3 TeV was Mrk 501 from observations during 1995 with the Whipple 10 m telescope (Quinn et al. 1996). The HEGRA Cherenkov telescope 1 (CT1) confirmed the Whipple 10 m detection, with a detection of >1.5 TeV γ -rays from Mrk 501 during 1996 (Bradbury et al. 1996). Then, in March 1997 the Whipple 10 m and HEGRA system detected a sustained γ -ray flux increase by a factor of over 15 relative to the 1995 discovery flux level (Catanese et al. 1997; Aharonian et al. 1997). Rapid γ -ray flares were detected from March to October 1997 by CAT, HEGRA, and the Whipple 10 m triggering X-ray observations with *RXTE* and *Beppo-SAX* (Lamer and Wagner 1998; Pian et al. 1998; Aharonian et al. 1999a; Aharonian et al. 1999b; Aharonian et al. 1999c; Djannati-Atai et al. 1999; Quinn et al. 1999). Figure 1.5 (left) shows X-ray and γ -ray flux and spectrum measurements of Mrk 501 from *RXTE* PCA and HEGRA system observations during 2 Apr. to 21 Jul. 1997 (Krawczynski et al. 2000). The X-ray flux level varied by a factor of 3 during time-scales of ~ 1 day, while the TeV flux varied by a factor of 30 over short time-scales of ~ 15 hours. The X-ray and TeV flux levels from near simultaneous observations (± 6 hours) showed significant correlation over the large range in fluxes. A clear hardening of the 3–25 keV X-ray spectrum with increasing X-ray flux was also evident, indicating

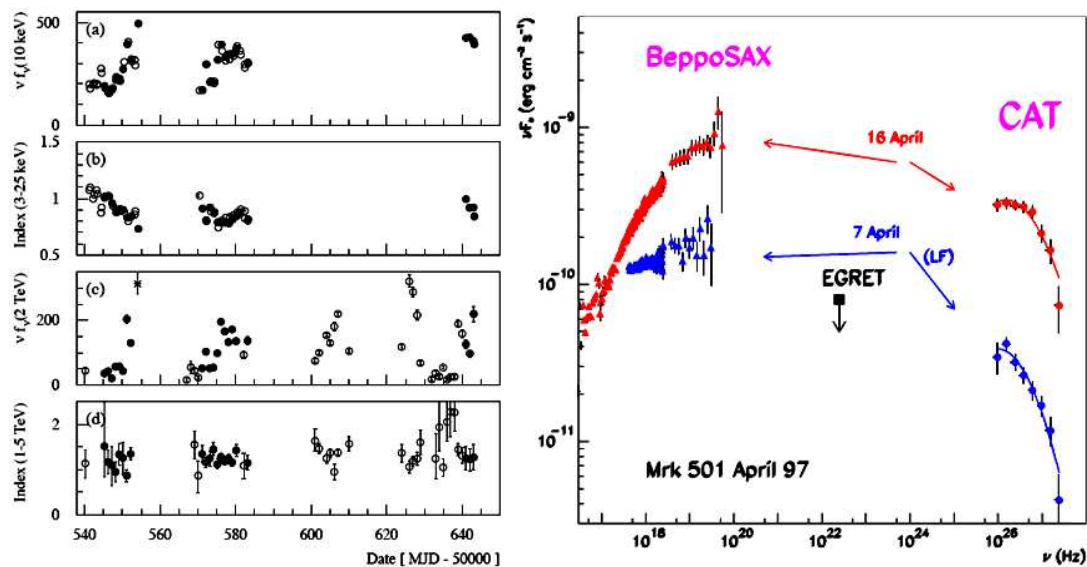


Figure 1.5: X-ray and γ -ray observations of Mrk 501 during 1997. (Left) (a) RXTE PCA 10 keV flux and (c) HEGRA system 2 TeV flux, both in 10^{-12} $\text{erg cm}^{-2} \text{s}^{-1}$. (b) RXTE PCA 3–25 keV and (d) HEGRA 1–5 TeV power law indices (Krawczynski et al. 2000). (Right) Beppo-SAX 0.1–200 keV and CAT 0.3–13 TeV spectrum from 16 Apr. 1997 (red), and from low flux (LF) data in 1997 (blue) (Djannati-Atai et al. 1999). The 16 Apr. CAT flux measurement is shown (right) by an asterisk in panel (c).

a shift in the first peak of the energy spectrum to higher energies (>100 keV). Figure 1.5 (right) shows the X-ray and TeV spectrum of Mrk 501 during Apr. 1997 in a high flux (red) and low flux state (blue) from Beppo-SAX and CAT observations. The TeV spectrum showed a shift in the peak energy to ~ 0.8 TeV with increasing flux level. Absorption of TeV γ -rays by pair production interactions with extragalactic background light (EBL) was not corrected for in the TeV spectrum (the EBL is discussed in section 1.2). The highly sampled X-ray and TeV observations of Mrk 501 in 1997 allowed for detailed interpretations of relativistic beaming in a jet (Krawczynski et al. 2000). The large shift in X-ray peak energy with moderate X-ray flux variation excluded the scenario in which only a changing doppler factor δ accounted for the variability. Both X-ray and γ -ray data were used to constrain a lower limit on the dopper factor of $\delta \geq 6.3$.

The Blazar Sequence (1998)

Drawing from a total sample of 126 radio and X-ray selected blazars, Fossati et al. constructed a spectral energy distribution (SED) from archival flux measurements at radio to X-ray energies for 117 sources (Fossati et al. 1998a). EGRET detections on 37 of the selected blazars at 100 MeV

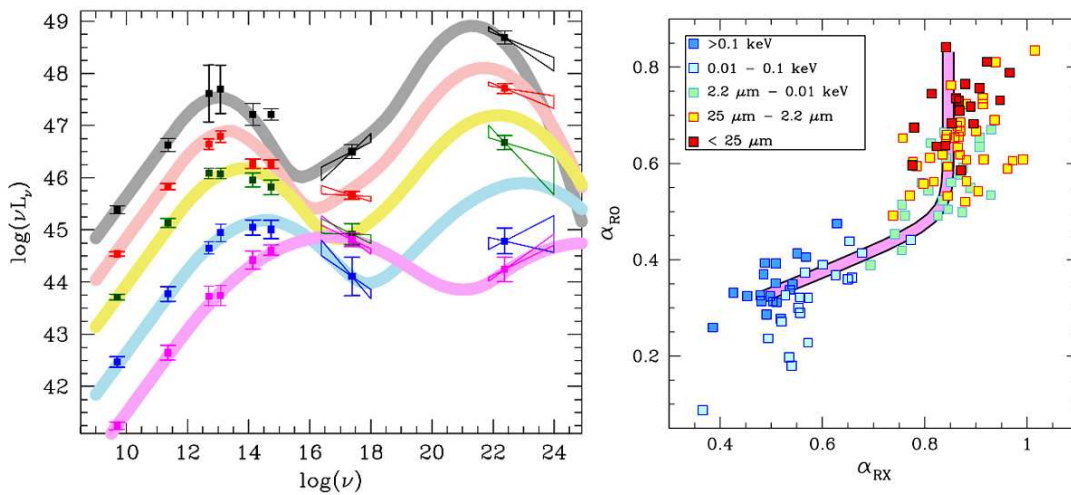


Figure 1.6: (Left) Average spectral energy distributions (SEDs) binned according to radio luminosity using a total of 126 blazars taken from 3 samples of 1-Jy radio selected BL Lacs, 2-Jy radio selected FSRQs, and X-ray selected BL Lacs from *Einstein* surveys (Fossati et al. 1998a; Köhl et al. 1981; Perlman et al. 1996; Wall and Peacock 1985). The analytical fits to the SEDs are intended to guide the eye, and were calculated from a combination of power law and log-parabolic models, as described in (Fossati et al. 1998a). (Right) is a so-called color-color diagram showing the radio to optical effective spectral index α_{RO} versus radio to X-ray index α_{RX} for the total blazar sample. The data points are color coded according to the estimated peak energy in the first component of the SED. The thick line is the color-color relationship derived from simulated SEDs. Figures from (Fossati 1998b).

allowed for a detailed study of the SED properties up to γ -ray energies. Figure 1.6 (left) shows the average blazar SEDs binned according to radio luminosity, fit with an analytical function to guide the eye. Two peaks are present in each of the SEDs, with a strong correlation between the energy position of the first and second components. Figure 1.6 (right) shows a color-color diagram of radio to optical effective spectral index α_{RO} versus radio to X-ray index α_{RX} using the full blazar sample. The diagram demonstrates the technique used to estimate the peak energy in the first component of the SED (interpreted as the synchrotron peak), with the points color coded according to the estimated peak energy. Recently, the validity of a simple blazar sequence in which most powerful blazars have low energy synchrotron peaks was tested using large well defined samples with relatively high sensitivity (Padovani 2007). The clear correlation shown in Fossati et al. between radio power and synchrotron peak energy is not evident in the recent samples. Selections effects are considered the main determining factor in the correlation seen in (Fossati et al. 1998a). However, targeted searches for high luminosity blazars with high synchrotron peak

energy in the X-ray band revealed only “intermediate” type blazars of relatively low power with synchrotron peaks below 0.1 keV for all but one of the studied blazars (Padovani 2002). This result lends tentative evidence for the physical basis of a blazar sequence, despite the need for further observations with a larger sample of blazars. The currently small population of detected blazars with synchrotron peak energies at X-ray energies, and second SED peak at GeV to TeV energies is discussed in section 1.2.

1.2 Properties of TeV Blazars

In the previous section, the discovery of blazar type objects in the nucleus of massive elliptical galaxies was reviewed. Here, a short overview is provided on the current status on blazars observations and interpretation. First, standard theoretical models on the relativistically beamed jet emission in blazars are outlined, following from the historical introduction of the work by (Jones et al. 1974a). The discovery of TeV emission from a growing number of blazars is outlined. Modifications to the measured γ -ray energy spectrum of TeV blazars by absorption processes with the extragalactic background light (EBL) are discussed.

Synchrotron Self-Compton Processes and Other Competing Blazar Models

The highly polarized and variable radio and optical emission of blazars suggests the origin of the continuum radio to X-ray component in the spectral energy distribution (SED) is from a population of synchrotron radiating electrons moving in a magnetic field within a jet oriented along our line of sight (Jones et al. 1974a; Jones et al. 1974b). In the Synchrotron Self-Compton model (SSC), the accelerated electrons produce both the low and high energy components of the SED. Under the simplest scenario, a single homogeneous region emits both synchrotron and inverse-Compton radiation, assuming that the synchrotron photons act as “seed” photons for inverse-Compton scattering by the relativistic electrons (Ghisellini et al. 1996). A highly correlated quadratic relationship is expected between the flux variability in the X-ray (synchrotron) and TeV γ -ray (inverse-Compton) bands, given by the ratio of the luminosities: $L_c/L_s = u_s/u_B$, where u_s is the energy density of synchrotron photons, and u_B is the energy density of the magnetic field. This implies that $L_c \propto L_s^2$, since $u_s \propto L_s$ (Takahashi et al. 1996). Alternative models explore the case where external seed photons are responsible for inverse-Compton scattering, which originate outside of the emitting region, either in the broad line region, or accretion disc surrounding the supermassive black hole (Sikora et al. 1994; Dermer and Schlickeiser 1994). The so-called external Compton models predict a much less correlated variability between the synchrotron and inverse-Compton components,

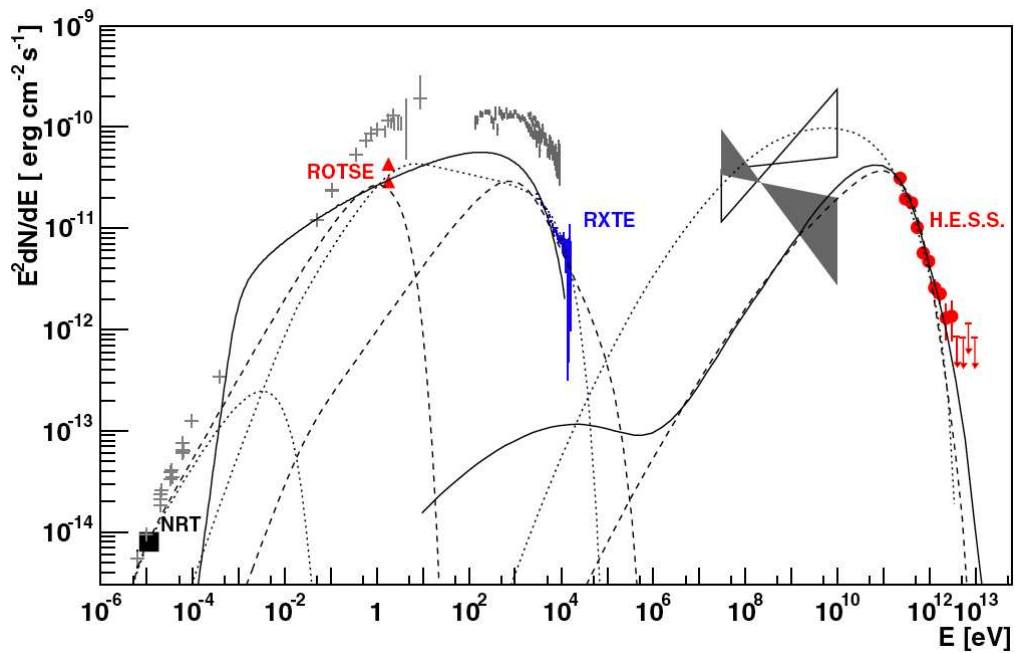


Figure 1.7: Spectral energy distribution (SED) of PKS 2155-304 from Oct. to Nov. 2003 (Aharonian et al. 2005c). Simultaneous optical (ROTSE), X-ray (RXTE), and TeV γ -ray (H.E.S.S.) observations are fit by a hadronic model (solid line), and a leptonic Synchrotron Self-Compton (SSC) model assuming a common origin for the optical and X-ray emission (dotted line), or if the optical emission is from a larger jet region (dashed line). Archival data is shown in grey, with bowtie spectra for the EGRET observations.

since variations in the external photon intensity could cause γ -ray flares without an increased flux at low energies (Krawczynski et al. 2004). A third emission model also attributes synchrotron radiation to the low energy end of the SED from nonthermal electrons, but accounts for high energy emission by proton induced cascades and synchrotron radiation from accelerated protons (Mücke et al. 2003; Mannheim 1998). In this model, secondary particles from the proton induced cascades undergo synchrotron radiation, emitting in the X-ray band. The contribution of this secondary synchrotron emission is relatively small compared to synchrotron emission from “primary” electrons, hence the X-ray and TeV γ -ray emission are not expected to be highly correlated in this framework. Figure 1.7 shows the SED of the TeV blazar PKS 2155-304 fit alternatively by three models. Simultaneous optical, X-ray, and TeV γ -ray observations from Oct. to Nov. 2003 were fit either by a hadronic model (Mücke et al. 2003), or two forms of the leptonic SSC model in (Katarzynski et al. 2003). In the SSC model, the optical emission is either assumed to have the same origin as the X-ray emission, or to originate in a large component of the jet. Neither leptonic, nor hadronic model was well constrained by this typical blazar SED.

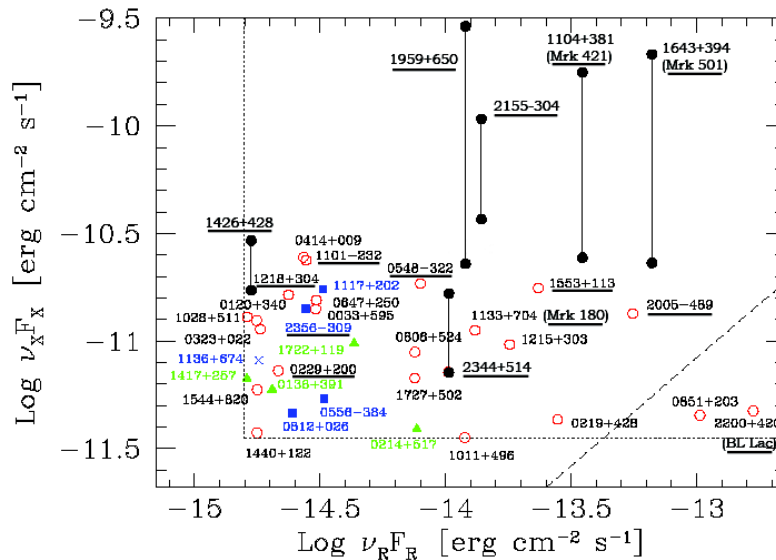


Figure 1.8: X-ray flux versus radio flux from a collection of blazars surveys (distinguished by the marker color and style). Currently known TeV blazars are underlined. The 6 known TeV blazars in 2002 are shown by black points, with the range of measured X-ray fluxes indicated. Figure adapted from (Costamante and Ghisellini 2002).

Discovery of TeV Emission in Blazars

A growing sub-class of blazars are termed TeV blazars due to their detection at TeV γ -ray energies. The term TeV blazar was first applied when only three blazars (Mrk 421, Mrk 501, and 1ES 2344+514) were known to emit TeV γ -ray radiation (Tavecchio et al. 1998). Table 1.1 lists the 17 currently known TeV blazars, and the year of discovery at TeV energies. Of the six TeV blazars detected before 2004, four were detected first by the Whipple 10 m, as discussed in section 1.1 for Mrk 421 and Mrk 501. The rapid discovery of TeV blazars after 2004 coincides with the start of operations of two highly sensitive imaging atmospheric Cherenkov telescopes: H.E.S.S. and MAGIC (see section 3.1.3). Three of the five Northern TeV blazars discovered by H.E.S.S. and MAGIC (1ES 0229+200, Mrk 180, and BL Lac) were observed previously by the Whipple 10 m, but only upper limits could be derived on the integral flux above 0.3 TeV (Horan et al. 2004). The selection criteria for selecting candidate TeV blazars are generally based on a high radio and X-ray flux, following from results in (Costamante and Ghisellini 2002). The expected blazar sequence of spectral energy distributions (SEDs) suggests that sources with peak synchrotron energy in the X-ray band will have a second peak at GeV to TeV energies (see section 1.1). The requirement for a high radio flux in addition to a high X-ray flux appears counter-intuitive, as this implies a lower synchrotron peak energy. Costamante and Ghisellini offered the interpretation of a high

Source	r.a.	dec.	z^a	Discovery ^b		References
	(hh mm ss)	(dd mm ss)		(Year)	(Tele.)	
Mrk 421	11 04 27	+38 12 32	0.031	1992	Whipple	Pun92
Mrk 501	16 53 52	+39 45 37	0.034	1996	Whipple	Qui96
1ES 2344+514	23 47 04	+51 42 18	0.044	1998	Whipple	Cat98
1ES 1959+650	19 59 59	+65 08 55	0.047	1999	7TA	Nis99
PKS 2155-304	21 58 52	-30 13 32	0.116	1999	Mark 6	Cha99
H1426+428	14 28 32	+42 40 21	0.129	2002	Whipple	Hor02
PKS 2005-489	20 09 25	-48 49 54	0.071	2005	H.E.S.S.	Aha05a
PG 1553+113	15 55 43	+11 11 24	>0.25	2006	H.E.S.S.	Aha06a
1ES 1101-232	11 03 37	-23 29 30	0.186	2006	H.E.S.S.	Aha06b
H2356-309	23 59 07	-30 37 41	0.165	2006	H.E.S.S.	Aha06c
PKS 0548-322	05 50 40	-32 16 18	0.067	2006	H.E.S.S.	Hof06
1ES 0347-121	03 49 23	-11 59 27	0.188	2006	H.E.S.S.	Aha07a
1ES 0229+200	02 32 48	+20 17 16	0.139	2006	H.E.S.S.	Aha07b
1ES 1218+304	12 21 21	+30 10 37	0.182	2006	MAGIC	Alb06a
Mrk 180	11 36 26	+70 09 27	0.045	2006	MAGIC	Alb06b
BL Lac	22 02 43	+42 16 40	0.069	2007	MAGIC	Alb07b
1ES 1011+496	10 15 04	+49 26 01	0.212	2007	MAGIC	Alb07c

Table 1.1: TeV blazars detected as of November 2007. The start operations in 2004 of the more sensitive H.E.S.S. and MAGIC IACT telescope systems is denoted by a horizontal line (see section 3.1.3) Notes: (a) A lower limit on the redshift for PG 1553+113 of > 0.25 is quoted, however a redshift > 0.74 is consistent with recent studies of the EBL (see text for details). (b) Listed are the IACT telescope systems which first discover each TeV blazar. References: Pun92: (Punch et al. 1992), Qui96: (Quinn et al. 1996), Cat98: (Catanese et al. 1998), Nis99: (Nishiyama et al. 1999), Cha99: (Chadwick et al. 1999), Hor02: (Horan et al. 2002), Aha05a (Aharonian et al. 2005a), Aha06a: (Aharonian et al. 2006a), Aha06b: (Aharonian et al. 2006b), Aha06c: (Aharonian et al. 2006c), Hof06: (Hofmann et al. 2006), Aha07a: (Aharonian et al. 2007a), Aha07b: (Aharonian et al. 2007b), Alb06a: (Albert et al. 2006a), Alb06b: (Albert et al. 2006b), Alb07c: (Albert et al. 2007c).

radio flux corresponding to an increased energy density of seed photons in the framework of the Synchrotron Self-Compton (SSC) model (Costamante and Ghisellini 2002). Figure 1.8 shows the X-ray flux versus radio flux for a large sample of blazars. All but one of the known TeV blazars fit into the upper region of high X-ray and radio flux, denoted by a dashed line. As seen in table 1.1, increasingly more distant blazars have only recently been detected by H.E.S.S. and MAGIC at TeV γ -ray fluxes a factor of >10 lower than the approximate baseline flux of Mrk 421 (see references in table 1.1). By comparing the luminosity of all known TeV blazars, it is shown that the closer Mrk 421 and Mrk 501 are indeed relatively weak TeV emitters (Wagner 2006). Besides the intrinsic source strength, observations of the TeV γ -ray flux and energy spectrum from blazars are significantly affected by absorption from the extragalactic background light (EBL), as described below.

Absorption of TeV γ -rays by Interactions with the Extragalactic Background Light

TeV γ -ray emission from blazars is attenuated by pair production interactions with photons from the extragalactic background light (EBL) (Gould and Schreder 1967). At energies above 1 TeV, γ -rays interact primarily with the infrared component of the EBL with wavelengths $> 1 \mu\text{m}$, while γ -rays with energy below 1 TeV with EBL photons in the near-infrared to ultraviolet band. Figure 1.9 shows the spectral energy distribution of the EBL from $0.1 \mu\text{m}$ to 1 mm. Direct measurements are indicated by data points, which were significantly affected by foreground emission from interplanetary dust (Hauser et al. 1998). Lower limits on the EBL strength are from the integrated light of galaxies using a stacking procedure from observations with the Hubble Space Telescope (HST) and Spitzer (Dole et al. 2006). The optical depth for pair production by the EBL $\tau(E, z)$ is derived from the SED of the EBL. The intrinsic γ -ray source energy spectrum is estimated with knowledge of the optical depth by:

$$\left(\frac{dN}{dE}\right)_{\text{int}} = \left(\frac{dN}{dE}\right)_{\text{obs}} \cdot [\exp(-\tau(E, z))]^{-1}$$

The observed γ -ray spectrum is softened due the EBL, with a reduction in the integral flux level. A recent set of models were developed for the evolution of the EBL, which predicted the optical depth as a function of energy and redshift, and are freely available (Kneiske et al. 2004). Figure 1.9 (bottom) shows a set of three models from (Kneiske et al. 2004). In the ‘‘Low IR’’ model, the infrared star formation rate is assumed to be at the lower limit from sub-mm galaxy number counts, while for the ‘‘Low SFR’’ model star formation is assumed decline rapidly with increasing redshift. Both of these assumption lower the EBL absorption of TeV γ -rays from relatively close blazars. Figure 1.10 (left) shows the mean free path of γ -rays under 4 EBL models. Figure 1.10

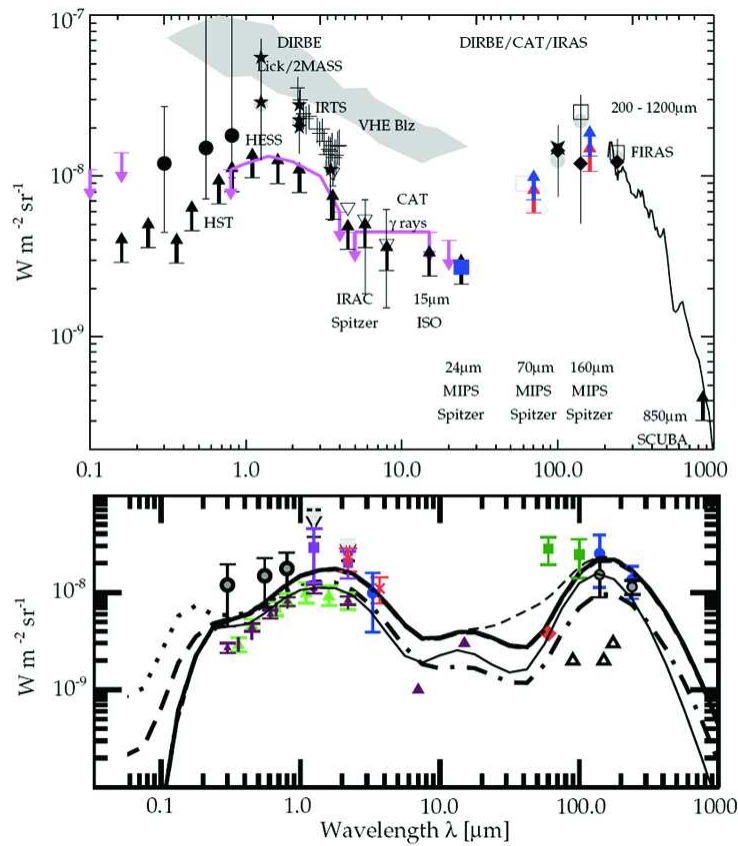


Figure 1.9: (Top) Spectral energy distribution of the extragalactic background light (EBL) from 0.1 μm to 1 mm, taken from (Dole et al. 2006). Lower limits on the EBL flux from Hubble Space Telescope (HST) and Spitzer measurements of integrated galactic light are shown by black and blue arrows. The pink line of upper limits on the EBL strength are from constraints by H.E.S.S. assuming the intrinsic energy spectrum of TeV blazars have a power law photon index $\Gamma \leq 1.5$ (Aharonian et al. 2006b). (Bottom) are shown model fits to the EBL spectral energy distribution, with a “Best fit” model shown by a thick solid line, a “Low IR” model by dot-dashed line, a “Low SFR” model by a thin solid line (Kneiske et al. 2004).

(right) shows the optical depth using these 3 models for a source with redshift $z = 0.031$ (Mrk 421), and $z = 0.129$ (H1426+428). The “Low SFR” model is shown to have the lowest $\tau(E, z)$ of the 3 models from 0.1 to 5 TeV. This relatively low level of EBL absorption is roughly consistent with recent upper limits placed on the strength of the EBL by observations of the distant ($z = 0.186$) TeV blazar 1ES 1101-232 by H.E.S.S. (Aharonian et al. 2006b). Assuming that the intrinsic TeV γ -ray energy spectrum of 1ES 1101-232 have a power law photon index $\Gamma \leq 1.5$, the EBL strength was restricted to only a factor of a few above the lower limits from integrated galactic light. Figure 1.10 (right) shows the mean free path of γ -rays under 4 different EBL models, all

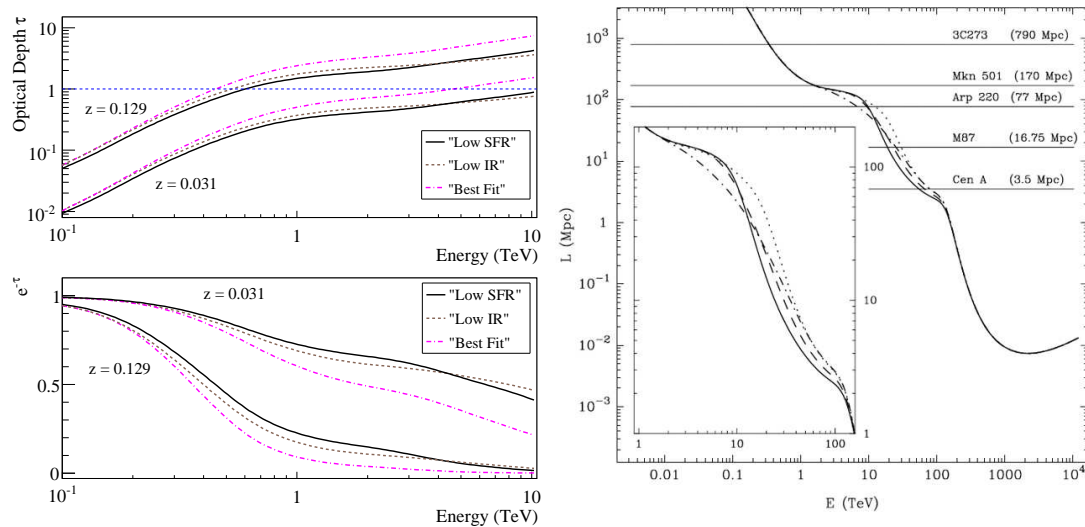


Figure 1.10: (Left) The optical depth τ to the EBL versus source energy for sources with redshift $z = 0.031$ (Mrk 421), and $z = 0.129$ (H1426+428) calculated using 3 models from (Kneiske et al. 2004). An optical depth of 1 is indicated by the blue dashed line. The EBL absorption term $\exp(-\tau(E,z))$ applied to the TeV γ -ray energy spectrum is also shown versus energy. (Left) Mean free path of γ -rays for 4 models of the EBL in (Aharonian et al. 2002b).

assuming a relatively high level for the EBL. In this work, the optical depth $\tau(E,z)$ from the “Low SFR” model is used to correct the measured energy spectrum from Whipple 10 m observations, with results in chapters 5–7.

Chapter 2

X-ray Instrumentation and Data

Reduction Methods

Cosmic photons with X-ray energies (0.1–100 keV) are absorbed high in earth’s atmosphere. X-ray astronomy began in the 1960s with rocket experiments, and since then all major X-ray observatories have been satellite based. Section 2.1 provides a short history and performance overview of past and current X-ray observatories. This chapter is focused on presenting the instrumentation and reduction methods applied to observations with *RXTE* (section 2.2), and *XMM-Newton* (section 2.3). X-ray observations and analysis results in this thesis are described in chapter 6.

2.1 Introduction to Past and Current X-ray Observatories

The first X-ray satellite mission was NASA’s *Uhuru* launched in 1970 (Giacconi et al. 1971). *Uhuru* completed the first X-ray all sky survey, detecting 339 sources in the 2–20 keV energy band. Several successive NASA X-ray observatories followed throughout the 1970s: Ariel V (1974–1980), HEAO-1 (1977–1979), HEAO-2 (renamed *Einstein* 1978–1981), and HEAO-3 (1979–1981). *Einstein* carried on board the first imaging X-ray instruments: the High Resolution Imager (HRI) with an angular resolutions of 2 arcsec, and the Imaging Proportional Counter with a 1 arcmin angular resolution and two orders of magnitude increase in sensitivity over past X-ray instruments (Giacconi et al. 1979). The first European Space Agency (ESA) X-ray observatory was EXOSAT (1983–1986) which carried on board two Low Energy (0.05–2 keV) imaging X-ray instruments with 18 arcsec angular resolution (de Korte et al. 1981). The field of X-ray astronomy matured rapidly with the launch of *ROSAT* (1990–1999), *ASCA* (1993–2001), *RXTE* (1995–present) and *Beppo-SAX* (1996–2002). *ROSAT* alone discovered over 150,000 new X-ray sources (Voges et al. 2000). From this generation of experiments, only *RXTE* is still in operation.

RXTE

RXTE carries on board three non-imaging X-ray instruments: the Proportional Counter Array (PCA), the High Energy X-ray Timing Experiment (HEXTE), and the All-Sky Monitor (ASM) (Bradt et al. 1993). The *RXTE* PCA instrument is comprised of 5 PCU detectors covering the 2–60 keV energy range with an energy resolution of $\sim 18\%$ ($E / \Delta E \sim 5.5$) and total effective area of 5200 cm^2 at 6 keV (Jahoda et al. 1996; Jahoda et al. 2006). High energy (20–200 keV) X-rays are detected by HEXTE at a comparable energy resolution of 15%, but with much lower sensitivity than PCA (see section 2.2) and (Rothschild et al. 1998). PCA and HEXTE both have a 1 degree field of view. The *RXTE* ASM scans nearly 80% of the sky during every orbit, providing long-term X-ray rate monitoring of ~ 350 sources in the energy band of 1.2–10 keV (Levine et al. 1996). X-ray point sources are identified in the wide 6×90 degree ASM field of view by shadow patterns in the slit masked detector. The systematic uncertainties in the ASM rate are large (5%), and only relative flux estimates are available for long (month time-scale) monitoring. A further description of the *RXTE* observatory and data reduction techniques are in section 2.2.

Chandra and XMM-Newton

Two very powerful imaging X-ray missions were launched in 1999: ESA's *XMM-Newton*, and NASA's *Chandra* Observatory. *Chandra* features a High Resolution Mirror Assembly (HRMA) of four nested grazing-incidence X-ray mirrors with a focal length of 10 m (Weisskopf et al. 2000). Mounted on the HRMA are two insertable grating systems: the Low Energy Transmission Grating (LETG) which intercepts 0.08–2 keV photons, and the High Energy Transmission Grating (HETG) consisting of Medium Energy Gratings (MEG, 0.4–4 keV) and High Energy Gratings (HEG, 0.8–8 keV). In the *Chandra* focal plane are the Advanced CCD Imaging Spectrometer (ACIS) and the High Resolution Camera (HRC). ACIS covers the energy range 0.1–10 keV with an angular resolution of 0.5 arcsec and effective mirror area of 800 cm^2 at 1 keV. HRC has *Chandra*'s largest field of view (30×30 arcmin) and a high angular resolution of 0.4 arcsec. Both instruments have a dedicated detector to read out the high resolution spectra dispersed by one of the sets of transmission gratings: ACIS-S reads out HETG spectra, and HRC-S reads out LETG spectra. The $E / \Delta E$ resolving power of HETG is 1000 at 1 keV.

Proving a complimentary mission, *XMM-Newton* offers high sensitivity imaging and spectroscopy (Jansen et al. 2001). *XMM-Newton* carries on board three grazing-incidence mirror modules in a co-axial arrangement with a 7.5 meter focal length. Mounted on two of the three mirror modules are fixed Reflection Grating Assemblies (RGAs) which deflect 58% of the total X-ray light. At the focus of each of the three X-ray telescopes is positioned one of the three European

X-ray Instrument	Launch (year)	Ene. Range (keV)	Ang. Res. (arcsec)	Eff. Area (cm ²)
<i>RXTE</i> PCA	1995	2.0–60	–	5200 ^a
<i>Chandra</i> ACIS	1999	0.1–10	0.5	800
<i>XMM-Newton</i> EPIC	1999	0.2–15	6	2100
<i>INTEGRAL</i> JEM-X	2002	3.0–35	–	400 ^a
<i>Swift</i> XRT	2004	0.2–10	18	110
<i>Suzaku</i> XIS	2005	0.2–12	120	1200

Table 2.1: Performance comparison for broadband X-ray instruments from all currently operating X-ray observatories. Effective areas are combined for instruments with multiple detectors (see text): *RXTE* PCA (5 PCUs), *XMM-Newton* EPIC (MOS1+MOS2+PN), *Suzaku* XIS (4 XISs). Note: effective areas are at 1 keV, except for (a) where the effective area is at 6 keV.

Photon Imaging Camera (EPIC) instruments. The EPIC MOS1 and MOS2 detect the non-deflected X-ray light from the two RGA equipped mirror modules, while the third mirror module and EPIC PN instrument comprise the third X-ray telescope. The PN instrument covers the energy range of 0.2–15 keV with a large effective area (1400 cm² at 1 keV) and moderate energy resolution ($E / \Delta E \sim 20$ –50). Both MOS and PN instruments have a field of view of 30×30 arcmin, with an angular resolution of 6 arcsec. In addition to EPIC are the Reflection Grating Spectrometer instruments (RGS1 and RGS2) comprised of the two RGAs and RGS Focal Cameras. RGS covers the 0.3–2.5 keV band with an energy resolution $E / \Delta E$ of 100–500. The *XMM-Newton* EPIC instrumentation and data reduction methods are outlined in section 2.3.

INTEGRAL, Swift, and Suzaku

Three other important X-ray and soft γ -ray observatories are currently taking data: the ESA and NASA built International Gamma-ray Astrophysics Laboratory (*INTEGRAL*) launched in 2002, the NASA *Swift* Gamma-ray Burst Explorer launched in 2004, and the Japan Aerospace Exploration Agency’s (JAXA’s) *Suzaku* X-ray Observatory launched in 2005. On board *INTEGRAL* is the JEM-X non-focusing imaging microstrip gas chamber X-ray detector with an energy range of 3–60 keV (Winkler et al. 2003). The *Swift* mission is dedicated to the study of gamma-ray bursts, although proposals for pointed target of opportunity (TOO) observations are granted (Gehrels et al. 2004). The focusing X-ray Telescope (XRT) on board *Swift* offers good angular resolution with a point spread function of 18 arcsec, but relatively small effective area of 110 cm² at 1.5

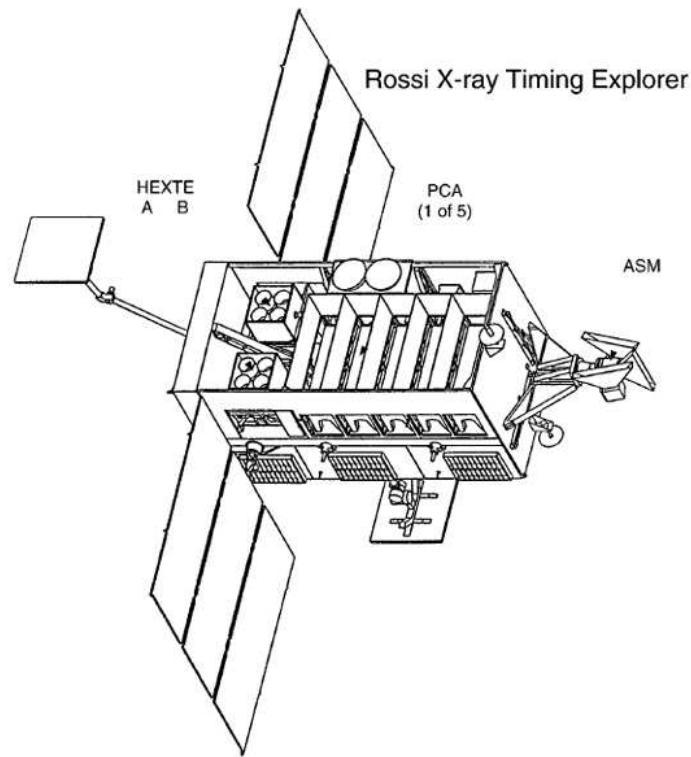


Figure 2.1: Diagram of the *RXTE* Observatory. Visible are the five PCA proportional counter units (PCUs). To the left are the two HEXTE cluster detectors. At the front of the spacecraft is the ASM instrument. Diagram from (Rothschild et al. 1998).

keV. *Suzaku* carries three X-ray detectors on board: the X-Ray Spectrometer (XRS), which is now inoperable, the X-ray Imaging Spectrometer (XIS), and the Hard X-ray Detector (HXD) (Kunieda et al. 2006). XIS is comprised of 4 CCD detectors (XIS0–XIS3) covering the 0.2–12 keV energy range with a large combined effective area of 1200 cm². The non-imaging HXD covers the energy range 10–600 keV. Table 2.1 compares the performance of broadband X-ray instruments from all currently operating X-ray telescopes.

2.2 The *RXTE* Observatory

The NASA built Rossi X-ray Timing Experiment (*RXTE*) observatory was launched in December 1995 and is currently fully operational. Figure 2.1 shows a diagram of the *RXTE* spacecraft. *RXTE* has a circular low-earth orbital period of ~ 90 minutes with an apogee of 580 km and perigee of 560 km. The three non-imaging X-ray instruments on board are the PCA, HEXTE, and ASM (introduced previously in section 2.1). PCA and HEXTE both have a 1 degree Full Width at Half Maximum (FWHM) beam, while the ASM features a very wide 6×90 degrees FWHM field

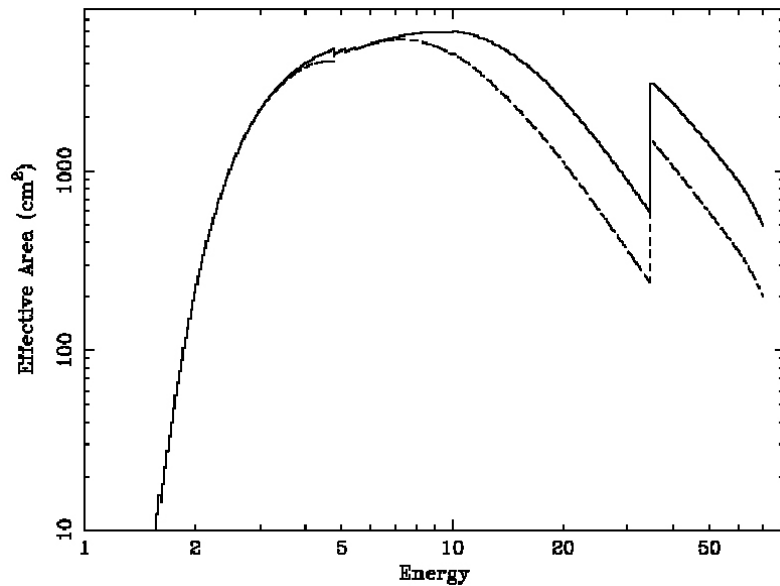


Figure 2.2: Combined effective area of the *RXTE* PCA instrument from all 5 Proportional Counter Units (PCUs) from all 3 xenon layers (solid line), and from the first layer only (dashed line). Only 2 of the 5 PCUs are operational for nearly all observations from 2000 to 2006, and only the first xenon layer is used in data reduction. Hence, the effective area is roughly the dashed line reduced by a factor of $2/5$ ($\sim 2100 \text{ cm}^2$ at 6 keV for 2 PCUs). Figure from (Jahoda et al. 1996).

of view. The ASM consists of three proportional counter Scanning Shadow Cameras (SSCs) mounted on a motorized rotation drive (Levine et al. 1996). Reduced light curves for all X-ray sources are publicly available at the ASM Products Database maintained by MIT and GSFC (*RXTE* ASM Data Products). *RXTE* HEXTE is designed to complement PCA observations by covering the high energy 20–200 keV band with an energy resolution of 15% (Rothschild et al. 1998). HEXTE contains eight Phoswich (NaI+CsI) detectors arranged in two clusters. The effective area of HEXTE at 50 keV is 1200 cm^2 . HEXTE has a relatively poor sensitivity, requiring a 10^5 sec exposure to detect a source at 1 mCrab (10^3 smaller X-ray flux than the Crab nebula supernova remnant). No HEXTE data is used in this thesis due to the typically short exposures (≤ 2.5 ksec) yielding low significances ($1\text{--}3 \sigma$) even for bright Mrk 421 observations (see chapter 6). The remainder of this section overviews the PCA instrumentation and data reduction procedures.

2.2.1 *RXTE* PCA Instrumentation

The *RXTE* PCA consists of five large proportional counter units (PCUs) designed for high timing and modest spectral resolution of relatively bright X-ray sources (Jahoda et al. 1996; Jahoda et al. 2006). Each PCU is constructed of a 1 degree FWHM collimator, a propane filled “veto” volume,

and three layers of xenon filled counters. The nominal energy range is 2–60 keV with an energy resolution ($E / \Delta E$) of ~ 5.5 . Figure 2.2 shows the effective area for all 5 PCUs combined, however for nearly all observations from 2000 to 2006 only 2 PCUs (PCU0 and PCU2) are operational, so the actual effective area is reduced by roughly a factor 2/5 ($\sim 2100 \text{ cm}^2$ at 6 keV for 2 PCUs). The PCU gains are monitored continuously with α particles from a ^{241}Am radioactive source on board. The primary *RXTE* PCA data mode is Standard-2, which reads out a 129 channel spectrum individually for each layer of each detector with an event resolution of 16 sec. Standard-2 is the only PCA data configuration used in this thesis. Below is an overview of *RXTE* PCA data reduction methods.

2.2.2 *RXTE* PCA Data Reduction

Reduction of *RXTE* PCA data is highly standardized due to the well tested and clearly documented FTOOLS and XANADU set of software tools (together named HEASoft), which are developed and maintained by NASA’s High Energy Astrophysics Science Archive Research Center (HEASARC 2007). All *RXTE* PCA data in this thesis are from the HEASARC public data archive and was reduced using FTOOLS 5.3. The full PCA data reduction chain using FTOOLS utilities is:

1. *xtfilt*: generate an updated filter file
2. *pcabackest*: generate modeled background files
3. *maketime*: generate a list of Good Time Intervals (GTIs)
4. *saextract*: extract light curves and spectra
5. *pcarsp*: generate response matrices (RSP)

Run *xtfilt* and Determine Which PCUs were Operational

Each stage is discussed here. First, with the *xtfilt* tool an observation filter file is created from so-called “housekeeping” information stored in the data archive. The filter file is examined to determine which PCUs were operational. For nearly all observations presented in chapter 6 it was found that only PCU0 and PCU2 detectors were operational during the entirety of each observation. For $\sim 10\%$ of observations PCU3 and (or) PCU4 were also turned on and taking data, however only PCU0 and PCU2 are combined here at a loss of sensitivity to ensure a uniform response. A further requirement is that only the top xenon layer is used from each PCU to achieve a high signal-to-noise ratio.

Run *pcabackest* to Model the Background

Since PCA is a non-imaging instrument, the background must be subtracted based on an a pri-

ori model. The model uses a parameterization of the varying internal, diffuse sky, and particle backgrounds from blank sky observations. The FTOOLS *pcabackest* tool produces synthetic background data by fitting the model files to the spacecraft and instrument conditions at the time when data was taken. PCA background models are available for bright or faint sources (<40 counts/sec/PCU). The faint model *pca_bkgd_cmfaintl7_eMv20051128.mdl* was applied to all data. Figure 2.3 shows the faint modeled background and energy spectrum of Mrk 421 from 19 April 2004 in a high flux state (92 cts/sec/PCU). At energies above 20 keV the Mrk 421 flux falls below the PCA sensitivity, and a good agreement between the faint source model and observed background is evident, even for this bright state.

Run *maketime* to Filter the Data

The PCU0, PCU2, and synthetic background data are filtered following a standard set of conservative cuts. First, the spacecraft must have a minimum elevation angle of $\geq 10^\circ$. Second, all data is rejected during the South Atlantic Anomaly (SAA) passage, when the increased particle flux raises significantly above the nominal background level. Data is also rejected up until 30 minutes after the peak in the SAA level. The third and fourth criteria are that the detector pointing offset must be $\leq 0.02^\circ$, and the electron contamination level must be less than 0.1. The FTOOLS *maketime* tool uses the selection criteria to produce a list of Good Time Intervals (GTIs) of good quality data.

Run *saextract* to Extract Light Curves and Spectra

Light curves and spectra of both the filtered on-axis X-ray events and synthetic background are extracted by *saextract* within the defined Good Time Intervals (GTIs). The FTOOLS *rex* script automates the filtering, background modeling, and data extraction once the list of observations, operational PCUs, xenon layers, background models, and selection criteria are defined. Due to the large number of *RXTE* PCA observations, the *rex* script was used for all data processing in this thesis. For several observations the results from *rex* batch processing were compared with results from carrying out each FTOOLS task separately, and were found to be in excellent agreement.

Run *pcarsp* to Generate the Energy Response for each PCU

A calibration database (CALDB) of indexed files is provided by HEASARC to generate the time dependent PCU energy responses. The *pcarsp* script creates an ancillary response file (ARF) and redistribution matrix function (RMF). The ARF accounts for the detector windows and collimator response, while the RMF corrects for redistribution of photon energies across different channels.

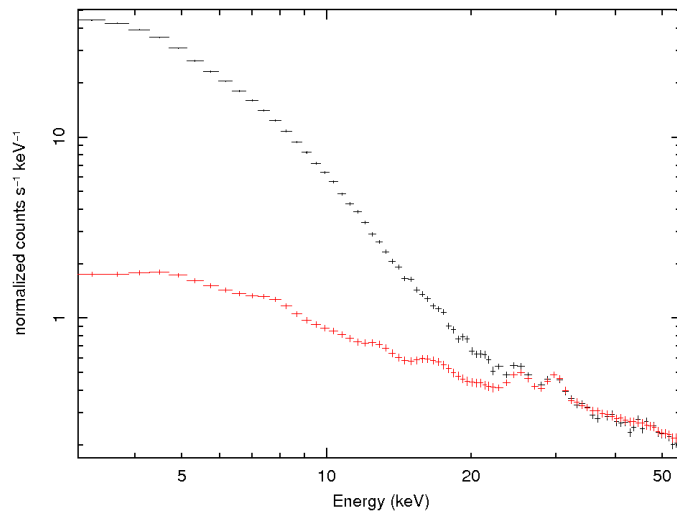


Figure 2.3: *RXTE* PCA spectrum of Mrk 421 (black) and modeled background (red) before subtraction from a 35 min exposure during 19 Apr. 2004. Mrk 421 is shown in a high flux state (92 counts/sec/PCU).

2.3 The *XMM-Newton* Observatory

The European Space Agency (ESA) X-ray Multi-Mirror (*XMM-Newton*) observatory was launched in December 1999, and is currently fully operational. Sir Isaac Newton is honored in the name for his study of spectroscopy. Figure 2.4 shows a diagram of the *XMM-Newton* spacecraft with the three mirror modules on the left and the focal plane EPIC X-ray instruments on the right. *XMM-Newton* is in a highly elliptical 48 hour orbit inclined at 40° to the equator, moving between a perigee of 7000 km and a southern apogee of 114,000 km (Jansen et al. 2001). This orbital path allows for ~ 40 hours of nearly continuous observations outside earth's radiation belt from the total 48 hour orbit. *XMM-Newton* carries on board three Wolter grazing-incidence mirror modules in a parallel axis configuration with a 7.5 meter focal length (the total length of *XMM-Newton* is 10 m). Each module consists of 58 gold-coated nested mirrors, the largest mirror diameter being 70 cm. The nested design is used to maximize the effective area of grazing incidence optics by filling the front aperture with very thin (0.5–1.1 mm) mirrors separated by 1 mm. Wolter telescopes enable X-ray imaging using two grazing incident reflections, first at a parabolic mirror, and second at a hyperbolic mirror. The two *XMM-Newton* mirror modules for the EPIC MOS1 and MOS2 detectors have Reflection Grating Assemblies (RGAs), which reflect 58% of the total light focused by the mirrors. For each RGA one RGS Focal Camera (RFC) is located along the dispersion direction. Each RFC consists of a linear array of 9 MOS CCD chips and has an $E/\Delta E$ resolving power of 100 to 500 over the energy range 0.3–2.5 keV. No RGS data has been

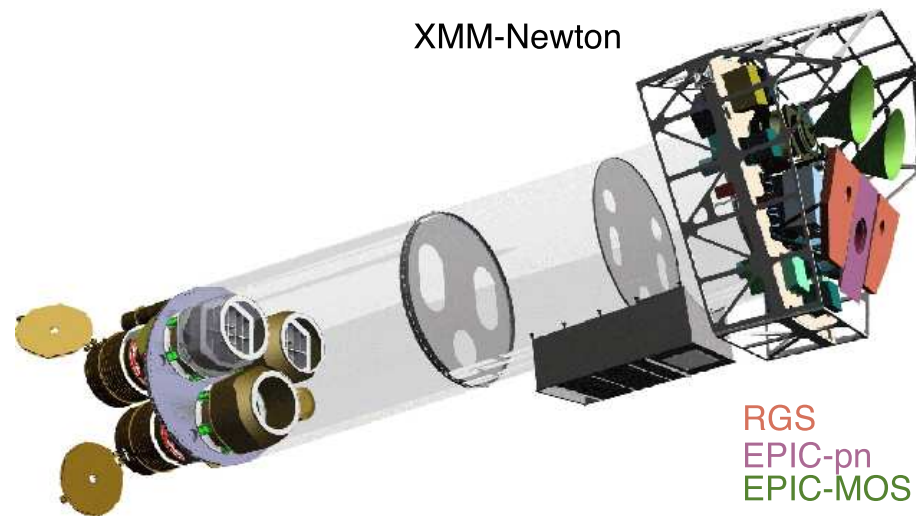


Figure 2.4: A diagram of the *XMM-Newton* observatory. The mirror modules are shown on the left, with Reflection Grating Assemblies (RGAs) mounted on two of the three mirror modules. The focal plane EPIC and RGS X-ray instruments are on the right. The two EPIC MOS are identifiable as cylinders with green horn radiators. The EPIC PN instrument is shown by a light blue box below the MOS detectors, and the RGS detectors are drawn as small cubes in the lower detector module. Diagram adapted from (Jansen et al. 2001).

analyzed in this thesis work, due to the smaller energy range and roughly one order of magnitude smaller effective area compared with the EPIC PN instrument. Figure 2.5 shows the effective area of the PN, MOS, and RGS instruments. The PN effective area is the largest ever for an imaging X-ray instrument. In addition to the EPIC and RGS X-ray instruments, *XMM-Newton* also has a co-aligned 30 cm optical/UV telescope, the Optical Monitor (OM). The OM is a sensitive CCD detector providing imaging with a ~ 1 arcsec angular resolution and spectroscopy over the waveband 180 to 600 nm. No OM data has been analyzed in this thesis.

2.3.1 EPIC Instrumentation

EPIC refers to three instruments: the MOS1 and MOS2 (Metal Oxide Semiconductor) CCD instruments, and PN (P-doped N-doped semiconductor) CCD instrument. PN consists of 12 CCDs of equal size (3×1 cm) built on a single wafer. The back illuminated PN CCDs detect X-rays by interactions with the silicon atoms, creating electrons and holes in numbers proportional to the energy of the incident photon. The electrons are captured in potential wells, and then transferred to readout nodes. MOS1 and MOS2 are equivalent arrays of 7 CCDs (each CCD is 2.5×2.5 cm in size). Both MOS and PN instruments have a field of view of 30×30 arcmin, with an angular

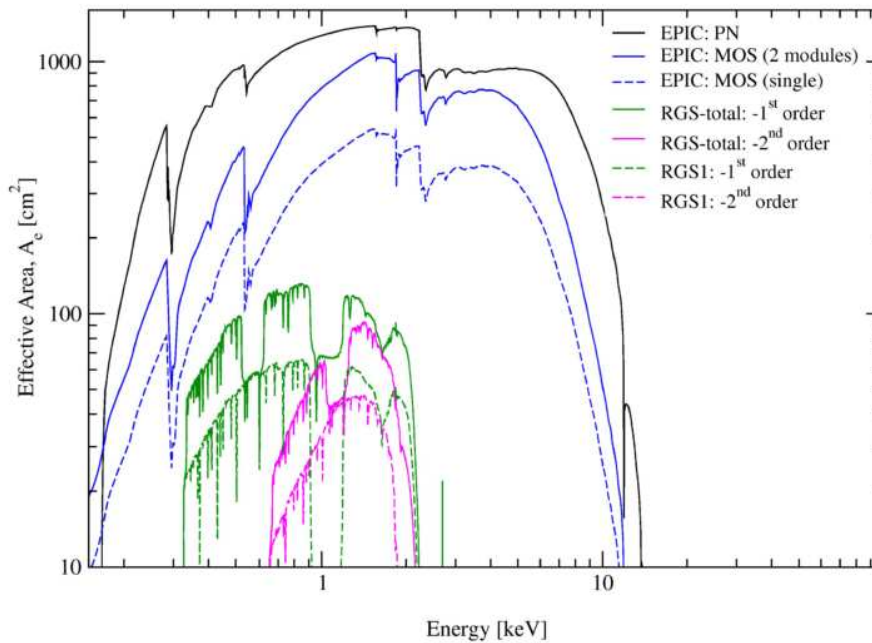


Figure 2.5: Effective areas of the *XMM-Newton* EPIC instruments (PN in black, MOS in blue), and the RGS instruments (RGS first (green) and second (pink) order dispersions). Figure from the *XMM-Newton* User Handbook at (*XMM-Newton* SOC).

resolution of ~ 6 arcsec. The instruments cover nearly the same energy ranges (PN: 0.2–15 keV, MOS: 0.2–12 keV). The instrument configurations are described below.

MOS and PN Operating Modes

A range of operating modes are available for each observation. In this thesis, only results from PN observations in Large Window, Small Window, and Timing modes are presented, primarily due to systematic considerations described here, and in section 6.2. The full list of standard modes are:

- (MOS and PN) Full Frame (FF): all pixels in all CCDs are read out ($\sim 97\%$ field of view)
- (MOS) Large Window (LW): 300×300 pixels in the central CCD are read out
- (PN) Large Window (LW): 198×384 pixels from the inner half of the 12 CCDs are read out
- (MOS) Small Window (SW): 100×100 pixels in the central CCD are read out
- (PN) Small Window (SW): 63×64 pixels from the CCD at the focal point
- (MOS and PN) Timing (T): One dimensional (X-axis) imaging from the focal point CCD

Photon Pile-up and Out-of-Time Events

Operating mode are chosen based on source characteristics in the field of view. For bright point source targets, such as Mrk 421, imaging mode observations suffer from two instrumental effects:

photon pile-up and out-of-time events. Photon pile-up occurs when more than one X-ray photon hit the same CCD pixel during the frame integration time (68 ms for PN in Full Frame mode). Instead of recording each photon, one X-ray is recorded with the combined energy of multiple X-rays. This results in an artificial hardening of the source spectrum and overall loss of flux. Photon pile-up is reduced in imaging modes by removing the inner core of the bright point source. The MOS instruments are more affected by pile-up than PN for all operating modes. FF mode has the highest pile-up factor, followed by LW and SW modes. Pile-up is best avoided with PN observations in Timing mode (only point sources with flux $> 3.8 \times 10^{-9}$ erg cm $^{-2}$ s $^{-1}$ over 2–10 keV suffer pile-up). This flux level is higher than the largest recorded X-ray flux for Mrk 421 (and for the other 2 fainter TeV blazars in this thesis).

Out-of-time events occur in PN and MOS imaging modes when X-ray photons are registered during the CCD read out time. These events get assigned a wrong Y-pixel value (RAWY), and are visible in the image as a strip of events running from the source location to the edge of the camera. Figure 2.6 shows Full Frame mode images of Mrk 421 from MOS1 (top left) and PN (top right) observations. The fraction of out-of-time events is highest for PN Full Frame observations (6.3%), and is evident in figure 2.6. The main effect of out-of-time events is broadening of line features in the source spectrum. Out-of-time events can be identified and subtracted from images or spectra, but have a small effect for sources with a continuum spectrum.

Optical Filters

A choice of three separate optical filters (thin, medium, and thick) is made for each observation depending on the brightness of the target X-ray source in the optical energy band. The X-ray effective areas of the PN and MOS instruments are reduced by the filters at low energies (0.6–2 keV) by $\sim 30\%$. The effective area is further reduced with increasing off-axis angle to the X-ray source, however all observations analyzed here are point sources centered at the focal point, or with a small offset (2 arcmin).

2.3.2 EPIC Data Reduction

The *XMM-Newton* Science Analysis System (SAS) developed and maintained by the Science Operations Center (SOC) at ESA is used for all *XMM-Newton* data reduction (*XMM-Newton* SOC). All data in this thesis (listed in chapter 6) is from the public *XMM-Newton* Science Archive (XSA) at the *XMM-Newton* SOC. Only data from the PN instrument in SW, LW, and Timing modes are presented in this thesis. Final spectra results from MOS data are not used in this analysis primarily due to the larger effect of photon pile-up and smaller effective area compared with PN. The PN

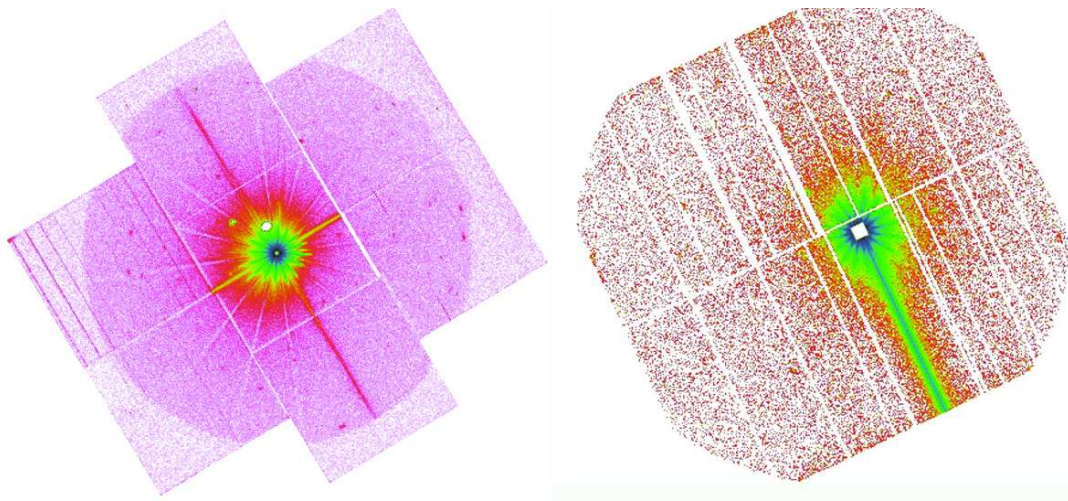


Figure 2.6: *XMM-Newton* MOS1 (left) and PN (right) Full Frame images of Mrk 421 from 14 Nov. 2002 (MOS1) and 7 June 2003 (PN). Mrk 421 has been observed 4 times in FF mode with the PN instrument (as of Feb. 2007) for calibration purposes with a square mask of 10×10 pixels removed in the core of the point spread function to reduce photon pile-up. The bright strip running from the source to the edge of the camera in the PN image is from out-of-time events.

Full Frame observations are not analyzed because of the masked calibration mode (see figure 2.6). Therefore, this section only outlines the data reduction of PN imaging and Timing mode observations.

Calibrating Photon Event Files

The *XMM-Newton* Science Archive contains Observation Data Files (ODF) and Pipeline Processing Subsystem (PPS) calibrated data for each observation. The ODF consist of uncalibrated X-ray photon event lists and “housekeeping” data. The PPS data is provided by the *XMM-Newton* Survey Science Center (SSC) and consists primarily of event files which were automatically pre-processed after data taking with a standard “pipeline” set of SAS tools and Current Calibration Files (CCFs). The SAS and CCF are continually revised, so for consistency it is recommended to pre-process the data directly from the ODF with the newest version of SAS and CCF. All data reduction here uses SAS 6.5 and CCF current up to Nov. 2006. Three steps are involved in calibrating PN event files. First, the task *cifbuild* is run to create a CCF Index File (CIF), which determines the set of CCF needed for each observation. Second, *odfingest* is run to inform the ODF summary file of the set of CCF and housekeeping data. Third, *epchain* combines several SAS tasks, including bad pixel rejection, to generate a calibrated PN event file.

Filtering Event Files

The SAS tool *evselect* is used for filtering PN event files, as well as generating images, light curves, and spectra. The standard filtering selections are on event patterns, quality flags, and energy range. The event pattern refers the number and pattern of pixels triggered for each event. The pattern values are: 0 for single pixel events, 1–4 for double pixel events, and 5–12 for triple and quadruple pixel events. Only single and double pattern events (0–4) are selected in this work. Quality flags are encoded in the event file with values defined by the event condition, such as hot pixels. The most conservative criteria (flag = 0) is used here. Finally, only events in the energy range 0.2–15 keV are selected.

Defining Source and Background Regions in the Image

After filtering the event file, *evselect* is run to generate an X-ray image of the active CCDs. Figure 2.7 shows PN images of Mrk 421 in the SW mode (top left) and Timing mode (top right). In imaging modes, a circular region containing the source point spread function PSF) is determined from the image. Using the selected source region, a filtered event file is generated with *evselect*. In PN Timing mode the CCDs are read out in a continuous mode (all events are out-of-time), and so Y-pixel values (RAWY) for all events are evenly spread out along the instrument. A rectangular region is selected that contains the source along the X-pixel (RAWX) direction and all RAWY pixels in the active CCDs. In both Timing and imaging modes, the background region is selected far from the source region to avoid contamination, as shown in figure 2.7.

Correcting for Possible Photon Pile-up

Possible photon pile-up is investigated by running the *epatplot* tool over the source region event file. Figure 2.7 (bottom left) shows the *epatplot* output for a 45 arcsec radius circular region centered on Mrk 421 in SW mode (image top left). *epatplot* displays the energy dependent fraction of single and double pixel events compared with a predicted model for no pile-up. The higher than expected fraction of double events (and decrease in single events) is a clear sign of pile-up. By choosing a core removed annulus pile-up is significantly reduced. Figure 2.7 (bottom right) shows the *epatplot* output for the same SW mode Mrk 421 observation, but from events in a source centered annulus with a radius of 10–45 arcsec. The *epatplot* pile-up plot for Timing mode data is not shown here since the single and double events agree well the expected model, evident of very little pile-up.

Generating Light Curves, Spectra, and Energy Responses

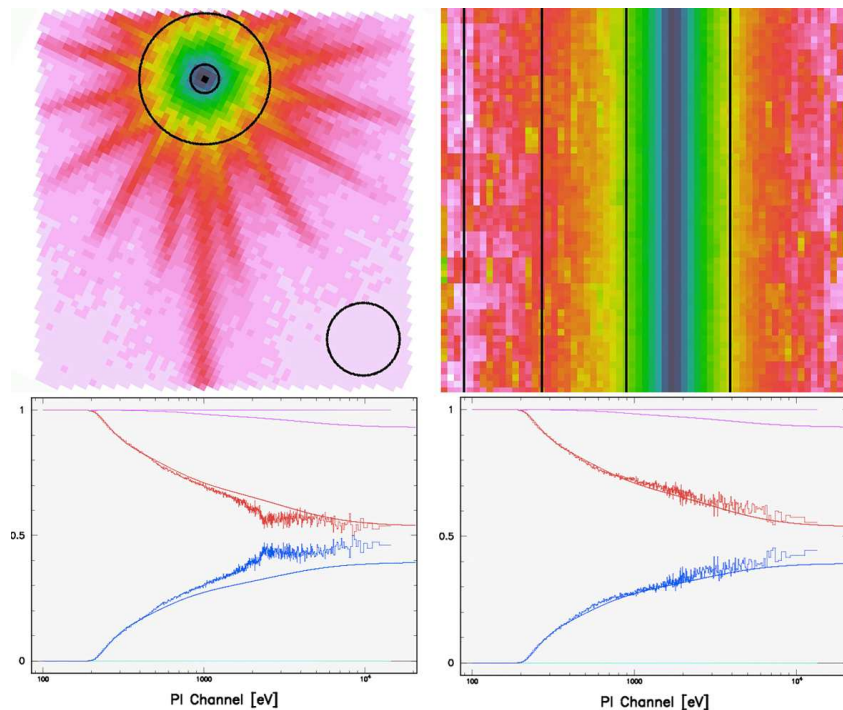


Figure 2.7: *XMM-Newton* PN Small Window (top left) and PN Timing (top right) images of Mrk 421 from 1 June 2003 (SW mode) and 9 Nov. 2005 (Timing mode). For SW mode, the source region is an annulus with a radius 10–45 arcsec centered on Mrk 421. The bottom plots show the energy dependent fraction of single (red) and double (blue) pixel events from the SW mode observation. Photon pile-up is evident by divergence of the single and double pixel events from model predictions for no pile-up (red and blue lines). Shown (bottom left) is the 45 arcsec radius circular region of Mrk 421, and (bottom right) the 10–45 arcsec annulus region (core removed).

Light curves and spectra are extracted from the source and background filtered event files using *evselect*. After generating a source spectrum, the source pixel area is calculated with *backscale* using corrections for bad pixels. The step is repeated for the background spectrum. For Small Window operating modes of bright sources, such as Mrk 421, a small $\sim 3\%$ fraction of the source X-ray flux will contaminate the background region, resulting in a slight systematic effect to the background subtracted flux and spectral shape. Comparing background regions, a maximum 5% systematic effect was found on the power law index and normalization parameters. Next, *arfgen* is run to create an ancillary response file (ARF) consisting of energy dependent vectors defining the effective area, filter transmission, and quantum efficiency of the instrument. The CIF from *cif-build* selects which calibration files (CCF) are used for each observation. Finally, *rmfgen* is run to generate a redistribution matrix function (RMF), providing the energy response. Spectral analysis methods and results are presented in chapter 6.

Chapter 3

Ground Based Gamma-ray Detection

Cosmic gamma-rays (0.1 MeV to >100 TeV) are absorbed high in earth's atmosphere, requiring either balloon or space based satellite observations for direct detection. Space based γ -ray astronomy began in the 1960s with small experiments, including Explorer-11, the first satellite to detect cosmic γ -rays (Kraushaar and Clark 1962). Four important past, present, and upcoming satellite γ -ray missions are: the Compton Gamma-Ray Observatory (*CGRO*) (1991–2000), *INTEGRAL* (2000–present), *AGILE* (2007–present), and the Gamma-ray Large Area Space Telescope (*GLAST*) (launch 2007). The EGRET instrument on board *CGRO* completed the first γ -ray sky survey at energies above 100 MeV, discovering 271 γ -ray sources (Hartman et al. 1999). *INTEGRAL* has two γ -ray instruments (SPI and IBIS) covering the energy range 15 keV to 10 MeV. The first census of IBIS detections >100 keV has yielded 49 sources (Bazzano et al. 2006). *AGILE*, launched in April 2007, features a very compact design to cover the 30 MeV to 50 GeV energy range with the GRID instrument (Tavani et al. 2006). Finally, *GLAST* is scheduled to launch in October 2007 and will carry the LAT instrument sensitive from 20 MeV to 300 GeV, offering a factor of >30 better sensitivity to EGRET for a 2 year sky survey (Gehrels and Michelson 1999).

Detecting γ -rays with Energies Above 10 GeV

At energies above 10 GeV the relatively large (0.8 m^2) effective area of the *GLAST* LAT instrument still yields low photon statistics even for strong sources. For example, the bright Crab nebula supernova remnant with a steady 10 GeV flux of $\sim 10^{-10} \text{ erg cm}^{-2} \text{ s}^{-1}$ will require a ~ 1 day exposure for a 5σ detection (*GLAST* LAT Team). The *GLAST* LAT upper energy limit is the highest of any space based γ -ray instrument. This chapter introduces the indirect detection of 0.01–100 TeV γ -rays with ground based telescopes using the Imaging Atmospheric Cherenkov Technique (IACT).

3.1 Imaging Atmospheric Cherenkov Technique

Detection of >700 GeV γ -ray emission from a cosmic source (the Crab nebula) was first achieved by the Whipple 10 m telescope from observation in 1986 to 1988 at the 9σ level using the newly developed Imaging Atmospheric Cherenkov Technique (Weekes et al. 1989). IACT telescopes image the induced Cherenkov radiation from large air showers when γ -rays interact with air molecules high in earth's atmosphere. Section 3.1 outlines the physical properties of air showers, followed by an introduction to the detection principles and performance of past and current IACT telescope systems. Section 3.2 describes the technical and observational operations of the Whipple 10 m telescope. Lastly, calibration procedures and simulations for the Whipple 10 m are presented in section 3.3.

3.1.1 Air Showers

A steady isotropic flux of high energy protons and heavy nuclei (hadronic cosmic rays) collide with Earth's atmosphere where the particles interact with surrounding air molecules, producing cascades of secondary particles and photons known as air showers. The majority of secondary particles in air showers travel faster than the speed of light in air and emit Cherenkov radiation detectable from the ground. Air showers are also formed when high energy γ -rays or electrons hit the atmosphere causing electromagnetic showers. Both γ -ray and hadron initiated air showers are described below.

γ -ray Initiated Air Showers

Gamma-rays with energy $E_0 \gg 1$ MeV (twice the electron rest mass) incident on earth's atmosphere interact with atomic nucleus at a height of 15–30 km above sea level, almost exclusively producing electron-positron pairs. The secondary electrons and positrons from pair production each emit one γ -ray via bremsstrahlung (due to deflection from atmospheric nuclei) within one radiation length $X_0^e = 37 \text{ g cm}^{-2}$ (300 meters at sea level). These secondary γ -rays then pair produce within a radiation length $X_0^\gamma = 9/7 \cdot X_0^e$. Figure 3.1 (top left) shows a simple cascading interaction model for γ -ray initiated showers based on (Heitler 1954). The number of particles in the shower grows exponentially, while the average energy per particle decreases exponentially. The lateral spread in the air shower is primarily from small angle Coulomb scattering of the electrons or photons off nuclei, resulting in a narrow cone of particle paths along the shower axis. The maximum number of particles is reached when the average particle energy falls below a critical energy ($E_c \simeq 81$ MeV in air) where the loss of energy per unit length by bremsstrahlung falls be-

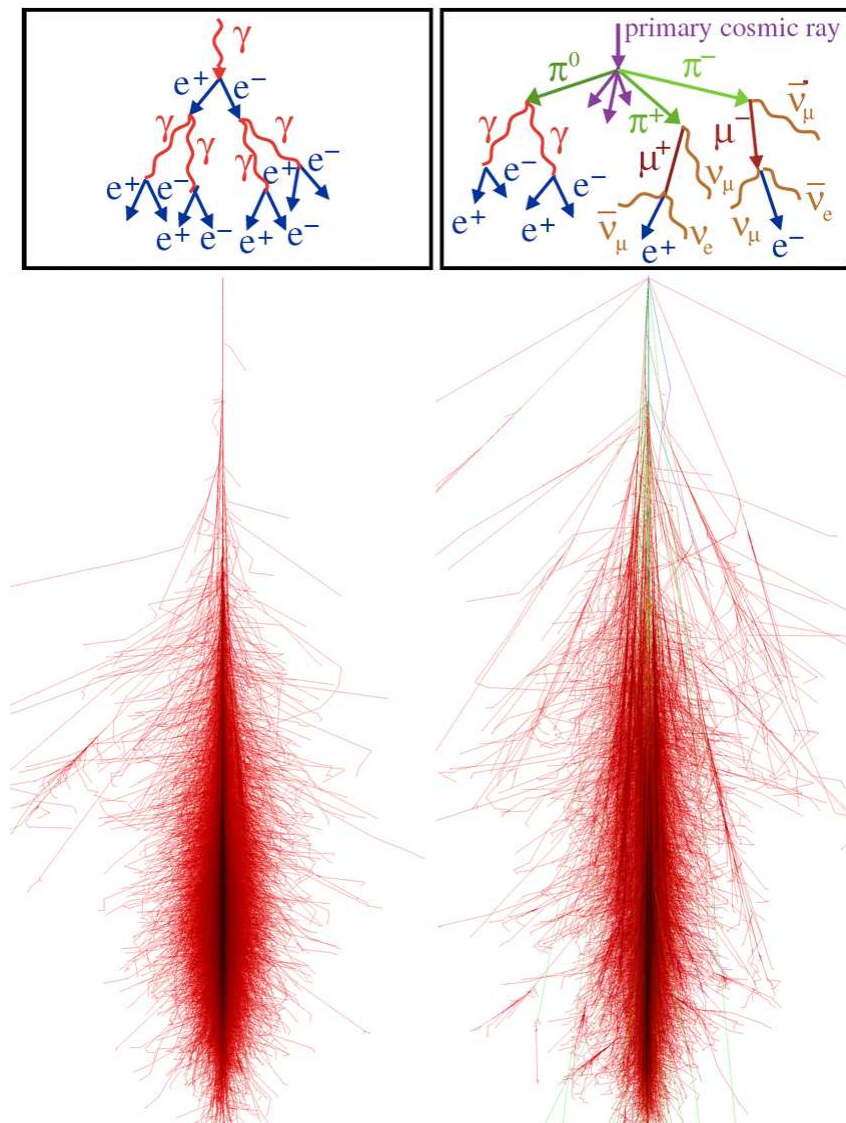


Figure 3.1: Simulated air showers initiated by either a (left) 1 TeV γ -ray or (right) 1 TeV cosmic ray proton using CORSIKA (Heck et al. 1998). The first interaction height is fixed at 30 km above sea level for both simulations. All particle paths are shown, including particles below the threshold energy to induce Cherenkov radiation. Electron, positron, and photon tracks are shown in red, muon tracks in green, and hadron tracks in blue. The shower core appears black because of the large density of particles tracks. CORSIKA simulations and images are courtesy of Fabian Schmidt (CORSIKA Images). Shown above the simulated showers are schematic diagrams for either (top left) γ -ray or (top right) cosmic ray initiated showers, courtesy of Deirdre Horan.

low the loss of energy per unit length by ionisation. The height of shower maximum and number of particles depends on the primary γ -ray energy E_0 . For example, a 1 TeV γ -ray initiated shower has a first interaction height of ~ 25 km, a shower maximum at ~ 8 km above sea level, and a total of $\sim 10^4$ particles. Figure 3.1 (left) shows a detailed simulation for a 1 TeV γ -ray air shower using CORSIKA (described in section 3.3.2).

Hadron Initiated Air Showers

High energy cosmic ray particles produce hadronic showers by strong inelastic scattering from an air nucleus. In this first interaction mostly pions (90%) are created, but also kaons and other light particles. About 1/3 of all generated pions are neutral pions (π^0) which decay almost instantly into two photons. These photons create electromagnetic sub-showers by pair production and bremsstrahlung interactions in the same manner as γ -ray initiated showers. The other 2/3 of pions are charged (π^\pm) and have a lifetime of $2.6 \cdot 10^{-8}$ s before mainly decaying into muons (μ^\pm). During the π^\pm lifetime interactions with air nuclei may occur, resulting in hadronic sub-showers of nuclei, protons, and neutrons. Muons in hadronic showers often penetrate to the ground, but may also decay into electrons and neutrinos. Figure 3.1 (top right) shows a diagram for the first interaction and resulting pion products in a hadronic shower. Shown below the diagram in figure 3.1 is a CORSIKA simulated air shower initiated by a 1 TeV cosmic ray proton. Compared with γ -ray air showers, the larger lateral extent and inhomogeneity of hadronic showers is due primarily to high fluctuations in hadronic interactions and the long transverse pion paths resulting in sub-showers over a large area. Also, hadronic showers develop closer to the ground than γ -ray showers due to the larger number of secondary particles and the longer hadronic interaction length X_0^p at GeV and TeV energies.

Cherenkov Light in Air Showers

Air showers contain a large number of particles with velocities exceeding the speed of light in air, which depends on the pressure at varying heights above sea level. Cherenkov photons are produced in coherent wave-fronts when relativistic charged particle polarize the surrounding atmospheric molecules (Jelley 1958). The number of photons emitted per unit length x and wavelength λ can be calculated using the Frank-Tamm equation:

$$\frac{dN}{dx d\lambda} = 2\pi\alpha Z^2 \frac{1}{\lambda^2} \left[1 - \frac{1}{\beta^2 n(\lambda)^2} \right]$$

where α is the fine structure constant, Z is the particle's charge, $\beta = v/c$ is the ratio of the particle's velocity v to the speed of light c in a vacuum, and $n(\lambda)$ is the wavelength dependent refractive in-

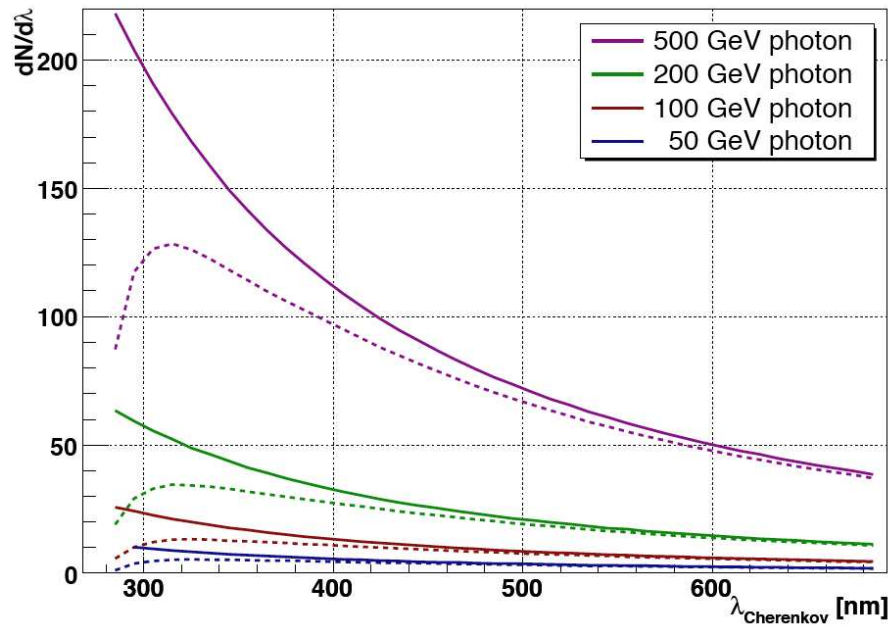


Figure 3.2: Cherenkov light spectra from vertical air showers initiated by γ -rays from 0.05–0.5 TeV energies. The solid lines show the Cherenkov spectra at a height of 10 km, while the dashed lines show the absorbed spectra at 2.2 km above sea level. Figure from (Wagner 2006).

dex. Figure 3.2 shows several example Cherenkov spectra from vertical γ -ray air showers near the height of maximum emission (10 km), and at 2.2 km above sea level where atmospheric absorption is evident in the UV band, primarily due to λ dependent Rayleigh scattering off air molecules. The Cherenkov light is emitted in a narrow cone with Cherenkov angle $\theta_c \simeq 0.5^\circ$ – 1.5° between the Cherenkov light and particle track. The minimum energy of a particle to emit Cherenkov radiation in a medium is given by $E_{\min} = \gamma_{\min} m_0 c^2$, where γ_{\min} is the minimum Lorentz factor, and m_0 is the particle's mass. Due to the linear dependence of E_{\min} on the particle's mass, electrons emit most of the Cherenkov light in air showers, with $E_{\min}^e > 22$ MeV for electrons, $E_{\min}^\mu > 4.6$ GeV for muons, and $E_{\min}^p > 40$ GeV for protons (Rao and Sinha 1988). For γ -ray initiated showers, the Cherenkov photon density is roughly a constant fraction of the primary γ -ray energy, and forms a nearly uniform light pool on the ground due to the near constant Cherenkov angle θ_c of emission. A typical 1 TeV γ -ray initiated shower generates a light pool of ~ 100 photons m^{-2} on the ground within a radius of 120 m during a time-scale of 10 ns. Figure 3.3 (left) shows a CORSIKA simulated light pool from a 0.3 TeV γ -ray air shower at 2300 m above sea level (the height of the Whipple 10 m telescope). Figure 3.3 (right) shows the simulated Cherenkov light density from a 0.5 TeV cosmic ray proton initiated air shower. Multiple light pools from several sub-showers are evident, covering a large total lateral area.

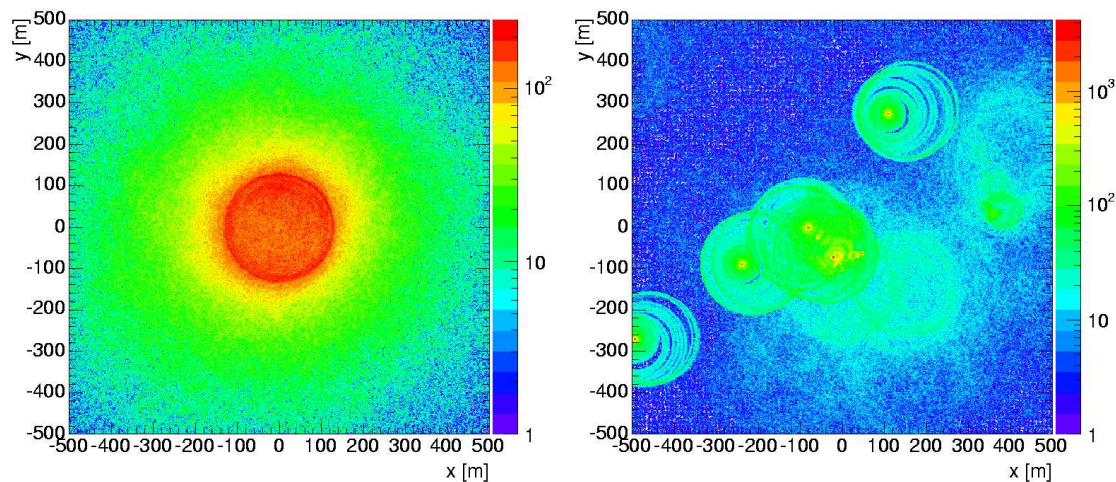


Figure 3.3: Simulated Cherenkov light density (m^{-2}) at 2300 m above sea level from vertical (0° zenith angle) air showers initiated by (left) a 0.3 TeV γ -ray, and (right) a 0.5 TeV cosmic ray proton. CORSIKA simulations and images are courtesy of Gernot Maier.

3.1.2 Detection Principles of IACT telescopes

Ground based Imaging Atmospheric Cherenkov Technique (IACT) telescopes track γ -ray sources in the sky using a large steerable dish of segmented mirrors with a fast camera at the focus to record the induced Cherenkov light from air showers. IACT cameras typically consist of >300 pixels of photo-multiplier tubes (PMTs) each having a $\sim 0.1^\circ$ diameter. A large $>2.5^\circ$ field of view is needed to fully contain Cherenkov images from >1 TeV γ -ray initiated air showers, particularly for extended γ -ray sources. IACT telescopes detect the faint rapid Cherenkov flashes above the noise level from the night sky background (NSB) with nanosecond time-scale event triggers. For example, the Cherenkov flash from a 1 TeV γ -ray is a factor ~ 5 brighter than the NSB during a clear moonless night when collected by a ~ 10 m diameter dish in $\sim 0.1^\circ$ size pixels over an integration window of ~ 20 ns.

γ -ray Selection and Reconstruction

IACT telescopes discriminate between γ -ray and cosmic ray initiated air showers based on the characteristic uniformity of Cherenkov light density on the ground, as shown in figure 3.3. For non-vertical γ -ray air showers, the elliptical Cherenkov light pool points in the direction of the primary γ -ray, identifying these images from the large background of isotropic fragmented cosmic ray showers. Since the number of Cherenkov photons in a shower is proportional to the number of shower particles, the primary γ -ray energy is reconstructed from the Cherenkov image intensity

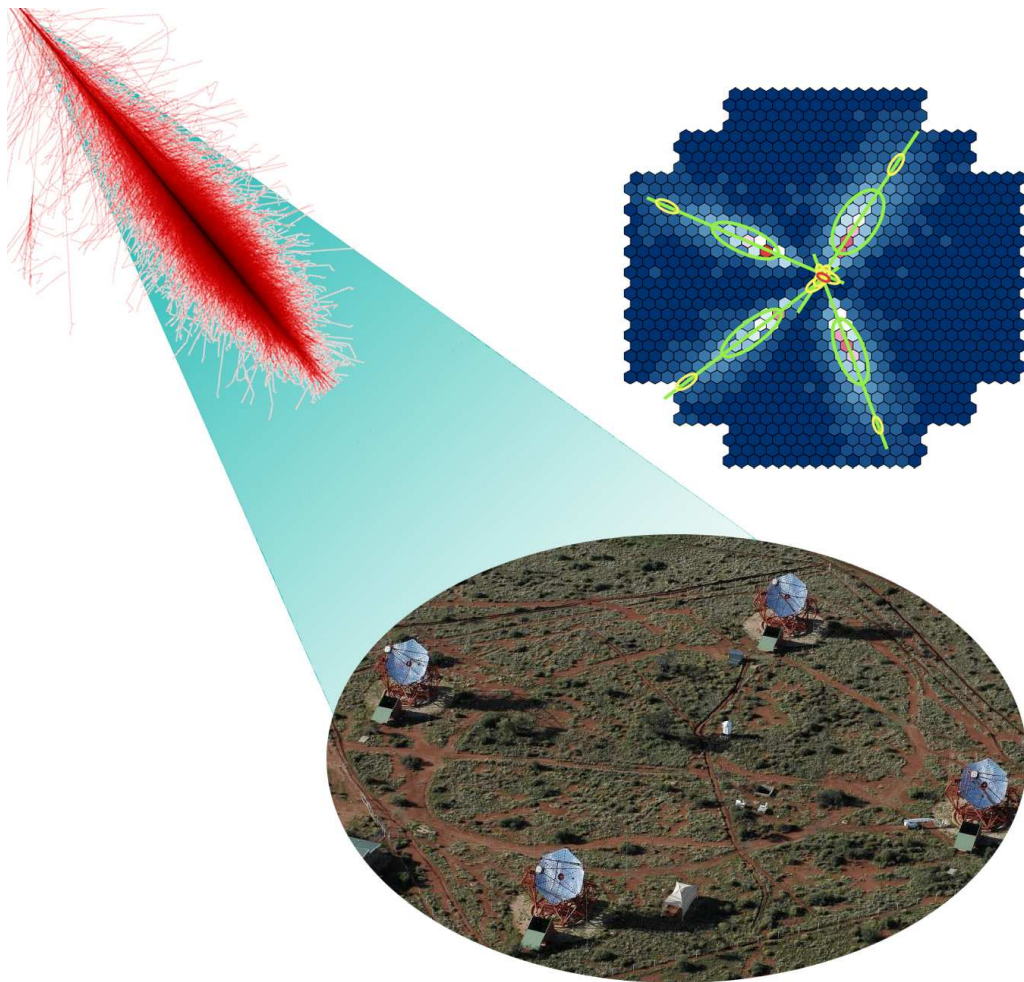


Figure 3.4: A montage of images showing the basic detection principle of IACT telescope systems. Shown (top left) is a CORSIKA simulated γ -ray air shower from figure 3.1 with the Cherenkov light yield represented by a blue cone. Shown (bottom right) is the H.E.S.S. system of 4 IACT telescopes, described in section 3.1.3. Shown (top right) are Cherenkov images of a simulated 7 TeV γ -ray air shower from each of the 4 H.E.S.S. cameras superimposed onto one camera, adapted from (Berge 2006).

and shower core location relative to the telescope. The effective area of single IACT telescopes is very large ($\sim 10^5 \text{ m}^2$ at 1 TeV), and is determined by the efficiency of detecting Cherenkov light. Using a single IACT telescope, the angular position of incident γ -ray is not directly measured, and is estimated based on the characteristic shape of γ -ray Cherenkov images from simulations. Section 4.2 describes in detail the γ -ray reconstruction methods applied to the single Whipple 10 m telescope. The basic detection principles pioneered with the Whipple 10 m are used in modern IACT telescope arrays. Stereoscopic arrays use a number of IACT telescopes arranged $\sim 100 \text{ m}$ apart with a $\sim 100 \text{ ns}$ coincidence window for event triggers from each telescope to reconstruct



Figure 3.5: Photographs of currently operating IACT γ -ray telescope systems. Shown are the (top) VERITAS and (middle) H.E.S.S. phase I four telescope systems. The bottom panel shows (far left) the MAGIC phase I telescope, (middle left) 1 of 4 CANGAROO-III telescopes, (middle right) TACTIC, and (far right) the Whipple 10 m telescope.

stereo events, which greatly reduces the background. Figure 3.4 shows the basic principle of γ -ray reconstruction. The Cherenkov light pool from a γ -ray shower in this stereoscopic observation is recorded at a different viewing angle with each telescope providing a geometric measurement of the source direction by the intersection point of image axes.

3.1.3 Past and Current IACT γ -ray Telescopes

This section presents an overview on the history and current status of IACT telescopes. Figure 3.5 shows photographs of all currently operating IACT telescopes. The first IACT telescope was the Whipple 10 m telescope, built in 1968 atop Mt. Hopkins, Arizona, USA, with the first imaging camera installed in 1982 (Weekes et al. 1989). Currently fully operational, the Whipple 10 m

Telescope(s)	Location	Start (year)	Mirr. ^a (m)	FOV (deg.)	E. Res. ^c (%)	E. Th. ^d (TeV)	Sens. ^e (σ/\sqrt{hr})
Whipple 10 m	Arizona, USA	1968	1×10	2.6	32	0.4	5
TACTIC	Rajasthan, IN	2000	1×3.5	3.4	40	1	1
CANG.-III	Australia	2004	4×10	4.0	29	0.6	2
H.E.S.S.	Namibia	2004	4×13	5.0	19	0.2	28
MAGIC	La Palma, ES	2004	1×17	3.5	22	0.1	20
VERITAS	Arizona, USA	2007	4×12	3.5	20	0.3	28

Table 3.1: Performance of current IACT telescope systems. Notes: (a) Telescopes of mirror diameter (m) are listed as tele. num. × m (b) Energy resolution. (d) Energy threshold. (e) Sensitivity for Crab nebula observations (for CANGAROO, 2 of 4 telescopes are used). References: Whipple 10 m (this work), TACTIC (Dhar et al. 2005), H.E.S.S. (Aharonian et al. 2006a), CANGAROO-III (Enomoto et al. 2006), MAGIC (Wagner et al. 2005), VERITAS (Kieda et al. 2007).

has a lower energy threshold of ~ 0.45 TeV and energy resolution of 31% (see section 4.4 for details). Generally, the upper energy limit for IACT telescopes is determined by low statistics from γ -ray sources with steep spectra, which for the Whipple 10 m is ~ 20 TeV. Over the energy range of 0.45–10 TeV, the Whipple 10 m sensitivity for observations of the Crab nebula is $\sim 5 \sigma/\sqrt{hr}$, as determined in section 4.5. Table 3.1 compares the performance of the Whipple 10 m telescope with other currently operating IACT telescope systems. Following the Whipple 10 m, the HEGRA Cherenkov telescope 1 (CT1) started observations in 1992 at La Palma, Spain, with an energy threshold of ~ 1 TeV (Mirzoyan et al. 1994). In 1996, the HEGRA system of five 3.4 m telescopes started stereoscopic observations (Daum et al. 1997). The HEGRA system achieved an energy threshold of 0.5 TeV, energy resolution of 10–20%, and sensitivity for the Crab nebula of $16 \sigma/\sqrt{hr}$ (Pühlhofer et al. 2003). Both the HEGRA system and CT1 stopped taking data in late 2002. Two IACT telescopes were built in Australia during the 1990’s, the CANGAROO 3.8 m telescope (1992–1998), and the Mark 6 telescope (1995–2000) (Hara et al 1993; Armstrong et al. 1999). Since 2004, the CANGAROO-III array of 4 IACT telescopes is currently taking observations. From this generation of experiments, two other IACT telescopes are noted here: CAT (1996–2003) in France, and TACTIC (2000–present) in India (Barrau et al. 1998; Dhar et al. 2005).

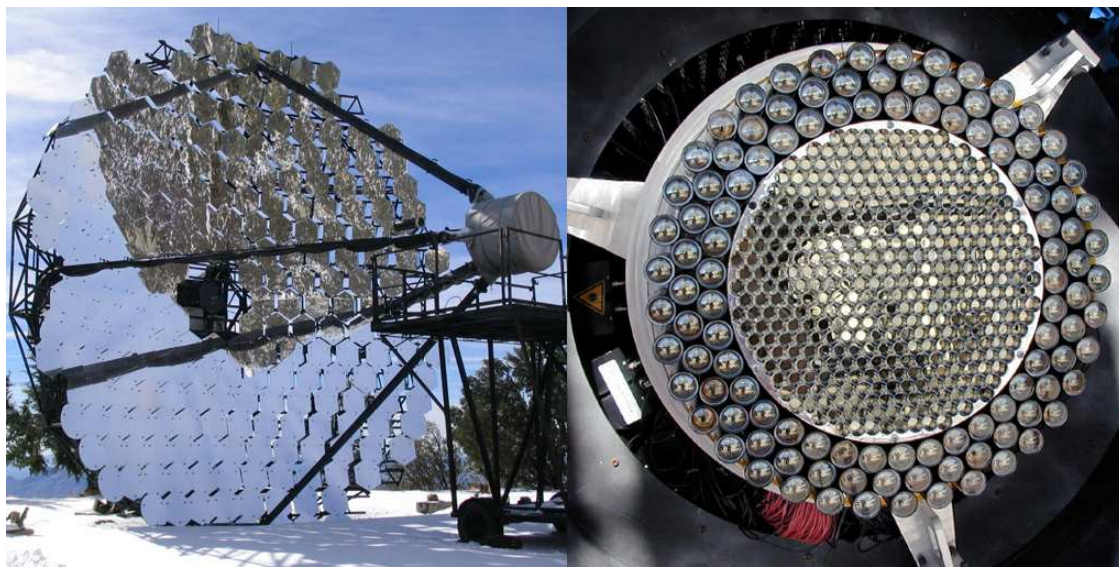


Figure 3.6: Photographs of the Whipple 10 m telescope. Shown (right) is the camera at the focus.

Modern IACT Telescope Systems

H.E.S.S., MAGIC, and VERITAS represent a new class of high sensitivity IACT telescope systems. H.E.S.S. phase I is an array of four 13 m telescopes in Namibia, southern Africa. Each H.E.S.S. phase I camera contains 960 pixels for a 5° field of view. H.E.S.S. features an energy threshold of ~ 0.2 TeV and sensitivity for the Crab Nebula of $28 \sigma/\sqrt{hr}$ (Aharonian et al. 2006a). Construction has started on a large 32 m tall by 24 m wide telescope positioned in the center of the H.E.S.S. array for combined phase II observations with the four 13 m telescopes starting in 2008 (Vincent et al. 2005). MAGIC is located at La Palma, Spain and started operations in 2004 with a single 17 m telescope (phase I), while construction has begun on a second 17 m telescope for stereoscopic observations in phase II (Mirzoyan et al. 2005). VERITAS is an array of four 12 m telescopes at the Whipple site in Arizona, USA and has started full operations in Spring 2007 (Holder et al. 2006; Kieda et al. 2007). The VERITAS sensitivity for Crab nebula observations is $\sim 28 \sigma/\sqrt{hr}$ over the energy range of 0.3–10 TeV.

3.2 The Whipple 10 m Telescope

The Whipple 10 m telescope is located on Mount Hopkins, Arizona, USA at an altitude of 2312 m. The site is run by the Smithsonian Institute's Fred Lawrence Whipple Observatory (FLWO). VERITAS and several large optical telescopes are also located near the site, which offers clear skies, low wind, and low humidity for a large fraction of moonless nights. The Whipple 10 m

is run by the VERITAS collaboration, which consists of over 70 members from the US, Canada, UK, and Ireland. Figure 3.6 (left) shows a photograph of the Whipple 10 m telescope taken during Dec. 2004. In this section, an overview is given of the Whipple 10 m instrumentation, with further details in (Kildea et al. 2007).

3.2.1 Telescope Mount and Optics

Built in 1968, the Whipple 10 m telescope has an altitude-over-azimuth positioner, which drives a steel optical support structure (OSS) balanced by lead counterweights. Four steel arms support a cylindrical focus box containing the camera within a focal plane of 7.3 m. The Whipple 10 m telescope has a slew speed of 1° per second, and tracking resolution of 0.01° . Supported by the OSS is the 10 meter diameter optical reflector consisting of 240 mirror facets in a Davies-Cotton design (Weekes et al. 1972; Davies and Cotton 1957). Using this design off-axis aberrations are reduced, although photon arrival times are spread out by ~ 6 ns. The mirrors are 61 cm wide and hexagonal in shape, with a thickness of 1 cm. A front coating of anodized aluminum was applied to the mirrors for optimal reflectivity in the blue to UV range. The peak mirror reflectivity at 310 nm is 85% with a gradual degradation over time due to environmental effects. The mirror point spread function (PSF) is measured by a CCD camera at the center of the dish, which images a bright star projected in the focal plane. The measured FWHM of 0.13° for the PSF is larger than the 0.12° diameter of each camera pixel. The mirror alignment procedures and PSF measurements are described in (Kildea 2002; Schroedter 2004).

3.2.2 Camera

Since 1982 the Whipple 10 m the camera has had four major upgrades, with the current camera installed in 1999. Figure 3.6 shows a photograph of the current camera mounted in the focus box. The inner camera consists of 379 photo-multiplier tube (PMT) pixels with 0.12° diameter, giving a total circular field of view (FOV) of 2.6° . The outer ring of 111 (0.25° diameter) PMTs were removed in 2003, and were not considered in this work. Light cones are placed in front of the inner PMTs to shield the PMT photo-cathodes from background light and to reduce photon losses from gaps between pixels. The PMT quantum efficiency is 20% over the blue to UV region with a 1–2 ns response. High voltage to the PMTs is supplied by three modules mounted on the telescope counterweights. Coaxial cables send the analog PMT signals to the electronics room, where the signal is AC-coupled to a ten-times amplifier. After this stage, the signal is split equally between the trigger system and readout system. Figure 3.7 shows the signal path through a schematic diagram for the 331 of 379 pixels contained in the trigger system.

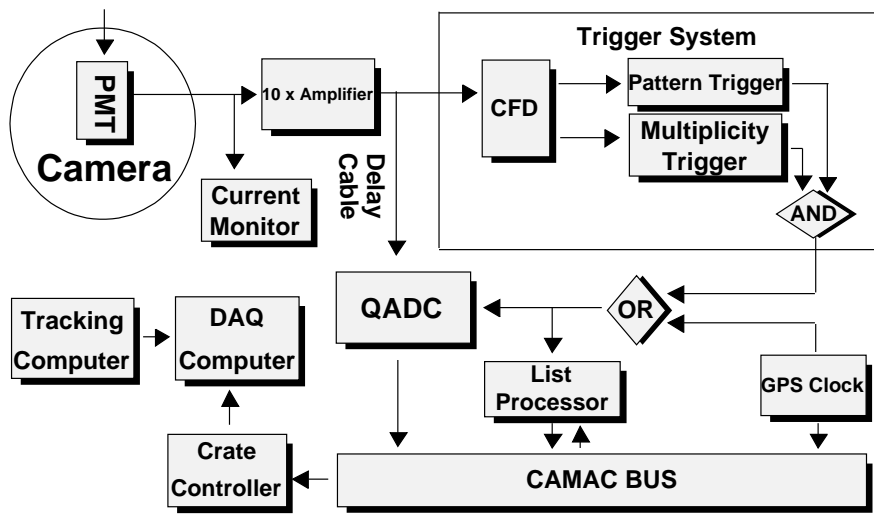


Figure 3.7: Schematic diagram of the Whipple 10 m signal path.

3.2.3 Trigger System

The trigger system is used to select Cherenkov events and avoid events containing only the night sky background (NSB) plus electronic noise. In the first stage, the signal in each pixel passes through constant fraction discriminators (CFDs). If the amplified PMT signal exceeds a determined threshold, then the CFD outputs a 10 ns wide pulse to both a multiplicity trigger and a pattern selection trigger (PST), as shown in figure 3.7. Within a window of 8 ns, the multiplicity trigger requires a coincidence of any 2 or 3 pixels to trigger, while the PST requires 3 or 4 adjacent pixels. The PST subdivides the inner 331 pixel camera into overlapping groups of 19 pixels, so that a pattern of 3 or 4 adjacent pixels is fully contained within at least one group (Bradbury and Rose 2002). Figure 3.8 shows the trigger rate versus CFD threshold using either a 2-fold coincidence for any pixel, or 3-fold adjacent pixel trigger as measured in Oct. 2001 by pointing the telescope at 0° zenith. At low CFD threshold values, fluctuations in the NSB dominate the trigger rate. For nearly all observations since 2000, a 3-fold adjacent pixel trigger is used with CFD thresholds ranging from 32–36 mV. The threshold level was determined by the transition point where the trigger rate becomes stable and is no longer NSB dominated.

3.2.4 Readout System

For each event passing the trigger system, an output pulse is sent to coincide with the delayed PMT signal reaching each channel’s charge analog-to-digital converter (QADC). The PMT signals are delayed by ~ 120 ns via coaxial cables. Once receiving an event trigger, the QADCs integrate each PMT signal for 20 ns. The integrated signal intensity is recorded in digital counts (dc) and

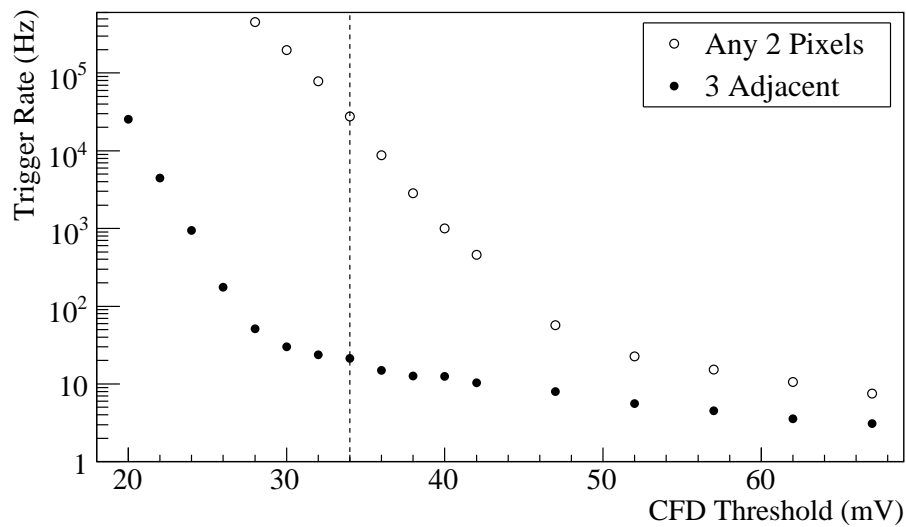


Figure 3.8: Whipple 10 m trigger rate versus CFD threshold as measured in Oct. 2001 at 0° zenith using (empty circles) the multiplicity trigger for any 2 pixels, or (filled circles) the PST set for 3 adjacent pixels. A CFD threshold of 34 mV was used for observations during 2001 to 2002, shown by the dashed line.

sent to a list processor. Events are stored in the list processor with their GPS time stamp until the acquisition software reads them out. The entire readout process takes ~ 0.4 ms, during which time the camera can not respond to further trigger signals (the system dead-time). During observations, the typical event rate is 10–30 Hz, resulting in a very low dead-time of 0.5–1.4%. Figure 3.9 shows the system dead-time as evident by the smallest time difference between consecutive events. A CAMAC bus system transfers the event data to a Data Acquisition (DAQ) computer, which also records the telescope elevation and azimuth. Further details of the readout system are in (Rose et al. 1995a).

3.2.5 Telescope Operation

The duty cycle of IACT telescopes is typically $< 10\%$ due to the general requirement of clear moonless nights for high quality observations. Since moonlight is a few orders of magnitude brighter than Cherenkov light, the Whipple 10 m normally only operates when the moon (and sun) are below the horizon. Operations during partial moonlight were tested with the Whipple 10 m, made standard for the HEGRA CT1 telescope, and have recently been studied with MAGIC (Pare et al. 1991; Kranich et al. 1999; Albert et al. 2007a). Additional constraints on the Whipple 10 m and VERITAS duty cycles are annual storms that pass through southern Arizona in August, causing operations to stop in July, and resume in September of each year. Figure 3.10 shows the

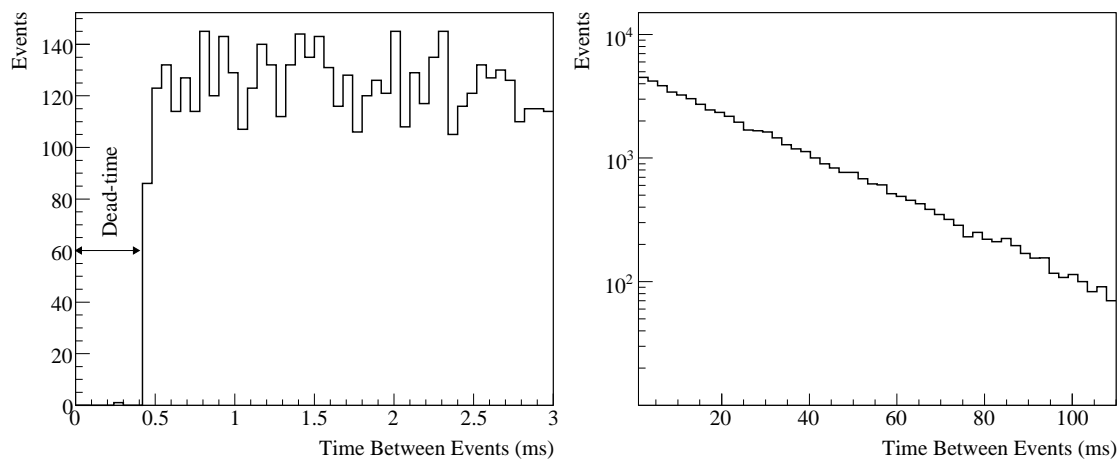


Figure 3.9: Whipple 10 m system dead-time of ~ 0.4 ms shown by the shortest time between consecutive events. Shown (right) is the same distribution, but at longer time differences on a logarithmic scale.

total number of moonless hours available to the Whipple 10 each night during 2006, and the actual number of hours taken for observations. Poor weather accounts for the main fraction of observing time lost, with a small amount ($\sim 3\%$) lost to due to telescope failures and engineering. The weather is monitored by the observer on a continual basis, including wind speed, temperature, and relative humidity readings. Section 3.2.6 describes the quality criteria used to reject observations during poor conditions.

Observation Modes

Observations with the Whipple 10 m are conducted in either a *Tracking* or *ON/OFF* mode. In the ON/OFF mode, the telescope tracks the source centered in the field of view for 28 minutes (ON), and then two minutes later re-tracks a corresponding sky region for 28 minutes with equivalent declination, but offset by 30 minutes in right ascension (OFF). This mode allows for direct background subtraction of cosmic ray events in the ON observation. The Tracking mode is defined by taking an ON observation of 10 or 28 minute exposure with no corresponding OFF sky observation. Due to the small field of view with the Whipple 10 m camera, it is not practical to use a so-called wobble mode. During wobble mode observations the background is determined from offset pointings which contain both the source position and background sky regions in the camera. All Crab nebula observations in this work were carried out in ON/OFF mode (see section 4.4), while 83% of the selected TeV blazar observations in this work were taken in Tracking mode (see section 5.1). The method for selecting the best OFF runs to Tracking data is described below.

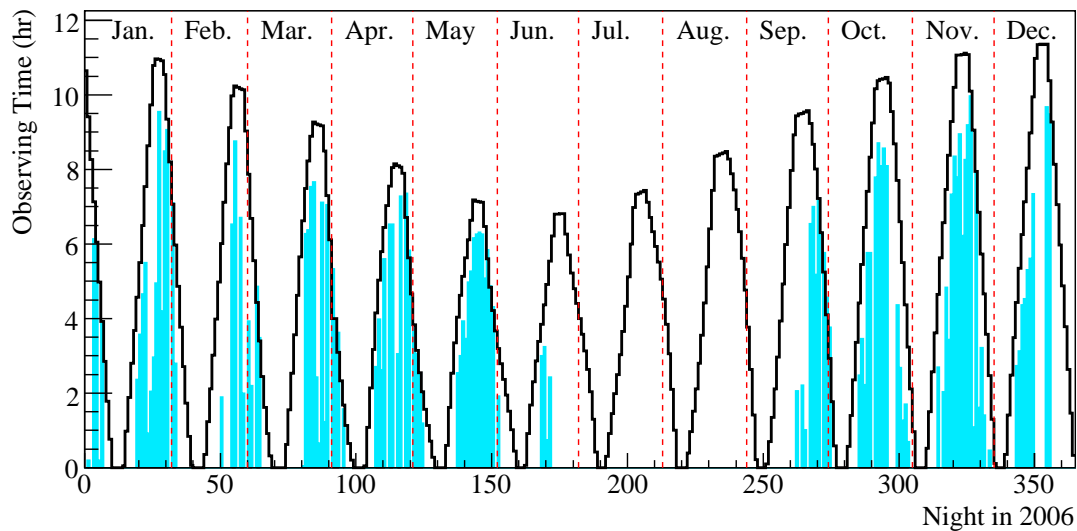


Figure 3.10: Whipple 10 m observing efficiency during 2006. The total hours spent observing each night is represented by the aqua (filled) distribution, with the number of available observing hours each night shown by the black (empty) distribution.

3.2.6 Data Quality and Background Sky Field Selection

Data is first selected according to the observing conditions and telescope performance noted during operations. The weather conditions are graded continually by the observers on a subjective scale of A, B, or C weather, with A weather defined for clear visibility, low humidity, and low winds, B weather for light cloud coverage, and C weather for significant cloud coverage. Only observations during A and B weather are used in this thesis. Additionally, the small fraction of observing runs with malfunctioning telescope tracking, trigger, or readout systems are rejected based on the observer's notes. The main criterion for run selection is the stability of the telescope event rate. Figure 3.11 shows for example the event rate from Crab nebula observations in March 2003 during B weather, and in January 2006 during A weather conditions. The variable rate in the B weather observation is evident by a larger RMS spread in event rate per 30 sec. bin. In this work, a quality cut on the event rate $\text{RMS} < 1.5 \text{ Hz}$ is used.

Background OFF Data Selection

Appropriate background OFF sky regions were best matched to Tracking mode observations based on the zenith angle Θ and observation time in Modified Julian Day (MJD) of each run following a simple matching routine introduced in (de la Calle Pérez 2003). In this method, a score is calculated for all possible pairs of Tracking and OFF runs passing data quality cuts, with the

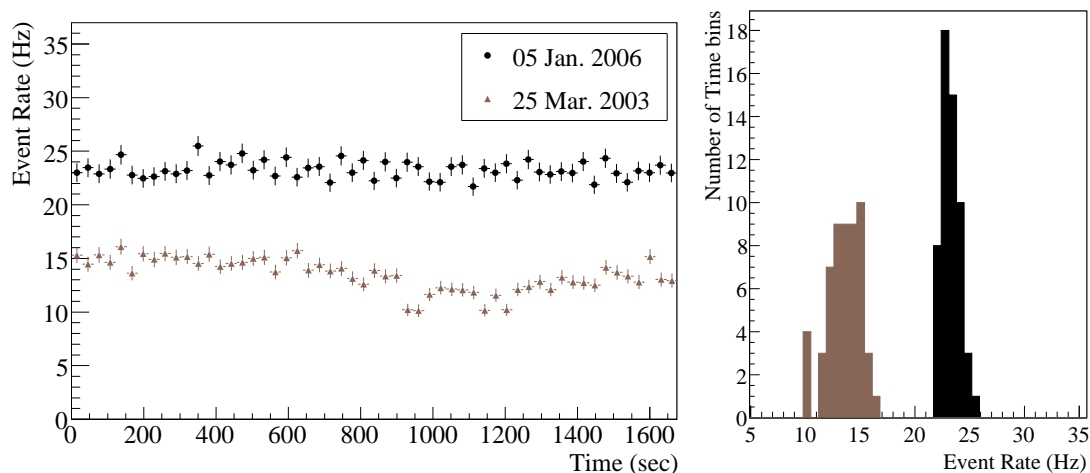


Figure 3.11: Whipple 10 m event rate from Crab nebula observations. Shown (left) in black circles is the event rate at 14° zenith during 5 Jan. 2006 in A weather, and from 25 Mar. 2003 at 29° zenith in B weather (brown). The lower event rate in the 2003 observation is due both to the larger zenith angle and lower detector efficiency (see figure 3.13). On the (right) are shown the event rate distributions. The RMS spread in the 2003 observation is > 1.5 Hz, resulting in the run being rejected.

lowest score representing the best match:

$$\text{Score} = \left| \frac{\text{MJD}_{\text{ON}} - \text{MJD}_{\text{OFF}}}{w_{\text{MJD}}} \right| + \left| \frac{\Theta_{\text{ON}} - \Theta_{\text{OFF}}}{w_{\Theta}} \right|$$

The weights were optimized to give the lowest spread in time and zenith angle from a large sample of data, with $w_{\text{MJD}} = 1$ and $w_{\Theta} = 2$. Each selected OFF run was required to be taken within 10 days before or after the Tracking run, with a difference of less than 10° in zenith angle. Differences in NSB levels between Tracking (ON) runs and OFF runs were corrected for in data reduction by adding artificial noise (see section 4.1). For the large sample of over 600 hours of TeV blazar observations presented in chapters 5 and 6, a total of 83% of the source observations were taken in Tracking mode. The OFF data used in this work was drawn from a total sample of 458.3 hours of data passing quality cuts, and is further detailed in section 5.1.1.

3.3 Whipple 10 m Calibration and Simulations

This section describes the applied calibration methods and detailed simulations generated for Whipple 10 m observations. Section 3.3.1 outlines the measurement techniques used to calibrate the intensity of recorded Cherenkov images. Section 3.3.2 describes the sample of air shower

and detector simulations used extensively in the data reduction and energy reconstruction routines implemented in this work for Whipple 10 m data.

3.3.1 Pixel Intensity Calibration

The image intensity of Cherenkov events measured by IACT telescopes is affected by atmospheric conditions, the telescope's optical system (mirror and light cone efficiencies), and the gain in the camera. In the first step, the camera is flat-fielded to correct for the non-uniform response of pixels across the field of view. The measured gain in the camera is then used to convert the Cherenkov signal from digital counts to photoelectrons. The time dependent efficiency of the optical system and PMTs in the camera was determined by comparing the intensity of muon events to the expected intensity from simulations. An overall detector efficiency is then defined in this work relative to the nominal gain when the camera was installed in 1999.

Pedestal and NSB Determination

The pedestal value in each pixel is defined by the mean signal in dc recorded in the absence of Cherenkov light. The pedestal distributions in the dark have a narrow Gaussian shape, with a mean of ~ 20 dc due to a small biasing current injected into each QADC to account for negative noise fluctuations (Kildea et al. 2007). During observations, the pedestals are measured at a rate of ~ 1 hz using artificial triggers containing no Cherenkov signal. The amount of night sky background (NSB) recorded during each QADC integration window dominates the width in the pedestal distribution, with a small noise contributions from the PMTs and electronics chain.

Camera Flat-fielding

The high voltages to each pixel are adjusted each September in an iterative flat-fielding process to achieve a relatively uniform response across the camera. After this flat-fielding, the remaining spread in pixel gains is $\sim 5\%$, which is corrected for on a nightly basis with 1 minute runs using light pulses from a nitrogen discharge tube mounted at the center of the reflector. The fast ~ 35 ns pulses illuminate the camera with a nearly uniform light intensity of ~ 10 – 150 photoelectrons (pe) at a rate of ~ 750 Hz. Flat-fielding coefficients g_i are determined for each pixel by comparing the pixel intensity to the mean intensity from all pixels for every pulse. Section 4.1 describes how the relative gain coefficients g_i are applied in standard data reduction.

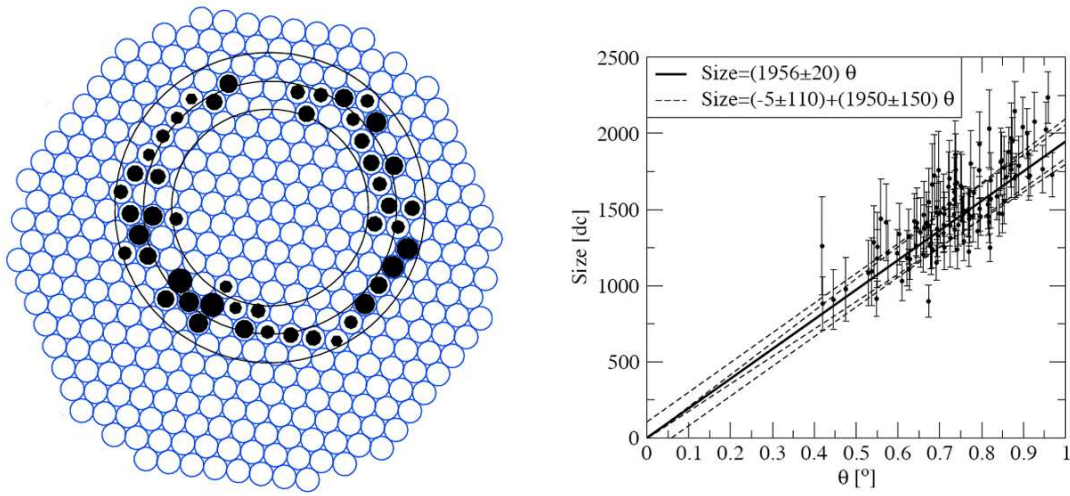


Figure 3.12: Calibration method using muon images. Shown (left) is an example muon event in the Whipple 10 m camera. (Right) is the distribution of total image intensity (Size) versus the Cherenkov angle (θ) for muon images taken from data in 2001. Figures from (Schroedter 2004).

Camera Gain from Measurements in Dec. 2000

Within the camera, the dc signal from 1 pe was measured in Dec. 2000 using a number of factors: the gain in the PMTs $G_o = 1.1 \cdot 10^6 \text{ e pe}^{-1}$, the QADC conversion ratio $F_{\text{QADC}} = 4 \cdot 10^{20} \text{ dc C}^{-1}$, the combined signal losses in the amplifiers and cables $A_s = 4.68$ in relative units, and $C_G = 1.6 \cdot 10^{-19} \text{ C e}^{-1}$. The total camera gain was estimated at $\text{dc/pe} = A_s \cdot G_o \cdot C_e \cdot F_{\text{QADC}} = 3.3 \pm 0.3 \text{ dc/pe}$ (Schroedter 2004). The calculated error included estimates on the systematic uncertainties in the measurements. Ideally, the camera gain should be measured on a daily to monthly basis, however a regular gain calibration program was never established for the Whipple 10 m. As a compromise, monthly muon measurements of the telescope efficiency are used to estimate the camera gain from 2000–2006.

Gain Calibration Using Muons

Muons produced in hadron initiated air showers with energies $\geq 4.6 \text{ GeV}$ passing nearly parallel, and within a few meters of the reflector at ground level will form clearly defined Cherenkov ring images in the camera. Fully contained muon image are selected and fit with a circle to determine the intensity in dc and Cherenkov angle θ_c . Figure 3.12 (left) shows a selected muon image and parametric fit in the Whipple 10 m camera. The expected muon intensity as a function of θ_c (proportional to the energy) is derived from simulated muons, defining the collection efficiency of the optical system and camera when compared to the data, as shown in figure 3.12 (right) (Rose

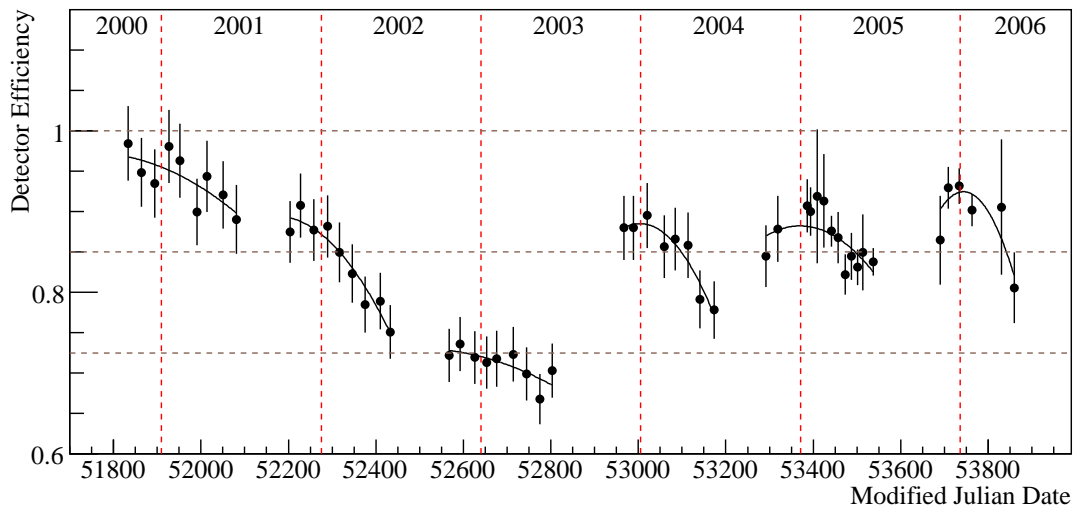


Figure 3.13: Whipple 10 m detection efficiency from 2000–2006 measured by muon images. The curved lines are parabolic fits to the efficiency for each observing year (starting in Sept.–Oct.). The brown dashed lines represent the efficiency of the three simulation sets described in section 3.3.2.

et al. 1995b; Schroedter 2004). Figure 3.13 shows the detector efficiency relative to Dec. 2000 taken from muon events collected during standard observation runs in ~ 20 day bins from 2000–2006. Results from an independent method using the image intensity of cosmic ray events at a fixed zenith angle were shown to agree within the $\sim 10\%$ systematic errors of either method (LeBohec and Holder 2003; Daniel et al. 2005). A continual degradation of the PMTs was the main contributing factor to the large drop in detector efficiency from 2000 to 2003. Raising the high voltage supply to the PMTs in October 2003 increased the gain to the level in late 2001.

3.3.2 Simulations

The CORSIKA package was used to generate a large sample of simulated γ -ray initiated air showers (Heck et al. 1998). CORSIKA simulates the development of air showers at the single particle level using interaction models for pair production, multiple Coulomb scattering, ionization losses, and other processes. The program EGS4 is used by CORSIKA to simulate the electromagnetic interactions, applying QED calculations from cross section measurements up to 200 GeV. Cherenkov emission from shower particles are simulated over the wavelength range 200 to 685 nm. Different atmospheric models are available to account for environmental effects, including absorption. CORSIKA records the photon position, direction, wavelength, and height of emission for each photon bunch that reaches the observational level within a spherical area centered on the

detector. CORSIKA simulated air shower particle tracks and Cherenkov photon density are shown by figures 3.1 and 3.3.

Detector Simulations

The output from CORSIKA air showers were processed through the Whipple 10 m configuration contained within the GrISU detector simulation package. GrISU simulates the layout and orientation of the 10 m reflector, and ray traces Cherenkov photons to the camera using the measured point spread function and mirror reflectivity. The light cones are simulated by simply increasing the photosensitive area of the PMT cathode. The PMT and read-out system are implemented using a simulated QADC response and measured quantum efficiency, but the pattern trigger is not simulated.

Sample of Simulated γ -rays

A large sample of simulated γ -ray events was generated with the CORSIKA, GrISU, and Granite analysis chain. Four sets of 10^6 γ -ray air showers were simulated at zenith angles of 10° , 20° , 30° , and 40° . A power law energy spectrum of the form $dN/dE = (E/1 \text{ TeV})^{-\Gamma}$ was used with $\Gamma = 2.5$ over the energy range of 0.2–20 TeV. Air showers were spread evenly over a circular region of radius 400 m centered on the detector. Each shower was used 10 times, with the core position randomly distributed for all events. The US76 atmospheric model was used for the Whipple 10 m observatory height of 2312 m. To account for the large shifts in detector efficiency from 2000 to 2006 shown in figure 3.13, the simulated showers were run through the detector chain with three different camera gains: 3.3 dc/pe, 2.8 dc/pe, and 2.4 dc/pe (100%, 85%, and 72.5% efficiency). The simulated night sky background (NSB) was $650 \text{ pe ns}^{-1} \text{ m}^{-2} \text{ sr}$. Events which triggered the simulated telescope were processed with the Whipple 10 m “Granite” package using the standard methods for observational data, as detailed in the following chapter.

Chapter 4

Whipple 10 m Data Reduction

Data reduction techniques for observations with the Whipple 10 m telescope developed in this work are described here in detail. Section 4.1 describes the method used for cleaning and parameterizing Cherenkov images. Section 4.2 provides an overview on the reconstruction techniques implemented to estimate the energy and direction of each event. Gamma-ray type events are selected from the large background of cosmic ray air showers using the image intensity, shape, and direction, as detailed in section 4.3. Section 4.4 describes how the γ -ray source flux and energy spectrum is determined using the effective area of the instrument and the number of selected γ -ray type events. Section 4.5 presents results from 65 hours of observations during 2000–2006 of the Crab nebula - the remnant of a supernova event, which occurred in 1054 AD at a distance of 2000 parsecs. Assumed to be a strong constant TeV γ -ray emitter, the Crab nebula was the first detected at TeV energies in 1989 by the Whipple 10 m, and has since served as the main calibration source for IACT telescope systems (Weekes et al. 1989; Aharonian et al. 2006d). The Crab nebula differential energy spectrum from the total 2000–2006 data set with the Whipple 10 m was best fit by a power law of the form $dF/dE = F_0 \cdot (E/\text{TeV})^{-\Gamma}$ over the energy range 0.45–8 TeV with spectral index $\Gamma = 2.64 \pm 0.03_{\text{stat.}}$ and flux normalization $F_0 = (3.19 \pm 0.07_{\text{stat.}}) \times 10^{-11} \text{ cm}^{-2} \text{ s}^{-1} \text{ TeV}^{-1}$. This result is shown consistent with previous measurements, giving confidence in the calibration and data reduction methods. Systematic uncertainties in the flux measurement are estimated at 30%, with an error of 0.15 in the spectral index measurement.

4.1 Image Processing

The Cherenkov image processing procedures described here are implemented in the Whipple 10 m “Granite” package. For each observation run, the mean pedestal value in each pixel $\langle \text{Ped} \rangle_i$ in units of digital counts (dc) is calculated from the 1 Hz artificial pedestal triggers, introduced in

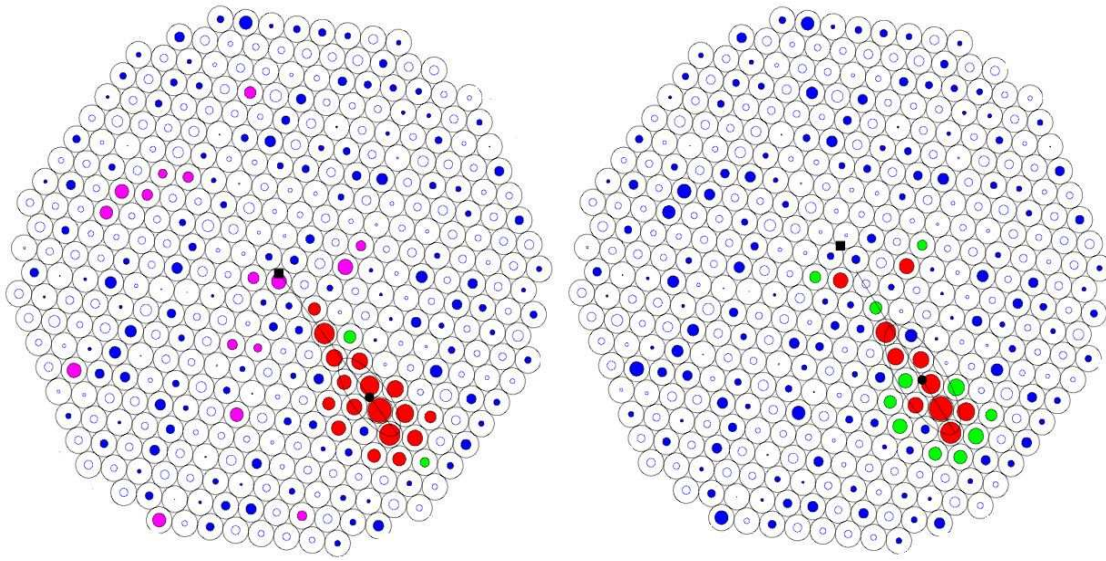


Figure 4.1: Whipple 10 m image cleaning methods for a simulated 0.27 TeV γ -ray shower with (left) islands and (right) regular cleaning. Pixels defined as bright are shown in red, boundary pixels in green. Pixels with varying noise levels below the cleaning threshold are shown in blue or pink.

section 3.3.1. The mean pedestal value $\langle \text{Ped} \rangle_i$ is subtracted from the triggered event signal S_i^{raw} to determine the Cherenkov intensity in each pixel. Non-uniformities in the camera are corrected for by applying flat-fielding coefficients g_i measured on a nightly basis (described in section 3.3.1). The corrected pixel intensities S^{corr} in dc are calculated by:

$$S_i^{\text{corr}} = g_i \cdot (S_i^{\text{raw}} - \langle \text{Ped} \rangle_i)$$

The last step before image cleaning corrects for differences in the night sky background between the ON source and OFF field runs. Gaussian distributed noise is added to both runs to equalize the RMS spread in the pedestal measurements.

Image Cleaning

After pedestal subtraction, the Cherenkov images are cleaned to exclude all channels that most probably contain only noise and no Cherenkov signal. The pedestal RMS in each pixel σ_i is used to determine the noise threshold above which a pixel is included in the image. Disabled or malfunctioning pixels are identified and excluded from image processing if σ_i is less than half the mean pedestal RMS over the whole camera. In the “normal” Whipple 10 m cleaning method, two optimized noise thresholds are defined as either requiring a signal-to-noise ratio for “bright” pixels of $S/N \geq 4.25\sigma_i$, or for “boundary” pixels (pixels adjacent to a bright pixel) of $S/N \geq$

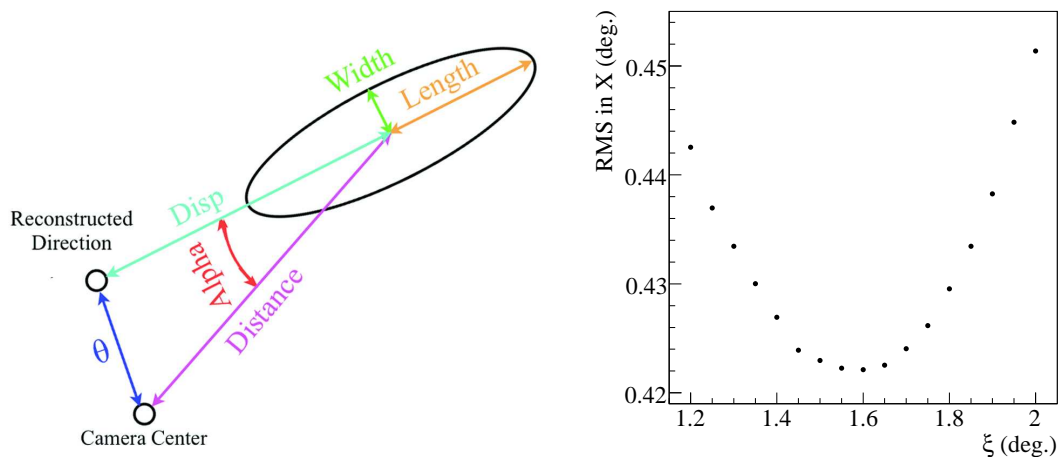


Figure 4.2: Shown (left) is a diagram of Cherenkov image shape and orientation parameters. (Right) is shown the optimized scaling factor $\xi = 1.6$ used to calculate the Disp parameter, as described in section 4.2.

$2.5\sigma_i$. Only pixels passing these two criteria are included in the image. An “islands” method was developed to overcome the problem that for low energy γ -ray images a few signal pixels may be below the normal bright/boundary threshold, and could be unnecessarily excluded (Bond et al. 2003). The method uses an additional island threshold, defining the image as one or more islands of bordering pixels with total $S/N \geq 5.5\sigma_i$ entirely surrounded by pixels with signal below the boundary threshold. The islands threshold uses a lower bright threshold of $S/N \geq 2.5\sigma_i$ and boundary threshold of $S/N \geq 1.25\sigma_i$. Figure 4.1 shows the Cherenkov image of a simulated 0.27 TeV γ -ray using (left) islands cleaning, and (right) normal cleaning. Islands cleaning was shown (as in figure 4.1) to be more effective than normal cleaning at excluding isolated pixels away from compact γ -ray images, while for fragmented cosmic ray images the inclusion of multiple islands assists in background discrimination, as described in 4.3. All Whipple 10 m data in this work was reduced with islands cleaning.

Image Parameterization

Cleaned Cherenkov images are parameterized according to the image intensity, shape, and orientation. The total intensity “Size”, and the intensity of the three brightest pixels Max1, Max2, and Max3 are recorded for each image. At this stage, the intensities are converted from dc to photoelectrons by using the gain lookup table dependent upon the observation date (described in section 3.3.1). The image centroid (X_c, Y_c) is calculated from the first moment of the light distribution. Image shape parameters are calculated using second moments, as described in (Hillas

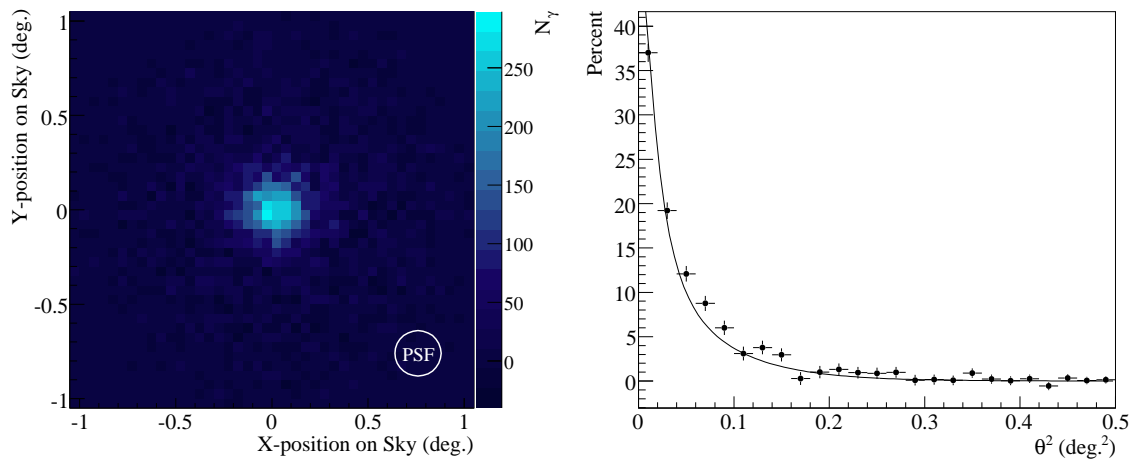


Figure 4.3: Reconstructed γ -ray direction of the Crab nebula within the Whipple 10 m camera system. The number of background subtracted events N_γ using Hard cuts are shown for the full 2000–2006 data set, as described in section 4.3. Shown (right) is the θ^2 distribution for the same Crab nebula data set, fit with the PSF from simulated γ -rays at 20° zenith angle.

1985; Reynolds et al. 1993). Figure 4.2 (left) shows a diagram of the “Hillas” image shape and orientation parameters. The Length and Width parameters are the RMS angular size of the major and minor axes, and are related to the longitudinal and lateral development of the air shower, respectively. The image orientation with respect to the camera center is defined by the angle Alpha. For source-centered observations, the angular Distance of the centroid to the camera center is related to the impact parameter (location of the shower core relative to the telescope).

4.2 Angular and Energy Reconstruction

The direction of each photon was reconstructed from the image shape and orientation, resulting in an angular resolution of $\theta_{68\%} = 0.12^\circ$. Lookup tables were generated using simulated γ -rays for the expected energy, Length, and Width of each event as a function of the Distance and Log(Size). The energy resolution for >0.5 TeV γ -rays at 20° zenith angle selected using Hard cuts is 31%, with a bias of 3.5% in energy reconstruction (selection cuts are described in section 4.3).

Disp method of Angular Reconstruction

A Disp method was developed for single IACT telescopes to estimate the γ -ray arrival direction (Lessard et al. 2001). Figure 4.2 (left) shows the Disp parameter, which is the angular distance between the image centroid and reconstructed source position. The Disp value is calculated from

the image ellipticity:

$$\text{Disp} = \xi \cdot \left(1 - \frac{\text{Width}}{\text{Length}} \right)$$

Figure 4.2 (right) shows how the scaling value ξ was optimized in this work using simulated γ -rays by determining the minimum in the RMS spread of projected x-directions for discrete values of ξ . The energy and zenith angle dependence of the optimized ξ value was small for simulations at 10–40° zenith angle, so for simplicity an optimized value $\xi = 1.6$ was applied to all data. Using the Disp value, the angular offset θ is calculated from the reconstructed source position relative to the camera center, as shown in figure 4.2. For all Whipple 10 m observations in this work, the telescope is pointed with the assumed source position at the center of the camera. Figure 4.3 (left) shows the reconstructed direction of selected γ -ray type events from observations of the Crab nebula during 2000–2006. The γ -ray point spread function (PSF) was determined from the θ^2 distribution of simulated γ -rays, since θ^2 yields a constant solid angle on the sky per bin. The simulated θ^2 distribution was fit with the sum of two one-dimensional Gaussian functions to estimate the point spread function (PSF):

$$\text{PSF} = A_{\text{abs}} \cdot \left[\exp\left(\frac{-\theta^2}{2 \cdot \sigma_1^2}\right) + A_{\text{rel}} \cdot \exp\left(\frac{-\theta^2}{2 \cdot \sigma_2^2}\right) \right]$$

The absolute amplitude A_{abs} is proportional to the number of events in the θ^2 distribution, while the standard deviation σ_2 is the 68% containment radius $\theta_{68\%}$ of the PSF. After applying Hard selection cuts (described in section 4.3) the best fit value is $\theta_{68\%} = 0.12^\circ$ for simulated γ -rays at 10–30° zenith angle. Figure 4.3 (right) shows the PSF fit to the θ^2 distribution from Crab nebula observations, with all parameters fixed except for A_{abs} . The good agreement between the fit and data demonstrates the Crab nebula is a point source for the Whipple 10 m.

Lookup Tables

Simulated γ -rays at 4 zenith angles and 3 telescope efficiencies (described in section 3.3.2) were used to fill lookup tables for the mean simulated energy E_{True} , Length, and Width as a function of Distance (approximation of the shower impact parameter) and $\text{Log}(\text{Size})$. To avoid biases, no selection cuts were applied to the simulated data. Lookup tables are used in this work for energy reconstruction and selection cuts to account for the strong dependence of γ -ray energy E_{True} and image shape parameters on Size, Distance, and zenith angle. Figure 4.4 shows the finely binned distributions on the (left), and lookup tables on the (right) for simulations at 20° zenith and 85% telescope efficiency. The lookup tables use large bins to fill in the finely binned distributions at Distance and $\text{Log}(\text{Size})$ values with few events. A two-dimensional Gaussian smoothing function was applied to the lookup tables with $\sigma_{\text{Dist}} = 0.05^\circ$ in Distance and $\sigma_{\text{Log}(S)} = 0.01$ in $\text{Log}(\text{Size})$.

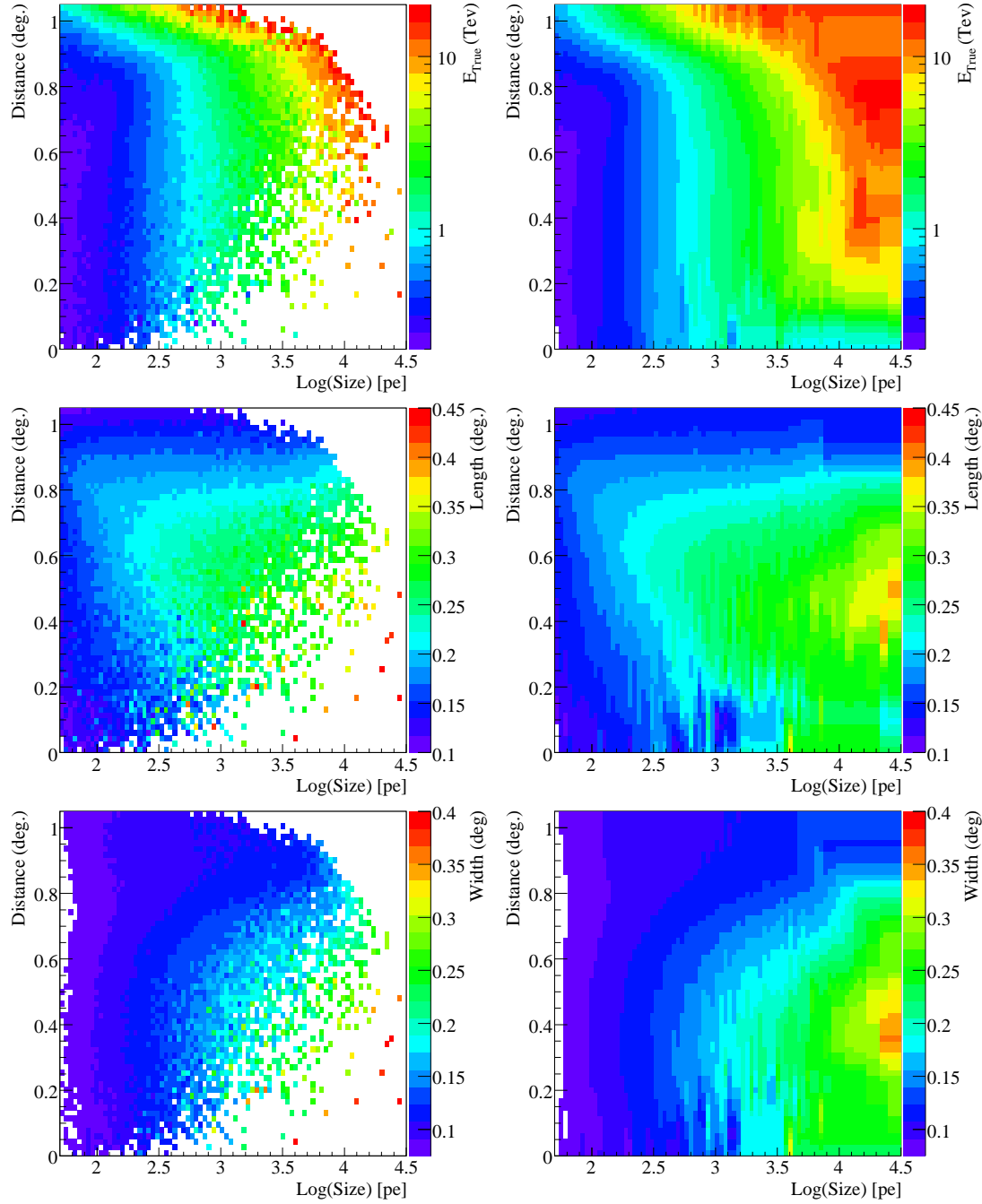


Figure 4.4: Lookup tables for mean simulated energy E_{True} , Width, and Length as a function of Distance and Log(Size). Shown (left) are finely binned distributions, and (right) the Gaussian smoothed distributions used in data reduction.

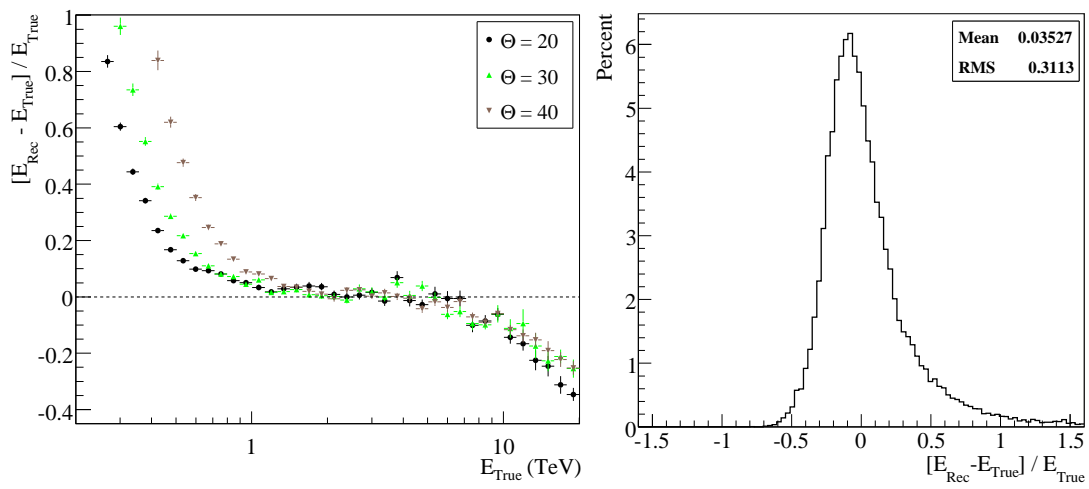


Figure 4.5: Shown (left) is the mean relative error in reconstructed γ -ray energy as a function of simulated energy E_{True} for zenith angles of 20° , 30° , and 40° after applying Hard cuts (selection cuts from table 4.1). Shown (right) is the distribution of relative reconstructed energy error for >0.5 TeV γ -rays at 20° zenith angle, also with Hard cuts.

Scaled Parameters

Reduced scaled parameters for the Length and Width (RSL and RSW) of each image were defined to facilitate simple selection cuts which take into account γ -ray image shape dependencies on Size, Distance, and zenith angle. For each event, the lookup tables are used to determine the expected values $\langle \text{Width} \rangle_{\text{Sim}}$ and $\langle \text{Length} \rangle_{\text{Sim}}$ together with the RMS spread σ_{Width} and σ_{Length} as a function of Distance and Size. The reduced scaled parameters (Width) is calculated as:

$$\text{RSW} = \frac{\text{Width} - \langle \text{Width} \rangle_{\text{Sim}}}{\sigma_{\text{Width}}}$$

The dependence on zenith angle Θ and telescope efficiency μ were accounted for by linear interpolation between μ and $\cos \Theta$. An example interpolation for $\Theta = 25^\circ$ is:

$$\text{RSW}(\mu, \Theta_{25}) = \text{RSW}(\mu, \Theta_{20}) + \frac{\cos \Theta_{25} - \cos \Theta_{20}}{\cos \Theta_{30} - \cos \Theta_{20}} \cdot [\text{RSW}(\mu, \Theta_{30}) - \text{RSW}(\mu, \Theta_{20})]$$

Figure 4.6 (top left and middle) show the distributions of RSW and RSL for simulated γ -rays at 20° zenith. The distributions have a mean of ~ 0 with an RMS spread of $\sim 1 \sigma$.

Energy Reconstruction

For each event, the reconstructed energy E_{Rec} was calculated from the lookup tables by linearly interpolating between μ and $\cos \Theta$ in the same way as for the scaled parameters. Figure 4.5 (left) shows the mean relative error of the reconstructed energy $(E_{\text{Rec}} - E_{\text{True}}) / E_{\text{True}}$ as a function of

simulated energy E_{True} at zenith angles of 20° , 30° , and 40° after applying Hard selection cuts. At low energies, E_{Rec} is overestimated due to events with intensity near the telescope trigger threshold. A usable energy range above E_{Safe} with a relative error of $< 10\%$ was determined for each zenith angle, with $E_{\text{Safe}} = 0.5$ TeV at 20° zenith angle. Figure 4.5 (right) shows the distribution of relative energy errors for >0.5 TeV γ -rays at $\Theta = 20^\circ$ selected with Hard cuts. The mean of the distribution is 3.5%, with an RMS spread of 31%, defined as the energy resolution.

4.3 γ -ray Selection

The Whipple 10 m event rate of ~ 20 Hz is dominated by cosmic ray air showers, resulting in a low signal-to-noise ratio of $\sim 10^{-3}$ for strong γ -rays sources (the Crab nebula γ -ray detection rate is ~ 0.05 Hz). In this work, efficient image parameter cuts were optimized to discriminate between fragmented cosmic ray air showers and compact γ -ray air showers. Once image cuts are applied, the detection significance and rate of a possible signal from a γ -ray point source is extracted by subtracting the number of events passing cuts in a corresponding OFF field sky region from the selected events in the source direction.

γ -ray Signal Determination

A subset of 10 hours of Crab nebula observations from 2000–2006 at $\sim 20^\circ$ zenith angle were used to optimize two sets of selection cuts: Hard cuts for measuring the γ -ray flux and energy spectrum with a high detection significance, and Loose cuts intended to limit the systematic biases in the energy spectrum measurement of a strong γ -ray signal. The selection cuts were optimized sequentially by first requiring image quality cuts (described below), and then by simultaneously adjusting image shape cuts. Lastly a directional Alpha cut was applied for the point source analysis in this work. A discussion of systematic effects of the selection cuts, particularly for weak γ -ray sources, is discussed at the end of this section. The significance of a γ -ray signal is defined by (Li and Ma 1983):

$$S = \sqrt{2} \cdot \left[N_{\text{ON}} \cdot \text{Ln} \left(\frac{1 + \varepsilon}{\varepsilon} \frac{N_{\text{ON}}}{N_{\text{ON}} + N_{\text{OFF}}} \right) + N_{\text{OFF}} \cdot \text{Ln} \left((1 + \varepsilon) \frac{N_{\text{OFF}}}{N_{\text{ON}} + N_{\text{OFF}}} \right) \right]^{1/2}$$

The number of excess γ -ray type events $N_\gamma = N_{\text{ON}} - \varepsilon \cdot N_{\text{OFF}}$ is calculated from the number of events N_{ON} in the ON source centered observation passing selection cuts, and the number of OFF field events N_{OFF} passing cuts, scaled by the ratio of the exposure time $\varepsilon = T_{\text{ON}} / T_{\text{OFF}}$. For ON observations with no corresponding OFF observation (Tracking runs, see section 3.2.5), ε is calculated as the ratio of background acceptances measured from the Alpha distributions of

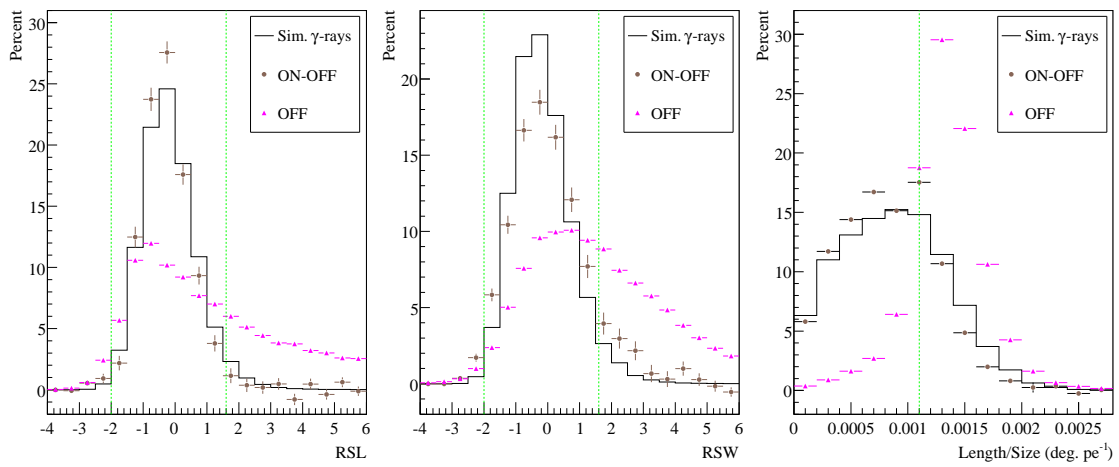


Figure 4.6: RSW, RSL, and Length/Size image parameter distributions with Hard cuts applied to all other parameters. The percentage of events in each bin are shown for simulated γ -rays at 20° zenith angle (black lines), γ -ray type events after background subtraction (ON-OFF, brown points), and background events in the OFF field (OFF, pink triangles). The data are from 65 hours of Crab nebula observations from 2000–2006 (summarized in table 4.2). Hard cut values for each parameter are represented by green dashed lines.

the ON and OFF runs. The Alpha distribution from simulated γ -rays shows only a few events above 25° , so in the case of Tracking runs ε was calculated from the ratio of background regions at 25 – 85° Alpha. The γ -ray detection rate is defined as:

$$R_\gamma = \frac{N_\gamma}{T_{\text{ON}}} \pm \frac{\sqrt{N_{\text{ON}} + \varepsilon^2 \cdot N_{\text{OFF}}}}{T_{\text{ON}}}$$

Image Quality Cuts

To ensure a sufficient image quality, events detected at the edge of the camera or with low intensity are rejected. Due to the small 2.6° field of view camera in the Whipple 10 m, nearly all simulated γ -ray images with Distance $> 0.8^\circ$ are partially truncated. An upper cut of Distance $< 0.95^\circ$ was chosen to include most γ -ray images not severely truncated, determined by the fractional intensity of image pixels on the camera edge. The cut on low intensity images of Size > 80 pe was chosen to reject events near the trigger threshold, since the pattern selection trigger was not implemented in the simulations.

Image Shape Cuts

Gamma-ray selections cuts rely on the characteristic differences in shape between Cherenkov images from cosmic ray and γ -ray air showers. Reduced scaled Length and Width parameters

(RSL and RSW, described in 4.2) were used to define the image shape cuts. Due to the larger lateral extent of Cherenkov light from cosmic ray air showers than from γ -ray initiated air showers, the RSW and RSL parameters are efficient at separating background events from γ -ray type events. Figure 4.6 shows a comparison of the RSL, RSW, and Length/Size parameter distributions from simulated γ -rays at 20° zenith angle and 85% telescope efficiency with background events and excess γ -ray type events passing all other Hard selection cuts (defined in table 4.1) from the total 2000 to 2006 Crab nebula data set in table 4.2. A reasonable agreement is shown between the simulated γ -ray and excess event distributions. The background discrimination power of the RSW and RSL cuts are shown by the high percentage of OFF events with RSW and RSL values above the upper Hard cut value (represented by a green dashed line).

Background of Muon Images

After applying image shape cuts (RSL and RSW) to Whipple 10 m observations, a large background remains of compact γ -ray like images produced by the Cherenkov light from muons in cosmic ray air showers passing within a few meters of the telescope (described in section 3.3). These events are rejected in IACT telescope arrays, which require triggers from multiple telescopes for a central event trigger (Holder et al. 2006). To limit the number of selected muon events, a Length/Size cut was developed for Whipple 10 m data based on the typically longer Length of muon images than γ -ray images with a similar intensity (Moriarty et al. 1997). Figure 4.6 (right) shows the the sharply peaked Length/Size distribution of background events (mainly muon events) and the Hard cut on Length/Size.

Hard and Loose Selection Cuts

For γ -ray sources of angular size consistent with the Whipple 10 m point spread function, the final selection cut is on the Alpha image direction parameter. Figure 4.7 (left) shows the Alpha distribution from selected events in the ON and OFF fields of the Crab nebula after applying Hard cuts to all other parameters. Table 4.1 shows the full set of Hard and Loose cuts. The optimized values were determined on the basis of the significance $\sigma/\sqrt{\text{hr}}$ and γ -ray rate from 10 hours of randomly chosen Crab nebula observations at $\sim 20^\circ$ zenith angle. Hard cuts were optimized for a high significance, while retaining a γ -ray detection rate of $\sim 3 \text{ min}^{-1}$. Loose cuts were chosen to avoid systematic uncertainties in the number of selected events introduced by cutting into steeply shaped regions of either the ON or OFF parameter distributions. The higher γ -ray rate with Loose cuts is mainly due to removing the Length/Size cut, and to a lesser degree on the looser RSL, RSW, and Alpha cuts at the expense of a lower significance. For weak γ -ray sources, both sets of

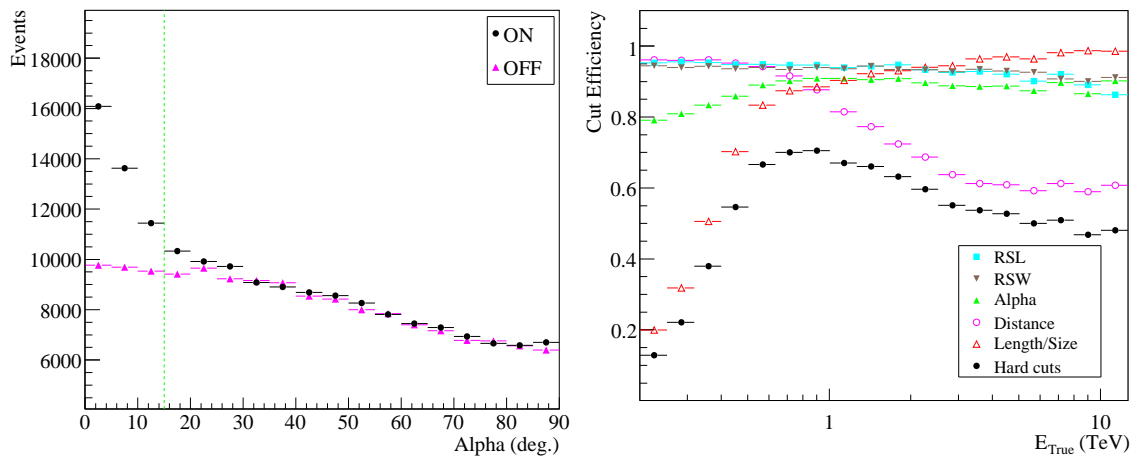


Figure 4.7: (Left) the Alpha distribution for Hard cut selected events in the ON observations (black points) and OFF fields (pink triangles) from the total Crab nebula data set. The excess of selected γ -ray type events is the number of ON events remaining after subtraction of OFF events at Alpha $< 15^\circ$ (Hard cut shown by the green dashed line) scaled by ϵ the ratio of ON and OFF exposures. Shown (right) is the efficiency of each Hard cut as a function of energy relative to all events passing the Size cut. Simulated γ -rays were used at 20° zenith angle.

selection cuts will give lower significances than for cuts optimized for a weak signal, however by using Hard or Loose cuts the systematic effect on flux measurements should be reduced compared to cuts which are more tightly optimized to the γ -ray parameter distributions. In this sense, Hard and Loose cuts are considered applicable to weak source analysis.

Figure 4.7 (right) shows the γ -ray efficiency of Hard cuts as a function of energy using simulated γ -rays at 20° zenith. The efficiency of each parameter cut is shown relative to the number of events selected after the Size cut was applied. The RSL and RSW are shown to be mostly independent of energy, whereas simple upper cuts on Length and Width reject a high fraction of high energy γ -rays with increasing mean Length and Width values, as shown in figure 4.4. The low efficiency at high energies due to the upper Distance cut of 0.95° is expected since high energy air showers with large impact parameters are mainly recorded at the camera edge. The strongly reduced efficiency at low energies due to the Length/Size cut is apparent. A total γ -ray detection efficiency relative to all triggered events was estimated from simulated γ -ray events. For Hard cuts the total efficiency is $\sim 42\%$, and for Loose cuts is $\sim 54\%$. The background rejection power of each cut was demonstrated by the total number of triggered events in OFF field observations rejected by the selections cuts. Hard cuts was shown to reject 98.3% of OFF events, while Loose cuts rejected 90.6% of OFF events.

Cut	Size (pe)	Distance (deg.)	RSL	RSW	Alpha (deg.)	Len./Size (deg./pe)	$\sigma/\sqrt{\text{hr}}$	R_γ (min. ⁻¹)
Hard	>80	0.2 - 0.95	-2.0 - 1.6	-2.0 - 1.6	<15	<0.0011	5.26	3.12 ± 0.18
Loose	>80	0.2 - 0.95	-2.0 - 2.0	-2.0 - 2.0	<22	–	3.56	5.51 ± 0.49

Table 4.1: Selection cuts based on image parameters. The listed significance $\sigma/\sqrt{\text{hr}}$ and rate R_γ of selected events are from 10 hours of observations of the Crab nebula during 2000–2006 at $\sim 20^\circ$ zenith.

4.4 Flux and Energy Spectrum Determination

The flux and energy spectrum from a γ -ray source is calculated from the number of selected excess events N_γ using the effective area of the instrument. The methods employed with the Whipple 10 m are verified in section 4.5 by comparing the measured γ -ray flux and energy spectrum of the Crab nebula from observations during 2000–2006. Two methods of calculating the integral flux were applied to the Crab nebula observations. The two methods show a reasonable agreement on month timescales for an expected constant γ -ray emission of $(2.05 \pm 0.06) \cdot 10^{-11} \text{ cm}^{-2} \text{ s}^{-1}$ with a spread in flux of 12–18% from the mean value.

Effective Area

The effective area of IACT telescopes is determined by the efficiency of collecting air shower Cherenkov photons. Simulated γ -rays (detailed in section 3.3) were used to calculate the effective area as a function of energy E , zenith angle Θ , and telescope efficiency μ . The maximum distance $R_o = 400$ m of the simulated air showers from the telescope was chosen to encompass the full impact parameter range of triggered events (0–270 m). The effective area is defined as:

$$A_{\text{eff}}(E, \Theta, \mu) = \pi \cdot R_o^2 \cdot \frac{N_{\text{trig.}}(E, \Theta, \mu)}{N_{\text{sim.}}(E, \Theta, \mu)}$$

The total number of simulated γ -rays is represented by $N_{\text{sim.}}(E, \Theta, \mu)$, and the number of detected events passing selection cuts as $N_{\text{sel.}}(E, \Theta, \mu)$. The effective areas were fit with an analytical function using 5 fit parameters p_i , modified from (Aharonian et al. 2001b):

$$A_{\text{eff}}(E, \Theta, \mu) = p_0 \cdot E^{p_1} \cdot [1 + (E/p_2)^{p_3}]^{-1} + p_4 \cdot E + p_5 \cdot E^2$$

Figure 4.8 shows the effective areas at 20° , 30° , and 40° zenith angle and 85% telescope efficiency. Shown (left) are the effective areas as a function of simulated energy E_{True} , and (right) the effective areas as a function of reconstructed energy E_{Rec} . The fall in the effective area at high energies is

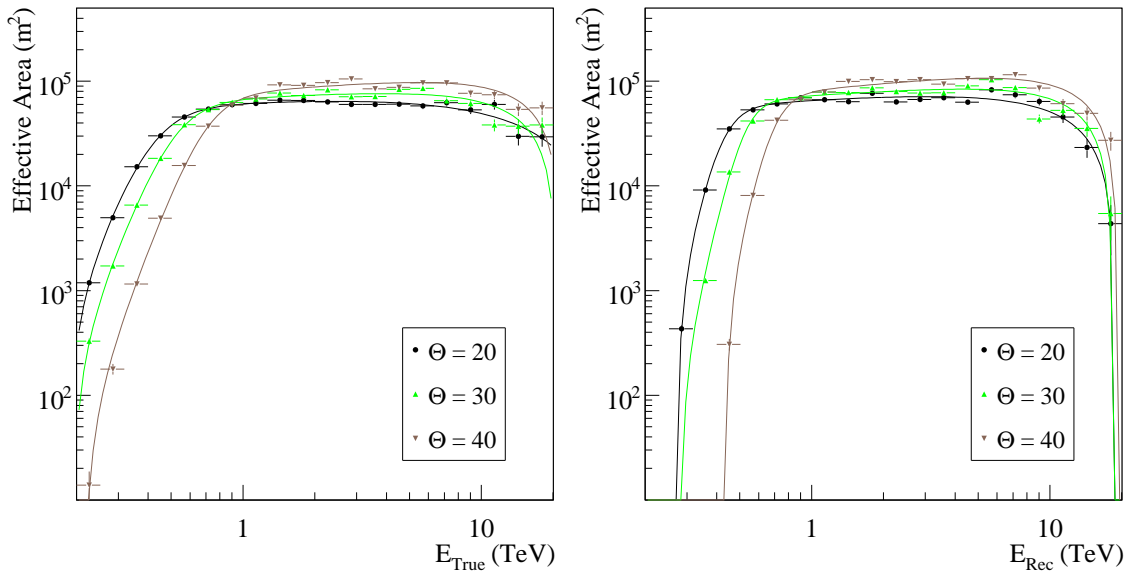


Figure 4.8: Effective collection area of the Whipple 10 m telescope with Hard cuts (left) as a function of true simulated energy E_{True} , and (right) as a function of reconstructed energy E_{Rec} at zenith angles of 20° , 30° , and 40° .

due mostly to the upper Distance selection cut, which rejects high energy air showers at large impact parameters detected close to the camera edge. The energy threshold E_{th} is defined by the peak in the differential γ -ray detection rate $dR/dE = A_{\text{eff}} \cdot dN/dE$. For the Crab nebula, the measured energy spectrum from 0.45–10 TeV follows a power law with $\Gamma = 2.64$. Figure 4.9 (left) shows the differential rate expected for the Crab nebula at 20° , 30° , and 40° zenith. Figure 4.9 (right) shows the energy threshold E_{th} for Hard and Loose cuts as a function of zenith angle determined from the peak in the differential rate. Shown for comparison is the safe energy E_{Safe} where the relative error in the energy reconstruction is $< 10\%$. The energy threshold is < 0.55 TeV at zenith angles $< 30^\circ$ after applying Hard cuts.

Energy Spectrum Determination

In order to account for biases in energy reconstruction, the energy spectrum is measured using the effective area as a function of reconstructed energy $A_{\text{eff}}(E_{\text{Rec}})$. The flux in energy intervals ΔE is determined by the number of excess events N_γ detected during an exposure with livetime T_{ON} . The effective area is calculated for each event passing selection cuts in the ON and OFF observations. Linear interpolation in $\cos \Theta$ and telescope efficiency μ follows the method described in 4.2. The

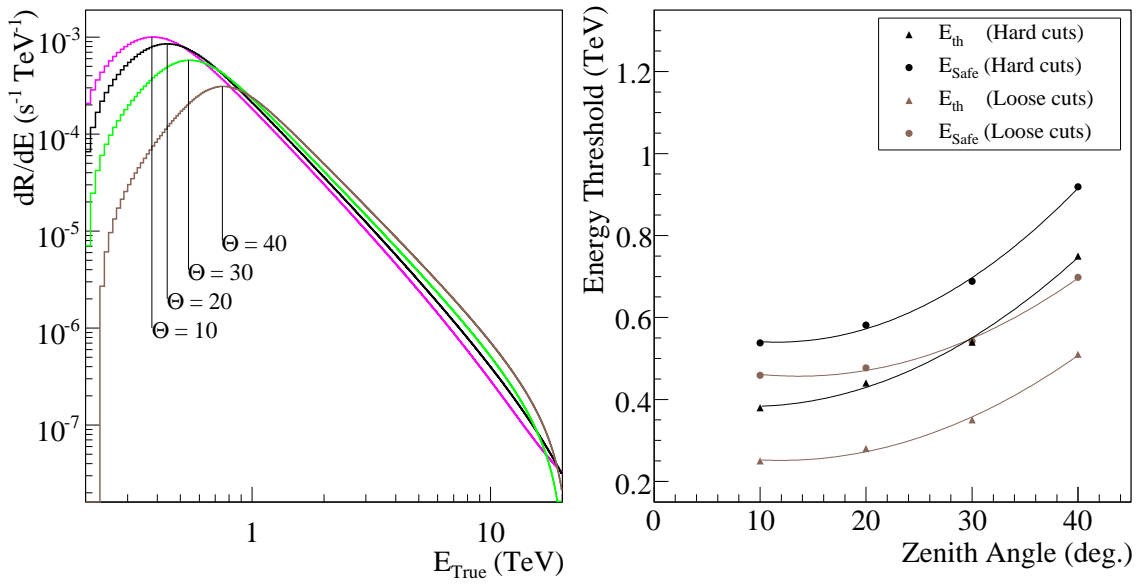


Figure 4.9: (Right) Differential γ -ray rate expected for the Crab nebula at 20° , 30° , and 40° zenith. (Left) The energy threshold E_{th} versus zenith angle, given by the maximum differential rate. The safe energy E_{Safe} is for energies with $< 10\%$ relative error in energy reconstruction.

flux in each energy bin is calculated as:

$$F(\Delta E) = \frac{1}{T_{\text{ON}}} \left[\sum_{i=1..N_{\text{ON}}} \frac{1}{A_i} - \varepsilon \cdot \sum_{j=1..N_{\text{off}}} \frac{1}{A_j} \right]$$

The ε ratio defined in section 4.3 is used to scale the effective area of OFF events. The energy bin width in $\text{Log}(E_{\text{Rec}})$ is set larger than the energy resolution, and is increased depending on the γ -ray signal strength. The lowest energy bin in the spectrum is limited by E_{Safe} , as shown in figure 4.9, while for the highest energy bin a significance of $> 2 \sigma$ and more than 10 excess events are required. Flux points are calculated at the mean energy in the bin, calculated from finely binned distributions of reconstructed energy E_{Rec} for the ON and OFF events. The error in the flux is estimated using standard error propagation, and did not include the error in the effective area calculation. A least-squares method is used to fit the flux points with a power law or curved spectral function. It is worth noting the effective area versus true energy E_{True} is independent of the simulated spectrum, while $A_{\text{eff}}(E_{\text{Rec}})$ is sensitive to the $E^{-2.5}$ simulated energy spectrum, so an iterative process of matching the simulated spectrum to the measured spectrum is the strictly correct method. A recent study has shown that the ratio of $A_{\text{eff}}(E_{\text{Rec}})$ from simulations with $E^{-3.2}$ to $E^{-2.0}$ simulated spectrum is less than 5% over the usable energy range of H.E.S.S. (Aharonian et al. 2006d). Here, corrections to the simulated spectrum were not applied.

Integral Flux Calculation

The integral flux above a chosen energy threshold $F_{>E_o}$ is estimated from the effective area and number of excess events N_γ . Two methods of calculating the integral flux are described here, and were used to measure the Crab nebula TeV γ -ray flux from Whipple 10 m observations during 2000–2006 (see section 4.5 below). In “method 1”, the effective area for each event is estimated using the reconstructed energy E_{Rec} following the same procedure used for the energy spectrum determination of $F(\Delta E)$ described above. The integral flux is measured over one energy interval $F(E < E_o)$, where the energy threshold E_o is at, or above E_{Safe} (see figure 4.9). Alternatively, a “method 2” uses all selected N_γ , and does not rely on the energy reconstruction. In this method, the effective area as a function of simulated energy $A_{\text{eff}}(E_{\text{True}})$ is used to determine the differential rate for an assumed power law type energy spectrum with photon index Γ (see figure 4.9). The excess number of events N_γ is given by:

$$N_\gamma = F_o \int_{E_{\text{min}}}^{E_{\text{max}}} \int_0^{T_{\text{Live}}} A_{\text{eff}}(E, \Theta(t), \mu(t)) \cdot \left(\frac{E^{-\Gamma}}{1 \text{ TeV}} \right) dt dE$$

N_γ is measured for each run, as described in section 4.3. Linear interpolation in $\cos \Theta$ and telescope efficiency μ yields the differential rate for each run with flux normalization F_o set to unity. F_o is then estimated by N_γ and the integral of the differential rate multiplied by the total livetime of the run T_{Live} . The integral was taken over the energy range $E_{\text{min}} = 0.1 \text{ TeV}$ to $E_{\text{max}} = 20 \text{ TeV}$, using the effective areas from the analytical fit functions. The flux above a certain energy E_{th} is:

$$F_{>E_o} = -\frac{F_o}{(1-\Gamma)} \cdot E_o^{(1-\Gamma)}$$

The main disadvantage of this method is that a fixed photon index must be chosen. During periods when the detection significance is less than 2 or 3 σ , an upper limit on N_γ is calculated at a 99.9% confidence level using the approach in (Helene 1983). The Helene method calculates upper limits based on the probability of N_γ excess events having a Gaussian distribution for a set confidence level.

4.5 Results from Crab Nebula Observations

Observations of the Crab Nebula with the Whipple 10 m during 2000–2006 are compared in this section with recent results from HEGRA, MAGIC, and H.E.S.S. to test the Whipple 10 m analysis methods developed in this work (Aharonian et al. 2004; Wagner et al. 2005; Aharonian et al. 2006d). The Whipple 10 m yearly and total flux and spectral shape measurements of the Crab nebula at energies of 0.45–8 TeV agree well with past results within the combined systematic and

Observing Period (Month/Year)	T_{Live} (hr)	N_{Runs}	Θ Range (deg.)	$\langle\Theta\rangle$ (deg.)	$\langle\text{Rate}\rangle$ (Hz)
10/2000 - 01/2001	13.2	29	10 - 27	18.8	29.7
10/2001 - 03/2002	23.9	52	10 - 30	17.1	28.0
11/2002 - 02/2003	8.3	18	10 - 28	17.2	17.6
11/2003 - 03/2004	5.5	12	10 - 27	17.8	23.5
10/2004 - 04/2005	5.5	12	10 - 24	15.0	22.0
10/2005 - 03/2006	8.8	19	10 - 29	18.6	22.8
Total	65.3	142	10 - 30	17.6	25.5

Table 4.2: Whipple 10 m observations of the Crab nebula during 2000–2006.

statistical errors. The systematic uncertainties were estimated by varying the analysis procedures, and from the remaining non-statistical yearly differences in the results. The main uncertainty was found to lie in accurately calibrating the large long-term variations in telescope efficiency.

Whipple 10 m Observations of the Crab Nebula

The Crab nebula was observed with the Whipple 10 m on a nearly nightly basis from October to April during moonless periods in 2000–2006. Table 4.2 shows a summary of the Whipple 10 m observations. A total of 142 runs were selected using the quality criteria described in section 3.2.6. All observations were carried out in the ON/OFF mode with dedicated OFF fields. Listed in table 4.2 is the mean event rate $\langle\text{Rate}\rangle$ in each data set, which is a measure of the telescope efficiency (see figure 3.13). The zenith angle Θ of observations was restricted to $\Theta < 30^\circ$.

Light Curve of the Crab Nebula

Due to the assumed constant TeV γ -ray emission from the Crab nebula, the long-term calibration of the Whipple 10 m and consistency of the integral flux measurement methods (described above in section 4.4) can be tested by measuring the Crab nebula integral flux over a period of many years. Figure 4.10 shows a light curve of the Crab nebula integral flux above 1 TeV from Whipple 10 m observations during 2000–2006 using the two methods described in section 4.4. Time bins were chosen to yield 3 nearly equal exposures in each year. A fit to a constant flux over the 6 years is shown for method 1 by a dashed line, and for method 2 by a solid line. The χ^2 per degree of freedom (dof) in the constant fit was 1.60 and 1.43 for methods 1 and 2, respectively. The mean integral flux $F_{1\text{TeV}}$ calculated by the two methods agree well within statistical errors

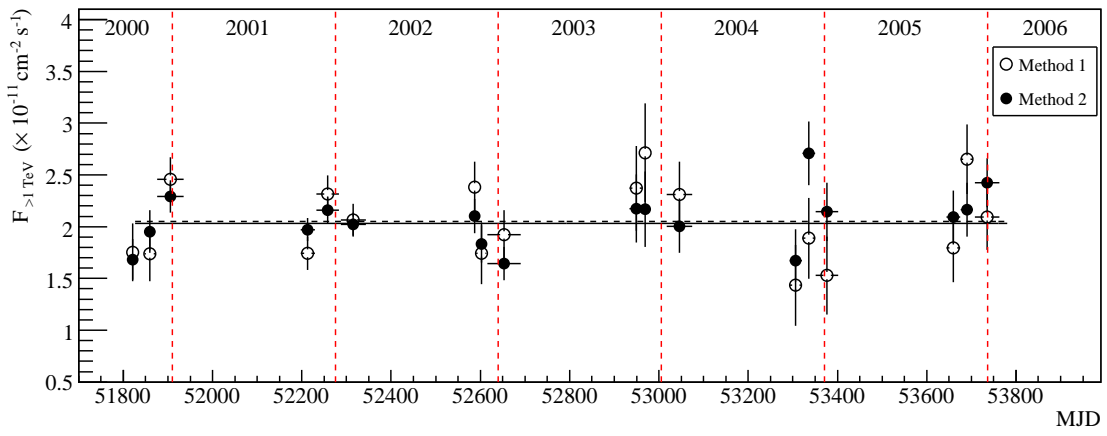


Figure 4.10: Crab nebula light curve of the integral flux above 1 TeV during 2000–2006 measured by two methods with the Whipple 10 m. The dashed and solid lines represent the best fits to a constant flux for method 1 and method 2, respectively.

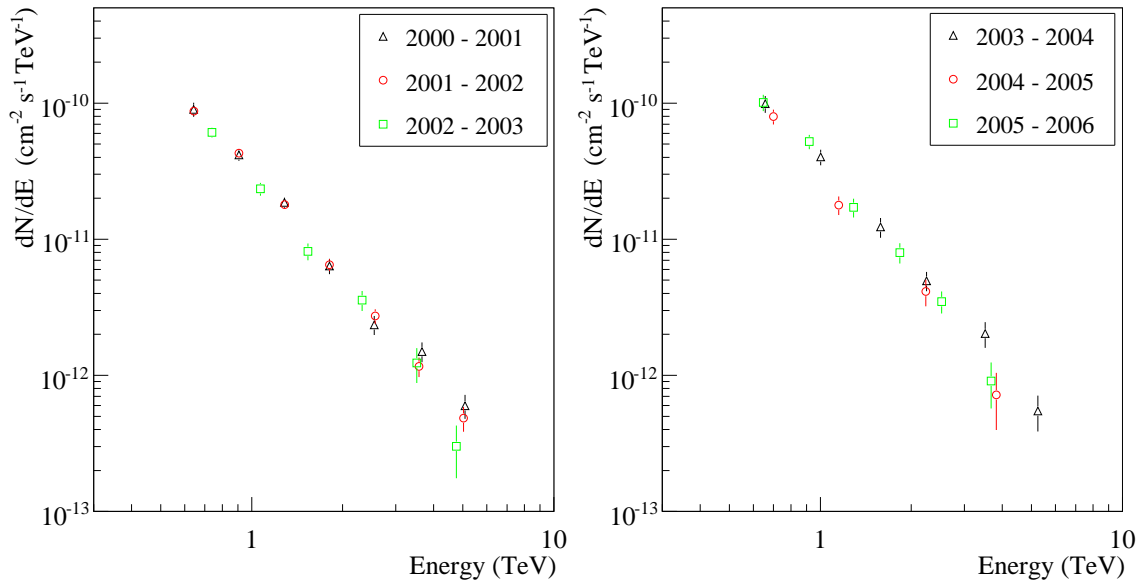


Figure 4.11: Whipple 10 m energy spectrum of the Crab nebula from 2000–2006.

of $(2.05 \pm 0.06$ and $2.03 \pm 0.04) \times 10^{-11} \text{ cm}^{-2} \text{ s}^{-1}$ for method 1 and method 2. A large RMS spread in $F_{1\text{TeV}}$ of 18% for method 1 and 12% for method 2 is evident.

Energy Spectrum of the Crab Nebula

Hard and Loose selection cuts were used to measure the energy spectrum of the Crab nebula. Table 4.3 shows results from a power law fit to the energy spectrum for different data sets. Listed are the significance σ and number of excess events N_γ in each data set. A reasonable agreement

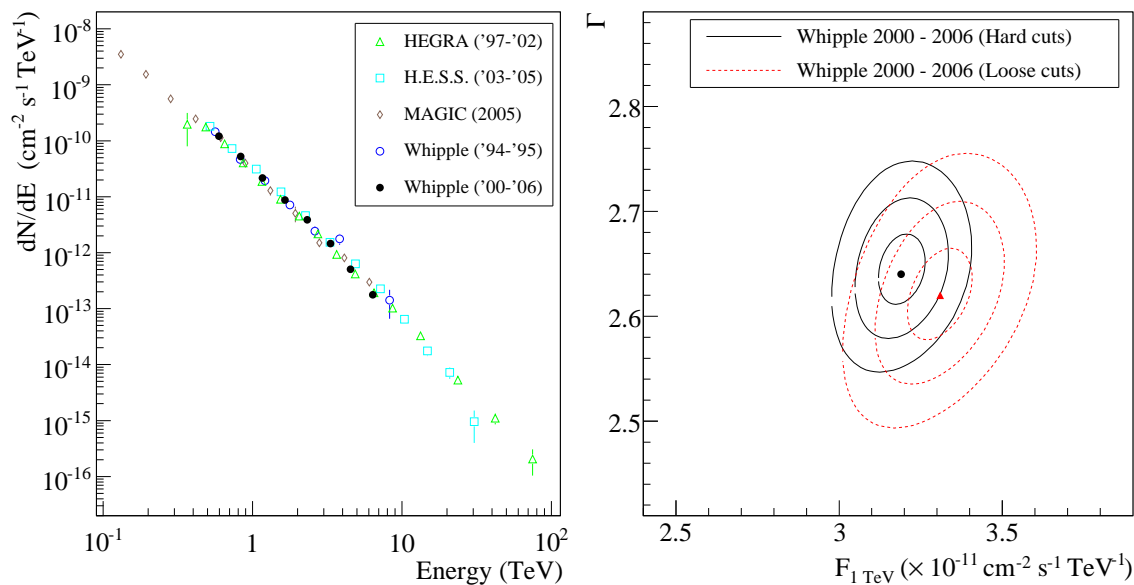


Figure 4.12: (Left) Total 2000–2006 measurement of the Crab nebula energy spectrum compared to past measurements by HEGRA, H.E.S.S., MAGIC, and the Whipple 10 m. (Right) Contour plot of the 68%, 95%, and 99.9% confidence intervals from the χ^2 fit to a power law for the total 2000–2006 data set using Hard cuts (black solid lines) and Loose cuts (red dashed lines). The best fit value using Hard cuts is shown by a black point, and for Loose cuts by a red triangle.

in the measured photon index Γ and flux normalization $F_{1\text{TeV}}$ is shown between data sets within statistical errors. The RMS spread in Γ between the data sets is 0.06, with a mean statistical error of 0.11 from each data set. The integral flux $F_{>1\text{TeV}}$ was calculated from the individual power law model fits. The RMS spread in the integral flux from year to year was 12%. Figure 4.11 shows the Whipple 10 m energy spectrum of the Crab nebula for all 6 yearly data sets. The flux points were rebinned according to the significance in the data set. A total TeV γ -ray Crab nebula energy spectrum from observations 2000–2006 was measured with both set of selection cuts. Using Hard cuts, the best fit model was a power law over the energy range 0.49–8 TeV with:

$$\frac{dN}{dE} = (3.19 \pm 0.07) \cdot \left(\frac{E}{1\text{TeV}} \right)^{-2.64 \pm 0.03} \times 10^{-11} \text{cm}^{-2} \text{s}^{-1} \text{TeV}^{-1}$$

Figure 4.12 (left) shows the total energy spectrum of the Crab nebula compared to past measurements with the Whipple 10 m in 1994–1995, HEGRA in 1997–2002, MAGIC in 2005, and H.E.S.S. in 2003–2005 (Mohanty et al. 1998; Aharonian et al. 2004; Wagner et al. 2005; Aharonian et al. 2006d). Due to the low energy threshold of MAGIC and high photon statistics in the HEGRA measurements, the combined Crab nebula energy spectrum from recent IACT observations covers a large energy range of 0.13–75 TeV. Figure 4.12 (right) shows a contour plot derived

Data Set (Year)	Cut	σ	σ/\sqrt{hr}	N_γ	F_\circ (f.u.) ^a	Γ	$F_{>1\text{TeV}}$ (f.u.) ^b	χ_r^2
'00-'01	Hard	19.4	5.32	2426	3.38 ± 0.19	2.57 ± 0.10	2.15 ± 0.15	0.32
	Loose	10.4	2.86	3685	3.35 ± 0.27	2.59 ± 0.12	2.11 ± 0.20	0.64
'01-'02	Hard	30.3	6.19	4445	3.10 ± 0.11	2.54 ± 0.06	2.01 ± 0.09	0.91
	Loose	17.1	3.49	7394	3.13 ± 0.17	2.52 ± 0.08	2.06 ± 0.13	1.51
'02-'03	Hard	19.9	6.91	1022	2.75 ± 0.16	2.66 ± 0.11	1.66 ± 0.12	1.03
	Loose	11.5	4.00	1774	2.98 ± 0.22	2.64 ± 0.14	1.82 ± 0.17	0.27
'03-'04	Hard	12.3	5.21	1076	3.75 ± 0.29	2.45 ± 0.10	2.59 ± 0.23	0.47
	Loose	9.7	4.13	2104	3.89 ± 0.36	2.61 ± 0.14	2.42 ± 0.26	0.22
'04-'05	Hard	13.0	5.54	1101	2.90 ± 0.26	2.68 ± 0.19	1.73 ± 0.20	0.75
	Loose	8.2	3.50	1657	3.13 ± 0.35	2.68 ± 0.24	1.87 ± 0.27	0.36
'05-'06	Hard	15.6	5.28	1769	3.58 ± 0.25	2.60 ± 0.12	2.24 ± 0.19	0.85
	Loose	11.3	3.80	3084	3.50 ± 0.33	2.65 ± 0.14	2.12 ± 0.23	0.83
Total	Hard	45.6	5.64	11886	3.19 ± 0.07	2.64 ± 0.03	1.95 ± 0.05	1.75
	Loose	28.0	3.48	19887	3.31 ± 0.10	2.62 ± 0.04	2.04 ± 0.07	0.48

Table 4.3: Energy spectrum of the Crab nebula with the Whipple 10 m from 2000–2006. Note: (a) The power law flux normalization F_\circ is in flux units f.u. of $10^{-11} \text{ cm}^{-2} \text{ s}^{-1} \text{ TeV}^{-1}$. (b) the integral flux $F_{>1\text{TeV}}$ is in $10^{-11} \text{ cm}^{-2} \text{ s}^{-1}$.

from the χ^2 fit errors in flux normalization $F_\circ(1 \text{ TeV})$ and photon index Γ for the total Whipple 10 m 2000–2006 energy spectrum using Hard and Loose selection cuts. The best fit values are shown to agree at the 2σ level.

Systematic Uncertainties

Contributing factors are estimated here for the systematic uncertainties in the absolute flux level (flux normalization F_\circ) and photon index Γ for power law fits to the reconstructed energy spectrum. The uncertainty in F_\circ is expected to be dominated by 4 factors: conversion of pixel intensities to photoelectrons, variations in the atmospheric condition, binning of the energy spectrum, and the applied selection cuts. As discussed in section 3.3.1, calibration of the pixel intensities relied on the time dependent telescope efficiency derived from muon events relative to a single measurement of the camera gain in late 2000. To estimate the uncertainty in F_\circ , the Crab nebula energy spectrum was measured using a telescope efficiency varying up to 10% from the nominal value.

A $\sim 22\%$ variation in F_{\circ} was found due to pixel intensity calibration alone. The effect on the absolute measured flux caused by varying atmospheric conditions relative to the simulated US74 atmospheric model (see section 3.3.2) was not tested here, but is estimated at $\sim 15\%$ based on the 10% effect determined for H.E.S.S. observations (Aharonian et al. 2006d). Rebinning the energy spectrum lead to a $\sim 5\%$ range in F_{\circ} . The systematic error due to selection cuts was estimated at 12% by the RMS spread in the integral flux between the yearly data sets using Hard and Loose cuts. Adding these 4 contributing factors in quadrature gives a conservative estimate of 30% uncertainty in absolute flux level.

Systematic uncertainties in the photon index Γ were estimated from the measured variations from the year to year data sets on the Crab nebula using the two set selection cuts, and from rebinning the energy spectrum. The RMS spread in Γ was 0.06 between the year data sets, as discussed above. Rebinning the energy spectrum resulted in a maximum deviation in Γ of 0.14. Adding these contributions in quadrature gives a systematic error on Γ of 0.15.

Chapter 5

Long-term Observations of TeV Blazars with the Whipple 10 m Telescope

A large sample is presented of Whipple 10 m observations on Mrk 421, Mrk 501, and H1426+428 from 2000 to 2006, with a total exposure of over 600 hours. Results from month timescale *RXTE* ASM X-ray rate and Whipple 10 m TeV γ -ray flux and energy spectrum measurements of TeV blazars are used to investigate the long-term duty cycle of each source. Section 5.1 describes the 2000–2006 Whipple 10 m data set on each source. Results from Mrk 421 observations are presented in section 5.2, with strong variability detected by the Whipple 10 m in both the integral flux above 0.6 TeV and spectral shape. Evidence is shown of a general shift to a harder spectrum with increasing flux in the 0.5–6 TeV energy band. The spectrum is well described by a power law with exponential cutoff at $E_c = 3.5$ TeV over a wide range of observed flux states. Variations were seen in the photon index between monthly observing periods at a similar flux state over the 6 year data set. Contemporaneous observations of Mrk 421 in February 2001 with HEGRA show a good agreement in the measured high state TeV γ -ray energy spectrum, however the HEGRA low flux energy spectrum is softer than that observed by Whipple 10 m at a slightly higher flux level. On month timescales, a potential correlation (with large spread) was shown between the simultaneous *RXTE* ASM rate and Whipple integral flux measurements. The Whipple 10 m monthly exposures recorded a large dynamic range in integral flux $F_{>0.6\text{TeV}}$ of 13–498% the flux level of the Crab nebula. Sections 5.3 and 5.4 present results from month timescale observations of Mrk 501 and H1426+428 during 2001 to 2006. The long-term TeV γ -ray flux of both sources was shown to remain near the Whipple 10 m detection limit. The intrinsic TeV γ -ray energy spectrum of each of the three blazars was estimated by correcting for absorption caused by interactions with the extragalactic background light (EBL).

5.1 Whipple 10 m Observations

Whipple 10 m observations of Mrk 421, Mrk 501, and H1426+428 during 2000–2006 offer the highest coverage on TeV blazars over this long period of any IACT telescope system. Section 5.1.1 specifies the data quality criteria and data reduction methods applied to all Whipple 10 m observations of TeV blazars in this work, with references to detailed descriptions in chapters 3 and 4. A summary is provided of the yearly data sets passing quality cuts for each source: Mrk 421 (section 5.1.2), Mrk 501 (section 5.1.3), and H1426+428 (5.1.4).

5.1.1 Data Selection

All observations of the three blazars were conducted in either 28 min. or 10 min. runs centered on the source. Data quality selection followed the methods described in section 3.2.6. Only runs with an RMS spread in the event rate < 1.5 Hz during “A” or “B” weather conditions were selected. An additional requirement was a mean zenith angle $< 30^\circ$ for each run. Since 83% of the selected Mrk 421, Mrk 501, and H1426+428 runs were taken without a corresponding OFF field run (of equivalent declination, offset by 30 min.), a large sample of OFF runs were selected for background determination using the same data quality criteria. The OFF data were taken from October 2000 to May 2006 for a total of 458.3 hours. The matching procedure in section 3.2.6 was used to select the best OFF run for each ON source run. Nearly all matched ON and OFF runs had a difference in zenith angle $< 5^\circ$ and were separated in time by less than 5 days. In several cases, one OFF run best matched a number of ON runs. The number of background events were scaled to the source observations both by the exposure, and by acceptance (see section 4.3). Data reduction followed the methods described in chapter 4. Cherenkov images were calibrated and processed with the “Granite” package (see section 4.1). At this stage, Gaussian noise was added to equalize differences in the night sky background between the source and OFF runs. The energy and reduced scaled image parameters were reconstructed for each image using lookup tables for the expected value as a function of $\text{Log}(\text{Size})$ and Distance from simulated γ -rays, as detailed in section 4.2. Hard image parameter cuts were applied to all data (see section 4.3).

5.1.2 Mrk 421 Observations

In 1992, Mrk 421 was first detected in the TeV γ -ray energy band by the Whipple 10 m (Punch et al. 1992). During the 2000–2006 period, Mrk 421 was observed between Nov. to May on most moonless nights to monitor for TeV γ -ray flux variability. Table 5.1 lists the observing periods and data selected in this work during 2000–2006. Data sets are divided by “seasons”, since observing

Observing Period (Month/Year)	T_{Live} (hr)	N_{Runs}	Θ Range (deg.)	$\langle\Theta\rangle$ (deg.)	$\langle\text{Rate}\rangle$ (Hz)
11/2000 - 05/2001	72.4	174	6 - 30	16.7	27.3
11/2001 - 05/2002	31.2	68	7 - 29	14.6	29.2
11/2002 - 05/2003	39.2	99	7 - 30	15.8	16.7
01/2004 - 05/2004	51.7	115	7 - 29	16.5	19.9
12/2004 - 05/2005	22.7	51	7 - 28	12.9	19.0
11/2005 - 05/2006	73.2	165	7 - 30	14.8	20.5
Total	290.3	672	6 - 30	15.5	22.4

Table 5.1: Whipple 10 m observations of Mrk 421 from 2000–2006. Listed for each yearly observing period are the livetime exposure T_{Live} in hours, number of observation runs N_{Runs} , mean zenith angle $\langle\Theta\rangle$ in degrees, and mean event rate $\langle\text{Rate}\rangle$ in Hz for all data passing quality selection.

periods typically start in October and end in June the following year. The number of ON source runs and exposure in each observing period was determined mostly by varying weather conditions, and to a lesser degree by runs rejected due to high zenith angle observations. The largest exposures were due to recorded increases in the TeV flux level, triggering a number of successful “target of opportunity” ToO multiwavelength campaigns with *RXTE* PCA (results in section 6.3), in addition to radio and optical telescopes, over periods ranging from a few days to 5 months. The total Whipple 10 m exposure on Mrk 421 of good quality data from November 2000 to May 2006 is 290.3 hours.

5.1.3 Mrk 501 Observations

Mrk 501 was the second TeV blazar discovered at TeV energies by the Whipple 10 m in 1996 (Quinn et al. 1996). The yearly observing periods on Mrk 501 with the Whipple 10 m begin mostly in February and end in June. Table 5.2 lists the Whipple 10 m observations of Mrk 501 during 2001–2006 presented in this work. The exposures in each observing period range from 6.2 to 19.6 hours, with a mean of 14.4 hours. The mean zenith angle $\langle\Theta\rangle$ of all selected observations was 16.6° . From 2001–2006, one multiwavelength campaign for joint *RXTE* PCA observations of Mrk 501 was triggered due to a moderate rise in the TeV γ -ray flux detected by the Whipple 10 m in June 2004 (see section 6.3).

Observing Period (Month/Year)	T_{Live} (hr)	N_{Runs}	Θ Range (deg.)	$\langle\Theta\rangle$ (deg.)	$\langle\text{Rate}\rangle$ (Hz)
02/2001 - 06/2001	16.9	41	8 - 27	16.2	25.2
03/2002 - 06/2002	10.9	26	9 - 29	14.7	26.0
02/2003 - 06/2003	6.2	31	8 - 29	14.8	15.6
02/2004 - 06/2004	16.9	55	8 - 29	17.2	18.3
03/2005 - 06/2005	15.8	35	11 - 30	20.9	17.0
11/2005 - 05/2006	19.6	43	9 - 28	16.1	16.4
Total	86.4	231	8 - 30	16.6	19.5

Table 5.2: Whipple 10 m observations of Mrk 501 from 2001–2006. Listed for each yearly observing period are the livetime exposure T_{Live} in hours, number of observation runs N_{Runs} , mean zenith angle $\langle\Theta\rangle$ in degrees, and mean event rate $\langle\text{Rate}\rangle$ in Hz for all data passing quality selection.

Observing Period (Month/Year)	T_{Live} (hr)	N_{Runs}	Θ Range (deg.)	$\langle\Theta\rangle$ (deg.)	$\langle\text{Rate}\rangle$ (Hz)
02/2001 - 06/2001	32.7	73	11 - 30	18.0	26.9
01/2002 - 07/2002	92.9	203	11 - 30	16.5	24.5
01/2003 - 06/2003	28.6	62	11 - 29	17.6	15.4
01/2004 - 06/2004	32.7	71	9 - 28	16.5	19.3
01/2005 - 06/2005	16.1	35	11 - 28	18.2	17.2
01/2006 - 05/2006	33.6	73	11 - 29	17.5	19.8
Total	236.6	517	9 - 30	17.1	21.8

Table 5.3: Whipple 10 m observations of H1426+428 from 2001–2006. Listed for each yearly observing period are the livetime exposure T_{Live} in hours, number of observation runs N_{Runs} , mean zenith angle $\langle\Theta\rangle$ in degrees, and mean event rate $\langle\text{Rate}\rangle$ in Hz for all data passing quality selection.

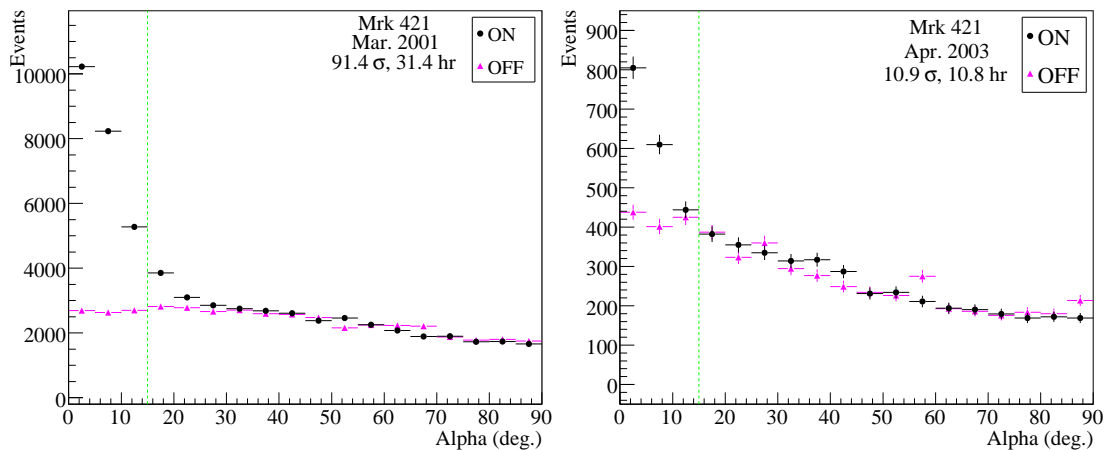


Figure 5.1: Alpha orientation parameter distributions after applying all other Hard cuts for ON observations of Mrk 421 (black points) and scaled OFF field observations (pink triangles, see section 3.2.6 for OFF run selection). The Hard cut of $\text{Alpha} < 15^\circ$ is represented by the green dashed line. Shown (left) is the Alpha distribution during a high TeV flux state in March 2001, with a 31.4 hour exposure resulting in a detection significance of 91.4σ . (Right) is shown the Alpha distribution during a low to medium flux state in April 2003.

5.1.4 H1426+428 Observations

The discovery of TeV γ -ray emission from H1426+428 with a significance $> 5 \sigma$ by the Whipple 10 m in 2001 is reanalyzed in this work, along with further Whipple 10 m observations up to 2006 (Horan et al. 2002). Table 5.3 lists the Whipple 10 m observing periods on H1426+428, which typically cover January to June of each year. The large exposure of 92.9 hours in 2002 with 203 selected runs resulted from a long-term 3 month joint observing campaign with *RXTE* PCA, presented in section 6.3.

5.2 Month Timescale TeV γ -ray Variability in Mrk 421

The large sample of Mrk 421 observations with the Whipple 10 m (summarized in section 5.1.2) were binned by time into ~ 20 day periods separated by ~ 10 days, dictated by the observing requirement of moonless nights. Gamma-ray events were selected using Hard cuts. A total γ -ray signal $> 3 \sigma$ was recorded for nearly all “monthly” observing periods, ranging from 2.5σ to 91.4σ . Figure 5.1 (left) shows the total Alpha image orientation parameter distribution of Hard cut selected events from Mrk 421 observations during March 2001. The strong 91.4σ signal yielded an excess of $N_\gamma = 15716.5$ selected γ -ray events in the source direction (at $\text{Alpha} < 15^\circ$) above the estimated background from matched OFF field observations. The exceptionally bright

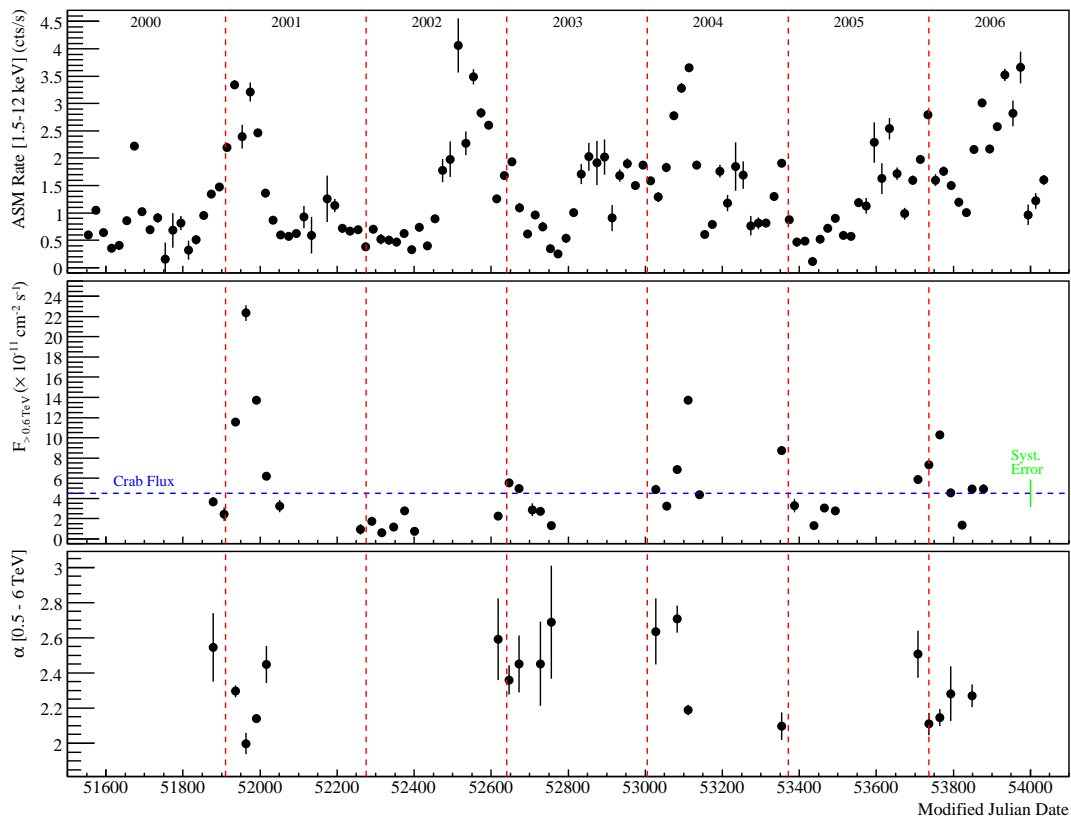


Figure 5.2: Long-term X-ray and TeV γ -ray light curve of Mrk 421 during 2000-2006. The top panel shows the mean *RXTE* ASM rate in 20 day time bins over the 1.5–12 keV band in units of counts per second. Shown in the middle panel is the Whipple 10 m integral flux $F_{>0.6\text{TeV}}$ in ~ 20 day bins. For reference, the Whipple 10 m Crab nebula flux level is represented by the blue dashed line, with the 30% systematic uncertainty in the flux shown by the green line (see section 4.5). Shown in the bottom panel is the photon index α from a power law with fixed exponential cutoff energy $E_c = 3.5$ TeV model fit to the energy spectrum over the energy range 0.5–6 TeV (see section 5.3.2).

long-term γ -ray flaring state of Mrk 421 from January to May 2001 is described below in detail in sections 5.2.1 and 5.3.2. For comparison, figure 5.1 shows the Alpha distribution from 10.8 hours of observations in April 2003, representing a relatively low to medium γ -ray flux state. The $>10\sigma$ total signal strength and high number of excess γ -ray type events ($N_\gamma = \sim 600\text{--}9000$) measured by the Whipple 10 m for a high fraction of the monthly periods allows for a detailed study of long-term variability.

5.2.1 Long-term X-ray and TeV γ -ray Light Curve of Mrk 421

A long-term TeV γ -ray light curve of Mrk 421 was constructed from integral flux measurements above 0.6 TeV with the Whipple 10 m. As described in section 4.4, the integral flux determination used a “method 1” of looking up the effective area on an event by event basis for all TeV blazar light curve calculations in this work. This method requires an energy threshold at (or above) E_{Safe} , where the relative error in energy reconstruction is less than 10%. All observations in this work were taken with a zenith angle $< 30^\circ$, which provided for an energy threshold of 0.6 TeV (see figure 4.9). “Method 1” does not require an assumed spectral shape, which is important when measuring the integral flux in sources with expected spectral variability as a function of flux, such as Mrk 421. The estimated systematic uncertainty in the flux measurements is 30%, as determined in section 4.4. To study the long-term flux variability at both X-ray and TeV energies, the complete reduced *RXTE* ASM light curve of Mrk 421 during 2000–2006 was taken from (*RXTE* ASM Data Products).

Figure 5.2 shows the X-ray and TeV γ -ray light curve of Mrk 421 measured by *RXTE* ASM and the Whipple 10 m in ~ 20 day bins during 2000–2006. The integral flux above 0.6 TeV flared dramatically by a factor > 9 beginning in December 2000 from $(2.44 \pm 0.67) \cdot 10^{-11} \text{ cm}^{-2} \text{ s}^{-1}$ (54% of the Crab nebula flux) in December 2000 to a peak flux $F_{>0.6\text{TeV}} = (22.3 \pm 0.77) \cdot 10^{-11} \text{ cm}^{-2} \text{ s}^{-1}$ in late February 2001 (a factor of 4.96 ± 0.17 brighter than the Crab nebula flux). The large month timescale flare was well resolved by the Whipple 10 m, with the TeV integral flux observed to return in May 2001 to the low flux state recorded in late 2000. The monthly *RXTE* ASM rate during the 2001 γ -ray flare also showed strong flaring, with a factor of ~ 10 increase in X-ray flux. Section 5.2.2 investigates a possible correlation between the X-ray and γ -ray fluxes, while section 6.3 presents the day timescale X-ray and TeV γ -ray flux variability seen during the 2001 flaring episode with a high coverage of *RXTE* PCA and Whipple 10 observations.

From the 6 year light curve of Mrk 421, large amplitude TeV γ -ray flaring was observed during January to April in both 2004 and 2006. The long-term TeV γ -ray integral flux in February to April 2004 rose steadily over 3 months from a factor of 0.72 ± 0.06 to 3.05 ± 0.04 of the integral flux from the Crab nebula. The large relative increase in *RXTE* ASM rate by a factor of 2.96 during this period presents a strong case for correlated long-term X-ray and TeV γ -ray emission in Mrk 421. Section 5.2.2 below discusses the possible correlation between the long-term X-ray and TeV γ -ray flux variability observed in Mrk 421. The bottom panel in the light curve of figure 5.2 shows the photon index α over the energy range 0.5–6 TeV from a power law with fixed exponential cutoff energy $E_c = 3.5$ TeV model fit to the Whipple 10 m energy spectrum of Mrk 421 during observing periods when a detection significance of greater than 10σ was recorded. Section 5.3.2 describes

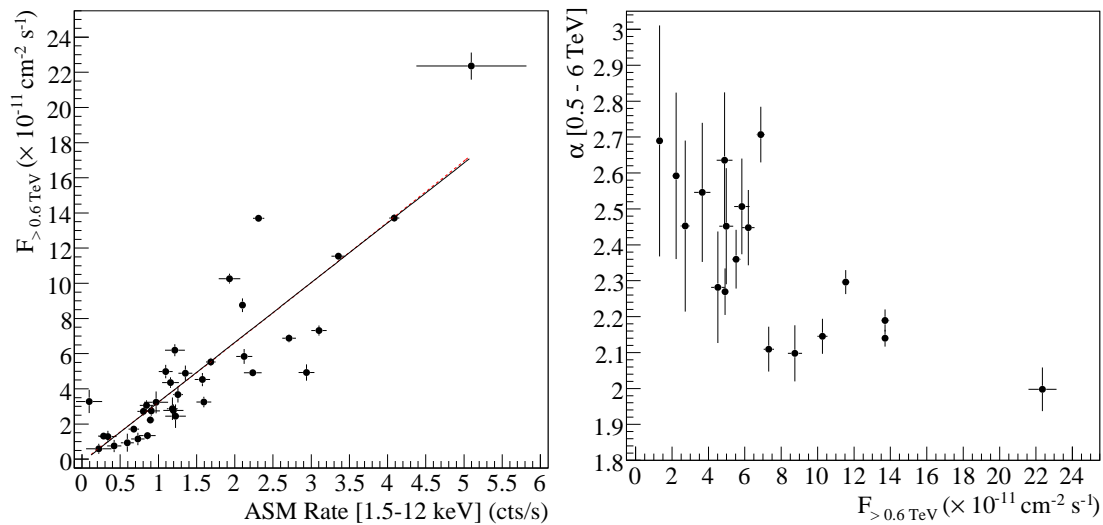


Figure 5.3: Correlation plots of Mrk 421. Shown (left) is the Whipple 10 m integral flux $F_{>0.6\text{TeV}}$ versus *RXTE* ASM (1.5–12 keV) rate from simultaneous ~ 20 day time bins. Linear (black line) and quadratic (red dashed line) functions were fit to the data. Shown (right) is the TeV γ -ray photon index α versus integral flux $F_{>0.6\text{TeV}}$, with α derived from a power law with fixed exponential cutoff energy $E_c = 3.5$ TeV model fit to the energy spectra (see section 5.3.2).

in detail the Whipple 10 m long-term energy spectrum results on Mrk 421.

5.2.2 Correlation of the X-ray and TeV γ -ray flux

To investigate a possible correlation of the *RXTE* ASM rate and Whipple 10 m integral flux in the long-term light curve of Mrk 421 (shown in figure 5.2), a strictly simultaneous *RXTE* ASM light curve was constructed for data taken during the Whipple 10 m observing periods. The weighted mean of the daily *RXTE* ASM rates was calculated in each time bin. The estimated 5% systematic error in the *RXTE* ASM rate was not taken into account (Levine et al. 1996). Figure 5.3 (left) shows the Whipple 10 m integral flux $F_{>0.6\text{TeV}}$ versus the *RXTE* ASM (1.5–12 keV) rate. Evidence is shown for a trend of higher X-ray flux during high TeV γ -ray flux levels on month timescales. To test for a linear relationship, the Pearson correlation coefficient r was calculated as:

$$r = \frac{\sum_{i=1} (F_i^\gamma - \overline{F^\gamma})(F_i^X - \overline{F^X})}{\sqrt{\sum_{i=1} (F_i^\gamma - \overline{F^\gamma})^2} \sqrt{\sum_{i=1} (F_i^X - \overline{F^X})^2}}$$

with simultaneous γ -ray and X-ray flux pairs F_i^γ and F_i^X , and mean values $\overline{F^\gamma}$ and $\overline{F^X}$. For a perfect linear correlation $r = 1$, while for a non-correlation $r = 0$. From the total Mrk 421 data set in figure 5.3, a weak correlation coefficient of $r = 0.22$ was calculated. The large spread results in a poor fit to a linear function of $\chi_r^2 = 19$. Under the Synchrotron Self-Compton (SSC) model,

a quadratic relationship is expected for the flux at GeV–TeV energies to the electron density (with a linear dependence at X-ray energies), as described in section 1.2. Hence, a quadratic function $F_i^X \propto (F_i^\gamma)^2$ was also fit to the data, resulting in a poor $\chi_r^2 = 24$. Shown (right) in figure 5.3 is the TeV γ -ray photon index α derived from power law with fixed exponential cutoff energy $E_c = 3.5$ TeV model fits (see section 5.3.2) versus the integral flux $F_{>0.6\text{TeV}}$. A general trend is shown of a harder TeV γ -ray spectrum with increasing TeV γ -ray flux.

5.2.3 TeV Energy Spectrum of Mrk 421 on Month Timescales

The energy spectrum of Mrk 421 in the 0.5–6 TeV band was recorded by the Whipple 10 m on month timescales over a large range in integral flux states. Energy spectrum determination followed the method described in section 4.4, and was calculated for each monthly Whipple 10 m observing period with a detection significance of $> 10 \sigma$. The energy bins were set larger than the 31% relative energy resolution of the Whipple 10 m, with a $> 2 \sigma$ detection required in the highest energy bin. A power law model (PL) was fit to each energy spectrum. Since curvature is expected in the Mrk 421 spectrum above 1 TeV based on previous IACT telescope measurements, a power law with exponential cutoff model (PLC) was also fit to the energy spectrum (Aharonian et al. 2002c; Krennrich et al. 2002; Aharonian et al. 2005b). The PLC model follows the form:

$$\frac{dN}{dE} = F_o \cdot \left(\frac{E}{1\text{TeV}} \right)^{-\Gamma} \cdot \exp\left(-\frac{E}{E_c}\right)$$

The position of the cutoff energy E_c is highly correlated to the photon index α , so typically past analyses of the Mrk 421 TeV γ -ray energy spectrum have tested for spectral curvature on a time averaged spectrum taken from observations during a long-term high flux state with high photon statistics (Aharonian et al. 2002c; Aharonian et al. 2005b). A similar approach was adopted here by measuring the Mrk 421 energy spectrum with Whipple 10 m observations from January to March 2001. The total exposure of 58.9 hours yielded a high number of excess events $N_\gamma = 28180.9$ at a significance of 113σ . A power law fit to the spectrum over an energy range of 0.5 to 6 TeV resulted in a poor χ_r^2 of 7.26, while a fit to the power law with exponential cutoff model gave an acceptable χ_r^2 of 1.17. The cutoff energy E_c was measured at $3.11 \pm 0.6_{\text{stat}}$ TeV, which is within the systematic and statistical errors of the cutoff energy measured by HEGRA of $E_c = 3.6 \pm 0.4_{\text{stat}} \pm 0.9_{\text{syst}}$ from contemporaneous data taken during November 2000 to May 2001 (Aharonian et al. 2002c).

For the monthly Whipple 10 m energy spectra, the PLC model with fixed cutoff energy $E_c = 3.5$ TeV was chosen (along with a simple power law model) to test for spectral variability in the photon index. Figure 5.4 shows the measured TeV γ -ray energy spectrum of Mrk 421 on

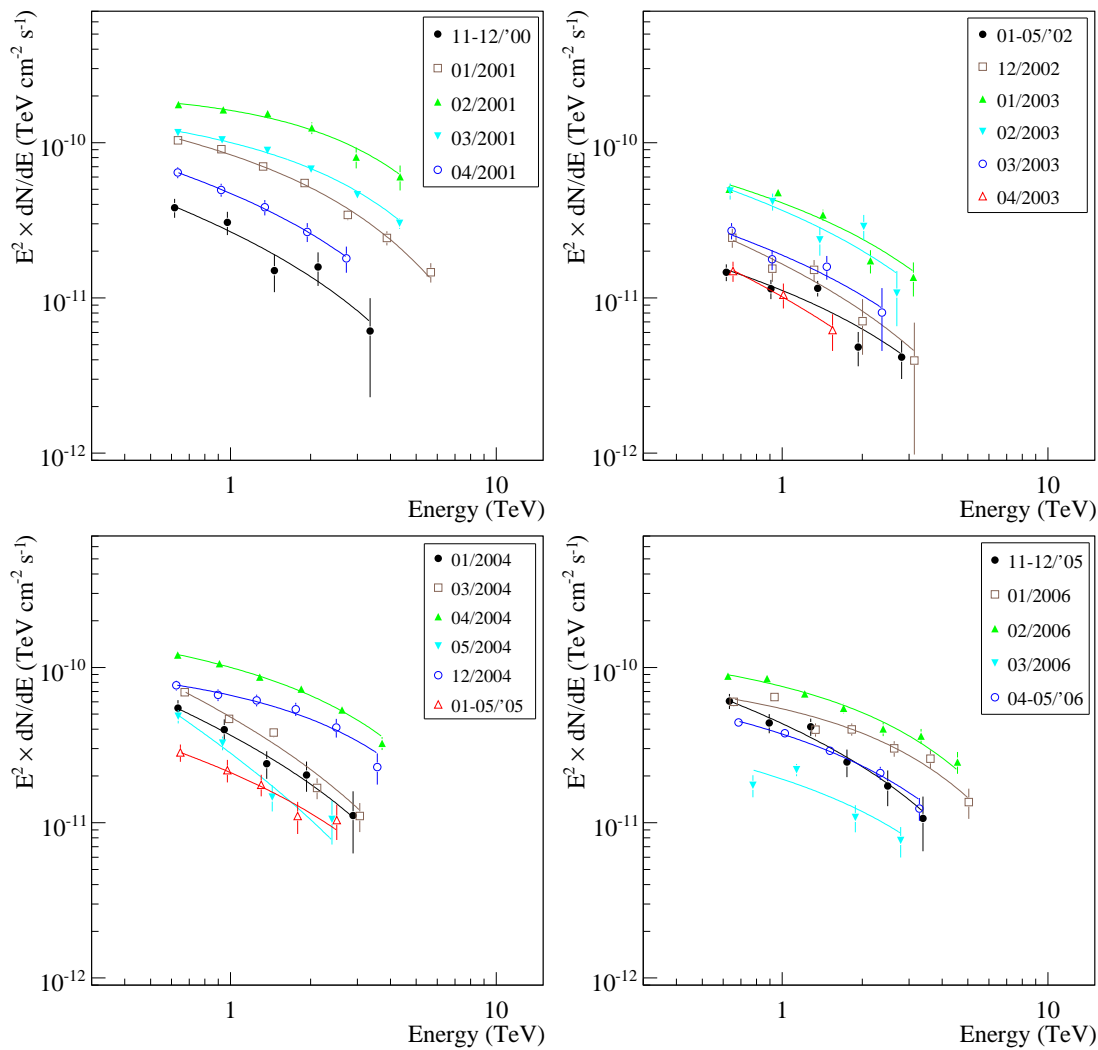


Figure 5.4: TeV γ -ray energy spectrum of Mrk 421 from Whipple 10 m observations during “monthly” observing periods from November 2000 to May 2006. The best fit function from a power law with fixed exponential cutoff $E_c = 3.5$ TeV model (PLC) is shown for each spectrum. Table 5.4 lists the fit parameters and χ_r^2 from either a power law or PLC model fit to the monthly energy spectra.

approximately monthly timescales during November 2000 to May 2006. Table 5.4 lists the best fit parameter and χ_r^2 values from model fits to a power law, or PLC model with fixed $E_c = 3.5$ TeV. For nearly all observation periods, the PLC model yielded a lower χ_r^2 than a power law, confirming the spectral curvature shown in figure 5.4. During the large December 2000 to May 2001 flare, the TeV γ -ray spectrum hardened from a PLC photon index $\alpha = 2.54 \pm 0.19$ at the onset of the flare to $\alpha = 2.00 \pm 0.06$ at the peak flux state in late February 2001. The γ -ray energy spectrum then softened during the decay of the flare event, as shown in the bottom panel of the long-term light

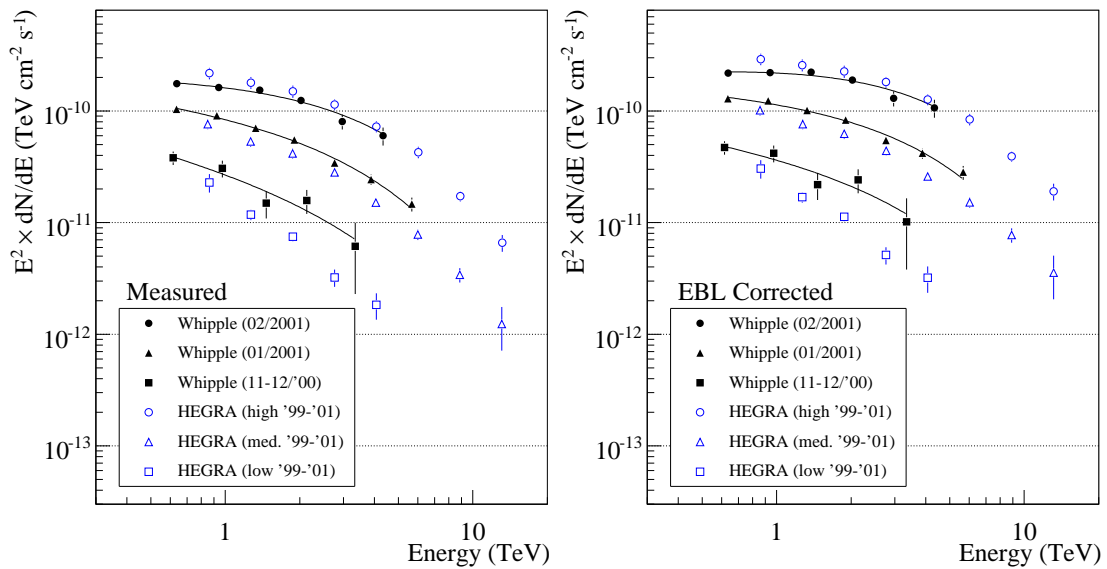


Figure 5.5: (Left) The TeV γ -ray energy spectrum of Mrk 421 measured during 3 observing periods in 2001 by the Whipple 10 m, and in 3 flux levels from HEGRA observations during 1999–2001 (Aharonian et al. 2002c). Shown (right) are the same energy spectra corrected for absorption by the EBL using the “Low-SFR” model in (Kneiske et al. 2004).

curve of figure 5.2. This month timescale flaring evident (clearly shown in the top left of figure 5.4) provides evidence for a shift in the spectral energy distribution (SED) to higher energies in the GeV to TeV band during the peak of long-term flare. For smaller long-term flaring events (shown in figure 5.2), no clear correlation is shown between the TeV γ -ray flux and spectral shape. It is important to note here that the measured TeV γ -ray energy spectrum of Mrk 421 is expected to have a lower absolute flux and softer spectrum than the intrinsic source photon spectrum due to absorption by the extragalactic background light (EBL), as shown below.

5.2.4 Absorption Corrected TeV Energy Spectrum of Mrk 421 during 1999–2001

As described in section 1.2, the γ -ray energy spectrum emitted by TeV blazars is partially absorbed due to photon-photon collisions with the extragalactic background light (EBL). The optical depth $\tau(E,z)$ for pair production in interactions with the EBL was derived in this work from the “Low-SFR” model in (Kneiske et al. 2004). The “Low-SFR” model was chosen as an approximate representation of the EBL spectral energy distribution (SED) based on recent limits to the EBL (Aharonian et al. 2006b; Dole et al. 2006). Figure 5.5 (left) shows the measured TeV γ -ray energy spectrum of Mrk 421 during low, medium, and high flux states in 2001 from Whipple 10 m observations. Also shown are HEGRA measurements taken from a large sample of observations

Obs. Period (Mon./Year)	T_{Live} (hr)	$F_{\circ}(\text{PL})$ (f.u.) ^a	Γ	χ_r^2	$F_{\circ}(\text{PLC})$ (f.u.) ^a	α	χ_r^2
11–12/'00	6.2	2.55 ± 0.24	2.91 ± 0.18	0.78	3.55 ± 0.33	2.55 ± 0.19	0.67
01/2001	24.8	7.92 ± 0.14	2.77 ± 0.03	7.26	11.12 ± 0.19	2.30 ± 0.03	0.94
02/2001	2.7	15.38 ± 0.51	2.45 ± 0.05	2.75	21.45 ± 0.71	2.00 ± 0.06	0.46
03/2001	31.4	9.54 ± 0.12	2.58 ± 0.02	14.24	13.31 ± 0.17	2.14 ± 0.02	1.03
04/2001	6.0	4.54 ± 0.22	2.81 ± 0.10	0.31	6.27 ± 0.31	2.45 ± 0.10	0.05
01–05/'02	28.5	1.07 ± 0.07	2.78 ± 0.13	2.58	1.51 ± 0.10	2.38 ± 0.14	0.78
12/2002	7.4	1.60 ± 0.14	2.95 ± 0.21	0.77	2.20 ± 0.19	2.59 ± 0.02	0.65
01/2003	9.9	3.92 ± 0.15	2.72 ± 0.08	4.65	5.44 ± 0.21	2.36 ± 0.08	2.81
02/2003	3.3	3.53 ± 0.26	2.82 ± 0.15	1.62	4.88 ± 0.36	2.45 ± 0.16	1.61
03/2003	7.7	1.84 ± 0.16	2.78 ± 0.23	0.76	2.51 ± 0.21	2.45 ± 0.24	0.83
04/2003	10.8	0.99 ± 0.12	2.97 ± 0.32	0.14	1.35 ± 0.16	2.69 ± 0.32	0.11
01/2004	4.6	3.54 ± 0.29	2.98 ± 0.18	0.19	4.87 ± 0.40	2.64 ± 0.19	0.20
03/2004	14.4	4.62 ± 0.15	3.08 ± 0.07	3.76	6.37 ± 0.20	2.70 ± 0.07	2.48
04/2004	19.8	9.57 ± 0.14	2.60 ± 0.03	6.10	13.3 ± 0.19	2.18 ± 0.03	0.58
12/2004	6.5	6.34 ± 0.26	2.52 ± 0.07	1.68	3.73 ± 0.27	2.10 ± 0.08	0.97
04–05/'05	9.7	2.04 ± 0.16	2.80 ± 0.17	0.25	2.80 ± 0.22	2.46 ± 0.18	0.42
11–12/'05	5.7	4.16 ± 0.27	2.90 ± 0.12	0.83	5.78 ± 0.38	2.51 ± 0.13	0.47
01/2006	15.7	5.20 ± 0.19	2.61 ± 0.05	3.14	7.20 ± 0.27	2.25 ± 0.06	2.12
02/2006	12.9	7.19 ± 0.18	2.58 ± 0.04	1.72	10.02 ± 0.26	2.14 ± 0.05	0.95
03/2006	17.2	1.87 ± 0.15	2.71 ± 0.15	4.98	2.54 ± 0.19	2.28 ± 0.15	2.9
04–05/'06	21.7	3.60 ± 0.11	2.68 ± 0.06	2.21	4.95 ± 0.15	2.27 ± 0.06	0.41

Table 5.4: Best fit model parameters for either a power law (PL), or power law with exponential cutoff (PLC) model fit to the TeV γ -ray energy spectrum of Mrk 421 observed on month timescales by the Whipple 10 m. For all PLC model fits, the cutoff energy was fixed at $E_c = 3.5$ TeV. The power law photon index Γ is listed, with the PLC model photon index referred to by α . Note: (a) The flux normalization values at 1 TeV for the two models $F_{\circ}(\text{PL})$ and $F_{\circ}(\text{PLC})$ are listed in flux units (f.u.) of $10^{-11} \text{ cm}^{-2} \text{ s}^{-1}$.

during 1999–2001 (Aharonian et al. 2002c). The observed Whipple 10 m and HEGRA high flux state energy spectrum agree well over the shared energy range of ~ 0.8 –5 TeV. A best fit to the Whipple 10 m high flux state energy spectrum in February 2001 using a power law with fixed exponential cutoff energy at $E_c = 3.5$ TeV resulted in photon index $\alpha = 2.00 \pm 0.06$. For the HEGRA observed high state energy spectrum, a photon index $\alpha = 2.06 \pm 0.03$ was found from a power law model with fixed exponential cutoff energy at $E_c = 3.6$ TeV. Figure 5.5 (right) shows the estimated intrinsic TeV γ -ray spectra of Mrk 421. For the high flux spectrum, a possible peak in the SED is indicated near the lower energy range of the Whipple 10 m, but the exact location is difficult to determine due to large uncertainties in the level of EBL absorption and the relatively small energy range of the Whipple 10 m. The high flux spectrum shows strong signs of curvature, with a poor χ_r^2 of 3.02 for a power law fit. A symmetrically curved log-parabolic model of the form:

$$\frac{dN}{dE} = F_o \cdot \left(\frac{E}{1 \text{ TeV}} \right)^{-(a+b \cdot \text{Log}(E/1 \text{ TeV}))}$$

was fit to the intrinsic spectrum, yielding a χ_r^2 of 0.27. The peak in the log-parabolic model is calculated by $E_p = (1 \text{ TeV}) \cot 10^{(2-a)/(2b)}$, giving an estimate of $E_p = 0.94 \pm 0.12$ TeV. The result is shown to be roughly consistent within the large range of $E_p \simeq 0.73$ –2 TeV previously calculated for the high flux TeV γ -ray spectrum of Mrk 421 from Whipple 10 m and HEGRA observations over a wide range of EBL levels (Dwek and Krennrich 2005a).

5.3 Results from Long-term Observations of Mrk 501

Results are presented from a total of 86.4 hours of Whipple 10 m observations on Mrk 501 during 2001–2006. Following the same methodology as with Mrk 421, observation periods of ~ 20 days were analyzed using Hard γ -ray selection cuts. For the majority of the “monthly” observing periods the detection significance was below 3σ , with a strong detection above 5σ determined in only four ~ 20 day periods. Figure 5.6 (left) shows the Alpha orientation parameter distribution of Mrk 501 during April 2004 over a total exposure of 2.9 hours. Shown on the (right) in figure 5.6 is the strongest monthly detection of Mrk 501 in June 2005 at a significance of 8σ from 4.8 hours of observations. The number of recorded γ -ray like excess events $N_\gamma = 311.2$ in the June 2005 data set is shown by the difference of the number of events in the ON and OFF field observations with $\text{Alpha} < 15^\circ$. The total number of excess events from the 86.4 hours of observations during 2001–2006 was $N_\gamma = 2300.2$, at a significance of 11.9σ . From the total of 231 observation runs (each of 10 or 28 min. duration), a maximum significance of 4.41σ was recorded on 15 June 2005, suggesting that no strong flaring event (on either day or month timescales) was recorded by

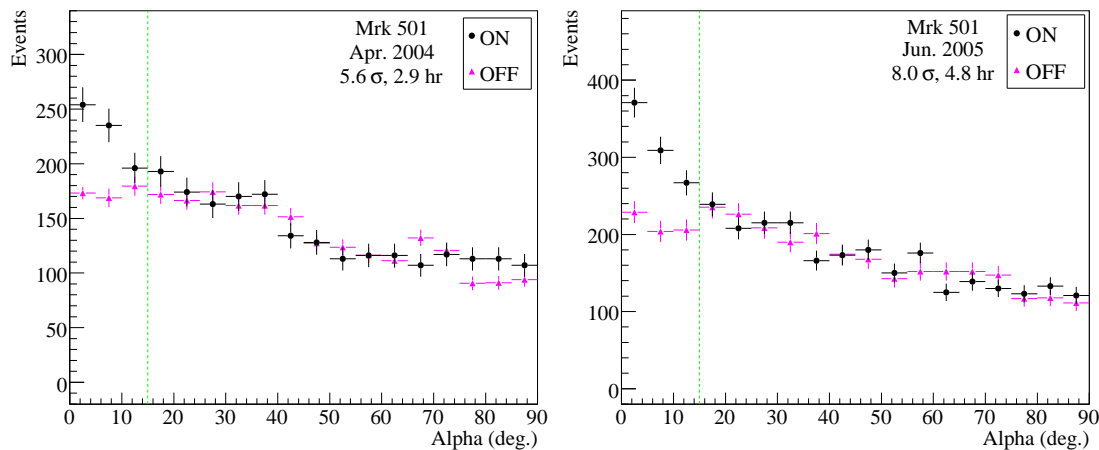


Figure 5.6: Alpha distribution of Mrk 501 ON field observations (black points) and scaled OFF runs (pink triangles) using Hard cuts. Shown (left) is the Alpha distribution for a 2.9 hour exposure of selected data during April 2004, and (right) is shown the Alpha distribution during June 2005 with a detection significance of 8σ .

the Whipple 10 m from 2001 to 2006. The long-term TeV γ -ray light curve of Mrk 501 over this period is shown below.

5.3.1 Long-term X-ray and TeV γ -ray Light Curve of Mrk 501

The integral flux above 0.6 TeV was calculated for each monthly observing period with the Whipple 10 m following a “method 1” described in sections 4.4 and 5.2.1. Due to the low overall detection rate, upper limits at the 99.9% confidence level were calculated on the integral flux $F_{>0.6\text{TeV}}$ for observing period with a $< 3\sigma$ detection level using the Helene method (see section 4.4). In addition to the long-term TeV light curve, the long-term X-ray flux levels during 2001–2006 were calculated from the reduced daily *RXTE* ASM rates in the 1.5–12 keV energy band, as obtained from (*RXTE* ASM Data Products). Figure 5.7 shows the X-ray and TeV γ -ray light curve of Mrk 501 measured by *RXTE* ASM and the Whipple 10 m from 2001 to 2006. The integral flux $F_{>0.6\text{TeV}}$ was shown to remained the flux level of the Crab nebula, with a mean of $F_{>0.6\text{TeV}} = (1.21 \pm 0.10) \cdot 10^{-11} \text{ cm}^{-2} \text{ s}^{-1}$, corresponding to 27% of the Crab nebula flux. In addition to the monthly Whipple 10 m integral fluxes, yearly mean values of $F_{>0.6\text{TeV}}$ were calculated, showing evidence of long-term TeV flux stability. Recently, the MAGIC collaboration published results of two large TeV γ -ray flaring events in Mrk 501 during 30 June and 9 July 2005, with a recorded integral flux in the energy range of 0.15–10 TeV at a factor of 3.48 ± 0.10 and 3.12 ± 0.12 the flux of the Crab nebula, respectively (Albert et al. 2007a). The two flaring events occurred after

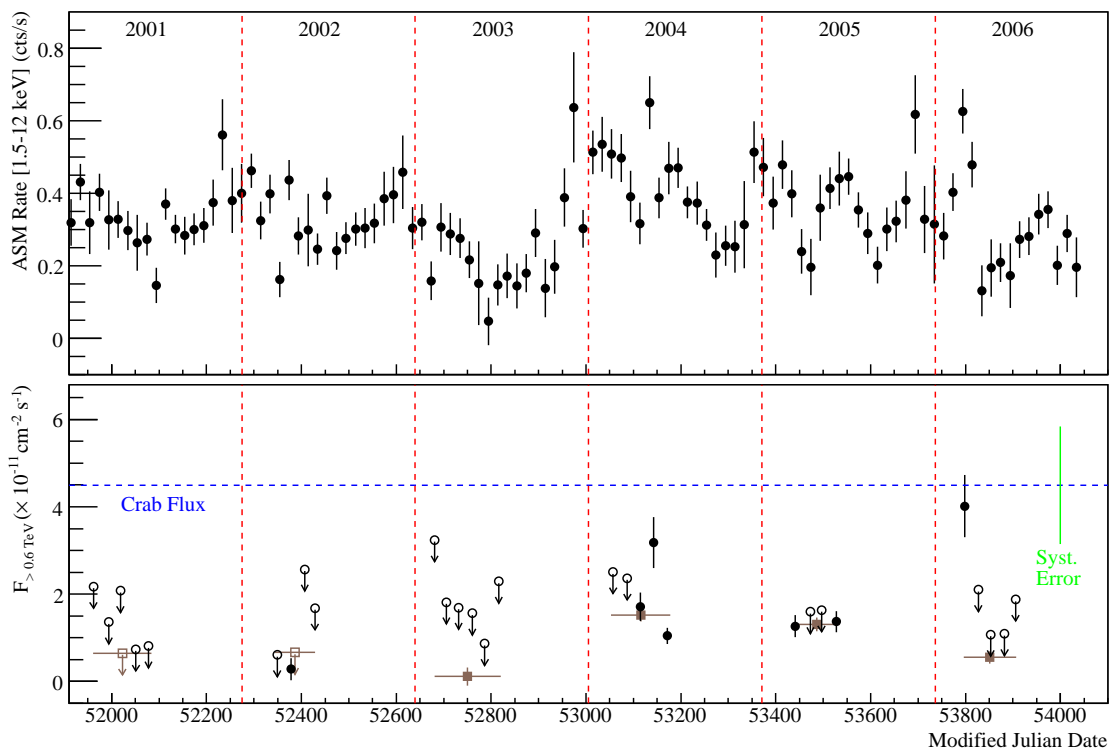


Figure 5.7: Long-term X-ray and TeV γ -ray light curve of Mrk 501 from 2001 to 2006. Shown in the top panel is the mean *RXTE* ASM rate in 20 day time bins. Whipple 10 m integral flux $F_{>0.6\text{TeV}}$ levels are shown on the bottom panel in ~ 20 day bins (black circles), and in “yearly” bins (brown squares). For Whipple 10 m observing periods with a detection significance $< 3\sigma$, upper limits at a 99.9% confidence level were calculated for the integral flux, shown by empty circles for monthly exposures, or by empty squares for yearly integrations. As a reference, the Whipple 10 m observed Crab nebula flux level above 0.6 TeV is shown by the blue dashed line, with the 30% systematic uncertainty in the flux shown by the green line (see section 4.5).

the Whipple 10 observing period ended (14 June 2005), but contemporaneous observations during early June 2005 show a reasonable agreement in a relative flux level of $\sim 20\text{--}50\%$ of the Crab nebula flux above the energy thresholds of the Whipple 10 m and MAGIC at 0.6 TeV and 0.15 TeV. A comparison of the light curve in figure 5.7 to long-term observations by the Whipple 10 m, HEGRA, and CAT during 1997–2000 show a consistent “baseline” of TeV γ -ray flux at $\sim 20\text{--}30\%$ of the Crab nebula flux, with the exception of a long-term elevated flux state in April to July 1997 (Albert et al. 2007a). The 1997 flaring state is discussed in section 1.1. In the following section, the TeV γ -ray energy spectrum of Mrk 501 is presented from Whipple 10 m observations in June 2005 when the source was in a low to medium flux state.

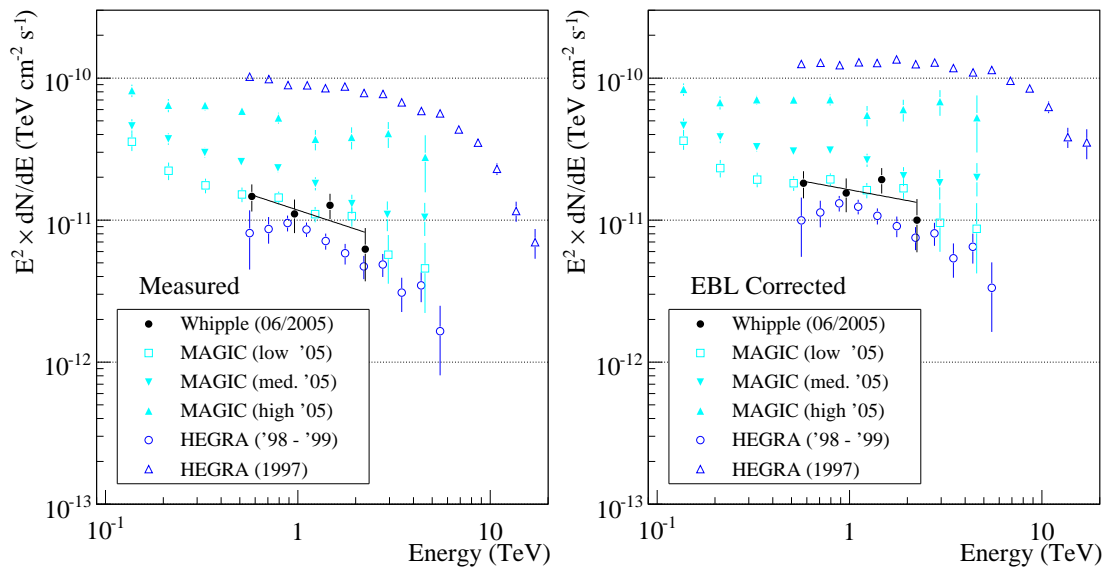


Figure 5.8: (Left) The TeV γ -ray energy spectrum of Mrk 501 measured by the Whipple 10 m in June 2005. The time averaged spectra from MAGIC observations at 3 flux levels during May to July 2005 are shown in aqua, in addition to HEGRA observations during at flux state in Apr. to May 1997, and at a low flux state in Apr. 1998 to Jun. 1999 (Aharonian et al. 2001a; Albert et al. 2007a). Shown on the (right) are the same energy spectra corrected for absorption by the EBL using the “Low-SFR” model in (Kneiske et al. 2004).

5.3.2 Absorption Corrected TeV Energy Spectrum of Mrk 501

The energy spectrum of Mrk 501 over the energy range 0.5–3 TeV was reconstructed from 4.78 hours of observations with the Whipple 10 m in June 2005. Figure 5.8 (left) shows the measured Whipple 10 m energy spectrum of Mrk 501. A power law fit the energy spectrum resulted in a χ_r^2 of 0.96. The energy spectrum follows the form:

$$\frac{dN}{dE} = (1.18 \pm 0.15) \cdot \left(\frac{E}{1 \text{ TeV}} \right)^{-2.44 \pm 0.24} \times 10^{-11} \text{ cm}^{-2} \text{ s}^{-1} \text{ TeV}^{-1}$$

Also shown in figure 5.8 is the 0.1–4.8 TeV energy spectra of Mrk 501 at 3 flux levels from MAGIC observations between May and July 2005 (Albert et al. 2007a). A power law photon index of $\Gamma = 2.45 \pm 0.07$ was measured for the MAGIC low flux energy spectrum, which agrees well within errors to the Whipple 10 m result over the same observing period at approximately the same flux level. For reference, the time averaged energy spectra measured by HEGRA are shown in figure 5.8 from observations in Apr. to May 1997 and Apr. 1998 to Jun. 1999 over an energy range of 0.5–24 TeV (Aharonian et al. 2001a). The HEGRA measured power law photon index of $\Gamma = 2.76 \pm 0.08$ in 1998–1999 is softer than either the Whipple 10 m or MAGIC energy

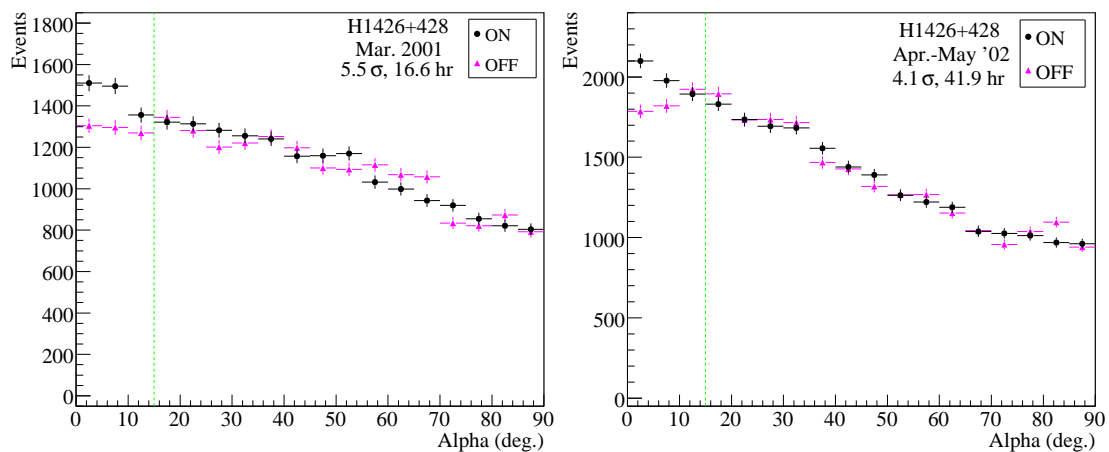


Figure 5.9: Alpha distribution of H1426+428 ON field observations (black points) and scaled OFF runs (pink triangles) using Hard cuts. Shown (left) is the Alpha distribution during March 2001, when the source was discovered at TeV energies by the Whipple 10 m at a significance $> 5 \sigma$ (Horan et al. 2002). (Right) is shown the Alpha distribution during April to May 2002 indicating a possible detection at the 4.1σ level with Hard cuts over an exposure of 41.9 hours.

spectrum, however the HEGRA observations include data at lower flux levels than in 2005. Figure 5.8 (right) shows the estimated intrinsic energy spectrum of Mrk 501 after applying corrections for absorption using the “Low-SFR” model in (Kneiske et al. 2004). Mrk 501 at a redshift of 0.034 has a similar optical depth to Mrk 421, resulting in a similar modification to the measured energy spectrum. A clear hardening in the energy spectrum is shown, with a power law photon index $\Gamma = 2.25 \pm 0.24$ estimated for the intrinsic spectrum observed by the Whipple 10.

5.4 Results from Long-term Observations of H1426+428

Whipple 10 m observations of H1426+428 from February 2001 to May 2006 resulted in a total exposure of 236.6 hours. Data reduction followed the same procedures outlined for Mrk 421 and Mrk 501 using Hard selection cuts. Figure 5.9 shows the Alpha parameter distributions for the two most significant monthly observing periods in March 2001 and April to May 2002. The 5.5σ detection level observed in March 2001 confirms the previous discovery of TeV γ -ray emission from H1426+428 by the Whipple 10 m (Horan et al. 2002). A joint observing campaign with *RXTE* PCA during April to May 2002 (described in section 6.1) resulted in a deep exposure of 41.9 hours of Whipple 10 m observations, yielding a weak detection of 4.1σ . Since the only strong detection was during the March 2001 observing period, upper limits at a 99.9% confidence level were calculated for the TeV γ -ray integral flux during all other observing periods.

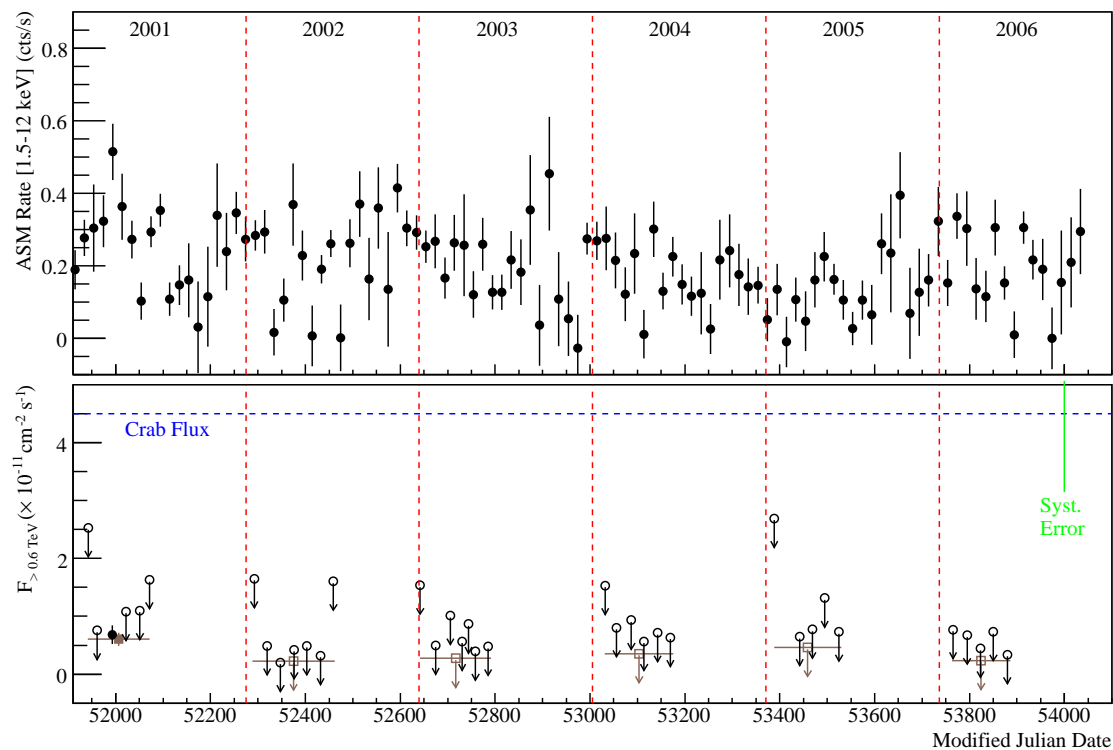


Figure 5.10: Long-term X-ray and TeV γ -ray light curve of H1426+428 from 2001 to 2006. Shown in the top panel is the mean *RXTE* ASM rate in 20 day time bins. The Whipple 10 m integral flux $F_{>0.6\text{TeV}}$ recorded in March 2001 with a significance of 5.5σ is shown in the bottom panel (black circle), together with the “yearly” detection (brown square). For Whipple 10 m observing periods with a detection significance $< 4 \sigma$, upper limits at a 99.9% confidence level were calculated for the integral flux, shown by empty circles for monthly exposures, or by empty squares for yearly integrations. As a reference, the Whipple 10 m observed Crab nebula flux level above 0.6 TeV is shown by the blue dashed line, with the 30% systematic uncertainty in the flux shown by the green line (see section 4.5).

5.4.1 Long-term X-ray and TeV γ -ray Light Curve of H1426+428

Figure 5.10 shows the *RXTE* ASM and Whipple 10 m long-term light curve of H1426+428 from 2001 to 2006. The *RXTE* ASM rates were calculated in 20 day time bins. Fitting a constant flux model to the monthly *RXTE* ASM rates resulted in a marginally poor χ_r^2 of 2.50, showing weak indications of long-term variability. For the Whipple 10 m results, upper limits at a 99.9% confidence level were determined for the integral flux $F_{>0.6\text{TeV}}$ for all but the total 2001 observations at a significance of 5.4σ , and for the March 2001 detection. During this integration, the flux was measured at $F_{>0.6\text{TeV}} = (0.68 \pm 0.16) \cdot 10^{-11} \text{ cm}^{-2} \text{ s}^{-1}$, corresponding to a factor of 0.15 ± 0.04 the flux of the Crab nebula above 0.6 TeV. This result agrees within errors to the integral flux above

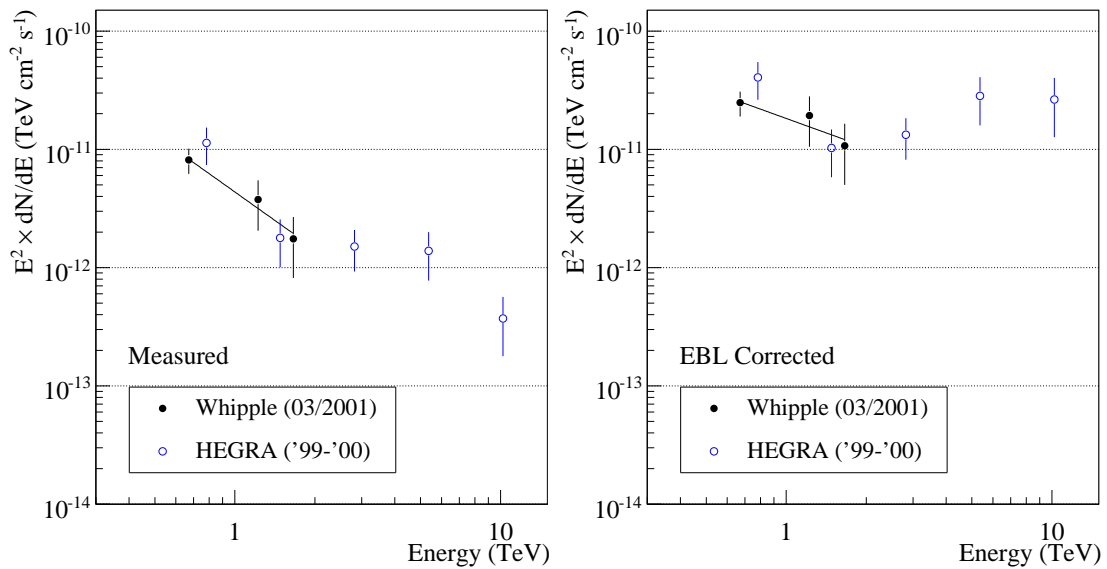


Figure 5.11: (Left) The TeV γ -ray energy spectrum of H1426+428 from Whipple 10 m observations in March 2001. Shown for comparison is the time averaged HEGRA energy spectrum H1426+428 from observations in Feb. to Apr. 1999 and Mar. to Jun. 2000 (Aharonian et al. 2002a; Aharonian et al. 2003). Shown on the (right) are the same energy spectra corrected for absorption by the EBL using the “Low-SFR” model in (Kneiske et al. 2004).

1 TeV observed by HEGRA in Feb. to Apr. 1999 and Mar. to Jun. 2000 at a factor of 0.20 ± 0.10 of the Crab nebula flux (Aharonian et al. 2002a). The following yearly (and monthly) Whipple 10 m flux upper limits exclude a strong long-term TeV γ -ray flare in H1426+428 from 2001 to 2006, however unresolved smaller short timescale flares during this period can not be excluded.

5.4.2 Absorption Corrected TeV Energy Spectrum of H1426+428

A 16.6 hour exposure on H1426+428 from Whipple 10 m observations in March 2001 was used to derive the TeV γ -ray energy spectrum. Due to a low total significance of 5.5σ , the Whipple 10 m spectrum covers a limited energy range of 0.5 to 2.8 TeV. Figure 5.11 (left) shows the measured Whipple 10 m energy spectrum of H1426+428 in March 2001. Also shown is the measured HEGRA energy spectrum over the energy range of 0.7 to 10 TeV (Aharonian et al. 2002a). The Whipple 10 m spectrum was best fit by a power law:

$$\frac{dN}{dE} = (0.44 \pm 0.09) \cdot \left(\frac{E}{1 \text{ TeV}} \right)^{-3.60 \pm 0.53} \times 10^{-11} \text{ cm}^{-2} \text{ s}^{-1} \text{ TeV}^{-1}$$

The soft spectrum agrees with a previous analysis of Whipple 10 m data in 2001, in which a power law photon index of $\Gamma = 3.50 \pm 0.35$ was measured over an energy range 0.4 to 2.5 TeV (Petty et al. 2002). A power law fit to the HEGRA energy spectrum of H1426+428 resulted in harder

photon index of $\Gamma = 2.6 \pm 0.6$ for energies extending up to 10 TeV (Aharonian et al. 2002a). Significant absorption of the energy spectrum above 0.5 TeV by the extragalactic background light (EBL) is expected due to the relatively moderate to high redshift of 0.129 (see figure 1.9). Following the analysis presented above for Mrk 421 and Mrk 501, the optical depth $\tau(E,z)$ to the EBL was derived from the “Low-SFR” model in (Kneiske et al. 2004). Figure 5.11 (right) shows the estimated intrinsic TeV γ -ray energy spectrum of H1426+428 for the HEGRA and Whipple 10 m spectrum calculated in this work. The Whipple 10 m energy spectrum hardens to a power law with photon index $\Gamma = 2.81 \pm 0.53$. The level of EBL absorption first tested on the HEGRA energy spectrum was much higher than the low level adopted in this work, and resulted in an intrinsic spectrum described by $E^{-1.9}$ (Aharonian et al. 2003). The HEGRA energy spectrum has subsequently been used by a number of authors to test for reasonable realizations of the EBL spectral energy distribution (Dwek et al. 2005b; Mazin and Raue 2007).

Chapter 6

X-ray and TeV γ -ray Variability in TeV Blazars

Results are presented from a large data set of near simultaneous *RXTE* PCA and Whipple 10 m observations from January 2001 to May 2006 on the 3 TeV blazars Mrk 421, Mrk 501, and H1426+428. In addition, publicly available *XMM-Newton* PN observations of the 3 TeV blazars were studied for variability in the broadband X-ray energy spectrum. The focus of this chapter is primarily to investigate possible correlations in the energy spectrum and flux state of TeV blazars at X-ray and TeV energies on day timescales. A total *RXTE* PCA data set on Mrk 421 of 662 hours was analyzed, along with 197 hours of contemporaneous Whipple 10 m observations. The joint observing campaigns were typically triggered by a combination of a high flux in both the *RXTE* ASM rate and Whipple 10 m detection rate over a period of two to three nights. During a large fraction of 2 to 6 month *RXTE* PCA and Whipple 10 m campaigns on Mrk 421 in 2003, 2004, and 2006 flaring above a medium to low flux state was observed in both the X-ray and TeV γ -ray bands. Spectral evolution from separate years was studied in detail using simultaneous X-ray and TeV energy spectra. Corrections to the observed Whipple 10 m energy spectrum were applied for a low level of absorption by the extragalactic backlight light (EBL). Overall, a large dynamic range of a factor > 20 was observed in both the X-ray integral flux $F_{3-20\text{keV}}$ and the TeV γ -ray integral flux $F_{>0.6\text{TeV}}$.

6.1 Joint *RXTE* PCA and Whipple 10 m Observations

This section provides an overview on the complete *RXTE* PCA data archive on Mrk 421, Mrk 501, and H1426+428 from 2001 to 2006. All *RXTE* PCA data was obtained through the public archive at (HEASARC 2007). *RXTE* PCA data reduction followed the standard procedures outlined in

section 2.2. Only data from PCU0 and PCU2 detectors were used, which were operational for all but one observing period - during Mrk 421 observations from 19 Apr. to 31 May 2006 only PCU2 was operational. Section 6.4 gives a detailed description of X-ray spectral analysis and integral flux calculations applied to the reduced *RXTE* PCA data. Contemporaneous, and in most cases near simultaneous, Whipple 10 m observations are summarized for each *RXTE* PCA observing period. All Whipple 10 m observations were reduced using Hard cuts, as described in section 4.3. Energy spectrum determination and integral fluxes were calculated using the methods in section 5.2. The joint *RXTE* PCA and Whipple 10 m data sets are described below for each source.

6.1.1 Observations of Mrk 421 with *RXTE* PCA and the Whipple 10 m

Table 6.1 lists all *RXTE* PCA observations of Mrk 421 from 2001 to 2006. Due to the occasionally non-sequential nature of *RXTE* PCA ObsIDs (observation identifications), only the first 5 digits are used in this work followed by a unique alphabetical label. The average exposure of each pointed observation $\langle T_{\text{Obs}} \rangle$ and total exposure T_{Tot} are given for each data set. Accounting for gaps during each pointing, the livetime was typically $\sim 20\text{--}30\%$ less than the quoted exposure time. For data sets on which results have been previously published, a reference is given for the referred paper. Table 6.2 summarizes the Whipple 10 m observations of Mrk 421 selected during each of *RXTE* PCA data set. The start and end date of all overlapping data (passing quality cuts) is given, with the *RXTE* PCA ObsID listed for reference. The number of days with observations N_{Days} and total livetime exposure T_{Live} are listed for each data set. During only one *RXTE* PCA campaign (ObsID: 80172 f in February to March 2003) was there no contemporaneous Whipple 10 m data selected due to poor weather conditions. The total significance σ using Hard cuts is listed for each data set. For all joint *RXTE* PCA campaigns, the Whipple 10 m detected a strong signal from Mrk 421. Figure 6.1 shows the *RXTE* PCA observing periods from 2001 to 2006 superimposed on the long-term *RXTE* ASM and Whipple 10 m light curve from figure 5.2 in section 5.2. High amplitude flux variability is shown during 5 and 6 month *RXTE* PCA campaigns in 2004 and 2006 on month timescales. The near simultaneous X-ray and TeV γ -ray variability on day timescales from *RXTE* PCA and Whipple 10 m observations is presented in section 6.3.

6.1.2 Observations of Mrk 501 with *RXTE* PCA and the Whipple 10 m

Table 6.3 summarizes the complete *RXTE* PCA data archive on Mrk 501 and H1426+428 from 2001 to 2006. Mrk 501 was observed only once over this period in June 2004 for a total of 8.2 hours. H1426+428 was observed in 4 separate periods, with a long-term campaign in 2002 of over 3 months. A total exposure T_{Tot} of 151 hours was taken during this campaign. Table 6.4 lists the

ObsID	Start Date	End Date	N_{Obs}	N_{Days}	$\langle T_{\text{Obs}} \rangle$ (hr)	T_{Tot} (hr)	Pub
50190 (a)	2001-01-24	2001-02-04	16	13	1.39	22.2	–
60145 (b)	2001-03-18	2001-04-01	46	14	2.83	130	Cu04,Gi06
70161 (c)	2002-12-03	2002-12-16	45	15	0.65	29.0	Re06
70161 (d)	2003-01-10	2003-01-14	14	5	0.54	7.51	Re06
80173 (e)	2003-02-20	2003-05-04	56	45	0.61	34.0	Bl05
80172 (f)	2003-02-26	2003-03-06	40	9	2.64	105	–
80173 (g)	2003-12-21	2004-04-21	70	65	0.58	40.5	Bl05,Gr05,Xu06
90148 (h)	2004-04-18	2004-05-13	23	13	1.07	24.6	Bl05,Gr05,Xu06
90138 (i)	2004-05-10	2004-05-21	9	6	1.30	11.7	Bl05,Gr05,Xu06
90148 (j)	2004-12-15	2004-12-22	8	8	0.29	2.31	–
91440 (k)	2006-01-06	2006-03-02	27	27	0.31	8.40	–
92402 (l)	2006-03-03	2006-04-18	22	22	0.27	5.90	–
92402 (m)	2006-04-19	2006-05-31	26	26	0.35	9.07	–
Total			402	258	0.99	662	–

Table 6.1: *RXTE* PCA observations of Mrk 421 from 2001 to 2006. The observation identification ObsID is given with an alphabetical label adopted in this thesis. The number of observations N_{Obs} , number of days during which data was taken N_{Days} , and mean observation exposure $\langle T_{\text{Obs}} \rangle$ in hours are listed for each data set. The total exposure in each data sets is given by T_{Tot} in hours. Previous publications: Kr01 (Krawczynski et al. 2001), Cu04 (Cui 2004), Gi06 (Giebels et al. 2007), Re06 (Rebillot et al. 2006), Bl05 (Blazejowski et al. 2005), (Grube et al. 2005), Xu06 (Xue et al. 2006).

overlapping Whipple 10 m data passing quality cuts on Mrk 501 and H1426+428. For the Mrk 501 campaign in June 2004, a total livetime exposure T_{Live} of 7.5 hours was selected. The total Whipple 10 m detection significance on Mrk 501 was 4.66σ , with no strong detection over 3σ recorded on any night. Figure 6.2 shows the *RXTE* PCA observing period on Mrk 501 in reference to the long-term X-ray and TeV γ -ray light curve in 2001–2006 from figure 5.3.1. The aqua colored band shows the *RXTE* PCA observing campaign in June 2004. These observations were taken during a relatively low TeV γ -ray flux state (see section 5.3.1 for a discussion of long-term TeV γ -ray variability in Mrk 501).

ObsID	Start Date	End Date	N_{Runs}	N_{Days}	T_{Live} (hr)	σ
50190 (a)	2001-01-24	2001-02-04	50	11	22.9	60.2
60145 (b)	2001-03-18	2001-03-31	67	13	29.5	89.5
70161 (c)	2002-12-04	2002-12-16	18	10	7.4	12.7
70161 (d)	2003-01-10	2003-01-14	13	5	5.6	21.2
80173 (e)	2003-03-07	2003-05-03	43	24	18.5	17.7
(g,h,i)	2004-01-18	2004-05-19	114	42	51.2	74.0
90148 (j)	2004-12-14	2004-12-20	9	4	4.1	16.9
(k,l,m)	2006-01-05	2006-05-28	127	38	57.7	52.2
Total			441	147	196.9	

Table 6.2: Whipple 10 m observations of Mrk 421 taken during the *RXTE* PCA observing periods (ObsID) listed in table 6.1. For Whipple 10 m observing periods covering more than one *RXTE* PCA observing period only the alphabetical labels taken from table 6.1 are listed. The start and end date of each Whipple 10 m observing period is given, along with the number of observations runs N_{Runs} , number of days (nights) during which data passed quality cuts N_{Days} , the total livetime exposure T_{Live} in hours, and total detection significance σ using Hard cuts (see section 4.3).

6.1.3 Observations of H1426+428 with *RXTE* PCA and the Whipple 10 m

As shown in table 6.3, H1426+428 was observed by *RXTE* PCA in 4 periods between 2001 and 2006, with a long-term campaign in 2002 of over 3 months. A total exposure T_{Tot} of 151 hours was taken during this campaign. Joint Whipple 10 m observations of H1426+428 within the *RXTE* PCA observing periods (listed in table 6.4) resulted in a total livetime T_{Live} of 87.5 hours for all data passed quality cuts. H1426+428 was not detected by the Whipple 10 m over any of the *RXTE* PCA observing periods. No Whipple 10 m data was taken during the last *RXTE* PCA observation in August 2004 (ObsID 90420 d), since from mid July to September the Whipple 10 m is routinely shut down to avoid damage by heavy storms (see section 3.2.5). However, simultaneous *XMM-Newton* observations were taken during the 4th and 6th of August 2004, allowing a cross calibration of the X-ray spectra, as described in section 6.4. Figure 6.3 shows the *RXTE* PCA observing periods for H1426+428 superimposed on the X-ray and TeV γ -ray light curve from 2001 to 2006 taken from figure 5.10. During the 3 month *RXTE* PCA campaign in 2002, significant month timescale X-ray variability is evident. Section 6.3 shows that day time scale flux doubling and spectral variability was observed by *RXTE* PCA during April 2002. In figure 6.3 the last *RXTE*

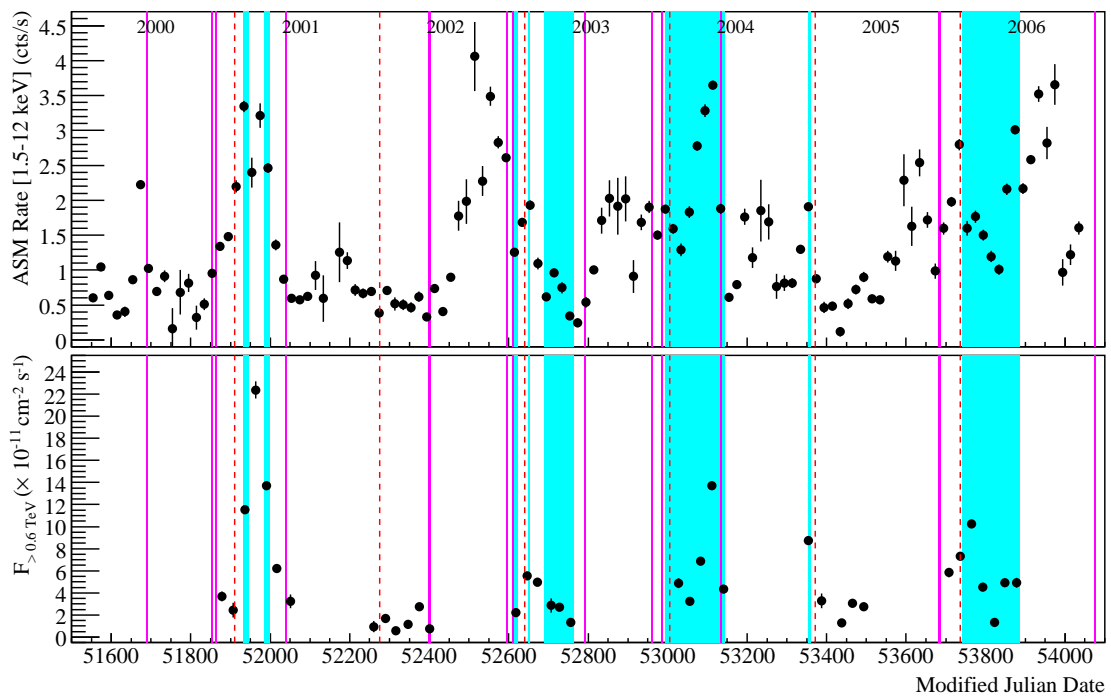


Figure 6.1: Long-term X-ray and TeV γ -ray light curve of Mrk 421 (adapted from figure 5.2). *RXTE* PCA observing periods are shown by aqua colored bands, with *XMM-Newton* observing periods shown in pink (summarized in section 6.2).

ObsID	Start Date	End Date	N_{Obs}	N_{Days}	$\langle T_{\text{Obs}} \rangle$ (hr)	T_{Tot} (hr)	Pub
Mrk 501							
90148 (a)	2004-06-12	2004-06-24	13	13	0.63	8.20	GI06
H1426+428							
60411 (a)	2001-05-19	2001-05-25	7	7	0.16	1.12	–
70154 (b)	2002-03-07	2002-06-15	120	68	1.26	151	Fa04
90135 (c)	2004-02-01	2004-02-17	6	5	1.38	8.30	–
90420 (d)	2004-08-04	2004-08-06	6	2	2.94	17.7	–
Total			139	82	1.44	178	–

Table 6.3: *RXTE* PCA observations of Mrk 501 and H1426+428 from 2001–2006. The ObsID identification is given with an alphabetical label adopted in this thesis. The number of observations N_{Obs} , number of days during which data was taken N_{Days} , and mean observation exposure $\langle T_{\text{Obs}} \rangle$ in hours are listed for each data set. The total exposure in each data sets is given by T_{Tot} in hours. Previous publications: GI06 (Gliozzi et al. 2006), Fa04 (Falcone et al. 2004).

ObsID	Start Date	End Date	N_{Runs}	N_{Days}	T_{Live} (hr)	σ
Mrk 501						
(a)	2004-06-12	2004-06-22	17	8	7.5	4.66
H1426+428						
(a)	2001-05-21	2001-05-24	5	3	2.3	2.73
(b)	2002-03-09	2002-06-15	182	54	83.4	2.58
(c)	2004-02-16	2004-02-17	4	2	1.8	1.26
Total			191	59	87.5	

Table 6.4: Whipple 10 m observations of Mrk 501 and H1426+428. Whipple 10 m observations of 501 and H1426+428 taken during the *RXTE* PCA observing periods (ObsID) listed in table 6.3. The start and end date of the Whipple 10 m observing period is given, along with the number of observations runs N_{Runs} , number of days (nights) during which data passed quality cuts N_{Days} , the total livetime exposure T_{Live} in hours, and total detection significance σ using Hard cuts (see section 4.3).

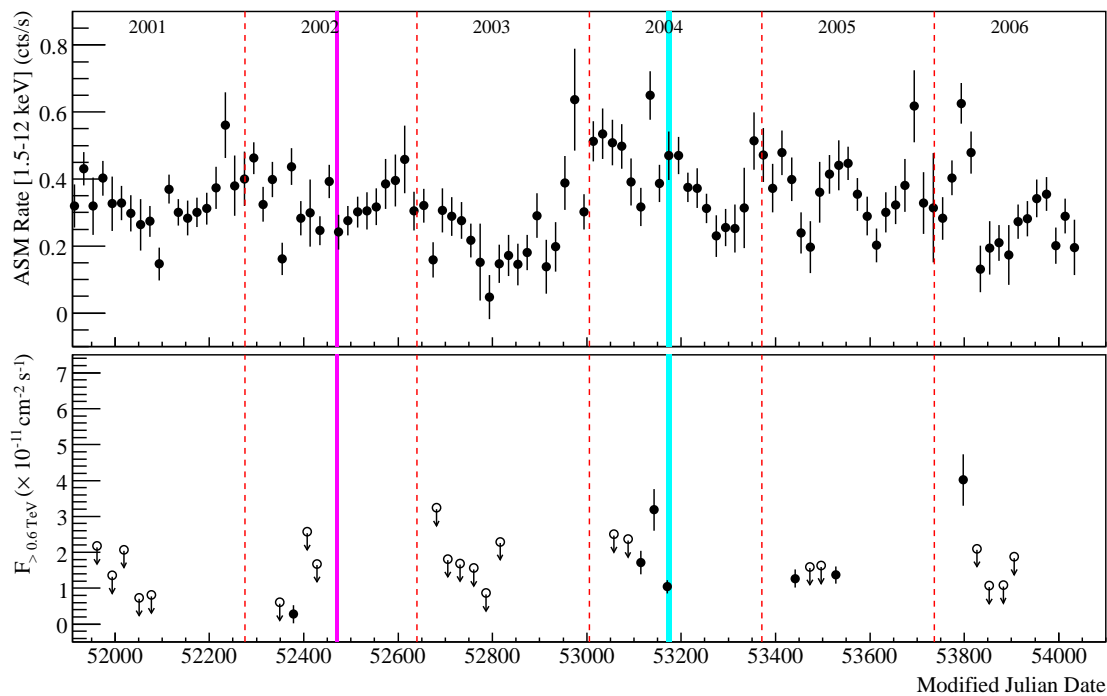


Figure 6.2: Long-term X-ray and TeV γ -ray light curve of Mrk 501 (adapted from figure 5.7). *RXTE* PCA observing periods are shown by aqua colored bands, with *XMM-Newton* observing periods shown in pink (summarized in section 6.2).

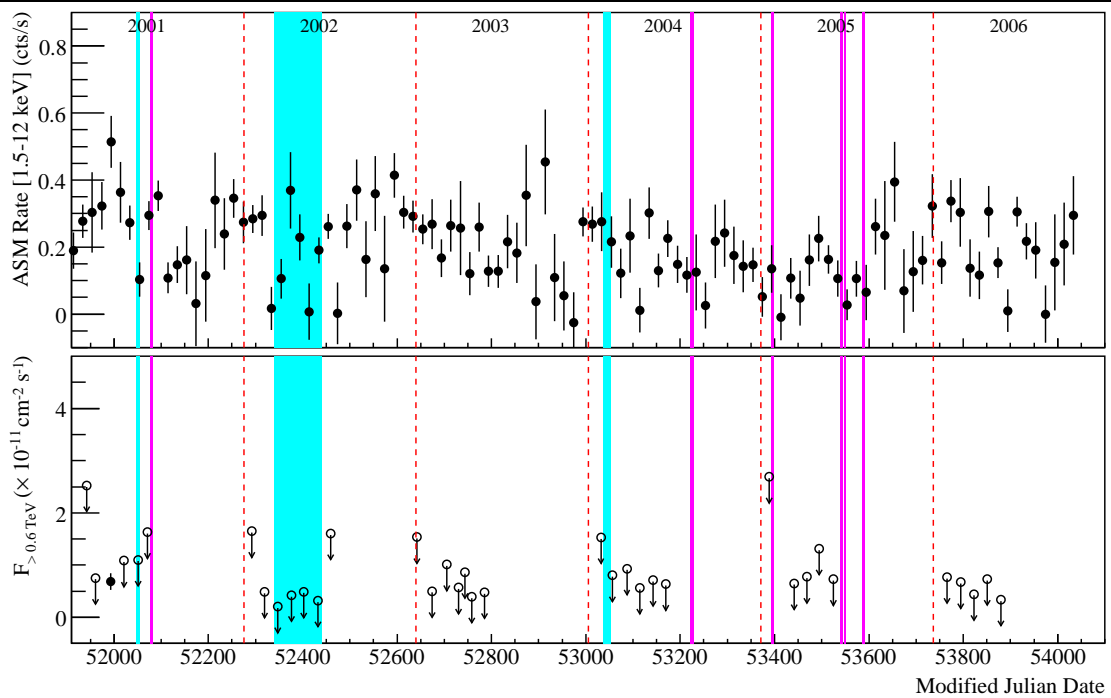


Figure 6.3: Long-term X-ray and TeV γ -ray light curve of H1426+428 (adapted from figure 5.10). *RXTE* PCA observing periods are shown by aqua colored bands, with the *XMM-Newton* observing periods shown in pink.

PCA observing period on H1426+428 in August 2004 (ObsID: 90420 d) is not visible, since the simultaneous *XMM-Newton* observation (shown by a pink band) is plotted on top of the *RXTE* PCA periods. The full set of *XMM-Newton* observations of H1426+428, Mrk 421, and Mrk 501 from 2000 to 2006 are described below in section 6.2.

6.2 XMM-Newton Observations

In this section all publicly available *XMM-Newton* observations of Mrk 421, Mrk 501, and H1426+428 are presented, current up the end of 2006. Over the first 7 years of operation, Mrk 421 was observed during 16 separate orbits, primarily for calibration purposes. Mrk 501 was observed by *XMM-Newton* in two consecutive orbits in July 2002. H1426+428 was observed during 7 orbits from 2001 to 2005. Only data from the PN instrument is analyzed in this work, as discussed in section 2.3. All data was obtained through the public archive at (*XMM-Newton* SOC). Data reduction followed the general procedures described in section 2.3. The *XMM-Newton* PN event files were calibrating using SAS 6.5. The PN operating mode for each observation is listed for each observation. Only results from Timing, Small Window, and Large Window operating mode observations are presented here. A summary of observations for each source is provided below.

6.2.1 Observations of Mrk 421 with *XMM-Newton*

Table 6.5 lists all *XMM-Newton* PN observations of Mrk 421 from 2000 to 2006. The start date and time are given for each observation, with both the total observing time T_{Obs} and livetime T_{Obs} in units of hours. The operating mode is listed for all observations. Special calibration modes are identified in 11 observations by a star, during which time Mrk 421 was offset from in the camera by either 2 or 3 arcmin, or by a dagger for Full Frame observations in a masked mode. To avoid uncertain systematic effects, no observations in the masked Full Frame were analyzed. Results from all other data are presented in section 6.4, with the exception of the SW observation in May 2006 when standard data screening rejected the entire observation. The cause of this non-uniform observation was not investigated here. In total, 21 observations of Mrk 421 with *XMM-Newton* PN were analyzed in this work, resulting in a livetime of 180 hours.

6.2.2 Observations of Mrk 501 and H1426+428 with *XMM-Newton*

Table 6.6 summarizes all *XMM-Newton* PN observations of Mrk 501 and H1426+428 taken up to 2006. For both sources, all observations were in the Small Window operating mode. As discussed above in section 6.1, the two *XMM-Newton* PN pointings on H1426+428 in August 2004 were taken simultaneously to *RXTE* PCA observations. The total *XMM-Newton* PN livetime on Mrk 501 was 2.53 hours, while for H1426+428 the livetime totaled 63.0 hours. Results on the broadband X-ray spectrum of Mrk 501 and H1426+428 from 0.6 to 10 keV from *XMM-Newton* PN observations are presented in section 6.4.

6.3 Results from *RXTE* PCA and Whipple 10 m Campaigns in 2001–2006

This section presents the results from *RXTE* PCA and Whipple 10 m campaigns described above in section 6.1. For each *RXTE* PCA observation the integral flux $F_{3-20\text{keV}}$ was calculated by a fit to the energy spectrum. The methods used for X-ray spectral analysis are described below. The Whipple 10 m integral fluxes $F_{>0.6\text{TeV}}$ were calculated on a nightly basis using a “method 1” described in sections 4.4 and 5.2.1. For selected nights with strong X-ray and TeV γ -ray flux variability, the Whipple 10 energy spectrum was measured using the methods detailed in section 4.4. All but two of the 13 *RXTE* PCA and Whipple 10 m campaigns on Mrk 421 from 2001 to 2006 are presented here. As described in section 6.1, no Whipple 10 m observations were taken during the 26 Feb. to 6 Mar. 2003 *RXTE* PCA observing period (ObsID: 80172 f), and the *RXTE* PCA results are not shown. Also, results during the short 8 day exposure in Dec. 2004 (ObsID:

ObsID ^a	Rev ^b	Start Time ^c	PN ^d	T _{Obs} ^e (hr)	T _{Live} ^f (hr)	Pub ^g
0099280101	0084	2000-05-25 (03h 54m)	T	6.31	4.66	Br01,Br03,Br05
0099280101	0084	2000-05-25 (11h 12m)	SW	9.02	5.88	Br01,Se02,Br03
0099280201	0165	2000-11-02 (00h 22m)	SW	10.2	6.74	Se02,Br03,Fo06
0099280301	0171	2000-11-13 (23h 54m)	SW	12.2	5.22	Se02,Br03,Fo06
0099280401	0171	2000-11-14 (14h 37m)	SW*	11.5	5.26	Br03,Fo06
0136540101	0259	2001-05-08 (08h 19m)	SW	10.4	7.15	Se02,Br03,Fo06
0153950601	0440	2002-05-04 (17h 42m)	LW*	10.2	9.54	Br03
0153950701	0440	2002-05-05 (05h 06m)	LW*	4.74	4.43	Br03
0136540301	0532	2002-11-04 (01h 18m)	FF [†]	6.12	4.10	Ra04
0136540401	0532	2002-11-04 (08h 11m)	FF [†]	6.11	3.90	Ra04
0136540701	0537	2002-11-14 (00h 58m)	LW	19.4	10.3	Ra04
0136540801	0537	2002-11-14 (22h 00m)	LW*	2.63	1.52	–
0136540901	0537	2002-11-15 (01h 36m)	LW*	2.63	1.70	–
0136541001	0546	2002-12-01 (23h 19m)	T	19.4	19.4	Ra04,Br05
0136541101	0546	2002-12-02 (20h 01m)	LW*	2.63	2.01	–
0136541201	0546	2002-12-02 (00h 03m)	LW*	2.63	1.98	–
0158970101	0637	2003-06-01 (13h 17m)	SW	11.4	7.02	Fo06
0158970201	0637	2003-06-02 (01h 28m)	FF [†]	2.11	1.32	–
0158970701	0640	2003-06-07 (21h 56m)	FF [†]	1.88	1.18	–
0150498701	0720	2003-11-14 (16h 34m)	T	13.3	5.58	–
0162960101	0733	2003-12-10 (21h 30m)	SW	8.34	4.84	Fo06
0158971201	0807	2004-05-06 (02h 58m)	T	18.0	7.12	Br05
0153951301	1083	2005-11-07 (20h 18m)	T	2.43	1.05	–
0158971301	1084	2005-11-09 (18h 39m)	T	16.3	8.54	–
0411080301	1184	2006-05-28 (21h 40m)	SW	3.21	–	–
0411080701	1280	2006-12-05 (12h 07m)	T	4.90	4.83	–

Table 6.5: *XMM-Newton* PN observations of Mrk 421 from 2000 to 2006. Notes: (a) Observation number, (b) revolution, and (c) start time of observation. (d) PN operating mode (* offset by 2 or 3 arcmin, † masked mode). (e) total exposure T_{Obs} in hours and (f) livetime T_{Live} in hours. (g) previous publications: Br01 (Brinkmann et al. 2001), Se02 (Sembay et al. 2002), Br03 (Brinkmann et al. 2003), Br05 (Brinkmann et al. 2005), Fo06 (Foschini et al. 2006), Ra04 (Ravasio et al. 2004).

ObsID ^a	Rev ^b	Start Date and Time ^c	PN ^d	T _{Obs} ^e (hr)	T _{Live} ^f (hr)	Pub ^g
Mrk 501						
0113060201	0474	2002-07-12 (17h 55m)	SW	1.72	1.21	BI04
0113060401	0475	2002-07-14 (19h 19m)	SW	1.89	1.32	BI04
H1426+428						
0111850201	0278	2001-06-16 (01h 25m)	SW	17.1	12.0	BI04
0165770101	0852	2004-08-04 (01h 13m)	SW	16.4	11.5	–
0165770201	0853	2004-08-06 (01h 20m)	SW	17.1	12.0	–
0212090201	0939	2005-01-24 (15h 44m)	SW	8.03	5.62	–
0310190101	1012	2005-06-19 (08h 34m)	SW	9.81	6.86	–
0310190201	1015	2005-06-25 (06h 21m)	SW	11.6	8.15	–
0310190501	1035	2005-08-04 (04h 59m)	SW	9.78	6.85	–

Table 6.6: *XMM-Newton* PN observations of Mrk 501 and H1426+428 from 2000 to 2006. Notes: (a) Observation number, (b) Revolution number, (c) Start date and time, (d) PN operating mode, (e) PN exposure in hours, (f) livetime in hours, and (g) previous publications: BI04 (Blustin et al. 2004).

90148 j) are not shown here. Following the results from the Mrk 421 campaigns, results from the Mrk 501 campaign in June 2004 are presented. This section concludes with the 4 month *RXTE* PCA and Whipple 10 m campaign on H1426+428 from March to June 2002 (ObsID: 70154 b).

6.3.1 *RXTE* PCA Spectral Analysis

The XSPEC 12 spectral analysis package was used for all *RXTE* PCA observations for model fits to the measured energy spectrum (HEASARC 2007). Three models were tested on each spectra: an absorbed power law (PL), power law with exponential cutoff (PLC), and log-parabolic model (LP). A reasonable model fit was determined by a χ_r^2 near unity, and by low residuals to the fit across the full energy range. Each model includes a correction term for galactic absorption. The log-parabolic and PLC models were chosen since each model requires only one additional fit parameter than a simple power law model to measure any possible curvature in the spectrum. The power law model followed the form:

$$\frac{dN}{dE} = F_o \cdot \left(\frac{E}{1 \text{ keV}} \right)^{-\Gamma} \cdot e^{-N_{\text{H,Gal}}\sigma(E)}$$

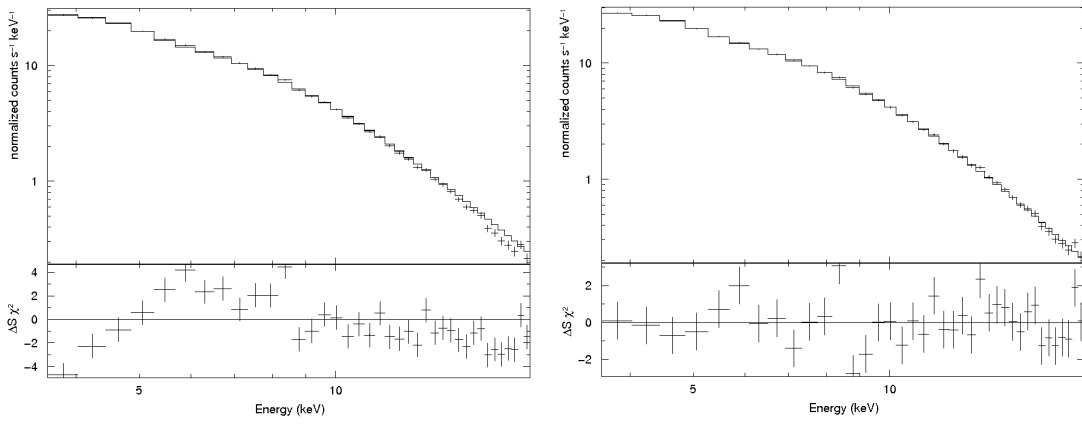


Figure 6.4: Spectral curvature in the *RXTE* PCA spectrum of Mrk 421 on 29 May 2006. (Left) Power law fit to the energy spectrum with fixed galactic absorption $N_{\text{H,Gal}} = 1.61 \cdot 10^{20} \text{ cm}^{-2}$. (Right) Log-parabolic model fit to the same *RXTE* PCA spectrum with fixed galactic absorption. The χ^2 residuals to the model fits are shown below each energy spectrum.

All absorption cross sections $\sigma(E)$ in cm^2 were calculated using the model in (Morrison and McCammon 1983). In all spectral fits, the column density was fixed to the Galactic value $N_{\text{H,Gal}}$. For Mrk 421, a galactic interstellar absorption column density $N_{\text{H,Gal}} = 1.61 \cdot 10^{20} \text{ cm}^{-2}$ was used from the HI emission line profile measured by (Lockman and Savage 1995). For Mrk 501, the column density $N_{\text{H,Gal}} = 1.71 \cdot 10^{20} \text{ cm}^{-2}$ was taken from (Dickey and Lockman 1990). For H1426+428, $N_{\text{H,Gal}} = 1.4 \cdot 10^{20} \text{ cm}^{-2}$ was taken from (Stark et al. 1992). The exponential cutoff (PLC) model followed the form $dN/dE = (dN/dE)_{\text{PL}} \cdot e^{E/E_c}$, with $(dN/dE)_{\text{PL}}$ representing the absorbed power law model, and E_c the free fit parameter on the cutoff energy in the spectrum. The log-parabolic model was given by:

$$\frac{dN}{dE} = F_{\odot} \cdot \left(\frac{E}{1 \text{ keV}} \right)^{-(a+b \cdot \text{Log}(E/1 \text{ keV}))} \cdot e^{-N_{\text{H,Gal}} \sigma(E)}$$

The spectral index at 1 keV is a , and b defines the curvature of a parabola. The best fit parameters can then be used to derive the peak in the Spectral Energy Distribution (SED) plotted as $\text{Log}(vF(v))$ versus $\text{Log}(v)$. The peak energy is given by $E_p = E_1 \cdot 10^{(2-a)/2b} \text{ keV}$, with $E_1 = 1 \text{ keV}$, and the peak $E^2 \cdot dN/dE$ flux given in terms of peak frequency ν_p by:

$$\nu_p F(\nu_p) = 1.6 \cdot 10^{-9} \cdot F_{\odot} \cdot E_1^2 \cdot 10^{(2-a)^2/4b} \text{ erg cm}^{-2} \text{ s}^{-1}$$

Statistical errors were derived by propagation of the errors in the fit parameters. When the energy spectrum covers a limited energy range, the measurement of the curvature term b has a large systematic uncertainty. Figure 6.24 shows the *RXTE* PCA energy spectrum of Mrk 421 on 29 May

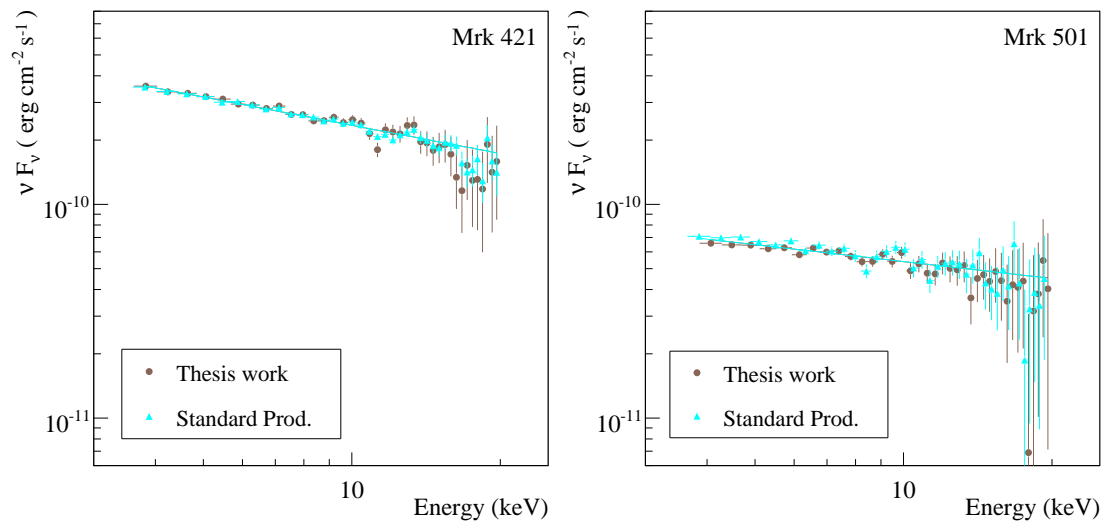


Figure 6.5: Comparison of Mrk 421 and Mrk 501 *RXTE* PCA energy spectra reduced as described in section 2.2 (Thesis work), and corresponding *RXTE* PCA spectra from HEASARC pipeline processing (Standard Prod.). (Left) Mrk 421 spectra from 25 May 2006 fit to an absorbed power law model. (Right) Mrk 501 spectra from 24 June 2004 fit to the same absorbed power law model, but with fixed $N_{\text{H,Gal}} = 1.71 \cdot 10^{20} \text{ cm}^{-2}$.

2006 to both an absorbed power law and log-parabolic model with fixed galactic column density. The power law fit yielded a poor χ_r^2 of 4.47, while the log-parabolic model yielded a reasonable χ_r^2 of 1.4. Significant curvature was seen in 33% of the total 402 *RXTE* PCA Mrk 421 observations, as estimated by a $\chi_r^2 > 1.5$. The integral flux derived from 3–20 keV was calculated from the fits to the power law, PLC, and log-parabolic models for all observations. The power law model was found to systematically underestimate the integral flux by $<2\%$. The power law photon index Γ offers the simplest description of the full 3–20 keV spectral shape, so all light curves in this work show the *RXTE* PCA integral flux and photon index from power law fits. For *RXTE* PCA observations of Mrk 501 and H1426+428 nearly all spectra were well fit by a power law. Figure 6.5 shows two example *RXTE* PCA energy spectra from Mrk 421 and Mrk 501 using the data reduction methods in section 2.2 compared to the Standard Products *RXTE* PCA spectra generated by HEASARC pipeline processing and provided by in the HEASARC data archive. Fitting an absorbed power law to both spectra simultaneous resulted in good χ_r^2 of ~ 1 , confirming that the data produce similar energy spectra. Data reduction in this work used the most current calibration files, including the energy response and background model, and should be more reliable than the Standard Products. The remainder of this section presents the *RXTE* PCA results from TeV blazar observations.

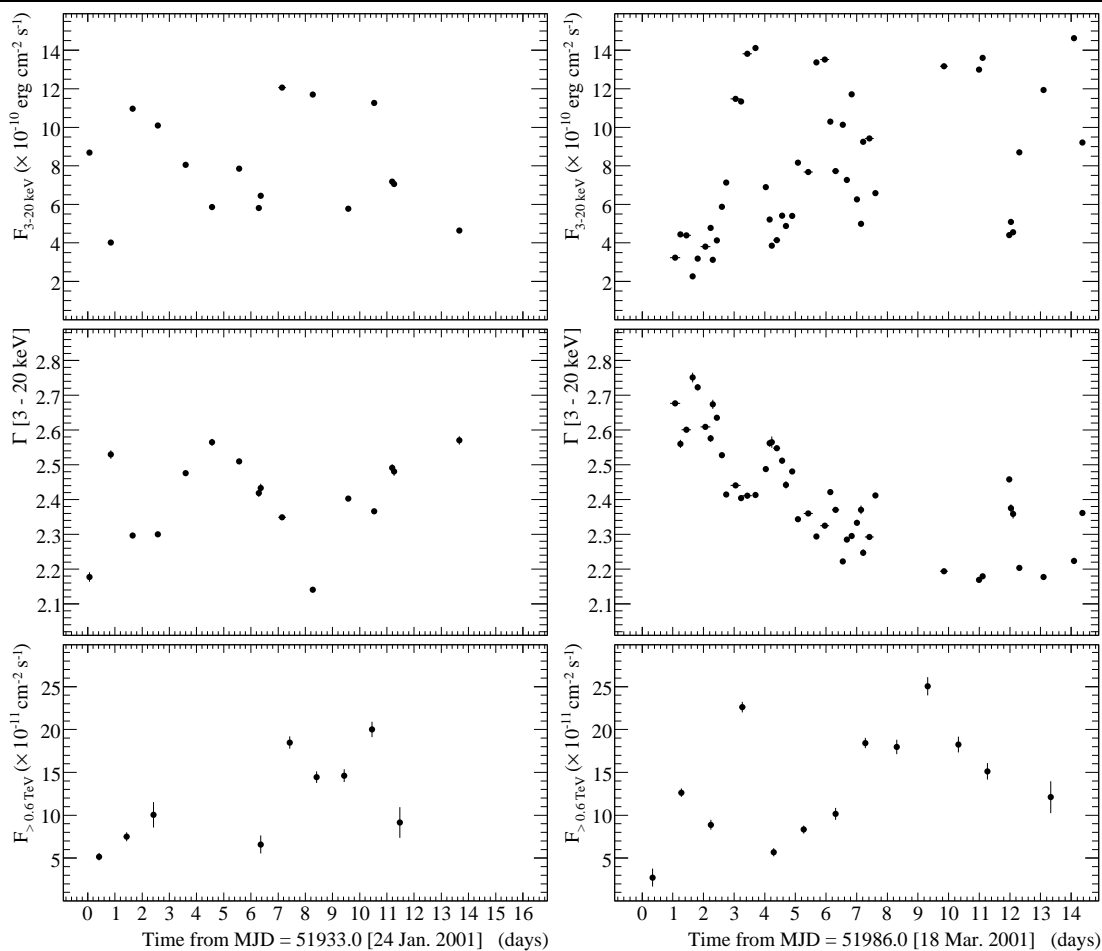


Figure 6.6: *RXTE* PCA and Whipple 10 m light curve of Mrk 421. (Left panels) show the ObsID 50190 (a) observations during 24 Jan. to 4 Feb. 2001. (Right panels) show the ObsID 60145 (b) observations during 18 Mar. to 1 Apr. 2001. (Top panels) the *RXTE* PCA 3–20 keV integral flux, (middle panels) the *RXTE* PCA power law photon index Γ , and (bottom panels) the Whipple 10 m integral flux $F_{>0.6\text{TeV}}$ in nightly exposures.

6.3.2 Mrk 421 in a High Flux State from 24 Jan. to 4 Feb. 2001

As presented in section 5.2.1, *RXTE* ASM and the Whipple 10 m observed Mrk 421 at an elevated flux level beginning in January 2001. In response, *RXTE* PCA observations (ObsID: 50190 a) were triggered on 24 January 2001 during the rising edge of the long-term flare (see figure 6.1). No previous publications could be found for the *RXTE* PCA and Whipple 10 m data during this period. Figure 6.6 shows on the top left the *RXTE* PCA 3–20 keV integral flux light curve derived from an absorbed power law fit to the energy spectra. The 1σ error bars on the integral flux measurements are in most cases hidden by the data point. The power law photon index Γ for each *RXTE* PCA pointing is shown below in the middle left panel. Strong X-ray flux and spectral variability was

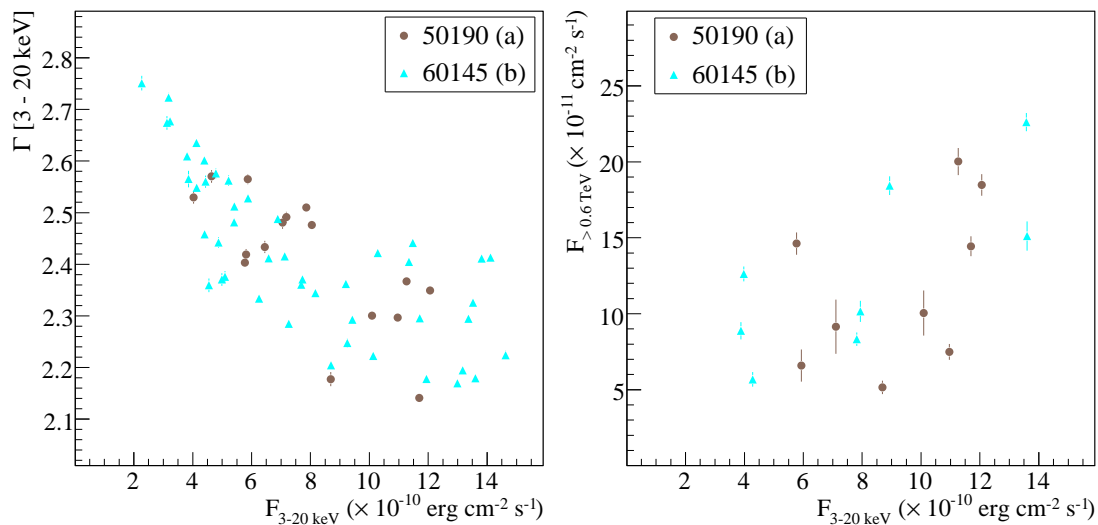


Figure 6.7: X-ray and TeV γ -ray correlation plots for Mrk 421 observations in Jan. and Mar. to Apr. 2001 (light curves in figure 6.6). Shown (left) is the *RXTE* PCA photon index Γ versus the 3–20 keV integral flux. (Right) is the Whipple 10 m integral flux $F_{>0.6\text{TeV}}$ versus the *RXTE* PCA 3–20 keV integral flux from observations taken within 5 hours of the Whipple 10 m nightly exposures.

observed over the 12 day period. Due to the sparse data sampling of typically < 1 hour per night, the shortest flaring timescale in this data set is not easily identified. A “baseline” flux of $F_{3-20\text{keV}} = (4.02 \pm 0.02) \cdot 10^{-10} \text{ erg cm}^{-2} \text{ s}^{-1}$ was observed on 24 Jan. 2001 (MJD = 51933.8), rising to an integral flux of $F_{3-20\text{keV}} = (11.0 \pm 0.02) \cdot 10^{-10} \text{ erg cm}^{-2}$ on the following night (MJD = 51934.6). Similar flux variability is seen between 4 other pairs of nightly observations. During the full observing period, the 3–20 keV power law photon index was seen to vary from 2.14 ± 0.01 to 2.57 ± 0.01 . Figure 6.7 (left) shows the *RXTE* PCA power law photon index Γ versus the 3–20 keV integral flux. A large scatter is shown, with a very poor χ_r^2 to a linear fit, however a general trend of a harder spectrum at higher flux states is shown. The near simultaneous Whipple 10 m integral flux $F_{>0.6\text{TeV}}$ in nightly exposures are shown on the bottom left of figure 6.6. Large amplitude flux variability is evident, with flux doubling seen between two nights. The TeV γ -ray flux was higher than the Crab nebula flux on all nights, ranging from $F_{>0.6\text{TeV}} = (5.15 \pm 0.43) \cdot 10^{-11} \text{ cm}^{-2} \text{ s}^{-1}$ to $F_{>0.6\text{TeV}} = (20.0 \pm 0.90) \cdot 10^{-11} \text{ cm}^{-2} \text{ s}^{-1}$. Figure 6.7 (right) shows the X-ray integral flux $F_{3-20\text{keV}}$ versus the Whipple 10 m integral flux for data taken within a coincidence window of 10 hours. A weak linear correlation coefficient of $r = 0.51$ is shown between the X-ray and TeV γ -ray flux (see section 5.2.2 for the r calculation). By visual inspection of figure 6.6, the tracking of flux states between unresolved flaring episodes is not clear.

6.3.3 Further High State Flaring in Mrk 421 from 18 Mar. to 1 Apr. 2001

Further observations of Mrk 421 during the long-term January to May flaring state were conducted with *RXTE* PCA from 18 Mar. to 1 Apr. 2001 (ObsID: 60145 b). Within this period, a nearly continuous coverage of *RXTE* PCA observations was taken from 19–26 March, with gaps of ~ 1 hour between pointings. Figure 6.6 (top right) show the X-ray integral flux light curve, with the power law photon index from each observation shown below. Two high amplitude X-ray flares were well resolved. In the first flare, the 3–20 keV integral flux was seen to rise steadily from 20 March (MJD = 51988.3) at a flux of $F_{3-20\text{keV}} = (3.13 \pm 0.02) \cdot 10^{-10} \text{ erg cm}^{-2} \text{ s}^{-1}$ to a peak on 21 March (MJD = 51989.7) with a flux of $F_{3-20\text{keV}} = (14.1 \pm 0.02) \cdot 10^{-10} \text{ erg cm}^{-2} \text{ s}^{-1}$. The integral flux then decayed to a flux level near the onset of the flare on 22 March (MJD = 51990.2). A second large flare followed within ~ 10 hours of the first flare, and showed a similar relative rise by a factor of 2.6 in integral flux. The estimated duration of the two resolved flares were 1.9 and 1.7 days, which is within the range of characteristic X-ray flaring timescales of ~ 1 –2 days found by a previous detailed temporal study of Mrk 421 in (Kataoka et al. 2001). Figure 6.6 (bottom right) shows the Whipple 10 m nightly integral flux light curve of Mrk 421 during the *RXTE* PCA campaign (ObsID: 60145 b) from 18 Mar. to 1 Apr. 2001. Strong variability is shown over a range in integral flux of $F_{>0.6\text{TeV}} = (2.72 \pm 1.05) \cdot 10^{-11} \text{ cm}^{-2} \text{ s}^{-1}$ to $F_{>0.6\text{TeV}} = (25.0 \pm 1.07) \cdot 10^{-11} \text{ cm}^{-2} \text{ s}^{-1}$. Figure 6.7 (right) show the Whipple 10 m integral flux versus *RXTE* PCA 3–20 keV flux for data simultaneous to within 5 hours over the 18 Mar. to 1 Apr. 2001 observing period. No clear correlation is evident. The sparse data sampling in this flare inhibits a detailed study of possible lags between the X-ray and TeV γ -ray light curves. In the Synchrotron Self-Compton (SSC) model, a time lag of the TeV γ -ray (Inverse Compton) emission is expected relative to the X-ray (Synchrotron) radiation when the electrons producing the Synchrotron radiation are at a lower energy than the electron population responsible for the TeV γ -ray emission (Krawczynski et al. 2000). When the seed photons to IC emission are external to the jet, than no lag is expected.

Simultaneous X-ray and TeV Spectral Variability in Mrk 421 during Mar. 2001

The X-ray spectral variability during the first large flare tracked the integral flux closely, with a clear hardening of the spectrum during the rising component. The X-ray spectrum then softened after the first flare peak on 21 March, but interestingly, over a 7 day period from 20–26 March a general trend was seen of the power law photon index hardening on a much long timescale than the flux variability. The correlation of *RXTE* PCA power law photon index to integral flux is shown in figure 6.7. A recent publication on this *RXTE* PCA campaign (ObsID: 60145 b) studied the short-term flux and spectral variability using a similar approach to the systematic study in this

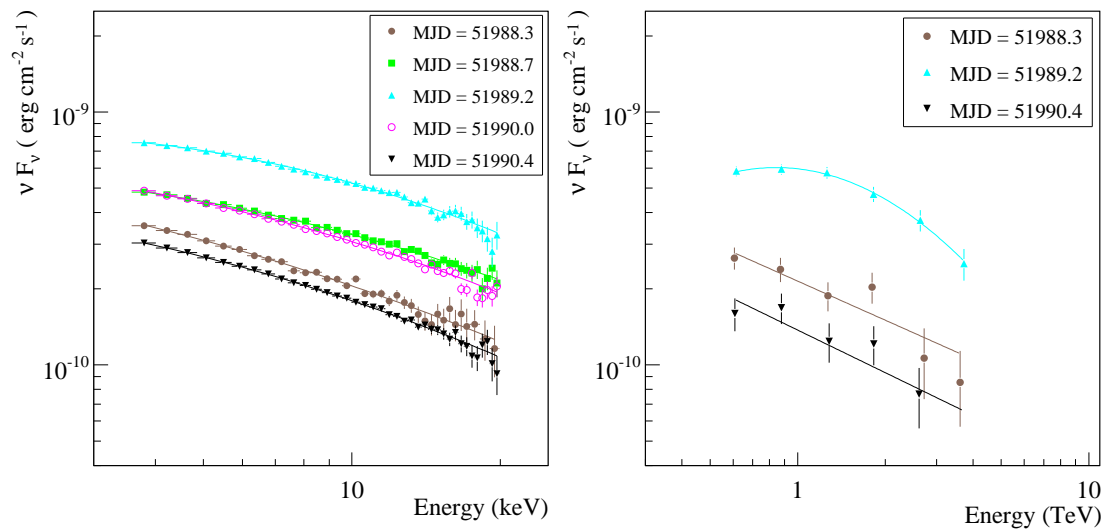


Figure 6.8: Simultaneous *RXTE* PCA and Whipple 10 m energy spectra of Mrk 421 from 20–22 Mar. 2001 (MJD = 51988–51990). (Left) *RXTE* PCA spectra from 3–20 keV. The 3 spectra with the highest integral flux were fit by a log-parabolic model, while the lower flux data was fit by a power law. For both models a fixed galactic absorption $N_{\text{H,Gal}} = 1.61 \cdot 10^{20} \text{ cm}^{-2}$ was used. (Right) Estimated intrinsic TeV γ -ray spectrum from nightly Whipple 10 m observations after correcting for absorption by the EBL using the “Low-SFR” model in (Kneiske et al. 2004). For the highest flux observation, a log-parabolic was fit to the energy spectrum, while the two lower flux spectra were fit by a power law model.

work (Giebels et al. 2007). The authors report a saturation of the photon index at high fluxes using a more complicated broken power law model. To test for spectral curvature and a possible shift in the peak synchrotron emission to energies at high flux levels to near the 3 keV lower energy limit of *RXTE* PCA, the fit results from log-parabolic model were considered. For the peak flux observation on 21 March (MJD = 51989.7) the log-parabolic fit yielded a χ_r^2 of 1.6 and curvature term $b = 0.37 \pm 0.01$. The derived synchrotron peak energy was $E_p = 2.14 \pm 0.19 \text{ keV}$. As discussed in section 6.4, the derived peak position from a log-parabolic model has large systematic errors when calculated from a limited energy range outside of the peak position, and so a detailed study of the spectral curvature and derived peak position using *RXTE* PCA was not pursued. Instead, the possibility of correlated spectral variability is investigated between the simultaneous X-ray and TeV γ -ray observations during the the flare from 20–22 Mar. 2001. The Whipple 10 m energy spectrum was measured for the three consecutive nights. Corrections for absorption by the extragalactic background light (EBL) were applied to the spectra, as discussed in section 5.3.2. Figure 6.8 shows the simultaneous *RXTE* PCA and Whipple 10 m energy spectra of

Mrk 421 from 20–22 Mar. 2001 (MJD = 51988–51990). The high flux X-ray spectrum show clear curvature, with poor χ_r^2 values to the power law fit, so the log-parabolic model fits are shown. For the two low flux *RXTE* PCA observations, the spectra were well fit by the power law model. The estimated intrinsic TeV γ -ray spectrum for the two low flux nights resulted in power law photon indices of $\Gamma = 2.51 \pm 0.10$ and $\Gamma = 2.56 \pm 0.13$, respectively. The X-ray power law photon indices for these observations were $\Gamma = 2.67 \pm 0.01$ and $\Gamma = 2.41 \pm 0.01$, respectively. The Whipple 10 m observations on the night of 21 Mar. 2001 (MJD = 51988.3) were during the peak in resolved X-ray flare. Strong curvature is shown in the intrinsic TeV γ -ray spectrum on this night, with a fit to a power law resulting in a χ_r^2 of 4.79. A log-parabolic fit described the data well. The peak energy in the intrinsic TeV γ -ray spectrum was calculated from the log-parabolic fit at $E_p = 0.85 \pm 0.22$ TeV. The X-ray spectrum on Mar. 2001 (MJD = 51988.3) was described above, with a peak energy of 2.14 ± 0.19 keV. The lack of intermediate flux levels observed by the Whipple 10 m over this flare did not allow for a detailed study of TeV γ -ray spectral evolution during the flare. In summary, the joint *RXTE* PCA and Whipple 10 m campaign in March 2001 caught Mrk 421 in strong flaring state. It is also useful to compare the X-ray and TeV variability in a low to medium flux state, as shown below for data in 2002 and 2003.

6.3.4 Variability of Mrk 421 in a Low to Medium Flux State in Dec. 2002 and Jan. 2003

In November 2002, Whipple 10 m observations of Mrk 421 recorded a rate a factor of ~ 3 above the expected Crab nebula rate, which together with a high *RXTE* ASM rate, lead to triggered *RXTE* PCA observations during 3–16 Dec. 2002 (ObsID: 70161 c), with follow up observations in 10–14 Jan. 2003 (ObsID: 70161 d). Figure 6.9 shows the light curve of *RXTE* PCA integral flux, *RXTE* PCA power law photon index Γ , and nightly Whipple 10 m integral fluxes above 0.6 TeV. During the first observing period in Dec. 2002, the X-ray flux of Mrk 421 was at a baseline flux of $F_{3-20\text{keV}} < 1.5 \cdot 10^{-10}$ erg cm $^{-2}$ s $^{-1}$, which is over a factor of ~ 2 lower than the estimated baseline X-ray flux in January and March 2001. The Whipple 10 m integral flux over this period remained below the flux level of the Crab nebula, and a fit to constant flux yielded a χ_r^2 of 2.12, showing marginal variability, primarily in the higher flux recorded on the last night of the campaign (16 Dec. 2002). The 10–14 Jan. 2003 observing campaign showed an increased flux level on 12 Jan. in both the X-ray and TeV γ -ray integral fluxes. Figure 6.10 shows for both observing periods in Dec. 2002 and Jan. 2003 the *RXTE* PCA photon index Γ versus the 3–20 keV integral flux on the left, and on the right the Whipple 10 m integral flux $F_{>0.6\text{TeV}}$ versus *RXTE* PCA 3–20 keV integral flux for observations simultaneous to within 5 hours. A relatively strong linear correlation coefficient

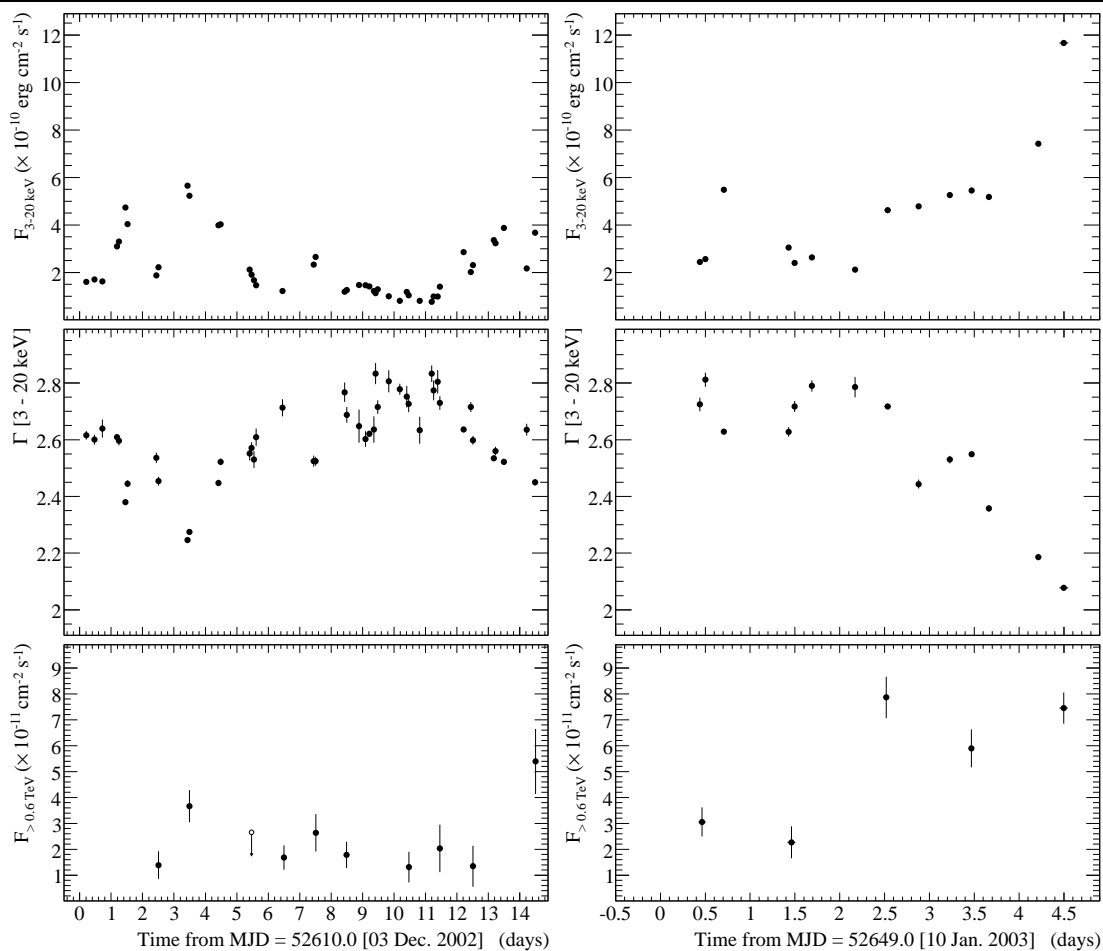


Figure 6.9: *RXTE* PCA and Whipple 10 m light curve of Mrk 421. (Left panels) show the ObsID 70161 (c) observations during 3–16 Dec. 2002. (Right panels) show the ObsID 70161 (d) observations during 10–14 Jan. 2003. (Top panels) the *RXTE* PCA 3–20 keV integral flux, (middle panels) the *RXTE* PCA power law photon index Γ , and (bottom panels) the Whipple 10 m integral flux $F_{>0.6\text{TeV}}$ in nightly exposures.

of $r = 0.91$ was calculated between the X-ray and γ -ray fluxes for the observations in Dec. 2002. The strongest variability was observed during the apparent rising edge of a large flare during 13–14 Jan. 2003. The TeV γ -ray spectrum was measured on both of these nights, and the intrinsic spectrum calculated following the method described in section 5.3.2. Figure 6.11 shows the *RXTE* PCA and Whipple 10 m energy spectra from 13–14 Jan. 2003. The X-ray spectrum shows a clear hardening at MJD = 52652.6, while at a slightly lower integral flux than the spectra 5.1 hours earlier. Evidence is shown of the flare originating at X-ray energies above 5 keV, with the rising component of the flare showing an increasingly hard spectrum, up to the the highest observed flux level (MJD = 52652.4) with a power law photon index of $\Gamma = 2.077 \pm 0.003$. The log-parabolic fit

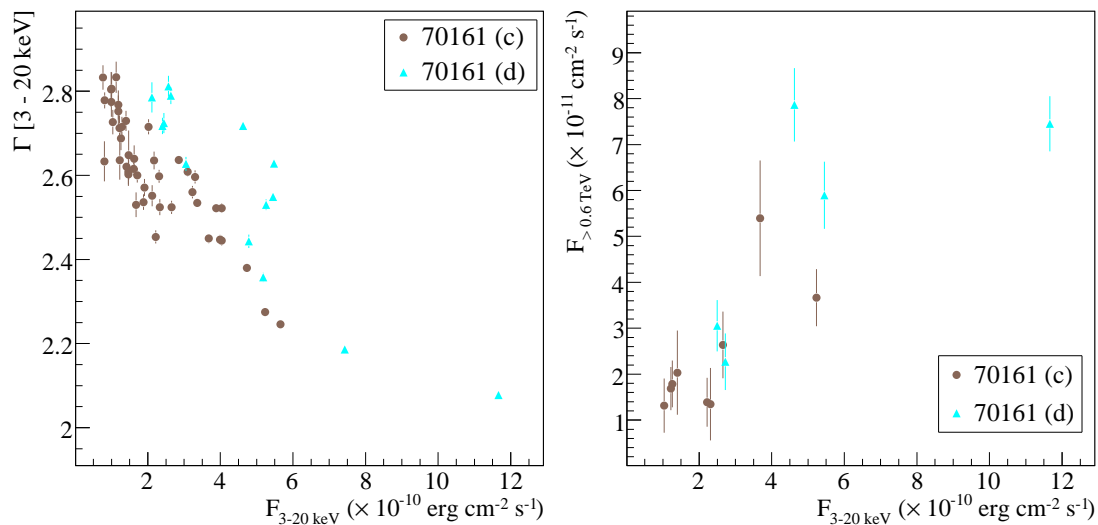


Figure 6.10: X-ray and TeV γ -ray correlation plots for Mrk 421 observations in Dec. 2002 and Jan. 2003 (light curves in figure 6.9). Shown (left) is the *RXTE* PCA photon index Γ versus the 3–20 keV integral flux. (Right) is the Whipple 10 m integral flux $F_{>0.6\text{TeV}}$ versus the *RXTE* PCA 3–20 keV integral flux from observations taken within 5 hours of the Whipple 10 m nightly exposure.

to the high flux energy spectrum yielded a much improved χ_r^2 of 1.22 compared to the χ_r^2 of 7.05 for the power law fit. Using the log-parabolic model, the synchrotron peak energy was estimated at $E_p = 4.73 \pm 0.56$ keV. The intrinsic TeV γ -ray spectra showed hardening with increased flux between the two nights. For the first night (MJD = 52652.4), a power law fit gave a photon index $\Gamma = 2.56 \pm 0.13$, while for the second night the best photon index was $\Gamma = 2.42 \pm 0.13$. The Whipple 10 m and *RXTE* PCA data for the total observing periods in Dec. 2002 and Jan. 2003 was previously published in (Rebillot et al. 2006). The authors detailed the X-ray spectral variability seen here, with very comparable results. In the previous analysis of Whipple 10 m data, the light curve was calculated by scaling the detection rate and normalizing to the rate observed for the Crab nebula during contemporaneous observations. This approach assumes the TeV γ -ray energy spectrum remains near the power law type spectrum of the Crab nebula. The integral flux values presented in this work were not biased in this way.

6.3.5 Two Month Study of Mrk 421 in a Low Flux State from Feb. to May 2003

RXTE PCA observations on Mrk 421 were scheduled for a period of over 2 months from 20 Feb. to 4 May 2003 (ObsID: 80173 e) to coincide with Whipple 10 m observations regardless of flux state. Figure 6.12 shows the light curve of *RXTE* PCA integral flux, *RXTE* PCA power law

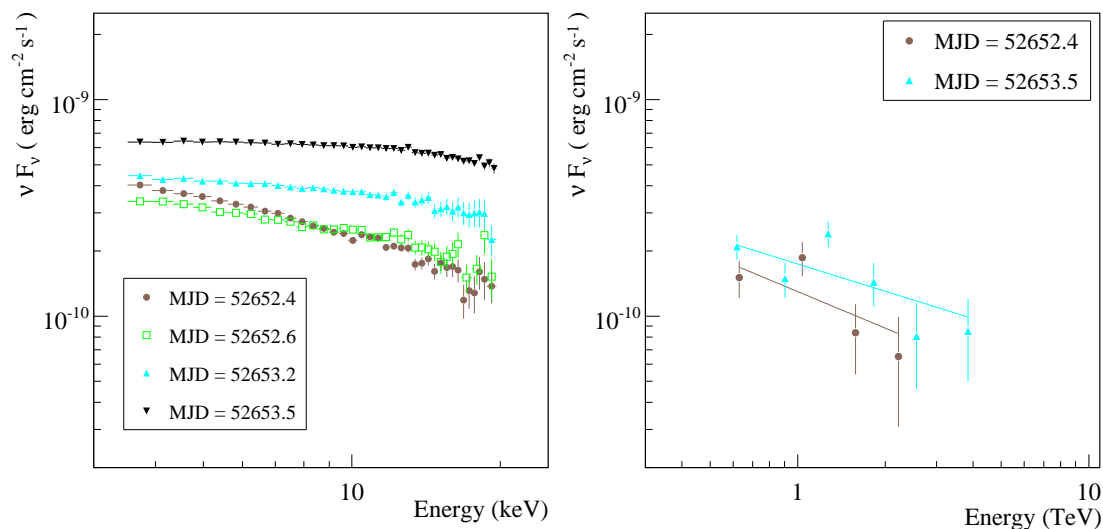


Figure 6.11: Simultaneous *RXTE* PCA and Whipple 10 m energy spectra of Mrk 421 from 13–14 Jan. 2003 (MJD = 52652–52653). (Left) *RXTE* PCA spectra from 3–20 keV. The spectra were fit by a log-parabolic model using a fixed galactic absorption $N_{\text{H,Gal}} = 1.61 \cdot 10^{20} \text{ cm}^{-2}$. (Right) Estimated intrinsic TeV γ -ray spectrum from nightly Whipple 10 m observations after correcting for absorption by the EBL using the “Low-SFR” model in (Kneiske et al. 2004). The intrinsic spectra were best fit by a power law model.

photon index Γ , and nightly Whipple 10 m integral fluxes above 0.6 TeV. A relatively small scale, but well resolved X-ray flare was observed in Feb. 2003 during a period when no Whipple 10 m observations passed data quality cuts due to poor weather. From 27–31 Mar. 2003 another well resolved flare was observed by *RXTE* PCA. The power law photon index tracked the 3–20 keV integral flux, hardening from $\Gamma = 2.38 \pm 0.01$ at a flux level of $F_{3-20\text{keV}} = (3.34 \pm 0.02) \cdot 10^{-10} \text{ erg cm}^{-2} \text{ s}^{-1}$ to $\Gamma = 2.11 \pm 0.01$ at the flare maximum of $F_{3-20\text{keV}} = (7.22 \pm 0.02) \cdot 10^{-10} \text{ erg cm}^{-2} \text{ s}^{-1}$. The Whipple 10 m data set is sparse during this X-ray flare, and no clear flare structure could be seen. For the remainder of the observing period in Apr. to May 2003 the X-ray and TeV fluxes were in a low flux state. A fit to a constant flux gives a baseline X-ray flux from of $F_{3-20\text{keV}} = (1.19 \pm 01) \cdot 10^{-10} \text{ erg cm}^{-2} \text{ s}^{-1}$, and for the TeV γ -ray data of $F_{>0.6\text{TeV}} = (2.02 \pm 0.15) \cdot 10^{-11} \text{ cm}^{-2} \text{ s}^{-1}$. Figure 6.13 (left) shows the *RXTE* PCA photon index Γ versus the 3–20 keV integral flux, and on the right the Whipple 10 m integral flux $F_{>0.6\text{TeV}}$ versus *RXTE* PCA 3–20 keV integral flux for observations simultaneous to within 1 hours. A linear fit to the *RXTE* PCA flux versus Whipple 10 m integral flux distribution yielded a good χ_r^2 of 0.76. The Feb. to May 2003 data set of *RXTE* PCA and Whipple 10 m observations was previously published in (Blazejowski et al. 2005). The X-ray integral fluxes and photon index for each observations were not presented

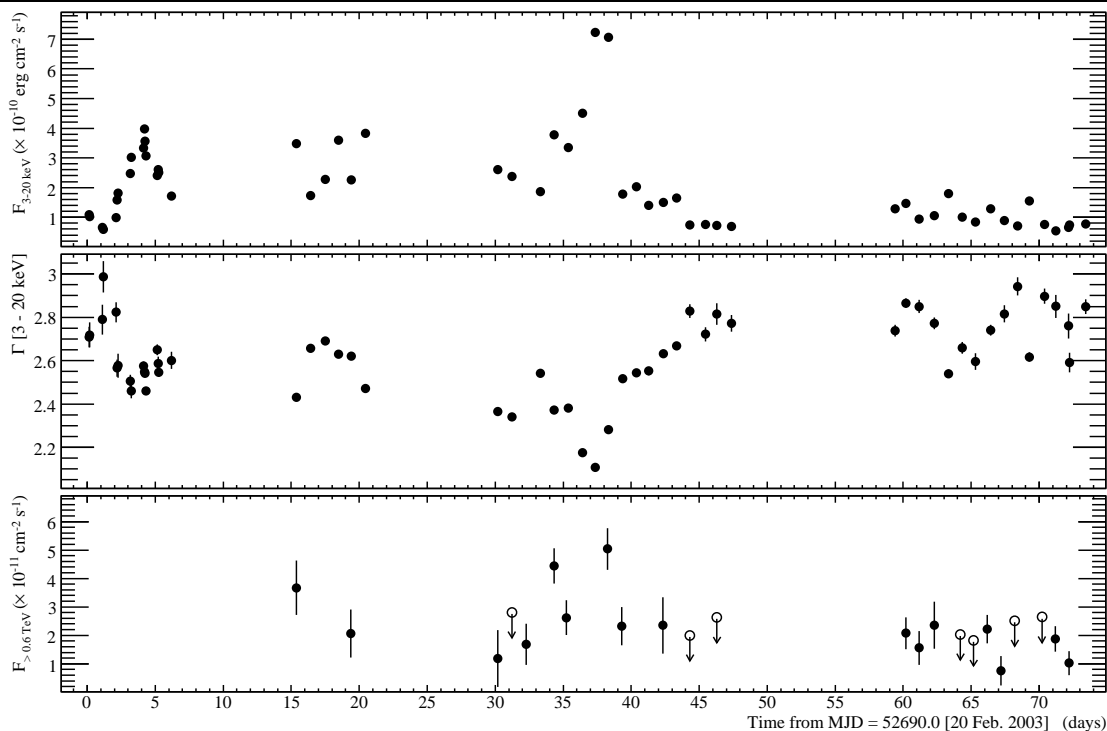


Figure 6.12: *RXTE* PCA and Whipple 10 m light curve on Mrk 421 from 20 Feb. to 4 May 2003 (ObsID 80173 (e) in table 6.1). Shown (top panel) is the *RXTE* PCA 3–20 keV integral flux, (middle panel) the power law photon index Γ over their energy band 3–20 keV, and (bottom panel) the Whipple 10 m integral flux $F_{>0.6\text{TeV}}$ in nightly exposures. A 99.9% confidence upper limit was calculated for Whipple 10 m observations at a detection level $< 2\sigma$ (shown by an open circle).

in the paper, with only the *RXTE* PCA counting rate discussed. The Whipple 10 m rate was given in the paper, which was referenced to the detection rate on the Crab in 2003. Presented below are *RXTE* PCA and Whipple 10 m observations over 6 months from Dec. 2003 to May 2004 at a higher flux state than in earlier 2003.

6.3.6 Strong Variability in Mrk 421 over 6 Months from Dec. 2003 to May 2004

The *RXTE* PCA nightly monitoring campaign of Mrk 421 in 2003 of a period of a few months was renewed over a longer period from 21 Dec. 2003 to 21 May 2004 (ObsIDs: 80173 g, 90148 h, and 90138 i). As in 2003, the *RXTE* PCA pointings were scheduled during the Whipple 10 m observing windows, with ~ 10 – 15 day gaps when no Whipple 10 m could be taken because the moon was above the horizon (see section 3.2.5) Figure 6.14 shows the Mrk 421 light curve from 21 Dec. 2003 to 21 May 2004 calculated from *RXTE* PCA integral fluxes, *RXTE* PCA power law photon indices Γ , and nightly Whipple 10 m integral fluxes above 0.6 TeV. For the first 3 months

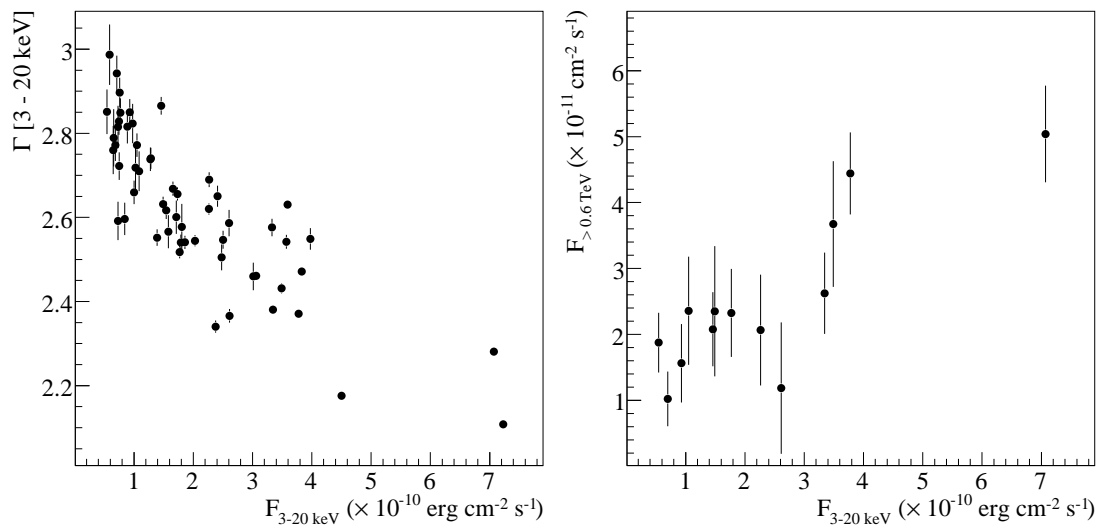


Figure 6.13: X-ray and TeV γ -ray correlation plots for Mrk 421 observations during 20 Feb. to 4 May 2003 (light curve in figure 6.12). Shown (left) is the *RXTE* PCA photon index Γ versus the 3–20 keV integral flux. (Right) is the Whipple 10 m integral flux $F_{>0.6\text{TeV}}$ versus the *RXTE* PCA 3–20 keV integral flux from observations taken within 1 hours of the Whipple 10 m nightly exposure.

of the observing period period the Whipple 10 m data sampling is very sparse, due mainly to poor weather conditions. Four small X-ray flares were observed during this period from Dec. 2003 to Feb. 2004. Starting on 15 Mar. 2004 a rapid decay in flux from a partially resolved was observed in both the X-ray and TeV γ -ray bands. The relative amplitude of the flux decrease between the nights 15–16 Mar. 2004 was a factor of 2.11 ± 0.04 in *RXTE* PCA 3–20 keV integral flux, while a decay in Whipple 10 m integral flux above 0.6 TeV was observed for the following nights of 16–17 Mar. 2004 at a relative factor of 2.03 ± 0.16 . Due to the sparse data sampling it is not clear whether a lag in the TeV γ -ray emission behind correlated X-ray emission was observed, or if shorter timescale variability is at work. In April 2004 a clear month timescale shift to a higher baseline integral flux at both X-ray and TeV γ -rays was observed. The X-ray power law photon index remained, on average, in a harder state in Apr. 2004 than from Dec. 2003 to Mar. 2004. Previous claims were made for a positive lag of TeV γ -ray emission leading the X-ray emission in Apr. 2004 by ~ 1 day (Blazejowski et al. 2005). The authors are careful point out the spurious nature temporal studies using sparse detection rates, which added further uncertainty to their analysis due to their lack of spectral information. A general conclusion was reached that many counter examples were present in the Apr. 2004 data set for the hypothesis of correlated X-ray and γ -ray flux states on day timescales. Correlations between the both the X-ray and TeV γ -ray flux

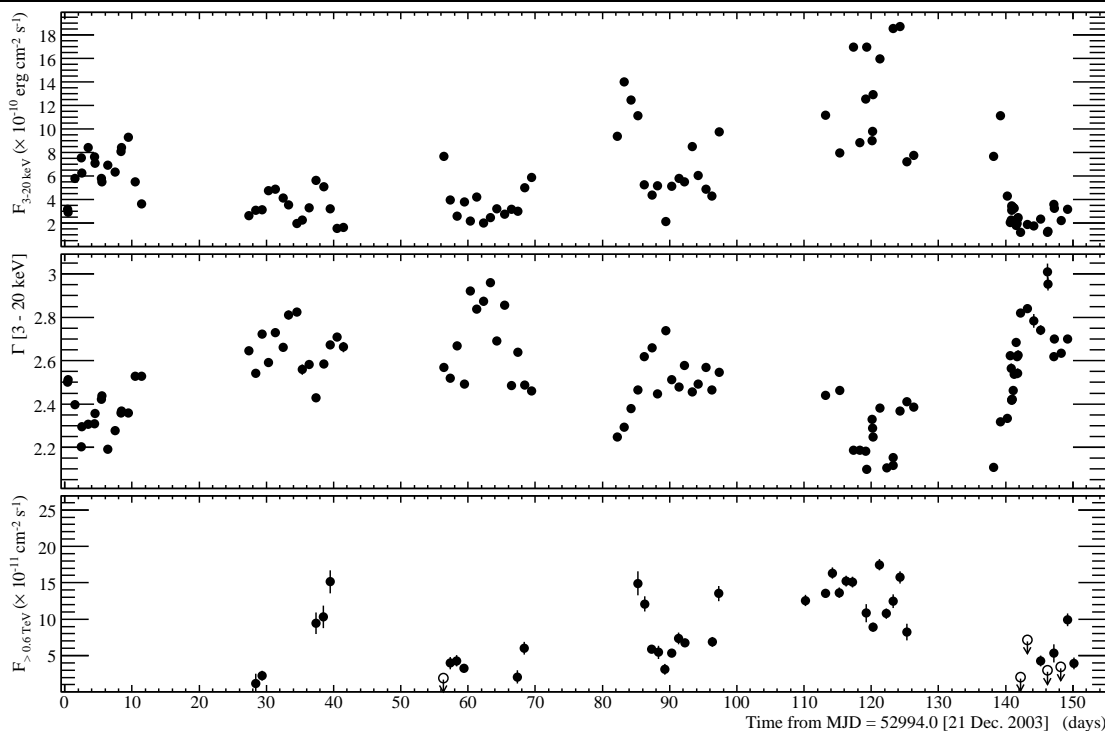


Figure 6.14: *RXTE* PCA and Whipple 10 m light curve on Mrk 421 from 21 Dec. 2003 to 21 May 2004 (ObsID: 80173 g, 90148 h, and 90138 i in table 6.1). Shown (top panel) is the *RXTE* PCA 3–20 keV integral flux, (middle panel) the power law photon index Γ over their energy band 3–20 keV, and (bottom panel) the Whipple 10 m integral flux $F_{>0.6\text{TeV}}$ in nightly exposures. A 99.9% confidence upper limit was calculated for Whipple 10 m observations at a detection level $< 2\sigma$ (shown by an open circle).

and spectral variability are studied here. Figure 6.15 (left) shows the *RXTE* PCA photon index Γ versus the 3–20 keV integral flux, and on the right the Whipple 10 m integral flux $F_{>0.6\text{TeV}}$ versus *RXTE* PCA 3–20 keV integral flux for observations simultaneous to within 1 hours. A large spread is shown for the near simultaneous X-ray and TeV γ -ray integral fluxes over the 6 month observing period, with a linear correlation coefficient r of 0.86. To test for isolated spectral correlations between the X-ray and TeV γ -ray bands during flaring events, the near simultaneous *RXTE* PCA and Whipple 10 energy spectra were calculated at near the peak X-ray flux from 19–21 Apr. 2004 (MJD = 53114–53116). Figure 6.19 (left) shows the *RXTE* PCA energy spectra from 3–20 keV, and (right) the near simultaneous intrinsic TeV γ -ray spectra for the nights 19–21 Apr. 2004 calculated from the Whipple 10 m energy spectra after correcting for a low level of absorption by the EBL (Kneiske et al. 2004). Interesting flux and spectral behavior is seen between the X-ray TeV γ -ray spectra. As shown in figure 6.11 for the X-ray flare in Jan. 2003, the

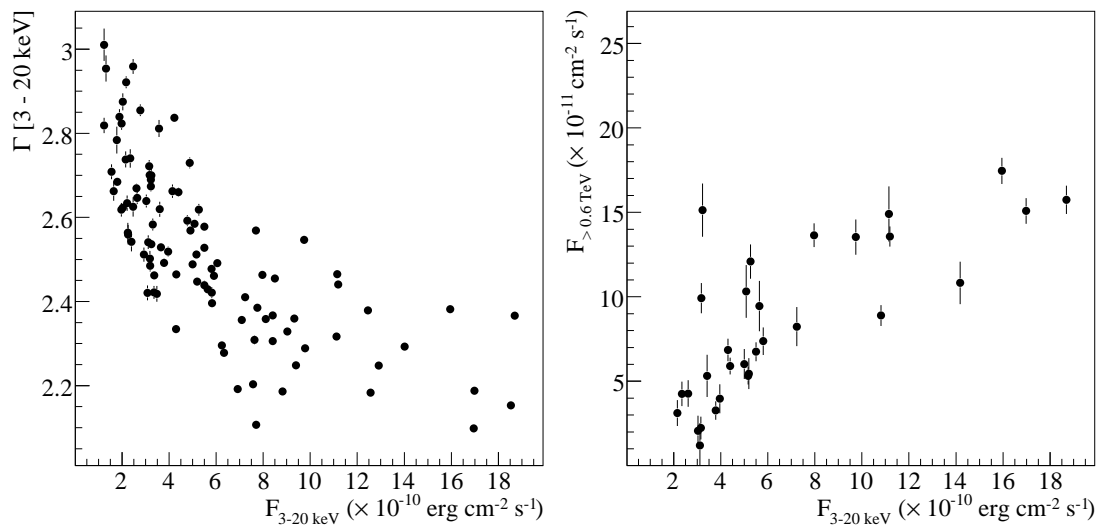


Figure 6.15: X-ray and TeV γ -ray correlation plots for Mrk 421 observations from Dec.2003 to May 2004 (light curve in figure 6.14). Shown (left) is the *RXTE* PCA photon index Γ versus the 3–20 keV integral flux. (Right) is the Whipple 10 m integral flux $F_{>0.6\text{TeV}}$ versus the *RXTE* PCA 3–20 keV integral flux from observations taken within 1 hours of the Whipple 10 m nightly exposure.

RXTE PCA energy spectrum was seen to soften on 20 Apr. 2004 before increasing in integral flux. The estimated intrinsic TeV γ -ray spectrum showed a correlated softening from a power law fit with photon index $\Gamma = 2.38 \pm 0.12$ on 19 Apr. 2004 to $\Gamma = 2.53 \pm 0.08$ on 20 Apr. 2004. Both the X-ray and TeV γ -ray spectra reached a harder state in 21 Apr. than on 19 Apr. with increased flux, however the TeV γ -ray flux level was lower on 21 Apr. than 20 Apr. Using the log-parabolic model, the peak in X-ray spectrum for 21 Apr. 2004 was calculated at $E_p = 4.97 \pm 0.96$ keV. The X-ray spectral variability of Mrk 421 during this flare in Apr. 2004 was previously published, but without simultaneous TeV γ -ray spectra (Grube et al. 2005). The TeV γ -ray integral flux of Mrk 421 in Apr. 2004 was independently measured by H.E.S.S. above an energy threshold of 2 TeV (Aharonian et al. 2005b). A factor of 4.3 in H.E.S.S. integral fluxes $F_{>2\text{TeV}}$ between nights was observed in 11–21 Apr. 2004, which was shown significantly higher than the variability from a preliminary analysis of Whipple 10 m data. Using the Whipple 10 m integral fluxes $F_{>0.6\text{TeV}}$ calculated in this work, the maximum relative change in flux during this period was by a factor 1.96. This results agrees with the conclusion that higher variability was observed at a higher (> 1 TeV) energies. The nightly energy spectrum from 1 to 15 TeV by H.E.S.S. was well fit by a power law with exponential cutoff $E_c = 3.1 \pm 0.5$ TeV, which is consistent with the monthly Whipple 10 m energy spectra presented in section 5.3.2.

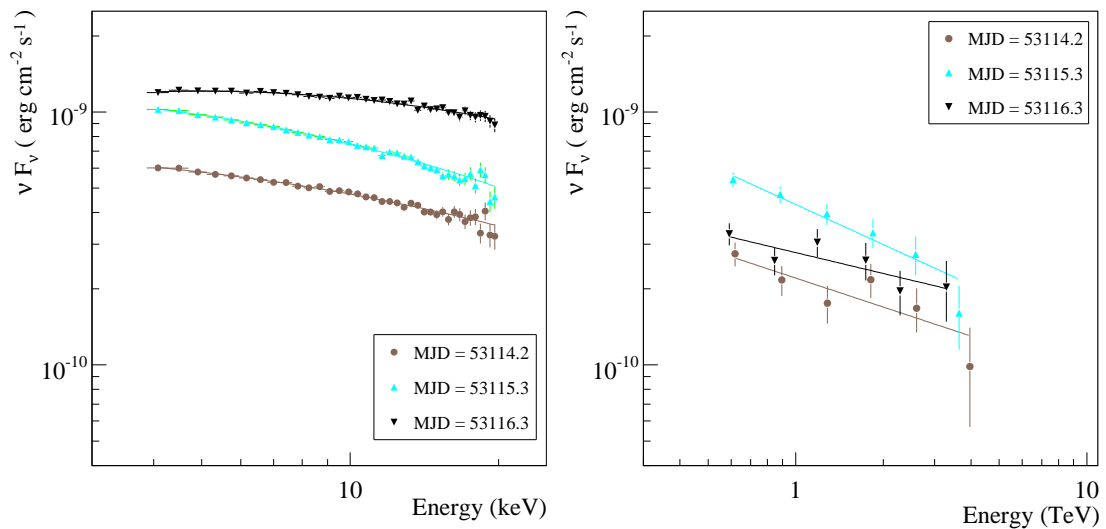


Figure 6.16: Simultaneous *RXTE* PCA and Whipple 10 m energy spectra of Mrk 421 from 19–21 Apr. 2004 (MJD = 53114–53116). (Left) *RXTE* PCA spectra from 3–20 keV. The spectra were fit by a log-parabolic model using a fixed galactic absorption $N_{\text{H,Gal}} = 1.61 \cdot 10^{20} \text{ cm}^{-2}$. (Right) Estimated intrinsic TeV γ -ray spectrum from nightly Whipple 10 m observations after correcting for absorption by the EBL using the “Low-SFR” model in (Kneiske et al. 2004). The intrinsic spectra were best fit by a power law model.

6.3.7 Further Strong Variability in Mrk 421 Over 5 Months from Jan. to May 2006

The most recent *RXTE* PCA and Whipple 10 m campaign was from 6 Jan. to 31 May 2006 (ObsIDs: 91440 k, 92402 l, and 92402 m). Similar to the 5 month campaign in 2004, *RXTE* PCA observations were scheduled to coincide nightly observations by the Whipple 10 m. Figure 6.17 shows the Mrk 421 light curve from 6 Jan. to 31 May 2006 calculated from *RXTE* PCA integral fluxes, *RXTE* PCA power law photon indices Γ , and nightly Whipple 10 m integral fluxes above 0.6 TeV. Strong flaring is evident in both the X-ray and TeV bands, however the flaring structures were not clearly resolved between nights, indicating variability on shorter timescales. By visual inspection, the X-ray and TeV γ -ray integral fluxes do not track each closely. Figure 6.18 shows (left) shows the *RXTE* PCA photon index Γ versus the 3–20 keV integral flux, and on the right the Whipple 10 m integral flux $F_{>0.6\text{TeV}}$ versus *RXTE* PCA 3–20 keV integral flux for observations simultaneous to within 1 hours. The X-ray to TeV γ -ray flux correlation plot shows a large spread ($r = 0.80$), with distinct “orphan” TeV γ -ray observations when a high TeV γ -ray integral flux was recorded simultaneously to a low X-ray flux. From 26–30 Jan. 2006, the TeV γ -ray flux state was seen to be highly variable, while the X-ray integral flux remained at nearly the same level of $F_{3-20\text{keV}} \simeq 4.3 \cdot 10^{-10} \text{ erg cm}^{-2} \text{ s}^{-1}$ before increasing flux. The X-ray and TeV γ -ray spectra

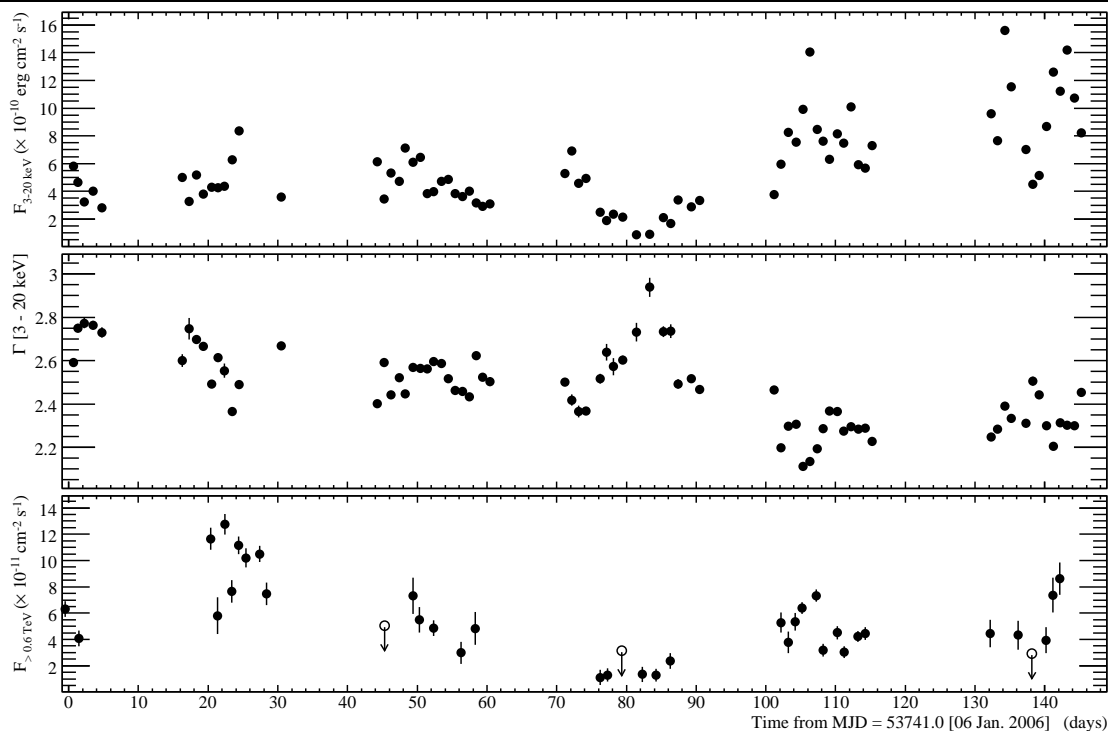


Figure 6.17: *RXTE* PCA and Whipple 10 m light curve on Mrk 421 from 6 Jan. to 31 May 2006 (ObsIDs: 91440 k, 92402 l, and 92402 m in table 6.1). Shown (top panel) is the *RXTE* PCA 3–20 keV integral flux, (middle panel) the power law photon index Γ over their energy band 3–20 keV, and (bottom panel) the Whipple 10 m integral flux $F_{>0.6\text{TeV}}$ in nightly exposures. A 99.9% confidence upper limit was calculated for Whipple 10 m observations at a detection level $< 2\sigma$ (shown by an open circle).

were investigated for the first “orphan” TeV γ -ray nightly observation on 28 Jan. 2006, and for the two following nights when the X-ray flux started to flare. Figure 6.19 shows for the nights 28–30 Jan. 2006 the *RXTE* PCA energy spectra from 3–20 keV on the left, and on the right the near simultaneous intrinsic TeV γ -ray spectra calculated from the Whipple 10 m energy spectra after correcting for a low level of absorption by the EBL (Kneiske et al. 2004). The X-ray flare shows a hardening of the energy spectrum on the first night of elevated flux level (MJD = 53763.4) similar to the spectral evolution seen in Jan. 2003 (see figure 6.11), but opposite to the softening of the X-ray spectrum during the rising flare edge in Apr. 2004, shown in figure 6.19. The TeV γ -ray spectrum was seen soften after the first night, and did not exceed the “orphan” flux level even as the X-ray flux increased over the next two nights. This flare demonstrates the complicated variability in Mrk 421 at X-ray and TeV γ -ray energies, which this thesis has tried to address through a detailed study of month long observations over 5 years.

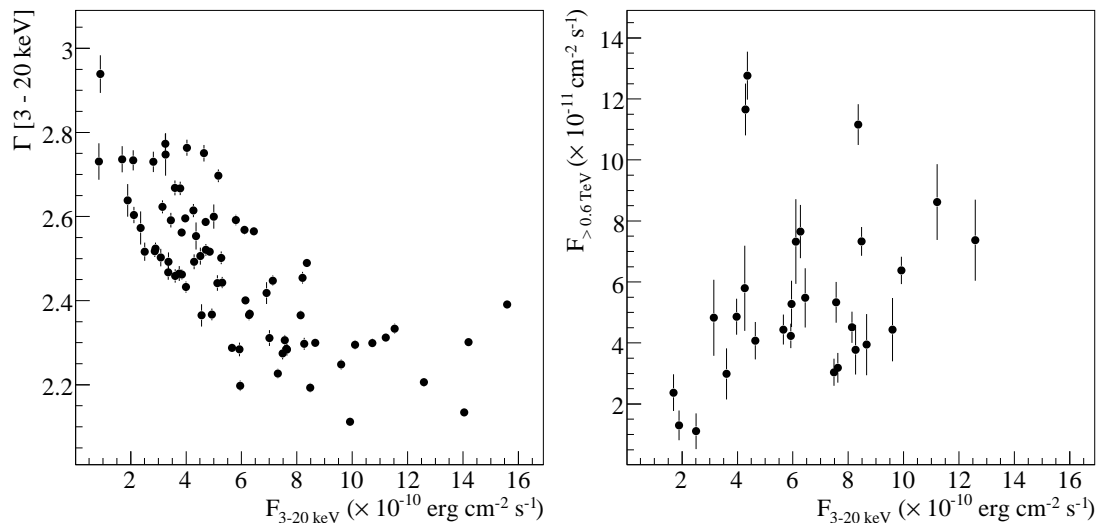


Figure 6.18: X-ray and TeV γ -ray correlation plots for Mrk 421 observations from 6 Jan. to 31 May 2006 (light curve in figure 6.17). Shown (left) is the *RXTE* PCA photon index Γ versus the 3–20 keV integral flux. (Right) is the Whipple 10 m integral flux $F_{>0.6\text{TeV}}$ versus the *RXTE* PCA 3–20 keV integral flux from observations taken within 1 hours of the Whipple 10 m nightly exposure.

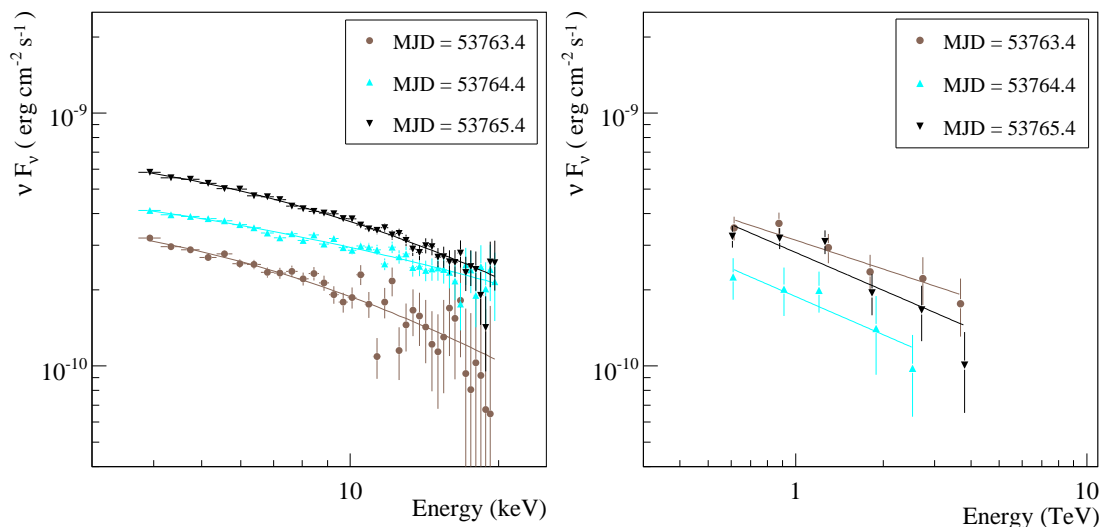


Figure 6.19: Simultaneous *RXTE* PCA and Whipple 10 m energy spectra of Mrk 421 from 28–30 Jan. 2006 (MJD = 53763–53765). (Left) *RXTE* PCA spectra from 3–20 keV. The spectra were fit by a log-parabolic model using a fixed galactic absorption $N_{\text{H,Gal}} = 1.61 \cdot 10^{20} \text{ cm}^{-2}$. (Right) Estimated intrinsic TeV γ -ray spectrum from nightly Whipple 10 m observations after correcting for absorption by the EBL using the “Low-SFR” model in (Kneiske et al. 2004). The intrinsic spectra were best fit by a power law model.

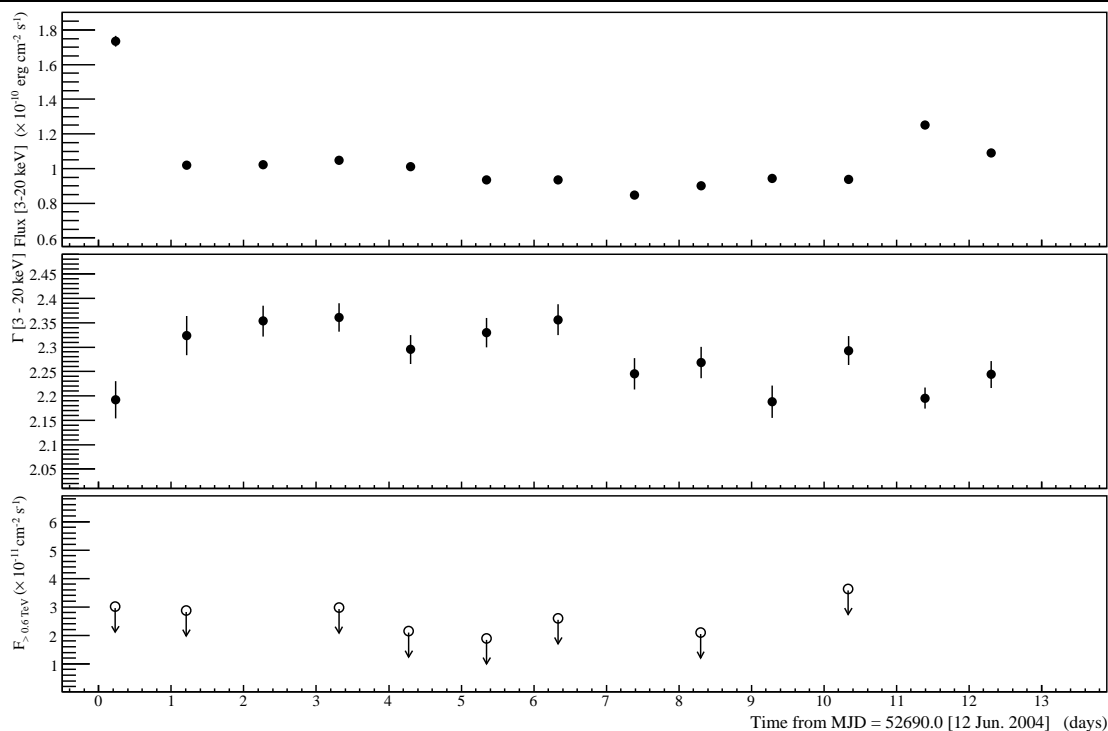


Figure 6.20: *RXTE* PCA and Whipple 10 m light curve on Mrk 501 from 12 to 24 Jun. 2004 (ObsID 91448 (a) in table 6.3). Shown (top panel) is the *RXTE* PCA 3–20 keV integral flux, (middle panel) the power law photon index Γ over the energy band 3–20 keV, and (bottom panel) the Whipple 10 m integral flux $F_{>0.6\text{TeV}}$ in nightly exposures. A 99.9% confidence upper limit was calculated for Whipple 10 m observations at a detection level $< 2 \sigma$ (shown by an open circle).

6.3.8 *RXTE* PCA and Whipple 10 m Results on Mrk 501 in June 2004

Mrk 501 was observed by *RXTE* PCA from 12 to 24 Jun. 2004 (ObsID: 91448 a). Whipple 10 m observations were taken on 8 nights during this period, by no detection above the 3σ level was observed on any of the nights. Figure 6.20 shows the *RXTE* PCA integral fluxes, *RXTE* PCA power law photon indices Γ , and 99% confidence upper limits on the nightly Whipple 10 m integral fluxes above 0.6 TeV. On the first night of 12 Jun. 2004, an elevated X-ray integral flux was recorded of $F_{3-20\text{keV}} = (1.73 \pm 0.03) \cdot 10^{-10} \text{ erg cm}^{-2} \text{ s}^{-1}$, while for the remaining 12 nights the X-ray integral flux remained nearly constant, with a mean of $F_{3-20\text{keV}} = (9.35 \pm 0.02) \cdot 10^{-10} \text{ erg cm}^{-2} \text{ s}^{-1}$. Figure 6.21 (left) shows the *RXTE* PCA photon index Γ versus the 3–20 keV integral flux. No clear trend is shown between the photon index Γ and integral flux, but due to the small range of sampled flux states, correlated variability can not be ruled out. Figure 6.21 (left) shows the *RXTE* PCA energy spectrum on the nights of 12, 22, and 23 Jun. 2004. The X-ray energy spectrum from the low flux night of 22 Jun. 2004 was well fit by a power law with photon

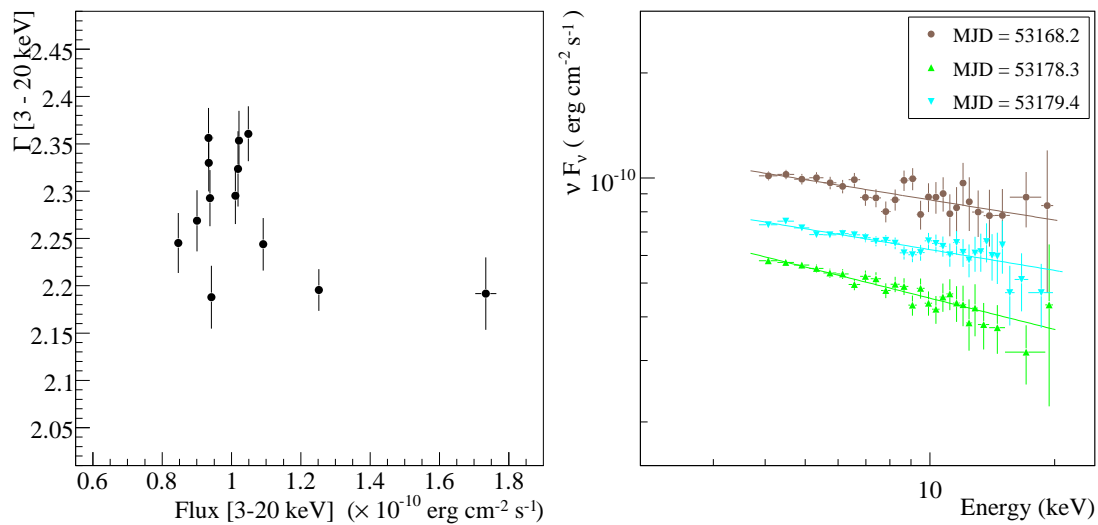


Figure 6.21: X-ray spectral properties of Mrk 501 from 12 to 24 Jun. 2004 (light curve in figure 6.20). Shown (left) is the *RXTE* PCA photon index Γ versus the 3–20 keV integral flux. (Right) is the *RXTE* PCA energy spectrum on 12, 22, and 23 Jun. 2004.

index $\Gamma = 2.29 \pm 0.03$, while the two higher flux observations had near equivalent, and slightly harder power law photon indices of $\Gamma = 2.19 \pm 0.03$ and $\Gamma = 2.19 \pm 0.02$.

6.3.9 *RXTE* PCA and Whipple 10 m Results on H1426+428 from Mar. to Jun. 2002

H1426+428 was observed by *RXTE* PCA over a period of 3 months from 7 Mar. to 15 Jun. 2002. A high coverage of simultaneous nightly observations were taken with the Whipple 10 m, however H1426+428 was not detected on any of the nights at a significance above 3σ . Figure 6.22 shows the *RXTE* PCA integral fluxes, *RXTE* PCA power law photon indices Γ , and 99% confidence upper limits on the nightly Whipple 10 m integral fluxes above 0.6 TeV. Strong X-ray variability was observed over the full 3 month period, showing complex spectral variability. X-ray integral flux doubling timescales of ~ 2 days was observed from 8–10 Mar. 2002. Figure 6.23 (left) shows the *RXTE* PCA photon index Γ versus the 3–20 keV integral flux. A large spread is observed, however weak evidence of a correlation between *RXTE* PCA integral flux and power law photon index is shown. Figure 6.23 (right) shows the *RXTE* PCA spectrum of H1426+428 from 19–21 Apr. 2004 when a large rise in integral flux was recorded. The X-ray spectrum of the three nights was very hard, ranging from $\Gamma = 1.48 \pm 0.05$ to $\Gamma = 1.54 \pm 0.04$. The spectra are well described by a power law, with no sign of curvature resolved in the *RXTE* PCA spectrum. The peak synchrotron energy is clearly above 20 keV, but the exact position is difficult to determine. This *RXTE* PCA data set was previously published in (Falcone et al. 2004). Results agreeing well with the analysis

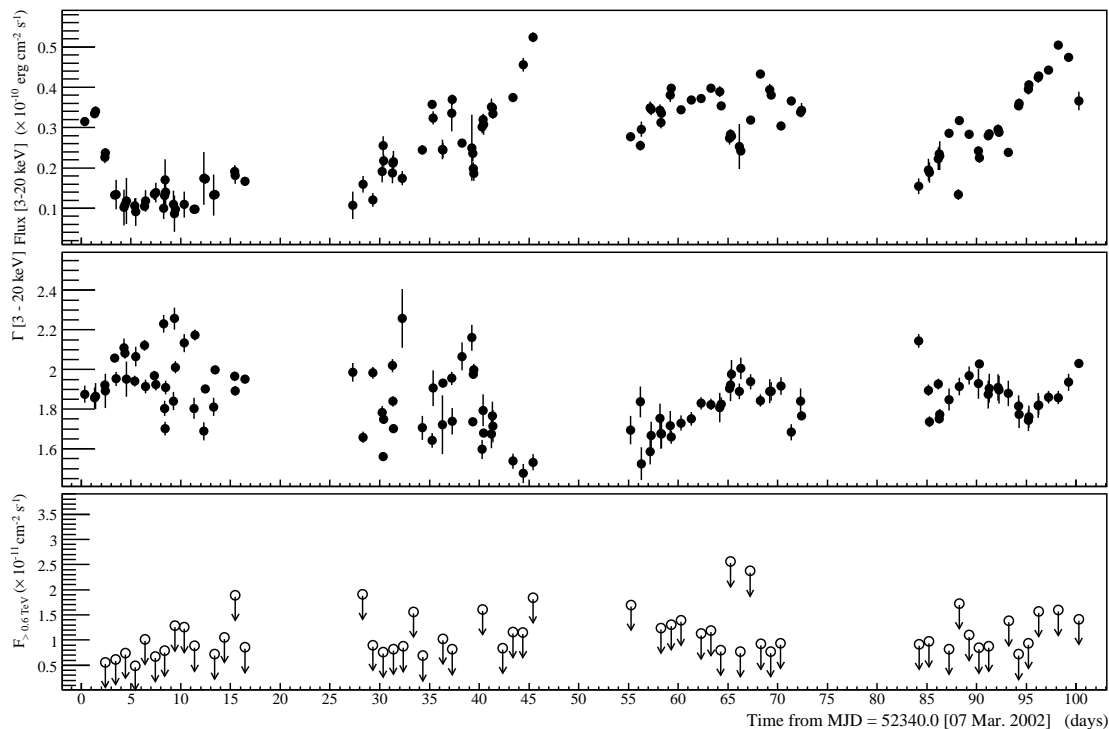


Figure 6.22: *RXTE* PCA and Whipple 10 m light curve of H1426+428 during 7 Mar. to 15 Jun. 2002 (ObsID 70154 (b) in table 6.3). Shown (top panel) is the *RXTE* PCA 3–20 keV integral flux, (middle panel) the power law photon index Γ over their energy band 3–20 keV, and (bottom panel) the Whipple 10 m integral flux $F_{>0.6\text{TeV}}$ in nightly exposures. A 99.9% confidence upper limit was calculated for Whipple 10 m observations at a detection level $< 2\sigma$ (shown by an open circle).

here were shown by the authors, who studied the spectral variability of a number of X-ray flares from this dataset in detail. The main conclusion was that spectral evolution appeared different from flare to flare, and that no characteristic variability could be determined.

6.4 XMM-Newton Spectrum of Mrk 421, Mrk 501, and H1426+428

The X-ray spectrum from 0.6–10 keV of Mrk 421, Mrk 501, and H1426+428 was determined from a set of near complete *XMM-Newton* PN observations from 2000 to 2006. The *XMM-Newton* spectra were fit by XSPEC 12 with 3 fit models following the method described in section 6.3. Figure 6.24 shows an example Mrk 421 spectrum fit to a power law or log-parabolic model, both with fixed galactic absorption $N_{\text{H,Gal}} = 1.61 \cdot 10^{20} \text{ cm}^{-2}$. The poor fit to the power law model is large χ^2 residuals at both the low and high energy ends of the spectrum. Significant variability was observed in nearly all of the Mrk 421 observations, however for simplicity the energy spectrum is

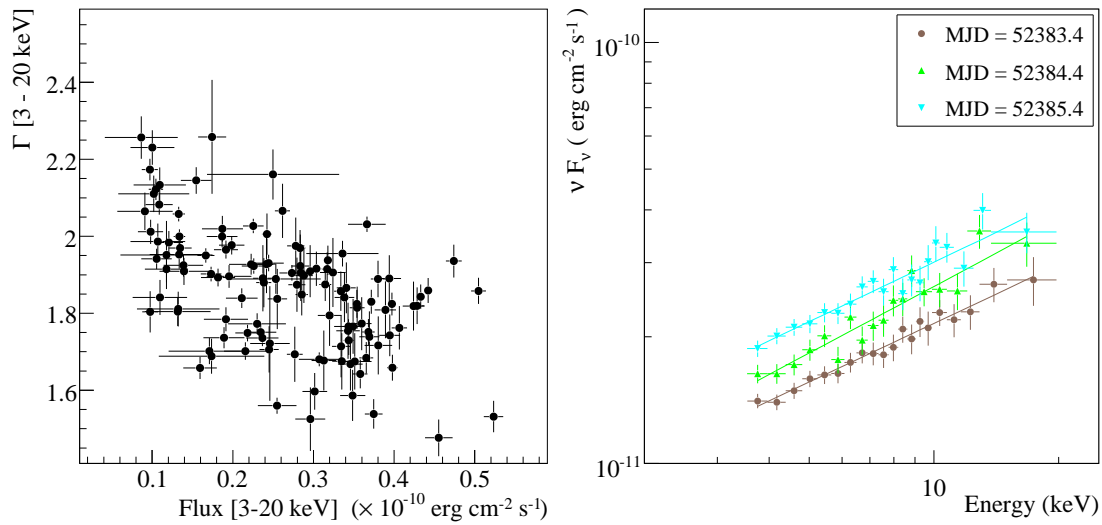


Figure 6.23: X-ray spectral properties of H1426+428 from 7 Mar. to 15 Jun. 2002 (light curve in figure 6.22). Shown (left) is the *RXTE* PCA photon index Γ versus the 3–20 keV integral flux. (Right) is the *RXTE* PCA energy spectrum from 19–21 Apr. 2002.

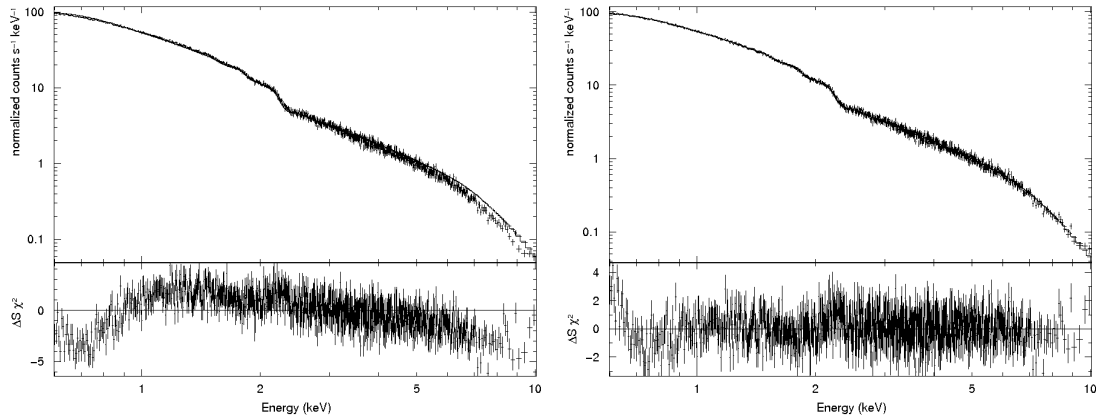


Figure 6.24: Spectral curvature in the X-ray spectrum of Mrk 421. (Left) Power law fit to the *XMM-Newton* PN energy spectrum of Mrk 421 on 10 Dec. 2003 with fixed galactic absorption $N_{\text{H,Gal}} = 1.61 \cdot 10^{20} \text{ cm}^{-2}$. (Right) Log-parabolic model fit to the same *XMM-Newton* PN spectrum. The χ^2 residuals to the model are shown below the energy spectrum.

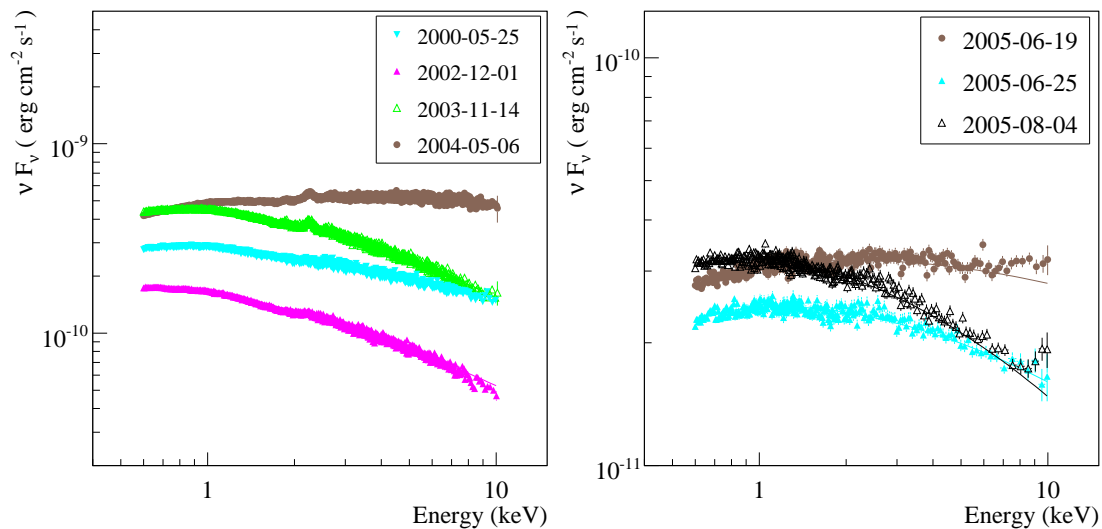


Figure 6.25: *XMM-Newton* PN energy spectrum of (left) Mrk 421, and (right) H1426+428.

presented for the total duration of each observation. Table 6.7 lists the best fit results to a power law or log-parabolic model for 21 *XMM-Newton* PN observations of Mrk 421. For 10 of the 21 observations, a fit to the power law model resulted in a poor $\chi_r^2 > 2$. A hard spectrum was recorded in the 0.6–10 keV band for observations at a high integral flux level. On 6 May 2004, a power law photon index of $\Gamma = 1.96 \pm 0.001$ suggests a peak synchrotron energy was $E_p > 10$ keV. Figure 6.25 (left) shows the *XMM-Newton* PN energy spectra of Mrk 421 from 4 observations, including the high flux 6 May 2004 observation. Spectral curvature is evident in each of the 4 selected energy spectra of Mrk 421. To test for curvature in each of the complete Mrk 501 and H1426+428 *XMM-Newton* PN data sets, both a power law and log-parabolic model were fit the spectra. Table 6.8 shows the model fit results for both sources. For H1426+428, the log-parabolic model gave consistently lower χ_r^2 values than with a power law model, however the the highest measured curvature term was a moderate $b = 0.25 \pm 0.02$. Figure 6.25 (right) shows the *XMM-Newton* PN energy spectrum of H1426+428 for 3 observations in 2005. The energy spectrum on 19 Jun. 2005 was seen to be much harder than on 4 Aug. 2005 at a comparable flux level. Detailed studies of the *XMM-Newton* PN data on the 3 TeV blazars are given for 18 of the 30 total observations, as referenced in tables 6.5 and 6.6, while for the other 12 observations, first results are presented here.

Start Date	$F_{0.6-10keV}$ (f.u.) ^a	Γ	χ_r^2	a	b	χ_r^2
2000-05-25	5.94 ± 0.01	2.24 ± 0.001	1.91	2.30 ± 0.001	0.10 ± 0.003	1.30
2000-05-25	6.44 ± 0.02	2.30 ± 0.001	1.27	2.25 ± 0.001	0.10 ± 0.005	1.05
2000-11-02	2.08 ± 0.01	2.55 ± 0.002	1.30	2.54 ± 0.002	0.15 ± 0.007	1.10
2000-11-13	8.20 ± 0.02	2.34 ± 0.001	3.37	2.34 ± 0.001	0.27 ± 0.004	1.18
2000-11-14	7.49 ± 0.02	2.36 ± 0.001	2.64	2.35 ± 0.001	0.23 ± 0.004	1.17
2001-05-08	5.71 ± 0.01	2.29 ± 0.001	2.85	2.29 ± 0.001	0.22 ± 0.004	1.20
2002-05-04	1.96 ± 0.01	2.74 ± 0.003	1.66	2.71 ± 0.002	0.42 ± 0.001	1.03
2002-05-05	1.15 ± 0.01	2.90 ± 0.007	0.88	2.84 ± 0.007	0.47 ± 0.002	0.72
2002-11-14	9.04 ± 0.02	2.13 ± 0.001	1.80	2.13 ± 0.001	0.15 ± 0.004	1.24
2002-11-14	9.33 ± 0.02	2.22 ± 0.003	1.70	2.19 ± 0.004	0.35 ± 0.001	1.19
2002-11-15	8.95 ± 0.02	2.22 ± 0.003	1.57	2.19 ± 0.004	0.37 ± 0.001	1.10
2002-12-01	3.40 ± 0.01	2.40 ± 0.001	5.96	2.40 ± 0.001	0.18 ± 0.002	1.77
2002-12-02	4.14 ± 0.01	2.42 ± 0.004	1.31	2.39 ± 0.004	0.39 ± 0.015	0.94
2002-12-02	4.90 ± 0.01	2.34 ± 0.004	1.39	2.30 ± 0.005	0.41 ± 0.016	1.01
2003-06-01	3.25 ± 0.01	2.55 ± 0.001	2.37	2.55 ± 0.002	0.29 ± 0.006	1.09
2003-11-14	9.68 ± 0.02	2.32 ± 0.001	10.90	2.32 ± 0.001	0.27 ± 0.002	1.88
2003-12-10	4.83 ± 0.01	2.29 ± 0.001	1.94	2.28 ± 0.002	0.23 ± 0.006	1.13
2004-05-06	14.22 ± 0.03	1.96 ± 0.001	3.65	1.96 ± 0.001	0.07 ± 0.001	2.46
2005-11-07	8.64 ± 0.02	2.35 ± 0.001	2.76	2.35 ± 0.002	0.27 ± 0.005	1.23
2005-11-09	9.05 ± 0.02	2.42 ± 0.001	12.90	2.42 ± 0.001	0.27 ± 0.001	1.77
2006-12-05	2.97 ± 0.01	2.63 ± 0.001	3.35	2.63 ± 0.001	0.27 ± 0.004	1.24

Table 6.7: Best fit model parameters for either a power law or log-parabolic model. Notes: (a) The integral flux in the 0.6–10 keV band is given in units (f.u.) of 10^{-10} erg cm⁻² s⁻¹.

Start Date	$F_{0.6-10keV}$ (f.u.) ^a	Γ	χ_r^2	a	b	χ_r^2
Mrk 501						
2002-07-12	0.869 ± 0.002	2.35 ± 0.01	1.02	2.26 ± 0.01	0.18 ± 0.0	0.99
2002-07-12	0.889 ± 0.002	2.31 ± 0.01	1.41	2.26 ± 0.01	0.10 ± 0.0	1.02
H1426+428						
2001-06-16	0.452 ± 0.002	1.81 ± 0.01	0.99	1.83 ± 0.01	0.02 ± 0.01	0.99
2004-08-04	0.413 ± 0.001	2.12 ± 0.01	1.46	2.01 ± 0.01	0.24 ± 0.01	1.07
2004-08-06	0.414 ± 0.002	2.13 ± 0.01	1.50	2.02 ± 0.01	0.24 ± 0.01	1.07
2005-01-24	0.492 ± 0.003	2.18 ± 0.01	1.38	2.07 ± 0.02	0.25 ± 0.02	1.13
2005-06-19	0.861 ± 0.002	2.00 ± 0.01	1.13	1.95 ± 0.01	0.11 ± 0.01	1.04
2005-06-25	0.627 ± 0.001	2.10 ± 0.01	1.23	2.03 ± 0.01	0.17 ± 0.01	1.04
2005-08-04	0.748 ± 0.002	2.22 ± 0.01	1.49	2.11 ± 0.01	0.24 ± 0.01	1.07

Table 6.8: Best fit model parameters for either a power law or log-parabolic model. Notes: (a) The integral flux in the 0.6–10 keV band is given in units (f.u.) of 10^{-10} erg cm⁻² s⁻¹.

Chapter 7

Interpretation

Long-term observations of Mrk 421 revealed strong, complicated X-ray and TeV γ -ray variability. Additionally, the TeV blazars Mrk 501 and H1426+428 were observed from 2001 to 2006 at low to moderate X-ray and γ -ray flux levels. Tentative conclusions on three important questions in TeV blazar studies are discussed in the context of previous claims and results:

1. Are the X-ray and TeV γ -ray flux states well correlated on day timescales?
2. Can averaged spectra from sparse observations characterize Spectral Energy Distributions?
3. How does the long-term X-ray and γ -ray flux variability differ between TeV blazars?

The first question is addressed in section 7.1 by combining simultaneous flux correlations from a large sample of *RXTE* PCA and Whipple 10 m observations on Mrk 421 spanning periods of up to 6 months. Section 7.2 presents SEDs for Mrk 421, Mrk 501, and H1426+428 using spectral results in this work, along with archive EUVE and EGRET data. Synchrotron Self-Compton (SSC) model curves are shown for the SEDs, together with a discussion of the varying model parameters. The second question is prompted both by a review of the Mrk 421 X-ray and TeV spectral variability shown in chapters 5 and 6, and by the construction of SEDs for all three TeV blazars from both simultaneous or time-averaged spectra. Section 7.3 answers the third question by comparing long-term *RXTE* ASM and Whipple 10 m flux measurements, as presented in chapter 5. Lastly, a short conclusion is reached based on these three questions: mainly the need for well sampled, high sensitivity multiwavelength observations of TeV blazars.

7.1 Correlation of X-ray and TeV γ -ray Flux States

For Mrk 421, a large spread was observed between the simultaneous X-ray and TeV γ -ray integral fluxes over a period of 6 years. Figure 7.1 shows the combined Whipple 10 m integral flux $F_{>0.6\text{TeV}}$

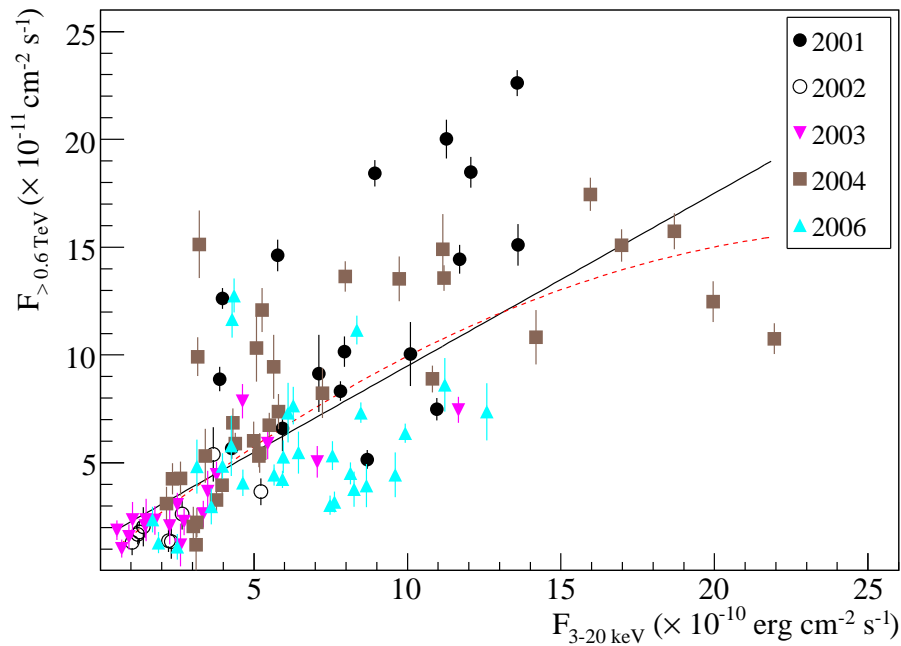


Figure 7.1: X-ray and TeV γ -ray flux correlation of Mrk 421 from all joint *RXTE* PCA and Whipple 10 m observations since 2000 (see sections 6.1 and 6.3). Linear (black line) and quadratic (red dashed line) functions were fit to the data.

versus the *RXTE* PCA 3–20 keV integral flux from all joint observations since 2000. A weak linear correlation coefficient of $r = 0.61$ is in contrast to significant linear correlations ($r > 0.9$) measured for partially resolved flares in chapter 6. Previous studies of Mrk 421 claimed highly correlated X-ray to TeV variability (Rebillot et al. 2006; Krawczynski et al. 2001). Here, a fit to the total Mrk 421 data set with either a linear or quadratic function yields a very poor χ_r^2 of >25 . As described in section 5.2.2, a quadratic function $F_i^X \propto (F_i^\gamma)^2$ is predicted in the Synchrotron Self-Compton (SSC) model due to the flux dependence on the electron density. Sparse temporal sampling with offsets of up to 10 hour between observations in the two energy bands diminish the power of variability studies. Examples of both “orphan” X-ray and TeV γ -ray flares were recorded, where a high flux was observed in one energy band, while the other band showed no significant flaring. Since flaring evolution was only partially resolved in all data sets, a characteristic flaring timescale was not clear. In summary, from this large data set no clear X-ray to TeV γ -ray flux correlation was evident, however the sparse sampling restricted a detailed temporal study.

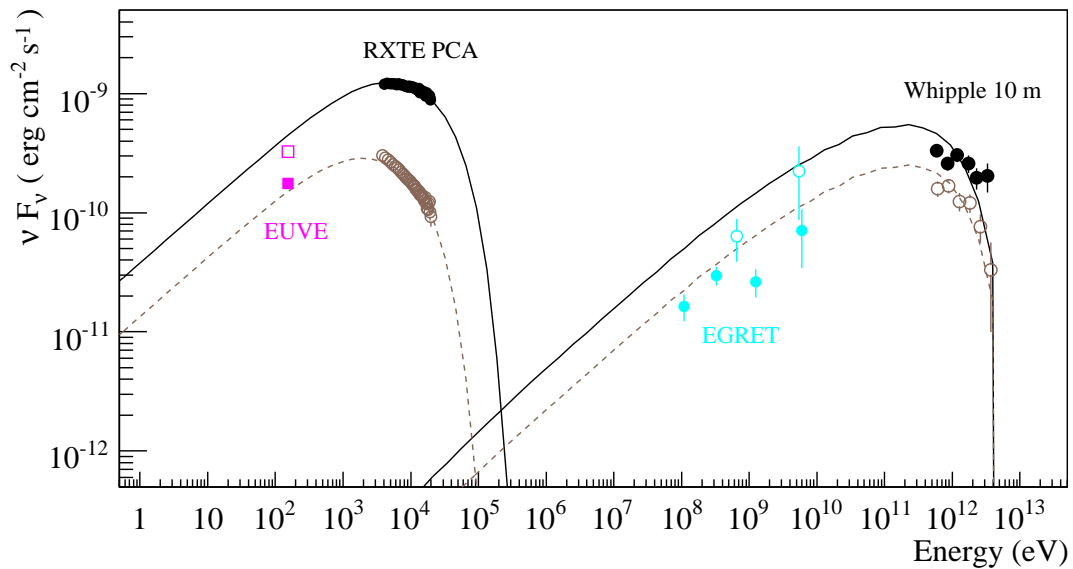


Figure 7.2: Spectral energy distributions of Mrk 421 from simultaneous *RXTE* PCA and Whipple 10 m observations at a high flux state on 21 April 2004 (black points), and at a low flux state on 22 March 2001 (brown open circles). The Whipple 10 m spectra were corrected for EBL absorption using the “Low-SFR” model in (Kneiske et al. 2004). The archive 1991–1994 EGRET spectrum (cyan) is from (Macomb et al. 1995). Extreme Ultraviolet fluxes are from EUVE observations in 1998 from (Tanihata et al. 2004). The parameters for the SSC model to the high flux state (solid line) are: $\delta = 15$, $B = 0.26$ G, $R = 7 \cdot 10^{15}$ cm, $w_e = 0.062$ ergs cm^{-3} , $p_1 = 2$, $p_2 = 3$, $\log(E_b) = 11$, $\log(E_{min}) = 6.5$, and $\log(E_{max}) = 11.5$. For the low flux state, the same SSC parameters are used, except $B = 0.11$ G, and $w_e = 0.08$ ergs cm^{-3} . The SSC model is from (Krawczynski et al. 2004).

7.2 Spectral Energy Distributions of TeV Blazars

This section addresses the issue of constructing spectral energy distributions (SEDs) for variable TeV blazars from either sparsely sampled, or time-averaged and non-simultaneous spectral results. Chapter 6 presented for Mrk 421 a large range of X-ray and TeV γ -ray spectral variability, showing different hardening and softening evolutions during the rising and decay phase of flares. Nonuniform spectral behavior at similar flux states was also shown for the TeV γ -ray time-averaged spectra in figure 5.4. To test whether consistent SEDs can be assembled from the Mrk 421 data, a well studied Synchrotron Self-Compton (SSC) model was constrained to simultaneous high and low flux state spectra. The model calculates an SED for a spherical jet component (blob) of radius R moving down a conical jet with Lorentz factor Γ (Krawczynski et al. 2004). A broken power law with spectral indices p_1 and p_2 is defined for the relativistic electrons between energy lim-

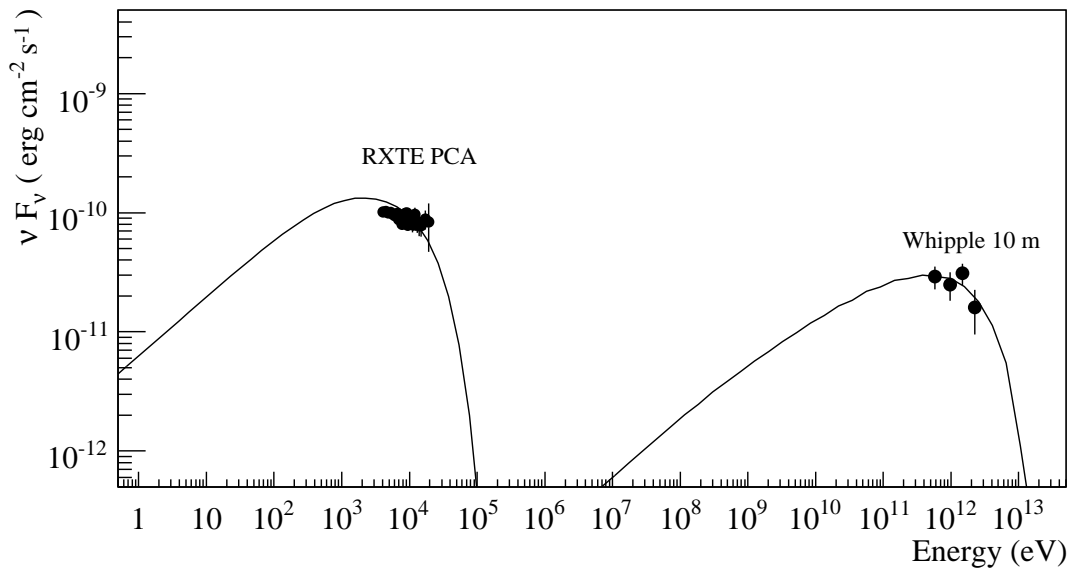


Figure 7.3: Non-simultaneous spectral energy distributions of Mrk 501 from a medium flux *RXTE* PCA observation on 12 June 2004, and from the Whipple 10 m EBL corrected energy spectrum in June 2005. The SSC model parameters are: $\delta = 25$, $B = 0.04$ G, $R = 10 \cdot 10^{15}$ cm, $w_e = 0.01$ ergs cm^{-3} , $p_1 = 2$, $p_2 = 3$, $\log(E_b) = 11.1$, $\log(E_{min}) = 6.5$, and $\log(E_{max}) = 11.7$.

its E_{min} and E_{max} . The radius R is set to values near $\sim 10^{15}$ cm dictated by the short-term γ -ray variability timescale of ~ 1 hour for $\delta \cong 20$. A magnetic field strength of $B = 0.26$ G was chosen based on previous SSC modeling of Mrk 421 (Blazejowski et al. 2005). In fact, all parameters in the SSC model were initially set to the fit values for the April 2004 high flux data in (Blazejowski et al. 2005). Figure 7.2 shows the spectral energy distributions of Mrk 421 from simultaneous *RXTE* PCA and Whipple 10 m observations presented in chapter 6. Specifically, the high flux state is from 21 April 2004, and the low flux state is from 22 March 2001. Using the previously published SSC input parameters for the April 2004 data, an electron spectrum normalization of w_e was initially adjusted to better match the April 2004 from this work. A good match was shown for the SSC model to the X-ray spectrum, however the Inverse-Compton component in the model is significantly softer than the EBL corrected Whipple 10 m energy spectrum. A better agreement is shown for the 22 March 2001 low flux spectra, however the magnetic field strength B was lowered in addition to w_e . In summary, using “reasonable” source parameters, the SED of Mrk 421 was roughly described by an SSC model, but it is not clear how each SSC source parameter is constrained.

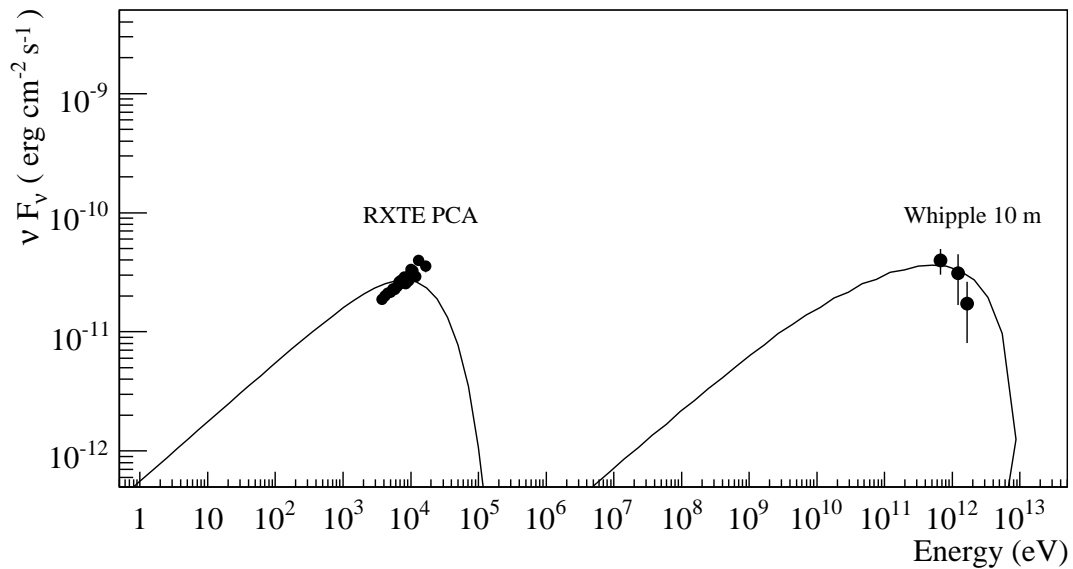


Figure 7.4: Non-simultaneous spectral Energy Distributions of H1426+428 from a medium flux *RXTE* PCA observation on 21 April 2002, and from the Whipple 10 m EBL corrected energy spectrum in March 2001. The SSC model parameters are: $\delta = 8$, $B = 0.035$ G, $R = 30 \cdot 10^{15}$ cm, $w_e = 0.045$ ergs cm^{-3} , $p_1 = 2$, $p_2 = 3$, $\log(E_b) = 11.9$, $\log(E_{min}) = 6.5$, and $\log(E_{max}) = 12$.

Spectral Energy Distributions of Mrk 501 and H1426+428

Due to the weaker Whipple 10 m detections of Mrk 501 and H1426+428 than for Mrk 421, time-averaged TeV γ -ray spectral were used with selected medium flux level *RXTE* PCA spectra to build SEDs. Figure 7.3 shows the spectral energy distributions of Mrk 501 from the *RXTE* PCA spectra on 12 June 2004, and the Whipple 10 m energy spectrum from 4.8 hours of data in June 2005. The TeV γ -ray spectrum was corrected for EBL absorption using the “Low-SFR” model in (Kneiske et al. 2004). The radius R and magnetic field strength B were initially set to the values for a high state Mrk 501 flare in (Krawczynski et al. 2000). However, these parameters required adjusting to match the medium state SED presented here, with a relatively low $\delta = 8$. Over a restricted range of parameter space, the SSC synchrotron spectrum remained significantly harder than the observed *RXTE* PCA spectrum. Still, due to the non-simultaneous data, it is difficult to draw conclusions on the appropriateness of the SSC modeling results. Motivated by the strong X-ray spectral variability shown for H1426+428 in section 6.3, an approximate medium flux level was chosen to build an SED with the Whipple 10 m energy spectrum from March 2001. Figure 7.4 shows the SED of H1426+428 using the *RXTE* PCA spectrum from 21 April 2002, and the Whipple 10 m spectrum in March 2001 corrected for EBL absorption. No good match could be attained using small deviations from the SSC parameter range applied to Mrk 421 and Mrk 501.

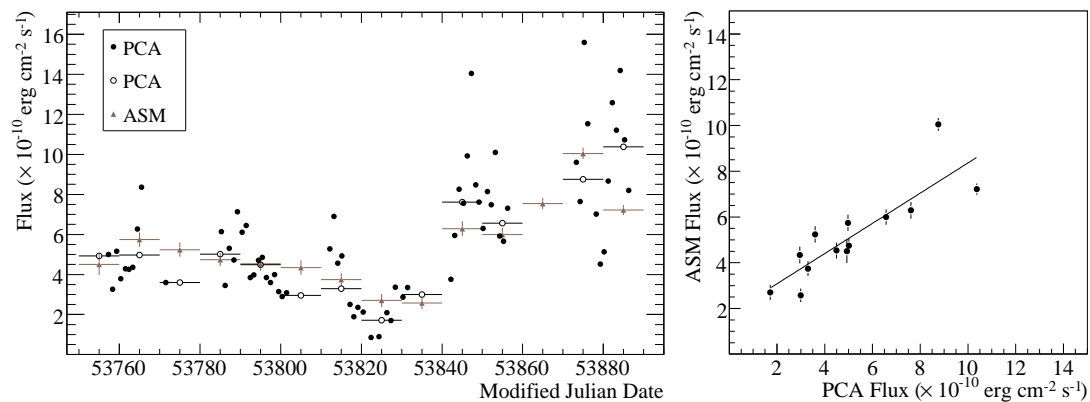


Figure 7.5: Correlation of derived *RXTE* ASM fluxes with *RXTE* PCA flux measurements of Mrk 421 in Jan. to May 2006. (Left) Light curve of Mrk 421, taken from figure 6.17, with time bins of 10 days for the mean *RXTE* PCA and ASM fluxes. (Right) Correlation of the simultaneous 10 day fluxes, with a linear fit to the data. *RXTE* ASM fluxes were calculated with the PIMMS tool using an input power law spectrum of $\Gamma = 2.5$ (HEASARC 2007).

The hard spectrum observed with *RXTE* PCA required an increase in the maximum energy E_{max} of the electron spectrum. Lastly, the large, nonuniform spectral variability within Mrk 421, and wide range of SSC parameters needed to constrain spectra between the 3 TeV blazars emphasizes the ambiguity in results based on selected SEDs.

7.3 Long-term X-ray and TeV γ -ray Flux Variability

The question of a characteristic year timescale variability in TeV blazars is addressed here using the long-term *RXTE* ASM and Whipple 10 m flux measurements presented in chapter 5. Before discussing results from the long-term light curves, the *RXTE* ASM rates are converted to flux units using spectral information from chapter 6. A cross-comparison of the measured *RXTE* PCA and derived ASM fluxes is presented below to verify the technique.

Determining the Long-term *RXTE* ASM Fluxes

A systematic study of the *RXTE* ASM flux measurements was made possible using the detailed day timescale *RXTE* PCA studies of TeV blazars in chapter 6, and from the PIMMS tool provided by (HEASARC 2007). The PIMMS tool calculates the expected count rate for a large number of X-ray missions, including *RXTE* ASM, using an input source spectrum over a given energy range. A joint light curve of Mrk 421 from Jan. to May 2006 was constructed to serve as a cross-comparison between the measured *RXTE* PCA fluxes and derived ASM fluxes (see sections 5.2.1

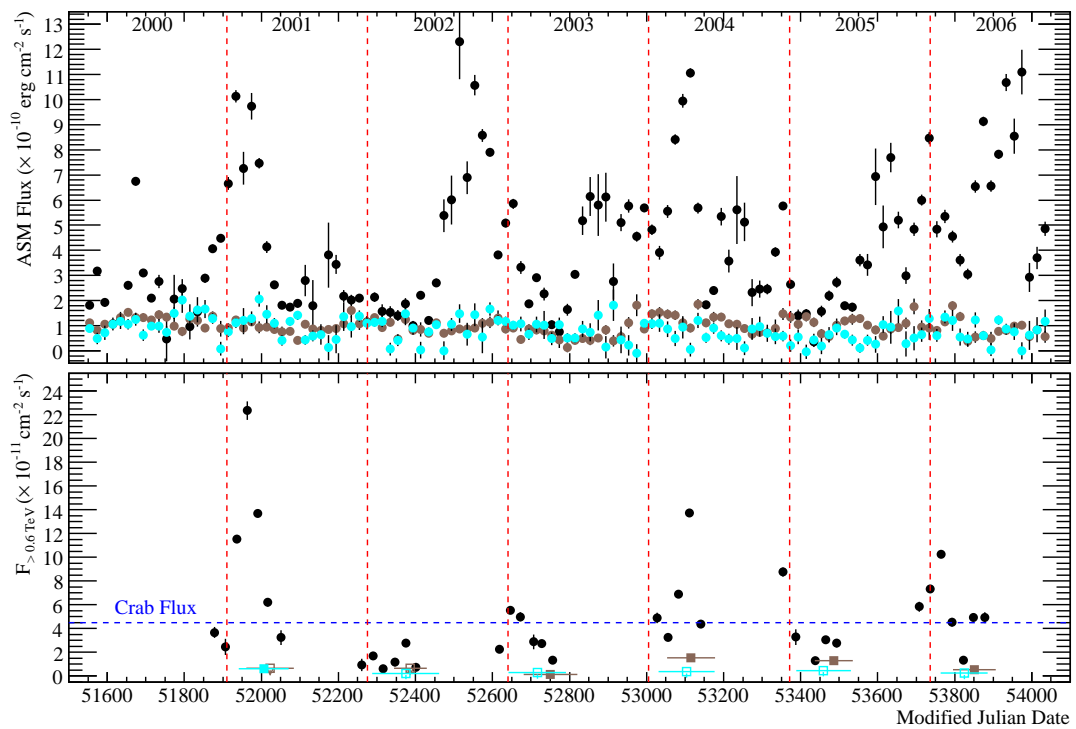


Figure 7.6: Long-term X-ray and TeV γ -ray light curve of Mrk 421 (black points), Mrk 501 (brown points), and H1426+428 (cyan points). For the Whipple 10 m integral fluxes $F_{>0.6\text{TeV}}$, upper limits at a 99.9% confidence level are shown by (empty squares).

and 6.3). The input Mrk 421 spectrum to the PIMMS tool was a power law with photon index $\Gamma = 2.5$ over the PCA energy range of 3–20 keV, as determined from figure 6.17. For Mrk 421, the redshift $z = 0.031$ and Galactic column density $N_{\text{H,Gal}} = 1.61 \cdot 10^{20} \text{ cm}^{-2}$ were the remaining inputs for the PIMMS tool. Figure 7.5 (left) shows the joint Mrk 421 light curve, with time bins of 10 days for the mean *RXTE* PCA and ASM fluxes. Figure 7.5 (right) shows a correlation of the *RXTE* PCA and ASM fluxes in bins of 10 days. A high linear correlation coefficient of $r = 0.93$ was determined for the Mrk 421 light curve, confirming that *RXTE* ASM count rate is reasonably calibrated at long integrations (>10 days) for sources with a known X-ray spectrum. However, as shown in section 6.3, TeV blazars exhibits a high degree of X-ray spectral variability, limiting the reliability of ASM fluxes. Still, it is useful to estimate the long-term X-ray fluxes of TeV blazars from the *RXTE* ASM count rates. For Mrk 501, the ASM fluxes were calculated from PIMMS using a power law input spectrum of $\Gamma = 2.3$, as estimated from figure 6.20. For H1426+428, an input power law input spectrum of $\Gamma = 1.8$ was used in PIMMS, as determined from figure 6.22.

Comparing the Long-term X-ray and TeV γ -ray Light Curve of TeV Blazars

Figure 7.6 shows a combined long-term light curve of Mrk 421, Mrk 501, and H1426+428 using the *RXTE* ASM and Whipple 10 m integral fluxes, as calculated in chapter 5. The significantly greater flaring amplitude of Mrk 421 relative to the other two TeV blazars is clear. The lack of strong month timescale flaring in either Mrk 501 or H1426+428 over a 5 year period highlights the unique long-term flaring nature of Mrk 421.

7.4 Conclusion

The three observational questions raised here are far from a complete synopsis of the open questions in TeV blazar studies. However, this discussion has led to the pointed conclusion that high sensitivity X-ray and TeV γ -ray observations with near continuous temporal coverage are needed to better resolve complex flaring states. To this aim, simultaneous X-ray observations with H.E.S.S. , MAGIC, and VERITAS offer many new insights into the flaring nature of TeV blazars. Particularly, the spectral evolution of rising and decaying phases on timescales of hours to minutes. These observations offer significantly more constraining limits to SSC and other emission models by defining more clearly the characteristic flaring timescales and possibly correlated flux and spectral states between energy bands.

Bibliography

- Aharonian, F. et al. 1997; A&A, 327, L5.
- Aharonian, F. et al. 1999a; A&A, 342, 69.
- Aharonian, F. et al. 1999b; A&A, 349, 11.
- Aharonian, F. et al. 1999c; A&A, 349, 29.
- Aharonian, F. et al. 2001a; ApJ, 546, 898.
- Aharonian, F. et al. 2001b; APh, 15, 335.
- Aharonian, F. et al. 2002a; A&A, 384, L23.
- Aharonian, F. et al. 2002b; A&A, 384, 834.
- Aharonian, F. et al. 2002c; A&A, 393, 89.
- Aharonian, F. et al. 2003; A&A, 403, 523.
- Aharonian, F. et al. 2004; ApJ, 614, 897.
- Aharonian, F. et al. 2005a; A&A, 436, L17.
- Aharonian, F. et al. 2005b; A&A, 437, 95.
- Aharonian, F. et al. 2005c; A&A, 442, 895.
- Aharonian, F. et al. 2006a; A&A, 448, L19.
- Aharonian, F. et al. 2006b; Nature, 440, 1018.
- Aharonian, F. et al. 2006c; A&A, 455, 461.
- Aharonian, F. et al. 2006d; A&A, 457, 899.
- Aharonian, F. et al. 2007a; A&A, 473, L25.

Aharonian, F. et al. 2007b; *A&A*, 475, L9.

Albert, J. et al. 2006a; *ApJ*, 642, L119.

Albert, J. et al. 2006b; *ApJ*, 648, L105.

Albert, J. et al. 2007a; accepted for *APh*, astro-ph/0702475.

Albert, J. et al. 2007b; *ApJ*, 666, 17.

Albert, J. et al. 2007c; *ApJ*, 667, 21.

Albert, J. et al. 2007d; *ApJ*, 669, 862.

Alfven, H. and Herlofson, N. 1950; *Phys. Rev.*, 78, 616.

Andrew, B.H. et al. 1969; *Nature*, 223, 598.

Angel, J.R.P. and Stockman, H.S. 1980; *ARA&A*, 18, 321.

Armstrong, P. et al. 1999; *Exp. Ast.*, 9, 51.

Baade, W. and Minkowski, R. 1954; *ApJ*, 119, 215.

Baade, W. 1956; *ApJ*, 123, 550.

Barrau, A. et al. 1998; *NIM A*, 416, 278.

Bazzano, A. et al. 2006; *ApJ*, 649L, 9.

Beckmann, V. 2001; Ph.D. thesis, Hamburg, Germany.

Berge, D. 2006; Ph.D. thesis, Heidelberg, Germany.

Bennett, A.S. 1962; *MNRAS*, 125, 75.

Blandford, R.D. and Rees, M.J. 1978; in *Pittsburg Conference on BL Lac objects*, ed. A.M. Wolfe.

Blazejowski, M. et al. 2005; *ApJ*, 630, 130.

Blustin, A.J. et al. 2004, *A&A*, 417, 61.

Bond, I.H., Hillas, A.M., Bradbury, S.M. 2003; *Aph*, 311, 321.

Bradbury, S.M. et al. 1996; *A&A*, 320, L5.

Bradbury, S.M. and Rose, H.J. 2002; *NIM A*, 481, 521.

Bradt, H.V. et al. 1993, A&AS, 97, 355B.

Brinkmann, W. et al. 2001; A&A, 365, L162.

Brinkmann, W. et al. 2003; A&A, 402, 929.

Brinkmann, W. et al. 2005; A&A, 443, 397.

Buckley, J.H. et al. 1996; ApJ, 472, L9.

Burbidge, G.R. 1970; ARA&A, 8, 369.

Catanese, M. et al. 1997; ApJ, 487, L143.

Catanese, M. et al. 1998; ApJ, 501, 616.

Cawley, M. et al. 1985; in Proceedings of the 19th ICRC, 1, 264.

Celotti, A. et al. 1998; MNRAS, 293, 239.

Chadwick, P.M. et al. 1999; ApJ, 513, 161.

Collin, S. 2006; in AIP Conference Proceedings, 861, 587.

CORSIKA Images; <http://www.ast.leeds.ac.uk/fs/>

Costamante, L. and Ghisellini, G. 2002; A&A, 384, 56.

Cui, W. 2004; ApJ, 605, 662.

Curtis, H.D.; PASP, 29, 52.

M.K. et al. 2005; ApJ, 621, 181.

Daum, A. et al. 1997; APh, 8, 1.

Davies, J. and Cotton, E. 1957; Journal of Solar Energy, 1, 16.

de Korte, P.A.J. et al. 1981; Sp. Sci. Rev., 30, 495.

de la Calle Pérez, I. 2003; Ph.D. thesis, University of Leeds, UK.

de Vaucouleurs, G. 1959; *Handbuch der Physik*, ed. Flugge, S. Springer-Verlag.

Dermer, C.D. and Schlickeiser, R. 1994, ApJS, 90, 945.

Dhar, V.K. et al. 2005; in Proceedings of the 29th ICRC, 4, 179.

- Dickey, J.M. and Lockman, F.J. 1990; ARA&A, 28, 215.
- Djannati-Atai, A. et al. 1999; A&A, 350, 17.
- Dole, H. et al. 2006; A&A, 451, 417.
- Dwek, E. and Krennrich, F. 2005a; ApJ, 618, 657.
- Dwek, E. et al. 2005b; ApJ, 634, 155.
- Enomoto, R. et al. 2006; ApJ, 368, 397.
- Falcone, A. et al. 2004; ApJ, 601, 165.
- Fanaroff, B.L. and Riley, J.M. 1974; MNRAS, 167, 31.
- Ferrarese, L. and Ford, H. 2005; Space Science Reviews, 116, 523.
- Foschini, L. et al 2006; A&A, 453, 829.
- Fossati, G. et al. 1998a; MNRAS, 299, 433.
- Fossati, G. 1998b; Ph.D. thesis, ISAS, Italy.
- Gaidos, J.A. et al. 1996; Nature, 383, 319.
- Gehrels, N. and Michelson, P. 1999; APh, 11, 277.
- Gehrels, N. et al. 2004; ApJ, 611, 1005.
- Ghisellini, G. et al. 1996; A&AS, 120, 503.
- Ghisellini, G. and Celotti, A. 2001; A&A, 379, L1.
- Giacconi, R. et al. 1971; ApJ, 165, L27.
- Giacconi, R. et al. 1974; ApJS, 237, 27.
- Giacconi, R. et al. 1979; ApJ, 230, 540.
- Giebels, B. et al. 2007; A&A, 462, 29.
- GLAST* LAT Team; <http://www-glast.slac.stanford.edu/>
- Gliozzi, M. et al. 2006; ApJ, 646, 61.
- Gould, R.J. and Schreder, G. 1967; Phys. Rev., 155, 1408.
-

Greenstein, J.L. and Schmidt, M. 1964; ApJ, 140, 1.

Grube, J. et al. 2005; in Proceedings of the 29th ICRC, 4, 407.

Hao, L. et al. 2005; ApJ, 129, 1783.

Hara, T. et al. 1993; NIM A, 332, 300.

Hartman, R.C. et al. 1992; ApJ, 385, L1.

Hartman, R.C. et al. 1999; ApJS, 123, 79.

Hauser, M.G. et al. 1998; ApJ, 508, 25.

Hazard, C. et al. 1963; Nature, 197, 1037.

NASA HEASARC; <http://heasarc.nasa.gov/>.

Heck, D. et al. 1998; FZKA 6019, <http://www-ik.fzk.de/corsika/>

Heitler, W. 1954; *Quantum Theory of Radiation*, Dover Press.

Helene, O. 1983; NIM A, 212, 319.

Hillas, A.M. 1985; in Proceedings of the 19th ICRC 3, 445.

Hillas, A.M. et al. 1998; ApJ, 503, 744.

Hoffmeister, C. 1929; Astro. Nachr., 236, 90.

Hofmann, W. et al. 2006; 23rd Texas Symposium, <http://www.texas06.com>

Holder, J. et al. 2006; APh, 25, 391.

Horan, D. et al. 2002; ApJ, 571, 753.

Horan, D. et al. 2004; ApJ, 603, 51.

Hubble, E.P. 1925; The Observatory, 48, 139.

Hubble, E.P. 1926; ApJ, 64, 321.

NASA Hubble Heritage Project; <http://heritage.stsci.edu/2000/20/index.html>

Johoda, K. et al. 1996; SPIE, 2808, 59.

Johoda, K. et al. 2006; ApJS, 163, 401.

Jansen, F. et al. 2001; A&A, 365, L1.

Jelley, J.V. 1958; *Čerenkov Radiation*, Pergamon Press.

Jones, T.W. et al. 1974; ApJ, 188, 353.

Jones, T.W. et al. 1974; ApJ, 192, 261.

Kataoka, J. et al. 2001; ApJ, 560, 659.

Katarzynski, K. et al. 2003; A&A, 410, 101.

Kauffmann, G. et al. 2003; MNRAS, 341, 54.

Kellermann, K.I. et al. 1971; ApJ, 169, 1.

Kennicutt, R.C. 1998; ARA&A, 36, 189.

Kerrick, A.D. et al. 1995; ApJ, 438, L59.

Khachikian, E.Y. and Weedman, D.W. 1974; ApJ, 189, L99.

Kieda, D. et al. 2007; in Proceedings of the 1st GLAST Symposium.

Kildea, J. 2002; Ph.D. thesis, University College Dublin, Ireland.

Kildea, J. et al. 2007; APh, 28, 182.

Kneiske, T.M. et al. 2004; A&A, 413, 807.

Kniffen, D.A. et al. 1993; ApJ, 411, 133.

Kondo, Y. et al. 1981; ApJ, 243, 690.

Kranich, D. et al. 1999; APh, 12, 65.

Kraushaar, W.L. and Clark, G.W. 1962, Phys. Rev. Lett., 8, 106.

Krawczynski, H. et al. 2000; A&A, 353, 97.

Krawczynski, H. et al. 2001; ApJ, 559, 187.

Krawczynski, H. et al. 2004; ApJ, 601, 151.

Krennrich, F. et al. 2002; ApJ, 575, L9.

Kühl, H. et al. 1981, A&A, 45, 367.

Kunieda, H. et al. 2006; SPIE, 6266E, 4.

Lamer, G. and Wagner, S.J. 1998; A&A, 331, L13.

LeBohec, S. et al 1998; NIM A, 416, 425.

LeBohec, S. and Holder, J. 2003; APh, 19, 221.

Lessard, R.W. et al. 2001; APh, 15, 1.

Levine, A.M. et al. 1996; ApJ, 469, L33.

Lichti, G. and Georgii, R. 2001; *The Universe Viewed in Gamma-Rays*, ed Schönfelder V. Springer Press.

Li, T.P. and Ma, Y.Q. 1983; ApJ, 272, 317.

Lin, Y.C. et al. 1992; ApJ, 401, L61.

Lockman, F.J. and Savage, B.D. 1995; ApJS, 97, 1.

Macdonald, G.H. et al. 1968; MNRAS, 138, 259.

Mackay, C.D. 1971; MNRAS, 154, 209.

Macomb, D.J. et al. 1995; ApJ, 449, L99.

Mannheim, K. 1998; Science, 279, 684.

Markarian, B.E. 1969; ApJ, 3, 24.

Maraschi, L. et al. 1986; ApJ, 310, 325.

Maraschi, L. et al. 1992; ApJ, 397, L5.

Mazin, D. and Raue, M. 2007; A&A, 471, 439.

Mirzoyan, R. et al. 1994; NIM A, 351, 513.

Mirzoyan, R. et al. 2005; in Proceedings of the 29th ICRC, 4, 23.

Mohanty, G. et al. 1998; APh, 9, 15.

Moriarty, P. et al. 1997; APh, 7, 315.

Morrison, R. and McCammon, D. 1983; ApJ, 270, 119.

Mücke, A. et al. 2003; APh, 18, 593.

Mushotzky, R. 2004; *Supermassive Black Holes in the Distant Universe*, ed Barger, A. Springer Press.

Nishiyama, T. et al. 199; in Proceedings of the 26th ICRC, 3, 370.

Oke, J.B. and Gunn, J.E. 1974; ApJ 189L, 50.

Osterbrock, D.E. 1978; Proc. Nat. Acad. Sci., 75, 540.

Padovani, P. 2002; ApJ, 581, 895.

Padovani, P. 2007; Ap&SS, 10509, 2.

Pare, E. et al. 1991; in Proceedings of the 22nd ICRC 1, 492.

Pian, E. et al. 1998; ApJ, 492, L17.

Perlman, E. et al. 1996; ApJS, 104, 251.

Perlman, E. et al. 2005; ApJ, 625, 727.

Petry, D. et al. 2002; ApJ, 580, 104.

Pühlhofer, G. et al. 2003; APh, 20, 267.

Punch, M. et al. 1992; Nature, 358, 477.

Quinn, J. et al. 1996; ApJ, 456, L83.

Quinn, J. et al. 1999; ApJ, 518, 693.

Rao, M.V.S. and Sinha, S. 1988; JPhG, 14, 811.

Ravasio, M. et al. 2004; A&A, 424, 841.

Rebillot, P.F. et al. 2006; ApJ, 641, 740.

Rees, M.J. 1966; Nature, 211, 468.

Rees, M.J. 1977; Annals N.Y. Acad. Sci., 302, 613.

Reynolds, P.T. et al. 1993; ApJ, 404, 206.

Ricketts, M.J. et al. 1976; Nature, 259, 546.

Roberts, M.S. and Haynes, M.P. 1994; *ARA&A*, 32, 115.

Rose, H.J. et al. 1995; in Proceedings of the 24th ICRC, 3, 464.

Rose, H.J. et al. 1995; in Proceedings of the 24th ICRC, 3, 766.

Rothschild, R.E. et al. 1998; *ApJ*, 496, 538.

RXTE ASM Data Products; http://heasarc.gsfc.nasa.gov/docs/xte/asm_products.html

Sandage, A. 1965; *ApJ*, 141, 1560.

Schroedter, M. 2004; Ph.D. thesis, University of Arizona, USA.

Schubnell, M.S. et al. 1996; *ApJ*, 460, 644.

Schwartz, D.A. et al. 1978; *ApJ*, 224L, 103.

Schwartz, D.A. and W.H. 1983; *ApJ*, 266, 459.

Sembay, S. et al. 2002; *ApJ*, 574, 634.

Seyfert, C.K. 1943; *ApJ*, 97, 28.

Shields, G. 1999; *PASP*, 111, 661.

Sikora, M. et al. 1994; *ApJ*, 421, 153.

Sparks, W.B. et al. 1996; *ApJ*, 473, 254.

Stark, A.A. et al. 1992; *ApJS*, 79, 77.

Stein, W.A. et al. 1976; *ARA&A*, 14, 173.

Swanenburg, B.N. et al. 1978; *Nature*, 275, 298.

Takahashi, T. et al. 1996; *ApJ*, 470, 89.

Tanihata, C. et al. 2004; *ApJ*, 601, 759.

Tavani, M. et al. 2006; *SPIE*, 6266E, 2.

Tavecchio, F. et al. 1998; *ApJ*, 509, 608.

Trimble, V. 1995; *PASP*, 107, 1133.

Ulrich, M. 1973; *ApL*, 14, 89.

Urry, M.C. and Padovani, P. 1995; PASP, 107, 803.

VERITAS website; <http://veritas.sao.arizona.edu>

Veron, P. and Veron, M.P. 1975; A&A, 39, 281.

Vincent, P. et al. 2005; in Proceedings of the 29th ICRC, 5, 163.

Visvanathan, N. 1969; ApJ, 155, 133.

Visvanathan, N. 1973; ApJ, 179, 1.

Voges, W. et al. 2000; IAU Circ. 7432.

Wall, J.V. and Peacock, J.A. 1985; MNRAS, 216, 173.

Wagner, R.M. et al. 2005; in Proceedings of the 29th ICRC, 4, 163.

Wagner, R.M. 2006; Ph.D. thesis, Technischen Universitt Mnchen, Germany.

Weekes, T.C. et al. 1972; ApJ, 174, 165.

Weekes, T.C. et al. 1989; ApJ, 342, 379.

Weekes, T.C. 2003; *Very High Energy Gamma-ray Astronomy*, IOP Pub.

Weisskopf, M. et al. 2000; SPIE, 4012, 2.

Wiedemann, H. 2003; *Synchrotron Radiation*, Springer Press.

Winkler, C. et al. 2003; A&A, 411, L1.

Wu, X. and Tremaine, S. 2006; ApJ, 643, 210.

Xue, Y. et al. 2006; ApJ, 647, 194.

XMM-Newton SOC; <http://xmm.vilspa.esa.es>

Acknowledgements

I would first like to acknowledge my supervisor Joachim Rose for his enthusiasm, rigor, and insight. Second, I am truly grateful to Tom Hartquist for facilitating the funding and support which has made this thesis work possible.

Immeasurable gratitude for the support and love of my family: Mom, Dad, and Matt.

A big thank you to the Leeds VERITAS group (both current and former members): Stella Bradbury, Ignacio de la Calle Perez, Michael Daniel, Michael Hillas, Jamie Holder, Johannes Knapp, Gernot Maier, Andy Smith, and Richard White for all your support.

I've greatly enjoyed working in the VERITAS collaboration. I'd like recognize Prof. Trevor Weekes and support staff at the Whipple Observatory for facilitating my several month-long extended observing stays. I'd also like to recognize Abe Falcone, Henric Krawczynski, and Martin Pohl for their exceptional insight and teaching of both scientific and technical matters. Thanks also to Deirdre Horan, Martin Schroedter, Steve Gammell, and John Quinn for further support.

Last but not least, I would like to thank all my close friends who I've been fortunate enough to share the past 5 years with. To my long-term supportive California friends: Brian Barnes, Jeff Excell, Ryan Fly, the Gillies family (Todd, Tyler, Katie, Pat, and Pete), the Hiersche family (Mike, Channy, Matt, and Peggie), Samuel Miller, and Heather Rosaasen. Thanks to other California friends: Jessalyn Aaland, Becky Brister, Jesse Eisenhower, Becca Hsu, Will Law, Ryan Randall, and Eva Wang. A big thanks to my former housemates at 76 Beechwood View in Leeds: Shaun Alcock, Daniel Chapman, Keri Morgan, and Anthony Thomson. Another big thanks to Peter and Carolyn Kain in Portugal. Finally, thanks to my other English and German buddies: Jonathan Allen, Stephen Best, Claire Broadley, Ricky Davison, Lena Eckhart, Ben Lane, Al Mulhall, Andrew Raine, Becky Ross, Matt Robson, Frederik Schikowski, and Neil Shumsky.